

INVESTIGATING THE NEXUS OF CLIMATE, ENERGY, AND WATER AT
DECISION-RELEVANT SCALES

A Dissertation

by

QIONG SU

Submitted to the Graduate and Professional School of
Texas A&M University
in partial fulfillment of the requirements for the degree of

DOCTOR OF PHILOSOPHY

Chair of Committee,	Vijay P. Singh
Co-Chair of Committee,	Srinivasulu Ale
Committee Members,	Bruce A. McCarl
	Raghavan Srinivasan
Intercollegiate Faculty Chair,	Ronald Kaiser

December 2021

Major Subject: Water Management and Hydrological Science

Copyright 2021 Qiong Su

ABSTRACT

Providing reliable and sustainable energy and water service faces multiple challenges, including increasing demand due to population growth and economic development, degradation of water resources, depletion of fossil energy resources as well as climate change. To mitigate climate change impacts, many countries have announced their Nationally Determined Contributions (NDC) in the Paris Agreement to reduce carbon dioxide (CO₂) emissions. Water and energy systems are interdependent and have complex dynamic interactions with the socio-economic system and climate change. Policies and measures designed to increase the efficiency in one system might significantly affect the other. This dissertation developed an integrated model to simulate the interactions among socioeconomics, energy consumption, water use, water infrastructure, and receiving water systems, and to identify cost-effective solutions to meet the water and energy demands under different economic development pathways and climate futures. The dissertation includes two major parts. Part I developed and evaluated an integrated model to simulate the carbon-energy-water nexus in urbanized regions by integrating a computable general equilibrium (CGE) model and the System Dynamics and Water Environmental Model (SyDWEM), i.e., CGE-SyDWEM. The integrated model can be used to aid policymakers in energy, carbon, and water sectors to understand the complicated synergistic effects of proposed carbon mitigation strategies and water engineering measures on local/regional energy consumption, CO₂ emissions, water resources balance, and water-environment change. Part II improved the integrated

model in simulating agricultural water demand and evaluating agricultural adaptation strategies to climate change, including (1) improving the representation of the agricultural water demand module in CGE-SyDWEM by assessing several less data-intensive reference evapotranspiration models for regional irrigation water demand estimation; (2) improving the seasonal weather forecasts for real-time regional crop modeling and irrigation scheduling; and (3) reducing the uncertainty in the estimation of Crop Water Stress Index (CWSI) which is used to develop water-stress-based deficit irrigation strategies for enhancing water use efficiency, thereby conserving water resources in agricultural production.

DEDICATION

To my father, in loving memory.

ACKNOWLEDGEMENTS

I am truly grateful and indebted to Dr. Vijay P. Singh and Dr. Srinivasulu Ale, who have advised, mentored, and inspired me a lot. They were greatly instrumental not only in encouraging my research interests but also teaching me how to be successful in life.

I am thankful to Dr. Vijay P. Singh for giving me the opportunity to write the textbook titled “Irrigation Engineering: Principles, Processes, Procedures, Design, and Management” with him and assist him in teaching BAEN 464 irrigation engineering at the undergraduate level. All the knowledge I learned through this long journey will be a treasure for my future research life. He is the most self-disciplined person I know. He is also dedicated, productive, and cooperative in research. All these qualities encourage me to become a better version of myself each and every day.

I am thankful to Dr. Srinivasulu Ale for giving me the opportunity to join the development of the crop model-based mobile app, idCROP (irrigation **d**ecision support system for **C**onserving **R**esources and **O**ptimizing **P**roduction), which became parts of this dissertation.

I am thankful to my committee members, Dr. Raghavan Srinivasan and Dr. Bruce A. McCarl, for their guidance and support throughout the course of this research. Special thanks go to Dr. Raghupathy Karthikeyan for his great mentoring of my first two years’ PhD study. I am thankful to Dr. Ronald Kaiser and Dr. Prakash Khedun for their supports.

Thanks to all the idCROP team members, including Dr. Curtis B. Adams, Dr. Keith Biggers, Dr. Sushil Himanshu, Dr. Jasdeep Singh, Dr. Yubing Fan, Eric Gonzalez, and Bala Sapkota.

There are also many graduate students who I would like to thank for their friendships, including Vaishali Swaminathan, Lorena Ortiz Duque, Achla Jha, Duncan Kikoyo, Vinit Sehgal, Jeongwoo Han, Yu Zhang, and Kyungtae Lee.

Thanks also go to my friends Dr. Liqiu Cheng, Dr. Ruoxi Wu, Nan Mao, Dr. Huan Wang, Dr. Mingming Ao, Kaiyi Zhang, Xiao Shen, Man Yang, and many colleagues and the department faculty and staff for making my time at Texas A&M University a great experience. Special thanks to Chunrui Ren and Liyu Wang.

I am very thankful to my husband Yun for his love and support. My mother Guizhen Wang, my brother Rui Su, my sister-in-law Yaling Li, my other family members, Ting Liu, Xiangying Yu, Dr. Caijie Wei, Long Han, Dr. Huan Chen, Dr. Weiyu Xu, Maozhen Qiu, Xiaoqian Chen, Ping Cui, Shuyan Xie, Zhikun Zhang, Yifei Yang, their supports have made it possible for me to reach my dreams.

CONTRIBUTORS AND FUNDING SOURCES

Contributors

This work was supervised by a dissertation committee consisting of Professors Vijay P. Singh and Srinivasulu Ale of the Department of Biological and Agricultural Engineering, Professor Raghavan Srinivasan of the Departments of Ecology and Conservation Biology and Biological and Agricultural Engineering and, Professor Bruce A. McCarl of the Departments of Agricultural Economics.

The CGE model simulation for Chapters 2 and 3 was provided by Dr. Hancheng Dai at Peking University in China. The field experiment in Chapter 8 was provided by Professors Curtis B. Adams and Srinivasulu Ale.

All other work conducted for the dissertation was completed by the student independently.

Funding Sources

Graduate study was supported by an assistantship from the Department of Water Management and Hydrological Science, Texas A&M University.

This work was also made possible in part by the FY2020-21 Water Seed Grant Initiative of Texas Water Resources Institute. Its contents are solely the responsibility of the authors and do not necessarily represent the official views of the TWRI.

NOMENCLATURE

A ² /O	Anaerobic-Anoxic-Oxic
AAO-MBR	Anaerobic-Anoxic-Oxic-Membrane Bio-Reactor
AO	Anaerobic-Oxic
CanCM3	Canadian Coupled Global Climate Model, version 3
CanCM4	Canadian Coupled Global Climate Model, version 4
CCSM4	Community Climate System Model, version 4
Cd	Cadmium
CES	Constant Elasticity of Substitution
CFSv2-2011	Climate Forecast System, version 2
CGE	Computable General Equilibrium
CH ₄	Methane
CO ₂	Carbon Dioxide
CO ₂ -eq	Carbon Dioxide Equivalent Greenhouse Gas Emissions
COD _{Cr}	Chemical Oxygen Demand
CONUS	Contiguous United States
Cr ⁶⁺	Hexavalent Chromium
CRU-TS	Climate Research Unit Time-Series
CWSI	Crop Water Stress Index
DAYMET	Daily Surface Weather and Climatological Summaries
DSSAT	Decision Support System for Agrotechnology Transfer

EFDC	Environmental Fluid Dynamic Code
ET	Evapotranspiration
ET ₀	Reference Evapotranspiration
FAO	Food and Agriculture Organization
GCMs	Global Climate Models
GDP	Gross Domestic Product
GEM/NEMO	Global Environmental Multiscale/Nucleus for European Modeling of the Ocean
GEOS-5	Goddard Earth Observing System
GFS	Global Forecast System
GHG	Greenhouse Gas
GLEAM	Global Land Evaporation Amsterdam Model
GPCP	Global Precipitation Climatology Project
GRP	Gross Regional Product
GWP	Global Warming Potential
Hg	Mercury
HLCA	Hybrid Life Cycle Analysis
LCA	Life Cycle Assessments
LEAP	Long-range Energy Alternatives Planning
N ₂ O	Nitrous oxide
NARR	North American Regional Reanalysis
NDC	Nationally Determined Contributions

NDVI	Normalized Difference Vegetation Index
NH ₃ -N	Ammonia Nitrogen
NMME	North American Multi-Model Ensemble
OD	Oxidation Ditch
Pb	Lead
PET	Potential Evapotranspiration
PGF	Princeton Global Forcing
SBR	Sequencing Batch Reactors
SyDWEM	System Dynamics and Water Environmental Model
TIMES	The Integrated MARKAL-EFOM System
TN	Total Nitrogen
TRMM	Tropical Rainfall Measurement Mission
WASP	Water Quality Analysis Simulation Program
WDI	Water Deficit Index
WEAP	Water Evaluation And Planning
WWTPs	Wastewater Treatment Plants

TABLE OF CONTENTS

	Page
ABSTRACT	ii
DEDICATION	iv
ACKNOWLEDGEMENTS	v
CONTRIBUTORS AND FUNDING SOURCES.....	vii
NOMENCLATURE.....	viii
TABLE OF CONTENTS	xi
LIST OF FIGURES.....	xvi
LIST OF TABLES	xxii
1. INTRODUCTION.....	1
1.1. Available Models to Simulate Regional Climate, Energy, and Water Nexus.....	2
1.2. Objectives.....	6
1.3. Organization of Chapters	8
2. CARBON MITIGATION IMPACT ON LOCAL INDUSTRIAL WATER USE AND POLLUTANT DISCHARGE.....	12
2.1. Introduction	13
2.2. Methodology	16
2.2.1. Integrated Economic and Water Model.....	16
2.2.2. Scenarios	21
2.3. Results	22
2.3.1. Energy Use and CO ₂ Emissions	22
2.3.2. Impacts on Macroeconomics and Industrial Outputs	25
2.3.3. Impacts on Water Withdrawals	27
2.3.4. Impacts on Water Pollutant Discharges	31
2.4. Discussion	33
2.4.1. Sensitivity Analysis	33
2.4.2. Policy Implications.....	35

3. MODELING THE CARBON-ENERGY-WATER NEXUS IN A RAPIDLY URBANIZING CATCHMENT	38
3.1. Introduction	39
3.2. Methodology	41
3.2.1. Integrated CGE-SyDWEM Model	41
3.2.2. SyDWEM	44
3.2.3. Model Calibration and Validation	47
3.2.4. Scenarios	50
3.3. Results	51
3.3.1. Energy Consumption and CO ₂ Emissions	51
3.3.2. GRP and Labor Force	53
3.3.3. Stress on Water Resources	55
3.3.4. Water Quality Change	56
3.4. Discussion	61
3.4.1. Effects of CO ₂ Mitigation Strategies on Water Use	61
3.4.2. Effects of Engineering Measures	63
3.4.3. Sensitivity Analysis	64
3.4.4. Policy Implications	66
4. ESTIMATION OF GREENHOUSE GAS EMISSIONS FROM INTEGRATED URBAN DRAINAGE SYSTEMS	68
4.1. Introduction	68
4.2. Methodology	74
4.2.1. GHG Emissions Calculation	74
4.2.2. Scenarios	80
4.3. Results	81
4.3.1. Direct GHG Emissions	81
4.3.2. Electricity-related GHG Emissions	83
4.3.3. Indirect External GHG Emissions	86
4.3.4. Integrated Urban Drainage System GHG Emissions	88
4.4. Discussion	91
4.4.1. Sensitivity Analysis	91
4.4.2. Policy Implications	95
4.4.3. Limitations	96
5. SELECTION AND IMPLEMENTATION OF REFERENCE EVAPOTRANSPIRATION METHODS FOR ESTIMATION OF REGIONAL IRRIGATION WATER DEMAND	98
5.1. Introduction	99
5.2. Methodology	103
5.2.1. FAO-PM Method	105

5.2.2. Temperature- and Radiation-based Methods	108
5.2.3. Model Evaluation	111
5.2.4. Study Area	112
5.3. Results	115
5.3.1. Comparison of Each Method with Original Constant Values	115
5.3.2. Calibration of Constant Values	120
5.3.3. Method Verification	124
5.3.4. Regionalization.....	125
5.4. Discussion	128
5.4.1. Sensitivity Analysis	128
5.4.2. Temperature Impacts on ET_0 Variations	133
5.4.3. Adjustment for Dry and Windy Conditions	134
5.5. Conclusions	136
6. A CALIBRATION-FREE PRIESTLEY-TAYLOR METHOD FOR REFERENCE EVAPOTRANSPIRATION ESTIMATION	138
6.1. Introduction	139
6.2. Methodology	142
6.2.1. Derivation of the Priestley-Taylor Method Following the Penman- Monteith Method	142
6.2.2. Sensitivity of Different Terms in the FAO-PM Method	144
6.2.3. Equilibrium Rate of Potential Evapotranspiration	145
6.2.4. Data	148
6.2.5. Statistical Analysis	149
6.3. Results	150
6.3.1. Comparison of Reference Evapotranspiration by Different Methods.....	150
6.3.2. Trends in Reference Evapotranspiration	152
6.3.3. Theoretical PT Coefficient	159
6.3.4. Validation of PT Coefficients under Different Climate Conditions.....	165
6.4. Discussion	168
6.4.1. Sensitivity Analysis	168
6.4.2. Trends in S_A , S_{u2} , and PT_a	169
6.5. Conclusions	173
7. CALIBRATION AND BIAS CORRECTION OF SEASONAL WEATHER FORECASTS FOR REAL-TIME REGIONAL CROP MODELING.....	174
7.1. Introduction	175
7.2. Methodology	180
7.2.1. Downscaling Method	180
7.2.2. Data	180
7.2.3. Crop Growth Simulation Model.....	181
7.2.4. Real-time Weather Forecasts Generation.....	183

7.2.5. Model Evaluation	185
7.3. Results and Discussion.....	185
7.3.1. Downscaling Method Evaluation for the Reference Period.....	185
7.3.2. Downscaling Method Versus Multi-Model Mean	189
7.3.3. Predictions at Different Lead Times	194
7.3.4. Cross-validation at Local Scale	195
7.3.5. Test for Crop Modeling.....	197
7.4. Conclusions	201
8. REDUCING THE UNCERTAINTY IN CROP WATER STRESS INDEX (CWSI) MODELS FOR IRRIGATION SCHEDULING	202
8.1. Introduction	203
8.2. Methodology	206
8.2.1. Crop Water Stress Index (CWSI) Calculation	206
8.2.2. Derivation of the Upper and Lower Boundary.....	207
8.2.3. Lower Boundary Derived from the Priestley-Taylor Method.....	211
8.2.4. Water Stress Based on Soil Water Balance	212
8.2.5. Field Experiment and Data Collection	213
8.2.6. Model Comparison	215
8.3. Results and Discussion.....	216
8.3.1. Canopy Cover during the Growing Season.....	216
8.3.3. Relationship with Crop Yield.....	221
8.4.4. Improved Method under Low Canopy Coverage.....	223
8.5. Conclusions	225
9. CONCLUSIONS	226
9.1. Outcomes.....	226
9.2. Limitations and Future Work	229
REFERENCES	232
APPENDIX A SUPPLEMENTARY DATA OF CHAPTER 2.....	268
APPENDIX B SYDWEM CALIBRATION AND VALIDATION	288
APPENDIX C SUPPLEMENTARY DATA OF CHAPTER 4.....	291
APPENDIX D EQUATIONS AND SUPPLEMENTARY DATA OF CHAPTER 5 ...	294
APPENDIX E SUPPLEMENTARY DATA OF CHAPTER 6	304
APPENDIX F SUPPLEMENTARY DATA OF CHAPTER 7	312

APPENDIX G SUPPLEMENTARY DATA OF CHAPTER 8.....	319
---	-----

LIST OF FIGURES

	Page
Figure 1.1 Schematization of the nexus of climate, energy, and water at decision-relevant scales investigated in this dissertation.	8
Figure 2.1 (a) Locations of Shenzhen and Shenzhen River estuary catchment and current/future water infrastructure; (b) water supply from different sources of Shenzhen (1990-2007); and (c) annual mean concentration of NH ₃ -N at monitoring stations S01 (1985-2010).	16
Figure 2.2 Research framework.	17
Figure 2.3 Variations in the (a) sectoral CO ₂ emissions and relative CO ₂ intensity, and (b) primary energy use and relative energy intensity under different scenarios.	23
Figure 2.4 Relative changes in (a) the selected macroeconomic indicators (b) the sectoral outputs (using a Logarithmic scale) between NDC and BaU scenarios in 2020 and 2030.	27
Figure 2.5 (a) Variations in the annual sectoral water withdrawals and relative water intensity under different scenarios; and (b) the carbon emission change (NDC compared with the BaU scenario) versus water use change (NDC compared with the BaU scenario) in 2020 and 2030 (Bubble size indicates sectoral water use intensity).	30
Figure 2.6 Variations in the annual sectoral pollutant loadings under different scenarios.	33
Figure 3.1 Conceptual integration of computable general equilibrium (CGE) and System Dynamics and Water Environmental Model (SyDWEM).	42
Figure 3.2 Data flow in the CGE-SyDWEM.	43
Figure 3.3 Comparison of simulated and measured GRP, population, and water consumption from 2002 to 2009.	49
Figure 3.4 Comparison of simulated and measured water level, BOD ₅ , and NH ₃ -N in October 2004.	49
Figure 3.5 Annual variation of (a) total primary energy consumption, (b) CO ₂ emission, (c) GRP (with its growth rates), and (d) labor force (with its	

growth rates) in Shenzhen under the reference scenario (C0E0) and CO ₂ mitigation scenario (C1E0).....	53
Figure 3.6 Annual variations of (a) total Water demand, (b) WSI and sectoral water demand under different scenarios including (c) current situation (2010) (d) C0E0 (2025) and (e) C1E0 (2025).....	56
Figure 3.7 Annual variations of BOD ₅ loading/discharge (a and c) and NH ₃ -N loading/discharge (b and d) from 2010 to 2025 under different scenarios.....	58
Figure 3.8 Variations of (a) BOD ₅ concentration and (b) NH ₃ -N concentration under different scenarios from 2010 to 2025 at four stations: (a) S01-Buji; (b) S03-Hekou; (c) S05-Tsim Bei Tsui; and (d) S06-Dongjiaotou (n=337).	60
Figure 3.9 Spatial distribution of BOD ₅ and NH ₃ -N concentration during ebb slack and flood slack under different scenarios in 2025.	61
Figure 4.1 Greenhouse gas emissions from integrated urban drainage systems and their interactions with the socio-economic system.	71
Figure 4.2 Annual variations of (a) direct CO ₂ -eq GHG emissions in different systems and relative direct GHG emission intensity, (b) direct GHG emissions by types and total wastewater treated, (c) COD _{Cr} treated, (d) TN treated, (e) COD _{Cr} discharge, and (f) TN discharge under BaU and NDC scenarios.....	83
Figure 4.3 Annual variations of (a) electricity consumption and electricity intensity and (b) electricity consumption-induced indirect GHG emissions and relative GHG intensity under BaU and NDC scenarios during 2007-2025.....	86
Figure 4.4 Annual variations of indirect external GHG emissions and relative GHG emission intensity from chemical use, maintenance, and administrative of WWTPs under BaU and NDC scenarios during 2007-2025.	87
Figure 4.5 Annual variations of (a) total GHG emissions and (b) GHG emission intensity from the integrated urban drainage systems under BaU and NDC scenarios during 1990-2025.....	89
Figure 4.6 (a) Wastewater flow and GHG emissions in individual systems under BaU scenario, (b) comparisons of direct and indirect GHG emissions under BaU scenario, and (c) the difference in GHG emissions between NDC and BaU in 2025.	90
Figure 4.7 Sensitivities of (a) volumetric wastewater treatment rate increase; (b) COD _{Cr} and (c) TN removal rate increase of WWTPs; and (d) GHG intensity	

reduction of imported electricity on total GHG emissions and GHG emission intensity under the NDC scenario in 2025.	92
Figure 4.8 Annual variations of (a) total GHG emissions and (b) GHG emission intensity from the integrated urban drainage systems under different scenarios during 1990-2025.....	94
Figure 5.1 Geographical locations of selected stations and climatic regions in Texas, United States.....	113
Figure 5.2 Comparison of mean monthly ET_0 simulated by different models using the original constants.	119
Figure 5.3 Comparison of mean monthly potential evapotranspiration simulated by different methods using the calibrated constant values.	123
Figure 5.4 Relative errors of mean monthly reference evapotranspiration estimates of each model at three stations..	125
Figure 5.5 Relative error of mean monthly reference evapotranspiration estimates of each model using regional average parameters in (a) humid (b) subhumid and (c) semiarid/arid climates from 1961 to 2010.....	127
Figure 5.6 Variations of sensitivity coefficients for monthly potential evapotranspiration for (a) available energy (A), (b) vapor pressure deficit (D), and aerodynamic resistance (ra) at each station from 1961 to 2010.....	130
Figure 5.7 Variations of sensitivity coefficient of available energy to the reference evapotranspiration under different climate conditions.	132
Figure 5.8 Variations of sensitivity coefficient of wind speed to the reference evapotranspiration (S_{u2}) under different climate conditions.....	132
Figure 5.9 Sensitivity coefficients for the monthly reference evapotranspiration for mean temperature at each station from 1961 to 2010.....	134
Figure 5.10 Comparison of mean monthly RMSE of ET_0 using (a) HS_T and (b) PT_R at 15 stations with default method, calibrated method, and adjusted method.	136
Figure 6.1 Comparison of reference evapotranspiration using different methods.....	152
Figure 6.2 Trends in the reference evapotranspiration using different methods.....	155
Figure 6.3 Linear regressions of ET_0 and the sensitivity coefficient.	156

Figure 6.4 Annual variations and trends in the reference evapotranspiration in different RH regimes.....	158
Figure 6.5 The theoretical PT coefficient (PT_a) and sensitivity coefficients of available energy (S_A) and wind speed (S_{U2}) for ET_0	161
Figure 6.6 Monthly mean of sensitivity coefficients of available energy (S_A) on reference evapotranspiration from 1948 to 2016.....	164
Figure 6.7 Monthly mean of sensitivity coefficients of wind speed S_{U2} ($-S_{ra}$) on reference evapotranspiration from 1948 to 2016.....	164
Figure 6.8 Comparison of reference evapotranspiration using the adjusted PT methods.....	166
Figure 6.9 Trends in the reference evapotranspiration using the adjusted PT methods.	167
Figure 6.10 Variations of S_A and S_{u2} to changes in meteorological variables.	168
Figure 6.11 Variations of the theoretical PT coefficient to changes in meteorological variables.....	169
Figure 6.12 Mann-Kendal annual trend tests of monthly PT coefficient (PT_a) from 1948 to 2016.	172
Figure 6.13 Area fractions of global land surface with positive trends and negative trends as well as the trends with statistically significant ($p<0.05$) for PT_a , S_A , and S_{u2} from 1948 to 2016.	172
Figure 7.1 Comparison of (a) monthly mean maximum temperature, (b) monthly mean minimum temperature, and (c) monthly total precipitation from NMME dataset (simulated by CanCM4 at 1° spatial resolution) and observations from DAYMET at 1 km spatial resolution in July 2019.	177
Figure 7.2 Schematic diagrams showing different downscaling methods: (a) delta addition; (b) delta correction; (c) quantile mapping; and (d) proposed method.	179
Figure 7.3 Schematic showing weather data inputs and processing.	184
Figure 7.4 Comparison of hindcast predictions of mean maximum temperature in the growing season (May to October) using different methods.	186
Figure 7.5 Comparison of hindcast predictions of mean minimum temperature in the growing season (May to October) using different methods.	187

Figure 7.6 Comparison of hindcast predictions of the total precipitation in the growing season (May to October) using different methods.	188
Figure 7.7 Comparison of mean maximum temperature forecast in the growing season (May to October) in 2019 using different methods.	191
Figure 7.8 Comparison of mean minimum temperature forecast in the growing season (May to October) in 2019 using different methods.	192
Figure 7.9 Comparison of total precipitation forecast in the growing season (May to October) in 2019 using different methods.	193
Figure 7.10 Mean maximum/minimum temperature and total precipitation predictions for June 2019 at different lead times using the downscaled method.	195
Figure 7.11 Monthly total precipitation predictions for December 2019 at different lead times using the downscaled method.	195
Figure 7.12 Comparison of monthly mean (a) T_{max} and (b) T_{min} , and seasonal total precipitation for the reference period (1982-2010) using DAYMET (Observation), CanCM4, and downscaled CanCM4 data at the Chillicothe station.	196
Figure 7.13 Comparison of daily (a) (b) T_{max} , (c)(d) T_{min} , and (e) monthly precipitation from DAYMET (Observation), CanCM4, and downscaled CanCM4 in 2019 at the Chillicothe station.	197
Figure 7.14 Comparisons of 2020 growing season prediction at the Chillicothe station using different weather datasets (lead 0m)..	199
Figure 7.15 Comparisons of (a) seasonal precipitation, (b) seed cotton yield, and (c) seasonal irrigation predictions using the downscaled and multi-model methods in the 2020 growing season at the Chillicothe station at different lead times.	200
Figure 8.1 Schematic representation of aerodynamic resistance (r_a) and canopy resistance (r_c) in different non-water stress baseline models.	209
Figure 8.2 Experimental plot plans at the Chillicothe research station.	214
Figure 8.3 Canopy cover changes through the growing season in 2020.	217
Figure 8.4 Crop water stress comparison using the original method (CWSI_PE) at three plots for each ET replacement.	218

Figure 8.5 Comparison of CWSI values using the four CWSI models and the DSSAT simulation under different ET replacements.....	220
Figure 8.6 Canopy to air temperature differences through the growing season in 2020.	221
Figure 8.7 Relationships between the seasonal averaged CWSIs and seed cotton yield.	222
Figure 8.8 (a) Water deficit index (WDI) variation under different water management regimes as a function of time and (b) the relationship between seasonal average WDI and seed yield cotton during the 2020 growing season at Chillicothe, TX.	224

LIST OF TABLES

	Page
Table 2.1 Configurations for the Two Scenarios.	22
Table 2.2 Relative Changes from the Projected Values in 2030 under the NDC Scenario.	35
Table 3.1 Configurations for the Four Scenarios.	51
Table 3.2 Summary of Water Engineering Measures	51
Table 3.3 Changes from Values in C1E1 in 2025 under Sensitivity Analysis (%).....	66
Table 4.1 GHG Emission Factors of Different Treatment Technologies in WWTPs from Recent Field Studies in China (mean \pm standard deviation).....	77
Table 4.2 Electricity Intensity of Four Treatment Stages using Different Treatment Technologies in WWTPs System.	79
Table 4.3 Chemical Cost, Maintenance Cost, and Administrative Cost per Unit of Wastewater Treated Using Different Technologies (RMB/10 ³ m ³) (2015 price).	80
Table 4.4 Configurations of Scenarios.	81
Table 5.1 Input Data Required by Different Methods.	105
Table 5.2 Summary of Selected Models with Default Constant Values.	110
Table 5.3 General Information and Monthly Average of the Main Climatic Variables of Selected Stations in Texas, United States (1961-2010).	114
Table 5.4 Regression Relationships (Y=mx) between FAO-PM ET _o and the Temperature-based Methods using Original Constant Values.	117
Table 5.5 Regression Relationships (Y=mx) between FAO-PM ET _o and the Radiation-based Methods using Original Constant Values.	118
Table 5.6 Comparison of the Temperature-based Methods Parameters before and after Calibration.	121
Table 5.7 Comparison of the Radiation-based Methods Parameters before and after Calibration.	122

Table 6.1 ET_0 Long-term Means and Trends under Different RH Regimes.....	159
Table 6.2 Priestley-Taylor Coefficients for Different Climatic Types and Required Weather Data.	167
Table 8.1 Development Stages and Basal Crop Coefficient K_{cb} of Seed Cotton (Ko et al., 2009).	215
Table 8.2 Seasonal Error Estimates for CWSI using the Four Models as compared against the DSSAT Simulation.	220
Table 8.3 Seasonal Averaged CWSI using the Four CWSI Models and the DSSAT Simulation under Different ET Replacements.	223

1. INTRODUCTION

Providing reliable and sustainable energy and water services faces multiple challenges, including increasing demand due to population growth and economic development, degradation of water resources, depletion of fossil energy resources as well as climate change (Liu et al., 2016a; WWAP, 2014). It is estimated that in 2050, globally, there will be 9.7 billion people, and we need 55% more water, 50% more food, and 80% more energy, with 52% more carbon dioxide (CO₂) emissions with no policy change (OECD, 2012). The situation is exacerbated in developing countries which are experiencing rapid urbanization. The shares of people living in urban areas are projected to increase from 55% in 2018 to 68% in 2050 globally, of which more than 90% of the increase will be from developing countries (UN, 2019). This rapid, often not well-planned, urbanization usually results in high water and energy use, CO₂ emission, and degradation of natural resources, bringing risks to local infrastructure, water, energy supply, and environmental safety (Dong and Liang, 2014; Gain and Giupponi, 2015; Qin et al., 2013). The ways and extent of local energy and water use also contribute to global climate change.

To mitigate climate change impacts, many countries have announced their Nationally Determined Contributions (NDC) in the Paris Agreement to reduce CO₂ emissions (UNFCCC, 2015). Water and energy systems are interdependent and have complex dynamic interactions with the socio-economic system and climate change. Policies and measures designed to increase the efficiency in one system might

significantly affect that in the other (Hussey and Pittock, 2012; Li, 2017; Rothausen and Conway, 2011). Strategies to mitigate carbon emissions can exert significant impacts on energy and socio-economic system and in turn alter the amount and structure of water uses in agricultural, domestic, and industrial sectors, as well as their geographic distribution. Water engineering measures to improve water quality and water use efficiency will be affected by the water use changes and may have trade-offs on energy use and CO₂ emissions. To develop an integrated modeling framework which is able to represent the linkages between climate, and socio-economic, water, and energy systems is crucial to identify the cost-effective solutions to meet water and energy demands under different economic development pathways and climate futures.

1.1. Available Models to Simulate Regional Climate, Energy, and Water Nexus

The impacts of CO₂ mitigation strategies on long-term economic and energy use have been widely studied (Dai et al., 2011; Dong et al., 2015; Wang et al., 2015; Wu et al., 2016). In China, several studies found that the implementation of China's NDC can reduce CO₂ emissions and energy consumption, and have adverse effects on economic output and employment in energy- and carbon-intensive industries (Dai et al., 2011; Dong et al., 2015; Wang et al., 2015; Wu et al., 2016). Furthermore, its co-benefits on air pollution reduction (Dong et al., 2015) and health effects (Wu et al., 2017; Xie et al., 2016) have gained much attention. Recently, some energy-water nexus studies have been carried out to analyze the impacts of CO₂ mitigation strategies on energy use and water consumption in the power generation sector (Arent et al., 2014; Cameron et al., 2014; Chandel et al., 2011; Huang et al., 2017; Talati et al., 2016). These studies investigated

water saving and CO₂ emission reduction under different CO₂ mitigation strategies and indicated that these strategies may increase or decrease water consumption due to the wide range of water use intensity of low-carbon emissions technology choices (Kyle et al., 2013; Liu et al., 2015; Talati et al., 2016). Also, there are increasingly integrated modeling tools, considering the broader nexus of water, energy, and food systems for CO₂ mitigation and climate adaptation purposes (Ermolieva et al., 2015; Howells et al., 2013; Kraucunas et al., 2015; Martinez-Hernandez et al., 2017). CO₂ mitigation strategies involving a carbon price can also promote the adjustment of industry structure to a low-carbon, high energy efficient one (Dong et al., 2015; Dong and Liang, 2014; Xing et al., 2011), which have extensive impacts on the water consumption and pollutant discharge in the economic system (Cooper and Sehlke, 2012). However, these cross-sector feedbacks have not been fully considered in current water-energy nexus studies. In addition, a whole economics-wide assessment of the impacts of CO₂ mitigation on water pollutant emission reduction is lacking. Some studies have assessed energy conservation and pollutant reduction using a technology-based bottom-up model in China's pulp and paper (Wen et al., 2015) and steel sectors (Wang et al., 2017). There are few studies integrating energy use, CO₂ emissions, economic and population growth, water resources stress and water quality change. An integrated model capturing the feedbacks among socio-economic, energy, and water systems is needed to help policymakers identify the possible co-benefits across these systems and formulate more effective policies and measures.

Available energy models and water system models usually assess CO₂ mitigation strategies and water engineering measures independently. In the energy sector, Long-range Energy Alternatives Planning (LEAP) (Heaps, 2016) and The Integrated MARKAL-EFOM System (TIMES) (Loulou, 2005) have been used to predict long-term energy planning and CO₂ mitigation strategies. Compared with these methods, the Computable General Equilibrium (CGE) model has been widely used to simulate the full range of the future economic system (e.g., industry output, domestic and international trade) and energy system (e.g., energy supply, consumption, and trade) (Cheng et al., 2016; Dai et al., 2011, 2012; Dai et al., 2016; Dong et al., 2015; Xie et al., 2016). In the water sector, hydrodynamics and water quality models, such as the QUAL2E (Brown and Barnwell, 1987), Water Quality Analysis Simulation Program (WASP) (Ambrose, 1987), MIKE 11 (DHI, 1993), and Environmental Fluid Dynamic Code (EFDC) (Hamrick, 2006), are suitable to evaluate the effects of engineering measures, such as increasing the volumetric wastewater treatments rate, upgrading the level of wastewater treatment, as well as increasing wastewater reuse and water transfer, on water quality improvement in rivers, lakes, reservoirs, and estuaries (Babbar, 2014; Doulgeris et al., 2012; Liang et al., 2015; Liu et al., 2012; Ning et al., 2001; Paliwal et al., 2007; Privette and Smink, 2017; Quijano et al., 2017; Su et al., 2014; Yu et al., 2016).

Many integrated water management models, such as Water Evaluation And Planning (WEAP) (Hollermann et al., 2010; Illich, 2006; Li et al., 2015b; Yates et al., 2005) and Elbe-DSS (de Kok et al., 2009; Hahn et al., 2009; Hermans and Hahn, 2007; Lautenbach et al., 2009), were developed to evaluate the effects of both socio-economic

and water engineering measures on water balance and water quality control. These integrated water models have been coupled with currently available energy models (e.g., the integration of LEAP and WEAP) to support planning for both water and energy systems (Howells et al., 2013; Purkey, 2011). Also, there are increasing integrated modeling tools, considering the broader nexus of water, energy, and food systems for carbon mitigation and climate adaptation purposes (Ermolieva et al., 2015; Howells et al., 2013; Kraucunas et al., 2015; Martinez-Hernandez et al., 2017).

However, the socio-economic components (e.g., population and economic growth) in these studies are regarded as external scenarios or using fixed-rate based on historical trends, and thus the feedbacks between different socio-economic components and between energy and water systems cannot be effectively captured (de Kok et al., 2009; Lautenbach et al., 2009; Qin et al., 2013). The System Dynamics and Water Environmental Model (SyDWEM) (Qin et al., 2011) model developed in our previous studies provides a useful tool to understand the interactions among socioeconomic, water infrastructure, and receiving water systems by treating the socio-economic dynamics as an internal sub-module. The SyDWEM model has been successfully applied to a rapidly urbanizing coastal region (Qin et al., 2011, 2013). In this dissertation, a newly developed CGE model was integrated with the upgraded version of SyDWEM (CGE-SyDWEM), including an improved hydrological and water quality model and calculation of energy use/GHG emissions from the water sector, to simulate energy and water systems simultaneously and support decision-making regarding the management of energy and water resources under carbon mitigation strategies. To utilize the developed integrated

model/platform in regions with a higher proportion of agricultural industry, we improved the integrated model in simulating agricultural water demand and evaluating agricultural adaptation strategies to climate change.

1.2. Objectives

The overarching scientific objective of this dissertation is to develop an integrated platform to simulate the interactions among socio-economics, energy consumption, water use, water infrastructure, and receiving water systems and to identify the cost-effective solutions to meet the water and energy demands under different economic development pathways and climate futures. The schematization of the nexus of climate, energy, and water at decision-relevant scales investigated in this dissertation and the objectives are illustrated in Figure 1.1.

Our specific scientific objectives include:

Objective 1: Evaluate the impact of CO₂ mitigation strategies on local industrial water use and water-related pollutants discharge.

Objective 2: Develop and evaluate an integrated model (CGE-SyDWEM) to simulate the carbon-energy-water nexus in urbanized regions, which can be used to aid energy, carbon, and water policy makers to understand the complicated synergistic effects of proposed CO₂ mitigation strategies and water engineering measures on local/regional energy consumption, CO₂ emissions, water resources balance, water environment change; and to design more effective policies and measures to ensure energy and water security in the future.

Objective 3: Evaluate the impact of proposed CO₂ mitigation strategies and water engineering measures on both the direct and indirect greenhouse gas emissions from the sewer system, WWTPs, and receiving water systems.

Objective 4: Evaluate temperature- and radiation-based methods for estimating regional reference evapotranspiration under different climatic conditions. Analyze the controlling weather parameters of ET_0 under different climatic conditions and improve the performance of selected models in arid, high wind conditions.

Objective 5: Derive an analytical expression for the Priestly-Taylor coefficient following the Penman-Monteith method and provide a calibration-free Priestley-Taylor coefficient for humid, arid, and arid/high wind climate, respectively.

Objective 6: Calibration and bias correction of seasonal weather forecasts for real-time regional crop modeling and irrigation scheduling by performing a bias correction statistical downscaling method.

Objective 7: Develop a novel, semi-empirical Crop Water Stress Index (CWSI) model based on the Priestly-Taylor equation and improve the representation of the non-water stress boundary with the assumptions of free water surface, saturated water surface, and well-watered surface.

The above objectives were achieved through a combination of economic modeling, water quality modeling, integrated model development, and crop model simulations, as explained in detail in the next section.

China, in Chapter 2. This integrated model was used to evaluate whether carbon mitigation strategies, i.e., fulfill China's NDC targets, would decrease or increase local industrial water use and water-related pollutants discharge.

To accomplish objective 2, the CGE model developed in Chapter 2 was integrated with SyDWEM, i.e., CGE-SyDWEM, to predict future energy use, CO₂ emissions, economic growth, local labor force migration and population growth, water resource stress, and water quality change at the watershed level in Chapter 3. CGE-SyDWEM was calibrated and validated in a rapidly urbanizing catchment in Shenzhen. The effects of both the CO₂ mitigation strategies and water engineering measures were evaluated using CGE-SyDWEM.

To accomplish objective 3, the CGE-SyDWEM developed in Chapter 3 was used to calculate the direct and indirect GHG emissions from integrated urban drainage systems, including sewer systems, WWTPs, and receiving water systems under long-term urbanization process in Chapter 4. The relative contributions of GHG emissions from the sewer system, WWTPs system, and receiving water system from 2010 to 2025 were quantified. The effects of CO₂ mitigation strategies and water engineering measures on GHG emissions from the three systems were evaluated.

To accomplish objective 4, three temperature-based methods, i.e., Thornthwaite (Th_T), Blaney-Criddle (BC_T), and Hargreaves and Samani (HS_T), and five radiation-based methods, i.e., Makkink (Ma_R), Priestley-Taylor (PT_R), Jensen and Haise (1963) (JH_R), Turc (Tu_R), and Abtew (1996) (Ab_R), were selected to compare with the Food and Agriculture Organization Penman-Monteith (FAO-PM) method at 15

climatological stations (1961-2010) with various climatic regions including types of climate arid, semi-arid, and humid tropical in Texas, United States, in Chapter 5. Each method with its original parameters was compared with the FAO-PM estimates and then calibrated using an automatic optimization method. The model verification study was conducted in selected stations to analyze the ability of the model to predict long-term ET_0 changes. Sensitivity analysis was then conducted to understand the structure of the model and quantify the contribution of each parameter to the variation of ET_0 . Based on the sensitivity analysis results, a calibration-free coefficient with monthly relative humidity (RH) as the only input was suggested to be multiplied with the HS_T or PT_R equations.

To accomplish objective 5, an analytical expression for the Priestly-Taylor coefficient was derived following the Penman-Monteith method in Chapter 6. A theoretical basis to the default value of 1.26 was provided and validated using a global gridded daily weather dataset at 0.25° spatial resolution (1948-2016). A calibration-free Priestley-Taylor coefficient for humid, arid, and arid/high wind climates was provided, respectively.

To accomplish objective 6, an improved downscaling method, namely bias correction or ‘nudging’ method, was used to produce 1-km gridded daily weather projections (maximum and minimum air temperatures and precipitation) over the contiguous United States (CONUS) from one representative NMME model, i.e., the Canadian Coupled Climate Model versions 4 (CanCM4) in Chapter 7. The seasonal weather forecast in real-time crop modeling was evaluated using a calibrated

CROPGRO-Cotton module of the Decision Support System for Agrotechnology Transfer (DSSAT) model at one experimental station in the semi-arid Texas Rolling Plains during the growing seasons of 2020.

To accomplish objective 7, in Chapter 8, three non-water stress boundary equations under the assumption of free water surface, saturated crop surface, and well-watered crop surface were derived and compared. A new non-water stress boundary equation with the assumption of free water surface using a less data-intensive method was derived. The uncertainty of using the four models in calculating CWSI was evaluated using cotton field experiment data conducted during the 2020 growing season at Chillicothe Research Station in Texas Rolling Plain, Texas.

In Chapter 9, the outcomes of this dissertation are summarized, and the limitations and future work specific to each chapter are also provided.

2. CARBON MITIGATION IMPACT ON LOCAL INDUSTRIAL WATER USE AND POLLUTANT DISCHARGE*

Carbon mitigation strategies have been developed without sufficient consideration of their impacts on the water system. This chapter evaluated whether carbon mitigation strategies would decrease or increase local industrial water use and water-related pollutants discharge using a Computable General Equilibrium (CGE) model coupled with a water withdrawal and pollutant discharge module. Shenzhen, the fourth largest city in China, was selected as the study area. To fulfill China's Nationally Determined Contribution (NDC) targets, Shenzhen's Gross Domestic Products (GDP) and welfare losses are projected to be 1.6% and 5.6% in 2030, respectively. The carbon abatement cost will increase from 56 USD/t CO₂ in 2020 to 274 USD/t CO₂ in 2030. Results reveal that carbon mitigation accelerates local industrial structure upgrading by restricting carbon-, energy-, and water-intensive industries, e.g., natural gas mining, non-metal, agriculture, food production, and textile sectors. Accordingly, carbon mitigation improves energy use efficiency and decreases 55% of primary energy use by 2030. Meanwhile, it reduces 4% of total industrial water use and 2.2-2.4% of discharges of two major pollutants, i.e., COD_{Cr} and NH₃-N. Carbon mitigation can also decrease petroleum (2.2%) and V-ArOH (0.8%) discharge but has negative impacts on discharge of most

* Reprinted with permission from "General equilibrium analysis of cobenefits and trade-offs of carbon mitigation on local industrial water use and pollutants discharge in China" by Qiong Su, Han-Cheng Dai, Huan Chen, Yun Lin, Yang Xie, and Raghupathy Karthikeyan, 2019. *Environmental Science & Technology*, 53(3):1715-1724, Copyright [2021] by American Chemical Society.

heavy metal(loid)s pollutants (increased by -0.01% to 4.6%). These negative impacts are evaluated to be negligible on the environment. This chapter highlights the importance of considering the energy-water nexus for better-coordinated energy and water resources management at local and national levels.

2.1. Introduction

With continuous population and economic growth, China has become one of the largest greenhouse gas emitters since 2006 (IEA, 2009). To mitigate climate change impacts, the Chinese government announced its NDC in the Paris Agreement to reduce CO₂ emissions per unit of GDP by 60% to 65% by 2030 compared with the 2015 level (UNFCCC, 2015). The implementation of China's NDC is supposed to improve energy use efficiency and accelerate industrial structure upgrading by decreasing the proportion of energy- and carbon-intensive industries (Dai et al., 2011; Wu et al., 2016). However, the industrial structure upgrading may also have significant impacts on water use and pollutant discharge in related industrial sectors, considering that energy and water are two basic inputs of industrial production (Jiang et al., 2014; Qin et al., 2013; Qin et al., 2014). Given this context, modeling the impacts of China's NDC on energy use, economic development, water use, and water-related pollutant discharges are crucial to design effective policies and measures for addressing energy and water issues.

Until now, most energy-water nexus studies of assessing the impacts of carbon mitigation strategies on water use still focus on a single industrial sector (Ackerman and Fisher, 2013; Khan et al., 2017; Zhang and Vesselinov, 2016) or two (Dodder et al., 2012). Carbon mitigation tends to increase water consumption in the electric sector at

both regional (Talati et al., 2016) and national (Cameron et al., 2014) scales in the U.S. But the impacts have high uncertainty due to the choice of energy sources and the cooling system (Chandel et al., 2011; Clemmer et al., 2013; Macknick et al., 2012). For example, studies in China showed that carbon mitigation promoted renewable energy technologies and reduced water consumption in the power generation sector (Huang et al., 2017; Li et al., 2012). Recently, the multi-sector model, like MARKAL, was used to simulate the energy and water competition between thermoelectric power generation and transportation sectors in the U.S. under different carbon mitigation scenarios (Dodder et al., 2012). However, these studies are limited to capture the cross-sector interactions and feedbacks among economic, energy, and water systems, and therefore, they cannot provide an integrated view of how carbon mitigation strategies affect the economic output and water use in different industrial sectors.

On the other hand, the impacts of carbon mitigation strategies on water-related pollutant emissions have not been well evaluated. The co-benefits between energy use and pollutant emissions in the energy-water nexus have been identified using technology-based bottom-up approaches in China's pulp and paper (Wen et al., 2015) and steel sectors (Wang et al., 2017). However, changes in energy and water use and pollutant emissions that may result from carbon mitigation are not quantitatively evaluated in these studies. In addition, sufficient regional details of sectoral water use and pollutant emission data are usually unavailable in developing countries like China.

To address these gaps, the impacts of China's NDC on local industrial water use and water-related pollutants discharge were evaluated by coupling a CGE model with a

water withdrawal and pollutant discharge module. The industrial sectors considered here include primary (e.g., agriculture), secondary (e.g., manufacturing, mining, power generation, and construction, etc.), and tertiary industries (e.g., construction, transportation, and services). The CGE model can be used to simulate the interaction between macro-economy and environmental systems at regional or global scales. This integrated economic and water model can evaluate the impacts of carbon mitigation strategies on the economic, energy, and water systems. Also, the possible co-benefits or trade-offs across these systems can be identified to support the designing of effective policies and measures.

Shenzhen was selected as the study area, and the reasons are: (1) it is a manifestation of China's rapid urbanization process. Shenzhen is the first Special Economic Zone of China, and it has been experiencing rapid urbanization since 1978. The population in Shenzhen has increased from 0.33 million in 1978 to 13 million in 2018, which increased almost 40 times. It had a total population of 0.7% of China and consumed nearly 4.3% petroleum and 3.1% natural gas in 2007 (2007 is the model simulation start year) (Table A1, Appendix A); (2) it has been chosen as a pilot city to perform China's NDC, which is the first carbon mitigation practice in developing countries; (3) it has limited local water resources and environmental capacity and is challenged in fulfilling the national industrial water conservation and main pollutants discharge reduction targets (i.e., chemical oxygen demand, COD_{Cr}, and ammonia nitrogen, NH₃-N) (Qin et al., 2011; Su et al., 2014) (Figure 2.1). Here, this chapter aims to (1) assess the impacts of China's NDC on the total amount and intensity of energy use

and sectoral CO₂ emissions; (2) evaluate the economic impacts in Shenzhen when China's NDC targets are achieved in 2030; and (3) quantify the impacts of carbon mitigation on local industrial water use and water-related pollutant discharges.

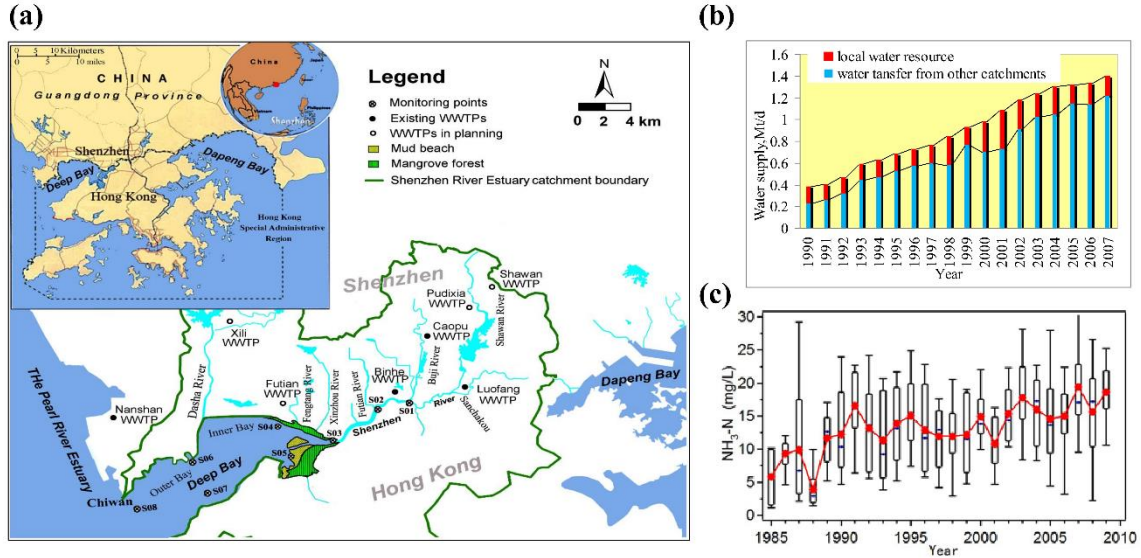


Figure 2.1 (a) Locations of Shenzhen and Shenzhen River estuary catchment and current/future water infrastructure; (b) water supply from different sources of Shenzhen (1990-2007); and (c) annual mean concentration of NH₃-N at monitoring stations S01 (1985-2010). Eight temporary monitoring stations, including Buji (S01), Futian (S02), Hekou (S03), Mangrove Park (S04), Tsim Bei Tsui (S05), Dongjiaotou (S06), Sheung Pak Nai (S07), and Bay mouth (S08).

2.2. Methodology

2.2.1. Integrated Economic and Water Model

The integrated model includes 1) a city-level CGE model and 2) a water withdrawal and pollutants discharge module. As shown in Figure 2.2, the CGE model can be used to estimate CO₂ emissions, energy use, macroeconomic impacts, e.g., GDP, government expenditure, warfare, import, and export, and detailed economic outputs for

each sector under different carbon mitigation scenarios. The economic outputs for each sector are the drivers of the water module so that the impacts of CO₂ mitigation strategies on sectoral water use and water-related pollutant discharges can be estimated.

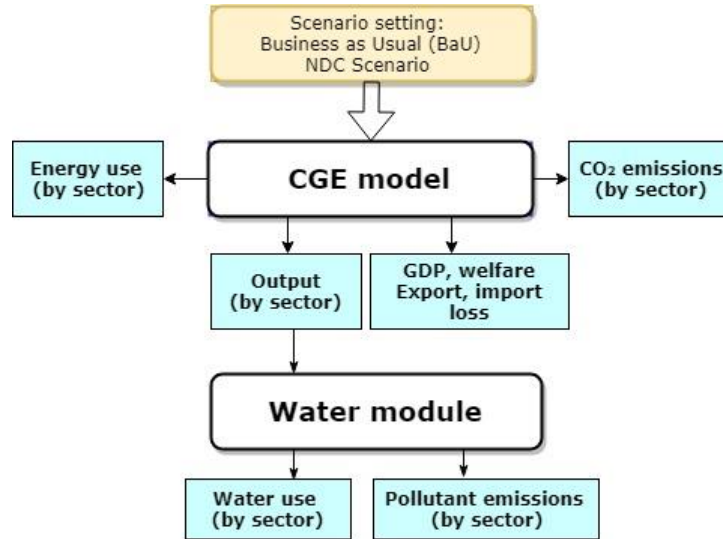


Figure 2.2 Research framework.

The major assumptions of the model include: (1) activity output of each sector follows a nested constant elasticity of substitution production function; (2) carbon abatement cost is evenly distributed in all sectors; (3) rates of technology-induced water use intensity/pollutant discharge change in different industrial sectors are assumed the same during the prediction period; (4) non-point source pollution from the agriculture sector is not considered due to its relatively small amount compared with emissions from other industrial sectors; and (5) water pollutant loads from construction, transport, and services sector are considered domestic pollutant sources and not included in the calculation.

2.2.1.1. IMED|CGE model

The CGE model can simulate the future economic system (e.g., industry output, domestic, and international trade) and capture the interactions and feedbacks among different industrial sectors, final consumers, and the rest of the world. The IMED|CGE (Integrated Model of Energy, Environment and Economy for Sustainable Development | Computable General Equilibrium) model used here has been widely used for assessing the economic and environmental impacts of China's CO₂ mitigation strategies at city (Tian et al., 2016; Wu et al., 2016), provincial (Dong et al., 2015; Xie et al., 2016), and national levels (Dai et al., 2011; Dai et al., 2016). The version used in this dissertation is a single-region, recursive dynamic CGE model for Shenzhen City with 22 economic sectors (Table A2, Appendix A). The 2007 input-output table and 2007 energy balance tables of Shenzhen were used for the base year calibration. The model includes a production block, a market block with domestic, government, and household income and expenditure blocks, and international transactions, which is similar to the one-region version (Dai, 2012). The outputs for each sector follow a nested constant elasticity of substitution (CES) production function. Inputs include material commodities, energy commodities, labor, capital, and resources (including water use). More details can be found in Appendix A.

2.2.1.2. Water Withdrawal and Pollutant Discharge Module

Once the economic outputs for each sector associated with different scenarios are known from CGE simulations, the effects of CO₂ mitigation strategies on water use and water pollutants discharge can be estimated using equations (2.1) and (2.2).

$$W_t = \sum_i W_{ti} = \sum_i OUT_{ti} \times WI_{ti} \quad (2.1)$$

$$P_t = \sum_i \sum_j P_{tij} = \sum_i \sum_j OUT_{ti} \times PI_{tij} \quad (2.2)$$

where t is the time (year); OUT_{ti} is the output of the i^{th} industry sector (million dollars); W_t and P_t represent the total water withdrawal and pollutant discharge in year t ; W_{ti} and WI_{ti} are the water withdrawals (million tons) and water intensity (water withdrawals per unit output, m^3 per million dollar) of the i^{th} industry sector, respectively. P_{tij} and PI_{tij} are pollutant discharge (tons) and pollutant discharge intensity (pollutant discharge per unit output, tons/million dollar) of the i^{th} industry sector and the j^{th} type of pollutants including COD_{Cr} , NH_3-N , petroleum, volatile phenol (V-ArOH), lead (Pb), hexavalent chromium (Cr^{6+}), mercury (Hg), cadmium (Cd), and Arsenic (As).

2.2.1.2.1. Water Intensity in Different Sectors

Time-evolving water intensity (WI) values were applied (Qin et al., 2011) considering the relatively long-term historical changes because of technology improvement, as shown in equation (2.3).

$$WI(t)_i = WI_{0i} \times \exp(\alpha_i \times T) \quad (2.3)$$

where WI_{0i} is the water withdrawal per unit output (m^3 /million dollar) of the i^{th} industry in the initial year (2014); T is year number since the initial year; α_i is the exponential rate of water intensity of the i^{th} industry; and e^{α_i} is considered the water intensity change rate (WR) of the i^{th} industry. Water use, or water withdrawal, is defined as the total amount of water removed from water resources. The term ‘water consumption’ used in this dissertation refers to water consumed, not available to be reused anymore.

To reduce the source uncertainty, the four-year mean values of water use intensity in each industrial sector were used for the initial year (WI_{0i}) calculation and are detailed in Table A3, Appendix A. The rates of technology-induced water use intensity change in different industrial sectors (WR) were calibrated using regression analysis of the historical data during the period of 2000 and 2015, with R^2 ranging from 0.78 to 0.98 (except 0.53 in the agricultural sector) (Table A4, Appendix A). Though the agricultural sector had a low R^2 due to its high variability over time, its impacts are negligible given that the water withdrawals from the agricultural sector only accounted for 4% of the total water withdrawal in 2015 in Shenzhen City.

2.2.1.2.2. Pollutant Intensity in Different Sectors

A similar procedure was applied to calculate the pollutant intensity (PI) values of different pollutants in each sector, as shown in equation (2.4):

$$PI(t)_{ij} = PI_{0ij} \times \exp(\beta_i \times T) \quad (2.4)$$

where PI_{0ij} are the j^{th} pollutant discharges per unit output ($\text{m}^3/\text{million dollar}$) of the i^{th} industry in the initial year (2014); T is year number since the initial year; β_i is the exponential rates of the pollutant discharge intensity of i^{th} industry; and e^{β_i} is considered the pollutant discharge intensity change rate (PR) of the i^{th} industry.

The initial year pollutant intensity values for each industrial sector were collected from the survey of pollutant sources of Shenzhen (2011-2014) (HSECSM, 2011-2014) and the mean value and its standard deviation for each sector are provided in Tables A5 and 6, Appendix A. The PR of COD_{Cr} was used to represent the technology-induced wastewater treatment improvement in different industrial sectors since it is the prime

water pollutant discharge control target in China. The PRs of COD_{Cr} were calibrated using regression analysis of the historical data during the period of 1996-2007 (HSECSM, 1996-2007) with R^2 ranging from 0.47 to 0.95 (Table A7, Appendix A). A national dataset (2002-2012) was used in sectors with insufficient data (NBS, 2012). Also, non-point source pollution from the agriculture sector is not considered due to its relatively small amount compared with emissions from other industrial sectors (Qin et al., 2014).

2.2.2. Scenarios

Two scenarios, including Business as Usual (BaU) scenario and a Nationally Determined Contributions (NDC) scenario, were evaluated. The BaU scenario simulated the economic, energy, and water system change without implementing explicit carbon mitigation or water-saving policies. The future GDP and population growth rate were based on Qin et al. (2011) and the 13th Five-Year Plan for economic and social development of Shenzhen (SZMG, 2016) as detailed in Table 2.1. The annual mean growth rates of GDP and population were set at 9.10% and 0.57% between 2007 and 2020, and 6.40% and 0.22% between 2020 and 2030, respectively. No CO₂ emission intensity constraint was considered in the BaU scenario. By contrast, the NDC scenario had a constraint on the CO₂ emission intensity of Shenzhen, which was set to decrease by 45% by 2020 and 65% by 2030 on the basis of the 2007 level, fulfilling China's NDC commitment (UNFCCC, 2015). The other settings in the NDC scenario were the same as those in the BaU scenario.

Table 2.1 Configurations for the Two Scenarios.

Scenarios	GDP growth rate	Population growth rate	Emission constraints
BaU	9.1% over 2007-2020; 7.9% over 2007-2030	0.57% over 2007-2020; 0.42% over 2007-2030	No emission constraints
NDC	Same as BaU	Same as BaU	Emission intensity reduced by 40% in 2020 and 65% in 2030

2.3. Results

2.3.1. Energy Use and CO₂ Emissions

Carbon mitigation substantially reduces the local CO₂ emissions and energy use, i.e., by 67% and 55% by 2030 compared with the BaU scenario, respectively (Figure 2.3). The total CO₂ emissions and the primary energy use under the NDC scenario in 2030 are projected to be 140.4 Mt and 0.30 EJ, respectively. The carbon intensity of Shenzhen in 2007 was 0.81 kg/USD, less than half of the mean value of China (1.7 kg/USD). The carbon intensity shows a slightly increasing trend under the BaU scenario, but with the carbon emissions constraint, it will decrease by 39% by 2020 and 64% by 2030, fulfilling the regional carbon intensity reduction target. In addition, the energy intensity decreases by 49% in 2030 under the NDC scenario, and the energy intensity reduction rate is much larger than the BaU scenario (decreases by 15%). When the constraint is imposed, carbon emission allowance becomes a scarce resource, and a carbon shadow price is generated endogenously in the CGE model. Carbon shadow price, or the carbon abatement cost, is considered the marginal cost to achieve the required emission reduction target (Su et al., 2018). It is an equilibrium price, which could balance the supply and demand of the carbon emission allowance. The supply of carbon emissions is represented by the future GDP and carbon intensity target, and the demand

is determined by the emissions requirement of different industrial sectors and households, which is influenced by the industrial output in different sectors and households' income level, respectively. The carbon abatement cost is evenly distributed in all sectors and will increase from 56 USD/t CO₂ in 2020 to 274 USD/t CO₂ in 2030 because of more stringent carbon constraints and adverse endogenous factors such as few available low carbon technologies and higher renewable energy prices in Shenzhen. The carbon abatement cost increases the production prices of all sectors, which is dependent on the carbon intensity of each sector. On the demand side, consumers respond to the price changes and will accordingly adjust their activities to decrease the demand for energy- and carbon-intensive products as well as fossil energy.

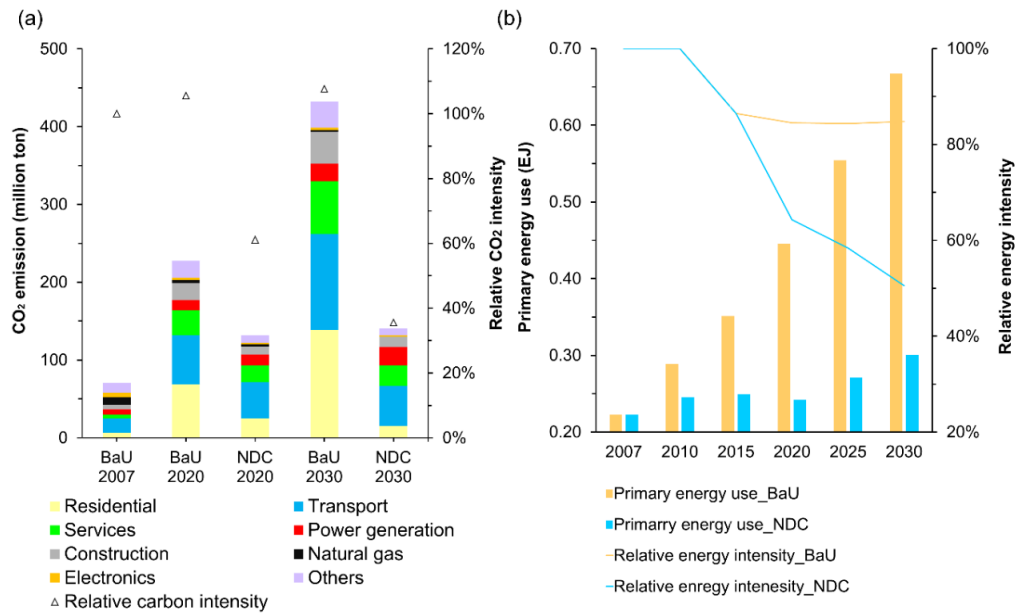


Figure 2.3 Variations in the (a) sectoral CO₂ emissions and relative CO₂ intensity, and (b) primary energy use and relative energy intensity under different scenarios.

Among all sectors in Shenzhen, the transport, natural gas, residential, power generation, construction, services, and electronics sector are the main contributors to CO₂ emissions and play an important role in achieving carbon mitigation targets. In 2007, these seven major sectors accounted for about 82% of the total CO₂ emissions, i.e., transport (25%), natural gas (14%), residential (10%), power generation (9%), construction (8%), services (8%), and electronics (8%) sectors (Figure 2.3a). Under the BaU scenario, the proportions of CO₂ emissions from residential, services, and construction sectors will significantly increase, while those from natural gas, power generation, and electronics sectors are decreasing from 2007 to 2030. With carbon mitigation, CO₂ emissions from most sectors are projected to be reduced by 53%-89% and their carbon intensity will decrease by 29%-88% by 2030 compared with the BaU scenario. The residential sector will decrease by the largest amount (70.5 Mt) in 2030, followed by transport (59.3Mt), services (36.1 Mt), and construction sectors (19.5 Mt). Accordingly, the transport sector contributes the largest CO₂ emissions under NDC scenario, followed by services and power generation sectors. Unlike other sectors, the carbon intensity of the power generation sector has a very limited decrease of 1% in 2030 under the NDC scenario. The reason is that the power generation sector has high reduction rate of autonomous carbon intensity since this sector can cut emissions through the adoption of renewable energy resources and efficient technologies even without the implementation of carbon mitigation strategies. For example, nuclear power accounts for 47% of the total energy source in the power generation sector in 2015 and non-fossil power contributes an increasingly higher proportion of the total power

generation. Even without the implementation of carbon mitigation, its carbon intensity decreases by 58% by 2030 relative to the 2007 level under the BaU scenario.

2.3.2. Impacts on Macroeconomics and Industrial Outputs

The implementation of carbon mitigation has macroeconomic impacts on Shenzhen with all selected indicators decreasing since carbon emission is not a free product anymore under the NDC scenario (Figure 2.4a). Among these macroeconomic indicators, the export and import will be influenced the most, with a loss of 3.3% and 3.6% by 2020 and 11.2% and 8.8% by 2030, respectively. The consumption is projected to be reduced by 2.0% by 2020 and 5.6% by 2030. The GDP and government expenditure will be slightly affected by a reduction rate of 0.1%-1.6% from 2020 to 2030. For example, the GDP loss of Shenzhen is projected to be 0.2% in 2020 and 1.6% by 2030, equivalent to 0.6 and 8.0 billion USD loss relative to the BaU scenario. Compared with the study of Shanghai (Wu et al., 2016), the GDP and welfare losses of Shenzhen are slightly lower to achieve China's NDC commitment, e.g., the GDP and consumption loss of Shanghai were 1.7% and 5.6% in 2030, respectively.

In contrast, Shenzhen suffers more export losses than Shanghai. The reason is that the main export products of Shenzhen are labor-intensive products, such as textiles, clothes, and toys. Those labor-intensive sectors suffer more considerable economic output loss with the carbon mitigation constraints. As shown in Figure 2.4b, the sectoral outputs of some labor-intensive sectors will be significantly affected, e.g., the manufactured gas sector will suffer the most loss (90%) in 2030, followed by natural gas mining (68%), transport (41%), non-metal (30%), and agriculture (12%) sectors. Other

labor-intensive industries such as food production, textile, services, and construction sector also suffer noticeable output losses, ranging from 1% to 5%. To achieve the carbon mitigation target, industrial sectors with higher carbon and energy intensity rely on reducing production and therefore would suffer economic losses. The projected total economic output losses are larger in 2030 (4%) than in 2020 (1%) due to the higher carbon intensity mitigation rate. The transport sector is the most influenced one and contributes 64% of the total outputs loss. This is because, in the current model setting, the transport sector still relies on traditional gasoline combustion engines, which is vulnerable to the carbon cost. Shenzhen is home to the most famous electric vehicle manufacturer - Biyadi. Therefore, to further reduce the carbon intensity in the transport sector, the Shenzhen government should promote new energy automobiles, such as hybrid and electric vehicles.

Carbon mitigation is beneficial to certain industries, e.g., the outputs of power generation (6%), electronics (6%), and paper (4%) sectors will have a slight increase in 2030. In addition to the higher reduction rate of autonomous carbon intensity in the power generation sector, carbon mitigation decreases the proportion of direct use of fossil fuel and increases the electrification rate in the whole economy. As a result, the production of the power generation sector will be expanded. Electronics and paper sectors are easier than other sectors to reduce the carbon intensity by adopting advanced technology and renewable energy resources, which is represented in the CGE model by the substitution of energy by capital. Meanwhile, their production efficiencies will be improved due to the lower carbon transformation.

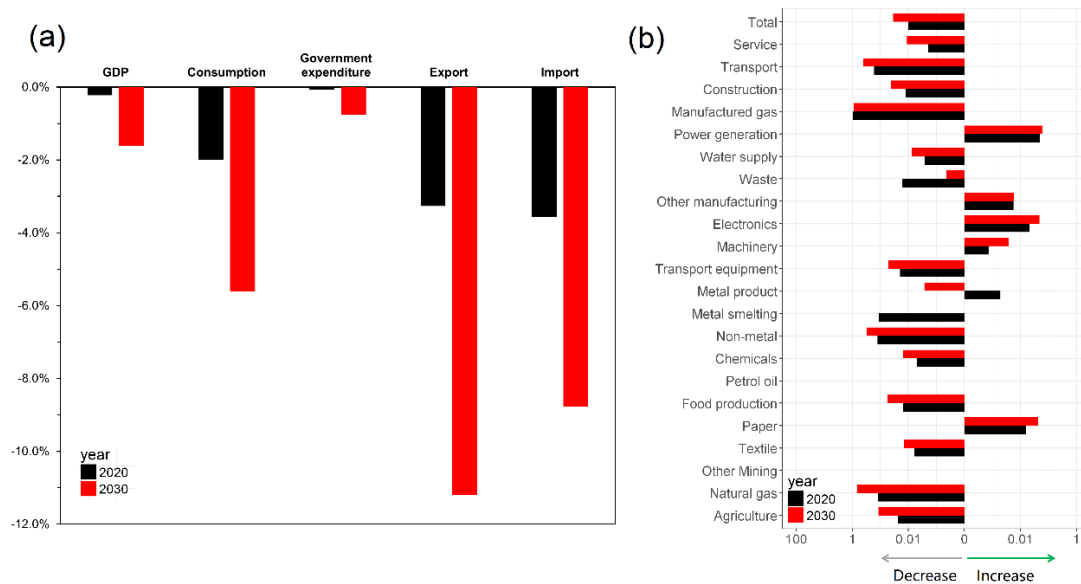


Figure 2.4 Relative changes in (a) the selected macroeconomic indicators (b) the sectoral outputs (using a Logarithmic scale) between NDC and BaU scenarios in 2020 and 2030.

2.3.3. Impacts on Water Withdrawals

Carbon mitigation accelerates local industrial structure upgrading by restricting carbon and energy-intensive industries. Since many of those industries are also water-intensive, it could be observed that carbon mitigation has co-benefits on local industrial water withdrawals. Under the BaU scenario, the total water withdrawals of Shenzhen will increase from 1,192 Mt in 2007 to 1,317 Mt in 2020 and to 1,252 Mt in 2030 (Figure 2.5a). Although the economic output in 2030 is nearly four times that in 2007, the total water withdrawals only increase by 5%. The main reason is that water intensity will be gradually reduced due to the water-saving technology improvement, e.g., the total WI reduces by 51% (2020) and 79% (2030) compared to the 2007 level under the BaU scenario (Figure 2.5a). Carbon mitigation can further reduce total water

withdrawals by 1% in 2020 and 4% in 2030, approximately 14 Mt and 47 Mt per year, respectively.

As shown in Figure 2.5b, carbon mitigation has uneven impacts on sectoral water use. To reduce local water use, it is expected that industrial sectors with comparatively higher water use intensity appear in the co-benefits quadrant instead of in the worse-offs and trade-offs quadrants. The synergistic water-saving effect is observed in most industrial sectors, e.g., services, transport, natural gas mining, non-metal, agriculture, food production, and textile sectors, and such effect is enhanced in 2030 compared to 2020 with more stringent carbon constraints. Compared to the sectors in the trade-offs quadrant, these sectors have higher WI, e.g., the mean water intensities (2011-2014) of natural gas mining, non-metal, agriculture, food production, and textile sectors were 4, 4, 335, 3, 16 times of that in the electronics sector (Figure A1 and Table A3, Appendix A). The decreasing proportion of these water-intensive industries will improve total water use efficiency, i.e., total WI decrease by less than 1% in 2030 compared with the BaU scenario. The limited decrease is because of the expansion of the services sector, e.g., under the BaU scenario, its proportion in total output is projected to increase from 24% in 2007 to 67% in 2030; in the same periods, the share of water withdrawals from the services sector increases from 25% to 70% (Figure 2.5a). In addition, WI in the service sector is close to the total WI, e.g., its WI is 5% higher than the total WI in 2030. Accordingly, the diminution of these water-intensive industries has limited effect on the reduction of total water intensity. Services and transport sectors are the top two contributors to the reduction of both carbon emission and water use (Figure 2.5b), and it

is estimated that there is a high potential to reduce water use by improving water use efficiency in the services and transport sector, e.g., a 10% reduction of industrial water use is expected by 2020 compared with the level in 2010 with the use of water-saving devices in these two sectors (Qin et al., 2013).

The carbon-water conflict is found in certain industrial sectors, such as power generation, paper, and electronics sectors. Carbon mitigation promotes production in these sectors. Thus, more attention should be paid to reduce water use intensity in these sectors, especially the power generation sector in the worse-offs quadrant, which has higher water intensity (Figure 2.5b, Table A3). Under the NDC scenario, water withdrawals from the power generation sector are projected to be enhanced by 6% because of its production expansion. Such trade-offs in water use may be exacerbated if high water use intensity technologies are used to reduce carbon emissions in the power generation sector. Water use intensity of the power generation is dependent on the choices of the cooling system and renewable energy penetration (Chandel et al., 2011; Clemmer et al., 2013; Li et al., 2017). In the study area, increasing the proportion of nuclear power may have co-benefits in water use since seawater is used for cooling in nuclear power generation. A study in China's nuclear power plants showed that the freshwater use in plants equipped with seawater closed-loop cooling technology was only 2% of traditional nuclear power plants (Lin and Chen, 2018).

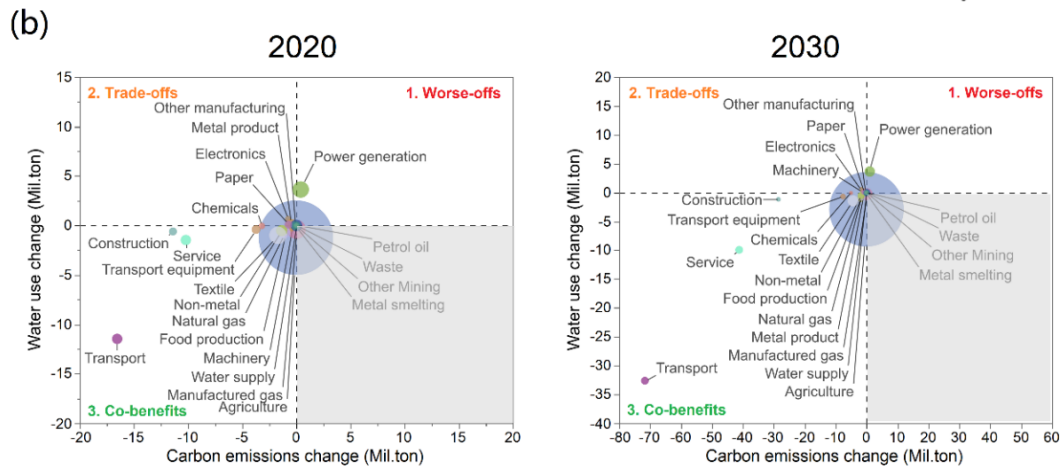
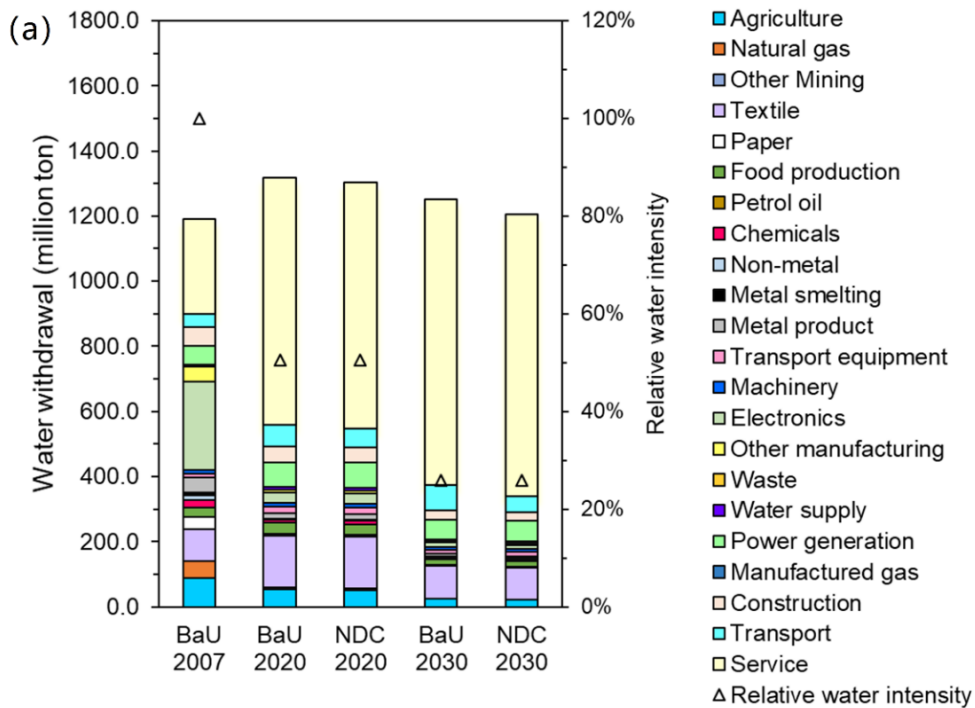


Figure 2.5 (a) Variations in the annual sectoral water withdrawals and relative water intensity under different scenarios; and (b) the carbon emission change (NDC compared with the BaU scenario) versus water use change (NDC compared with the BaU scenario) in 2020 and 2030 (Bubble size indicates sectoral water use intensity). In quadrant 4 (grey area), sectors have no water use and energy use change because of relatively small outputs).

2.3.4. Impacts on Water Pollutant Discharges

As shown in Figure 2.6, carbon mitigation can reduce COD_{Cr}, NH₃-N, petroleum, and V-ArOH discharges but slightly increase the discharges of heavy metal(loid)s, including Pb, Hg, Cd, and As. In 2030, the COD_{Cr}, NH₃-N, petroleum, and V-ArOH discharges under the BaU scenario are estimated to be 1.9×10^4 t, 1.7×10^3 t, 10.1 t, and 0.8 kg, respectively. Under the NDC scenario, the two main pollutants discharges will decrease by 2.2-2.4%, namely 431 t (COD_{Cr}) and 41 t (NH₃-N). The decrease of these two pollutants is also attributed to the local industrial structure upgrading under the NDC scenario. Many of the carbon and energy-intensive industries have higher pollutant discharge intensities, e.g., the mean COD_{Cr} and NH₃-N discharge intensities (2011-2014) of non-metal, food production, and textile sectors were 3, 4, 8 and 3, 4, 7 times that of the electronics sector (Table A5, Appendix A), respectively.

Carbon mitigation has trade-offs on heavy metal(loid)s discharges, e.g., the Pb, Cr, Hg, Cd, and As discharges will slightly increase by 0.43, -0.02, 0.03, 0.5, and 1.9 kg by 2030, respectively, corresponding to the increase rates of 2.0%, -0.01%, 4.3%, 3.8 %, and 4.6% of the BaU scenario. Unlike COD_{Cr} and NH₃-N, heavy metal(loid)s discharges are dominated by particular industries. For example, under the BaU scenario, the metal sector discharges 61% of V-ArOH, 53% of Pb, and 94% of Cr; the electronic sector discharges 46% of Pb, 38% of Hg, 81% of Cd, and 43% of As; the power generation sector discharges 41% of Hg. Accordingly, these pollutants discharges are sensitive to the implementation of carbon mitigation strategies. Carbon mitigation promotes the productions in electronics and power generation sectors and therefore increases the

discharges of Pb, Cd, As, and Hg. The increased discharges of heavy metal(loid)s have limited impacts on the local water environment. The contributions of heavy metal(loid)s on the Water Pollution Index (WPI) of Shenzhen River was as high as 5% during the period of 1984-1997, but the heavy metal(loid)s discharges have been well controlled, and their effects on water environment became negligible since 1997 (Qin et al., 2011). Results show that the heavy metal(loid)s discharges will be decreased in 2030 relative to the 2007 level under both scenarios, e.g., Pb, Hg, Cd, and As discharges are projected to decrease by 49%, 97%, 56%, and 63% in 2030 under BaU scenario, respectively.

It should also be noted that the technology-induced reduction in pollutant discharge is larger than the reduction induced by industrial structural change. As shown in Figure 2.6, the textile and food production sectors are the top two contributors to COD_{Cr} and NH₃-N discharges, accounting for about 27% and 28% (COD_{Cr}), and 24% and 30% (NH₃-N) in 2020 under the BaU scenario, respectively. The pollutant intensity reduces much faster in the textile sector than in the food production sector due to the wastewater treatment technology improvement (Table A6, Appendix A). With similar increase rates of economic outputs during the period of 2020-2030, the textile sector reduces by 84% of pollutant emissions, but the food production sector increases by 43% and becomes the top emitters of COD_{Cr} and NH₃-N in 2030 under both scenarios. Although carbon mitigation can reduce pollutant discharge in the food production sector by 5%, more effort should be made to improve cleaner technology.

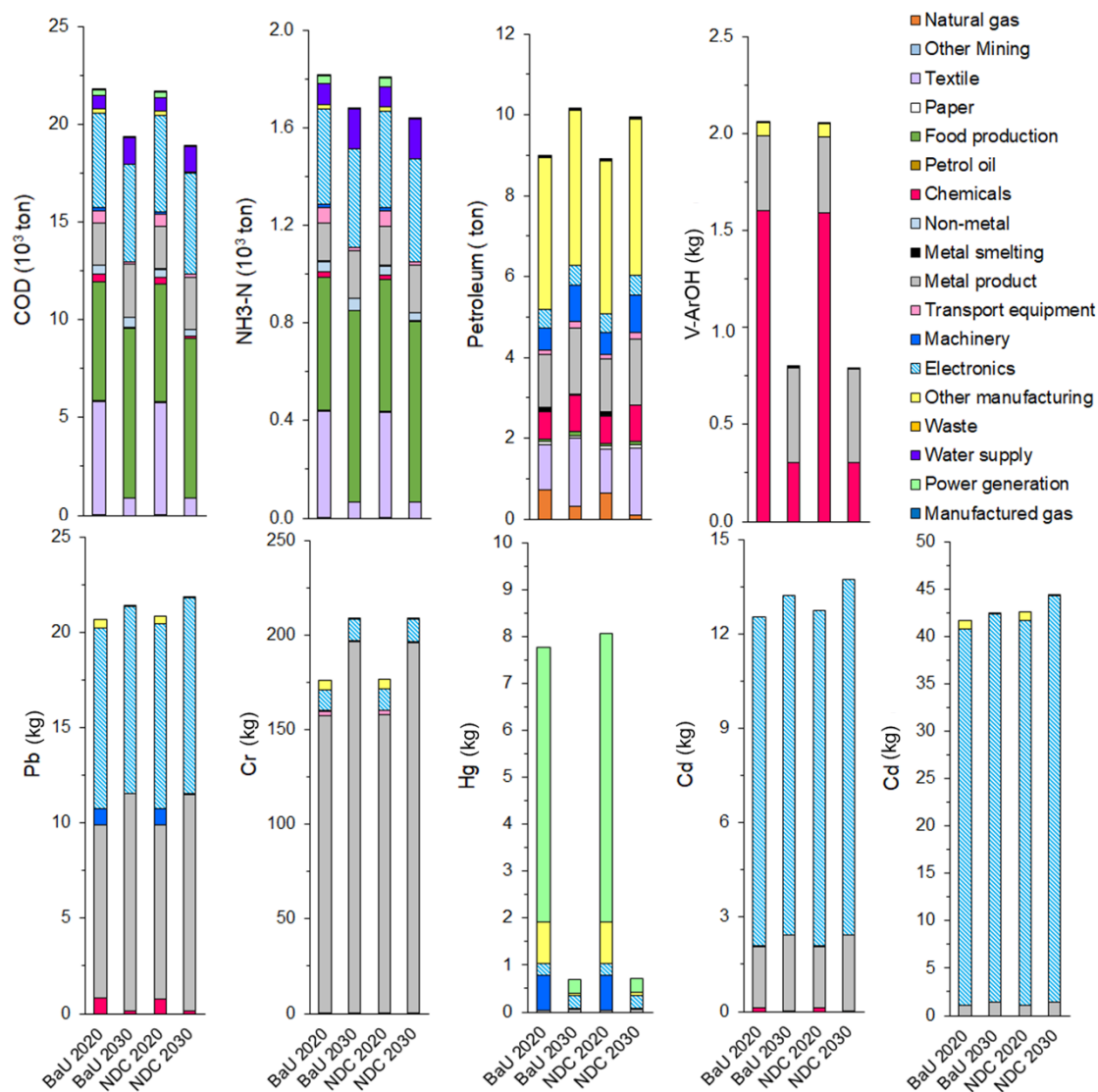


Figure 2.6 Variations in the annual sectoral pollutant loadings under different scenarios.

2.4. Discussion

2.4.1. Sensitivity Analysis

Given that the long-term projections may involve considerable uncertainties, several additional scenarios were analyzed to gain a better understanding of how the water use and pollutant discharge may potentially change with a range of different key

factors. The uncertainties include (1) the assumption of future economic growth in the CGE model and (2) the calculation of future water withdrawals and pollutants discharge. The first uncertainty was assessed by adding two GDP growth rates scenarios to the CGE model, i.e., the annual average GDP over 2007-2030 increased from 7.9% to 9.1% or slowed down to 6.7%, corresponding to the 28% higher or 22% lower GDP in 2030 than that in the BaU scenario. The energy use, CO₂ emission, GDP loss, water demand, and pollutants discharge in 2030 under the GDP_high and GDP_low scenarios are compared with the values in the NDC scenario, and their relative change rates are shown in Table 2.2. The GDP and welfare losses are less sensitive to GDP growth rate changes than the energy use, CO₂ emission, water demand, and water pollutants discharge. In addition, the impacts of the GDP growth rate changes in the energy use, CO₂ emission, and water use are slightly larger than most of the water pollutant discharges except for Hg. Regarding the secondary uncertainty, 95% CI of WR and PR in each sector was calculated, and their impacts on total water use and pollutant discharges are also shown in Table 2.2. Water demand ranges between -17.0% and 29.7%, COD_{Cr} and NH₃-N discharges range between -5.0% and 29.8%, petroleum discharge between -8.5% and 9.6%, Pb, Cr, Cd, and As between -0.8% and 3.6, and V-ArOH and Pb between -41.6% and 190.4%. This indicates that V-ArOH and Pb discharge are very sensitive to technology improvement in wastewater treatment. Nevertheless, the projected V-ArOH and Pb discharge are only 0.56 and 0.42 kg under NDC scenario in 2030 so that the large variability of these two pollutants is not likely to have a significant influence on the results.

Table 2.2 Relative Changes from the Projected Values in 2030 under the NDC Scenario.

Parameters	GDP_high	GDP_low	Upper	Lower
Energy use	30.00%	-23.10%	-	-
CO ₂ emission	28.40%	-22.30%	-	-
GDP losses	9.90%	-16.50%	-	-
Welfare losses	4.09%	-3.76%	-	-
Water demand	27.90%	-18.90%	29.70%	-17.02%
COD _{Cr}	25.00%	-19.30%	29.76%	-4.95%
NH ₃ -N	25.40%	-19.60%	26.41%	-4.44%
Petroleum	24.80%	-17.90%	9.61%	-8.52%
V-ArOH	25.80%	-19.60%	117.18%	-29.06%
Pb	25.70%	-22.70%	3.60%	-0.77%
Cr	25.50%	-20.70%	2.07%	-0.34%
Hg	30.70%	-27.50%	190.74%	-41.55%
Cd	24.90%	-22.50%	0.57%	-0.14%
As	24.30%	-23.00%	1.01%	-0.12%

‘-’ indicates not applicable.

2.4.2. Policy Implications

Currently, the energy-water nexus has been given scant consideration in energy and water management in China. One possible reason is that policymaking related to energy and water are performed by different departments without fully understanding the each other’s needs. The integrated model developed in this study captures the cross-sector interactions and feedbacks among economic, energy, and water systems, and thus it can be used to help policymakers identify the possible co-benefits or trade-offs across these systems and design effective policies and measures. The suggested strategies include: (1) mitigating the energy-water conflict. Carbon mitigation promotes the electrification rate in the whole economy and expands the production in the power generation sector. Due to its relatively higher water use intensity, trade-offs in water use in the power generation sector are observed. However, power plants may prefer to save

energy other than water under the current examination system (Lin and Chen, 2018). Therefore, incentive measures, such as allowances for water-saving and preferential taxes for power plants equipped with low water intensity technology, should be promoted to improve water use efficiency in power generation. In addition, to reduce the negative impacts of carbon mitigation on the heavy metal(loid)s discharges, the local government should close small-size plants which cannot satisfy the national discharge standards, particularly in sectors, such as chemical, metal produces, electronic, and power generation. Also, cleaner technologies should be promoted in both existing and new plants by setting pollutant discharge standards; (2) promoting the energy-water co-benefits. The transport and services sectors are the top two contributors to the reduction of both CO₂ emissions and water use. It should be noted that to fulfill the carbon mitigation target, the transport sector is projected to suffer significant economic losses, e.g., its economic output will be reduced by nearly 41% by 2030 compared with the BaU scenario. To reduce these economic losses, low-carbon transport policies, including speed control, an intelligent transport system, and mass transit systems improvement are suggested (Zhang et al., 2018). These two sectors also have lower levels of water-related pollutant emissions and high potential to reduce water use intensity, which implies that the local government should pay more attention to the utilization of water-saving technologies in these sectors.

Based on the analysis, more coordinated policies need to be designed to ensure water and energy security in the future, especially in the light of governmental reform that the carbon mitigation responsibility was moved into the newly founded Ministry of

Ecology and Environment in 2018. The chapter highlights the importance of integrated approaches in energy and water resources management. Although the current study focuses on a populated, developed megacity in southeast China, the framework could be applied at the city, region, and national scales, especially in areas with severe competition for energy and water resources.

3. MODELING THE CARBON-ENERGY-WATER NEXUS IN A RAPIDLY URBANIZING CATCHMENT²

Energy and water systems are interdependent and have complex dynamic interactions with the socio-economic system and climate change. Few tools exist to aid decision-making regarding the management of water and energy resources at the watershed level. In this chapter, the CGE model developed in Chapter 2 was integrated with the upgraded version of SyDWEM (CGE-SyDWEM) to simultaneously simulate energy and water systems and support decision-making regarding the management of energy and water resources and carbon reduction policy. The integrated model was tested in the Shenzhen River estuary catchment, which is located in the most urbanized area of Shenzhen, China. The effects of both the CO₂ mitigation strategies and the water engineering measures were evaluated. CO₂ mitigation strategies have the potential to reduce 46% CO₂ emissions and 41% energy use in 2025 compared with the reference scenario. CO₂ mitigation strategies are also found to be effective in promoting industrial structure adjustment by decreasing the output of energy- and water-intensive industries. Accordingly, it can alleviate local water stress and improve water environment, including a 4.1% reduction in both domestic water use and pollutant emissions, a 16.8% water demand reduction in the labor-intensive industry sector, and 4.2% and 4.4%

² Reprint with permission from “Modeling the carbon-energy-water nexus in a rapidly urbanizing catchment: A general equilibrium assessment.” by Qiong Su, Han-Cheng Dai, Yun Lin, Huan Chen, and Raghupathy Karthikeyan, 2018. *Journal of Environmental Management* 225: 93-103, Copyright [2021] by Elsevier.

decreases in BOD₅ and NH₃-N loads in all industrial sectors, respectively. It is necessary to implement water engineering measures to further alleviate water resource stress and improve water quality. Using this integrated model, planners from water and energy sectors could examine the cross-sectoral feedbacks, especially the impacts of CO₂ mitigation strategies on water demand and pollutant discharges as well as water quality change in the receiving waters.

3.1. Introduction

To ensure energy and water security as well as the adaptation to climate change, the Chinese government has implemented a series of policies and measures for CO₂ mitigation, energy and water-saving, and pollutant emission reductions. Recently, the NDC in the Paris Agreement was announced to reduce CO₂ emission intensity (CO₂ emissions per unit of GDP) by 60% to 65% by 2030 on the basis of the 2005 level (UNFCCC, 2015). At the same time, the 13th Five-Year Plan for economic and social development (NPC, 2016) proposed that energy and water use efficiency (energy and water use per unit of GDP) should be improved by 30% and 18% in 2020, respectively, compared with the 2015 level. In addition, two main water pollutant control targets were set to improve surface water quality, including a 10% reduction of industrial chemical oxygen demand (COD_{Cr}) and ammonia nitrogen (NH₃-N) discharge in 2020 compared with the 2015 level. Water and energy systems are interdependent, and thus policies and measures designed to increase efficiency in one system may significantly affect another (Hussey and Pittock, 2012; Li, 2017; Rothausen and Conway, 2011). To aid decision-makers to meet these goals efficiently, there is a need to integrate CO₂ mitigation

strategies with water resources management. The integrated approach helps better understand the links between energy and water systems and their dynamic interactions with socio-economic development and CO₂ emissions.

In this chapter, the CGE model developed in Chapter 2 was integrated with the upgraded version of SyDWEM (CGE-SyDWEM) to simulate energy and water systems simultaneously and support decision-making regarding the management of energy and water resources and carbon reduction policy. The boundary of this study is the Shenzhen River estuary and its associated watershed, i.e., the Shenzhen River estuary catchment. It is located in the most urbanized area of Shenzhen (Figure 2.1). It borders Shenzhen to the north and Hong Kong to the south. It is adjacent to Dapeng Bay to the east and the Pearl River Estuary to the west. Deep Bay is a half-enclosed and shallow bay with a total area of 115 km² and an average depth of 2.9 m. The bay can be divided into an inner bay and an outer bay from head to mouth. Shenzhen River, with a total length of 14 km, is influenced by the irregular, mixed semidiurnal tide of the South China Sea. The tidal flow can reach the upstream of the Shenzhen River. This area has a mild, subtropical maritime climate with a mean annual temperature of 22.4°C and precipitation of 1,933 mm, of which 78% falls in wet periods (from April to September). With rapid economic and population growth, the Shenzhen River estuary catchment faces challenges in meeting the increased water and energy demand.

The specific objectives of this chapter are to (1) examine the performance of the integrated CGE-SyDWEM in simulating the interactions among socio-economic, energy, carbon, and water environmental systems; (2) evaluate CO₂ mitigation strategies

on local labor force migration and population growth; (3) evaluate the co-benefit of CO₂ mitigation strategies on water use saving and pollutant emission reduction; and (4) assess if current water engineering measures can satisfy water demand, water pollutant reduction, and environmental targets.

3.2. Methodology

3.2.1. Integrated CGE-SyDWEM Model

Figure 3.1 illustrates the conceptual integration of the CGE model and SyDWEM model. The energy-water system in the rapidly urbanizing catchment is a complex system, including socio-economic, energy, water infrastructure, and receiving water systems. The CGE model is used to simulate city-level socio-economic and energy system changes under CO₂ mitigation strategies. SyDWEM is used to simulate the sub-catchment level of socio-economic, water infrastructure, and receiving water systems. The two models are integrated through the socio-economic system. For example, the CGE model predicts city-level industrial output change under CO₂ mitigation strategies, and then the SyDWEM model translates these changes into sub-catchment levels. Both models considered 22 sectors, and SyDWEM further classifies them into five main sectors, including primary industry, i.e., agriculture, labor-intensive industry, e.g., textiles and paper products, technology-intensive industry, e.g., electronic equipment and machinery, capital-intensive industry, e.g., new material and energy industry, and tertiary industry, e.g., service industry. In order to unify the database of the two models, the relative change of industrial structure was used to integrate the two models. Also, the two models share the same inputs, such as labor and capital (Figure 3.2).

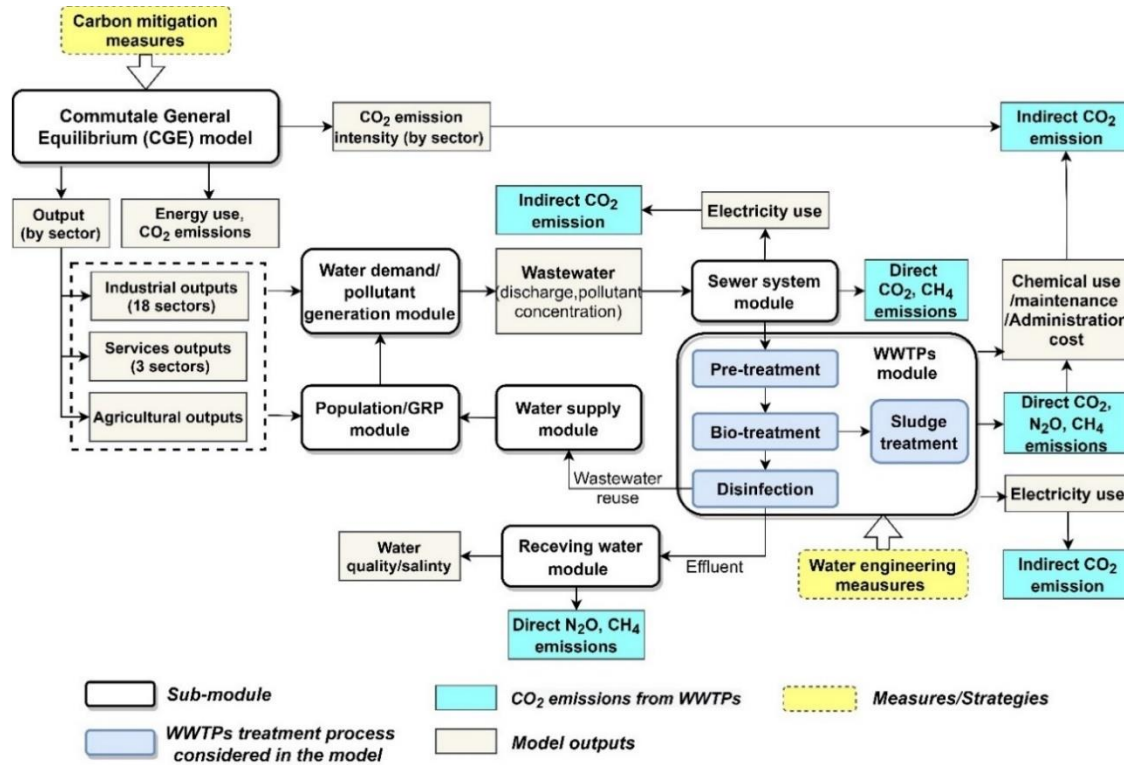


Figure 3.1 Conceptual integration of computable general equilibrium (CGE) and System Dynamics and Water Environmental Model (SyDWEM).

The interactions and feedbacks among different systems include: (1) CO₂ mitigation strategies affect the socio-economic system, e.g., economic outputs in different industrial sectors, and energy system, e.g., CO₂ emissions and energy use; (2) economic outputs of different industrial sectors influence sub-catchment level gross regional product (GRP) change and labor force demand. Here, GRP is similar to GDP, but for regional analysis; (3) sub-catchment level socio-economic change affects water demand, and wastewater generation from domestic and industrial activities; (4) the spatial distribution of wastewater is simulated by the sewer and WWTPs systems, which are linked with water quality model; (5) wastewater can be further treated and reclaimed,

and becomes an important source of water supply system; (6) water supply system supports population and economic development; and (7) the implementation of water engineering measures (e.g., wastewater treatment, reuse, and water supply) might lead to additional energy use and CO₂ emissions. If the change is small compared with the overall energy use and CO₂ emissions in the study area, this feedback might be negligible. Using the integrated model, energy planners can evaluate the proposed CO₂ mitigation strategies on water demand and pollution emissions. Water planners can better understand the rapid socio-economic development and provide effective support for population and economic growth. Also, water engineering measures impacts on energy use and CO₂ emissions can be evaluated by energy planners.

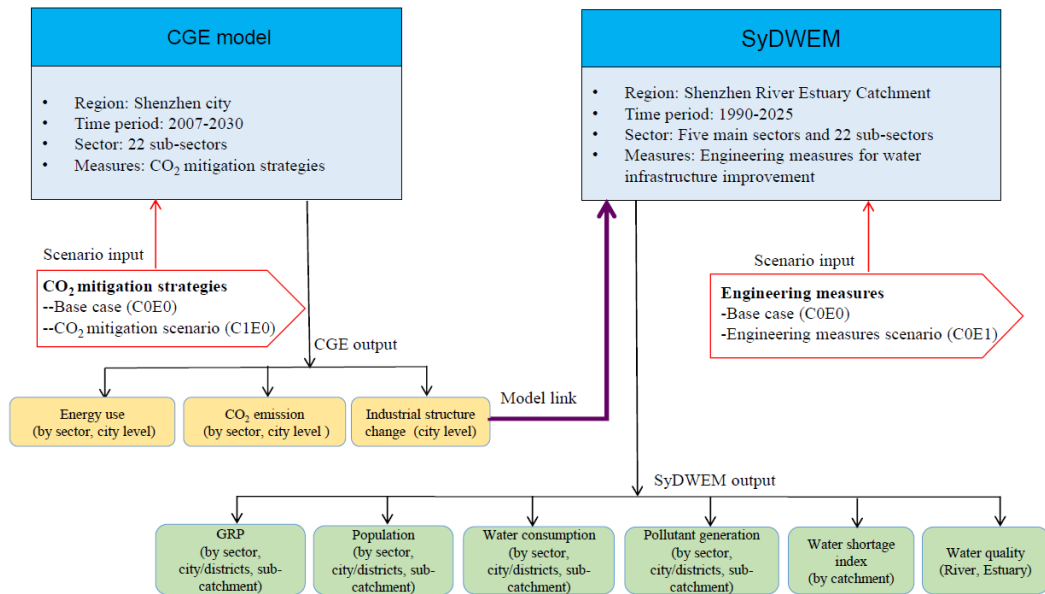


Figure 3.2 Data flow in the CGE-SyDWEM.

Understanding the spatial and temporal scale differences is important in model coupling. For spatial scales, socio-economic and energy systems are developed at the administrative district level; sewer and WWTPs systems are based on their service areas; water supply and receiving water systems are considered at watershed levels. For temporal scales, socio-economic and energy systems are projected at an annual step; water demand and supply, sewer and WWTPs system are simulated daily; receiving water module is set to seconds to capture the dynamic variations of flow and water quality in the river and estuary. The annual and daily data could be downscaled to seconds for model coupling.

The major assumptions of the integrated model include: (1) GRP, population, water demand, and pollutant generation are assumed uniformly distributed in the built-up area of the catchment; (2) water level and water quality of the open boundary in the hydrological water quality model are assumed not to change in the future; and (4) water pollutant loads from tertiary industry are assumed to be included in the domestic sector.

3.2.2. SyDWEM

SyDWEM was developed to describe the socio-economic, water infrastructure, and the change of receiving water system in the Shenzhen River catchment during 1990-2020 (Qin et al., 2011, 2013). The model is upgraded to meet the requirements of this study in the following five aspects: (1) simulation period was extended to the year 2025. Results of labor productivity for each industry in 2025 have been compared with the data in Japan (JPC, 2016) and Hong Kong (Census and Statistics Department of Hong Kong, 2016) to guarantee the projection for each industry falling in a reasonable range; (2)

previous industrial structure was considered as a decision variable, and its effect on GRP and population growth was evaluated using scenario analysis. In the updated SyDWEM, industrial structure is predicted by the CGE model and treated as an inner-module of the integrated model; (3) Nanshan District and associated sub-catchments in the Shenzhen Estuary are added. The estimated parameter values for GRP growth of Nanshan District are shown in Table B1, Appendix B; (4) two additional water quality parameters (i.e., BOD₅ and NH₃-N) are incorporated into the updated model; and (5) river/estuary water quality model has been upgraded to a two-dimensional (2D) model from a one-dimensional model. The details of the input parameter values for the upgraded SyDWEM can be found in Table B2, Appendix B. The main components and functions for each module are described as follows:

(1) Population/GRP module: Population is determined by the projection of birth, death, and labor force migration. Labor force migration dominates the population growth in rapidly urbanizing areas and is interacted with economic growth. Subcatchment level GRP is calculated based on the Cobb-Douglas production function (Qin et al., 2011). Labor force and net investment are the two main drivers of future GRP growth. Future net investment is based on local planning. Future labor force demand is determined by the projected changes in labor productivity and industry structure. SyDWEM can simulate GRP and population growth at both administrative and sub-catchment scales.

(2) Water demand/pollutant generation module: Domestic and industrial water demand and BOD₅ and NH₃-N generation are predicted in this module. Water demand and pollutant generation from all sectors are based on population growth, economic

development, water use efficiency, pollutant loads per capita, pollutant loads per GRP, and the projected changes in the industrial structure.

(3) Water supply module: Water supply capacity is based on the calculation of local groundwater and surface water resources, available reclaimed wastewater, and available water transferred from other catchments. Local groundwater and surface water resources are estimated from the groundwater resources development rate and rainwater collection ability in the reservoirs at the upstream of the Shenzhen River, respectively. Available reclaimed wastewater and transferred water from other catchments are based on the reclaimed wastewater reuse ratio and water transfer quota, respectively, which is in accordance with the local water resources plan.

(4) Sewer and WWTPs module: Wastewater discharged into the receiving water includes wastewater linked to the sewer system and treated by WWTPs, untreated wastewater assumed to discharge into the nearby river, and part of the effluent of WWTPs, which may be reused and back to the water supply module. For example, policymakers can adjust the reclaimed wastewater reuse ratio to provide more water for residential or industrial reuse. The efficiency of wastewater treatment infrastructure influences the amount of wastewater and pollutant discharged into the receiving water and the amount of wastewater reused in industries and domestic activities.

(5) Receiving water module: Environmental Fluid Dynamic Code (EFDC) (Hamrick, 2006) is employed to simulate hydrodynamics and water quality changes in the Shenzhen River estuary. Since the estuary is very shallow, unstratified, and well-mixed, a two-dimensional depth-averaged tidal flow model is developed. The model

contains 2382 active grid cells covering the entire Shenzhen River estuary. Grid sizes vary with the distance from the river, i.e., comparatively smaller cells are near the river mouth (around 100*100m), and larger cells are in the mouth of the bay (around 250*250m). The open boundary is located in the southwest of Deep Bay (Chiwan). Water level for the open boundary is obtained from the tide table of the South China Sea. The upstream boundary discharge was obtained from the measurements by Hu (2007). The BOD₅ and NH₃-N are taken as representative variables of water quality. The EFDC model runs at a time step of 10s with a cold start of 15 days to obtain initial conditions and another 15 days for result analysis.

3.2.3. Model Calibration and Validation

Observed data from 1990 and 2001 for GRP, population, and water demand are used for model calibration, and data from 2002 and 2009 are used for model validation. Parameters required for the EFDC of the Shenzhen River estuary have been calibrated in our previous study (Su et al., 2014). Simulated wastewater and pollutant discharges in 2004 were used for water quality model inputs. The model was validated using water quality data obtained in the water sampling monitoring during 17–18 and 25–26, Oct 2004. Eight temporary stations were established (Figure 2.1). Water level, BOD₅, and NH₃-N at the three stations, including S03 (at the river mouth), S05 (at the inner bay), and S06 (at the outer bay), were chosen to compare with measured data.

Maximum relative error (M) and normalized standard error (E) are used to evaluate model performance. The M and E are calculated using equations (3.1) and (3.2).

$$M = \max[(S_i - M_i)/M_i] \quad (3.1)$$

$$E = \frac{\sqrt{\frac{1}{n(n-1)} \sum_{i=1}^n (S_i - M_i)^2}}{\frac{1}{n} \sum_{i=1}^n M_i} \quad (3.2)$$

where, S_i is the i th simulated value; M_i is the corresponding measured value; and n is the number of measurements.

The receiving water module performance is evaluated via correlation coefficient (r) defined as follows:

$$r = \frac{\sum_{i=1}^n (S_i - \bar{S})(M_i - \bar{M})}{\sqrt{\sum_{i=1}^n (S_i - \bar{S})^2 \sum_{i=1}^n (M_i - \bar{M})^2}} \quad (3.3)$$

where S_i is the i th simulated value; M_i is the corresponding measured value; n is the number of data; and \bar{S} and \bar{M} are the simulated and measured averages, respectively. The value of r ranges from -1 to 1. In general, a value greater than 0.7 suggests a good agreement in model prediction.

Validations of GRP, population, and water consumption from 2002 to 2009 are shown in Figure 3.3. M for GRP, population, and water consumption in different districts/towns range from 0.0% to 9.8%, and E ranges from 1.0% to 2.6%. The correlation coefficients for water level, BOD₅, and NH₃-N at the three stations (S03, S05, S06) range from 0.92 to 0.97, 0.67 to 0.84, and 0.65 to 0.73, respectively (Figure 3.4). The validation results indicate that the updated SyDWEM model can simulate the relationship among GRP, population, water demand, and wastewater treatment as well as spatial and temporal variation of hydrodynamics and water quality in the Shenzhen River estuary.

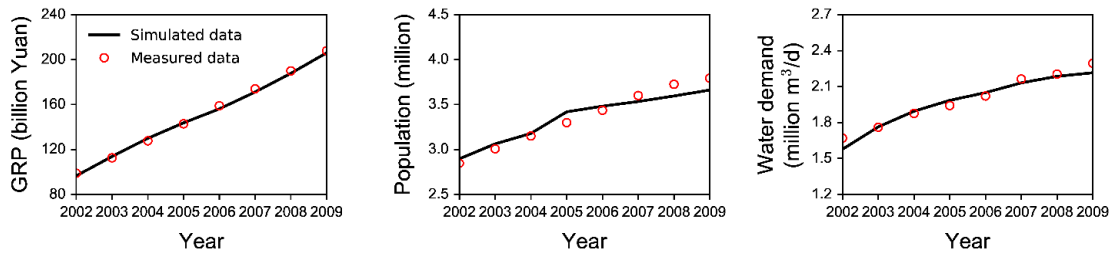


Figure 3.3 Comparison of simulated and measured GRP, population, and water consumption from 2002 to 2009.

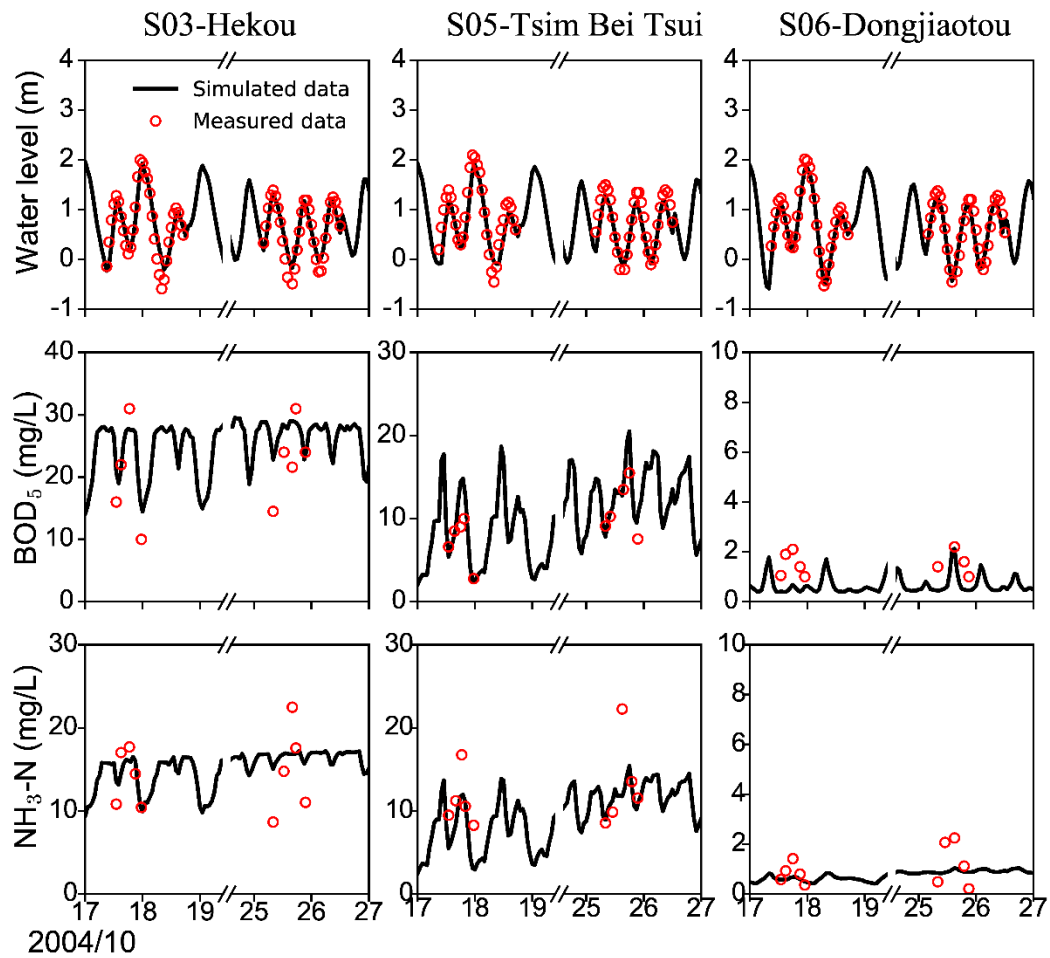


Figure 3.4 Comparison of simulated and measured water level, BOD₅, and NH₃-N in October 2004.

3.2.4. Scenarios

Four scenarios, including C0E0, C1E0, C0E1, and C1E1, were set up to address the research questions (Table 3.1). C0E0 is a reference scenario that simulates the socio-economic, energy, and water system change without implementing CO₂ mitigation strategies or engineering measures. Future economic and population growth of Shenzhen in the CGE model was based on the results from the previous version of SyDWEM (Qin et al., 2011) and was provided in Chapter 2 Table 2.1. The capacity and technology of water infrastructure system in 2009 will persist between 2010 and 2025. The C1E0 scenario evaluates the effects of CO₂ mitigation strategies. This scenario differs from the reference scenario only in that it includes a constraint on CO₂ emissions. A carbon cap is set so that the CO₂ emission intensity of Shenzhen will be reduced by 45% by 2020 and 65% by 2030 compared with the 2007 level, which is consistent with China's newly announced NDC.

The C0E1 scenario evaluates the effects of engineering measures on future water resource stress and water quality change in the catchment. The development of the socio-economic system in the future is the same as C0E0, and there is no CO₂ emission intensity constraint. Table 3.2 lists water engineering measures assessed in this study, including three categories: (1) improving water use efficiency (M1, M2); (2) increasing water supply capacity (M3, M4); and (3) increasing the efficiency of wastewater infrastructure system (M5, M6). These measures are based on the water infrastructure planning of Shenzhen (SZUPLRB, 2003), and sensitivity analysis and possible range of

each measure have been analyzed in our previous study (Qin et al., 2013) and are summarized in Table 3.2.

Table 3.1 Configurations for the Four Scenarios.

Scenarios	Emission constraints	Engineering measures
C0E0	No constraints	No engineering measures upgraded in 2025
C1E0	Emission intensity reduced by 40% in 2020 and 65% in 2030	Same as C0E0
C0E1	Same as C0E0	Engineering measures upgraded
C1E1	Same as C1E0	Same as C0E1

Table 3.2 Summary of Water Engineering Measures

Measures/decision parameters	The possible % increase relative to C0E0
M1: Industrial water recycling technology upgrade	10%
M2: Decreasing pipeline leakage	5%
M3: Increasing water transfer	20%
M4: Increase reclaimed wastewater reuse	10%
M5: Improving volumetric wastewater treatment rate	Increase to 90%
M6: Pollutants removal rate of WWTPs	Increase to 80% (NH ₃ -N) and 90% (BOD ₅)

3.3. Results

3.3.1. Energy Consumption and CO₂ Emissions

Total primary energy consumption under C0E0 will increase to 0.46 EJ by 2025, which is more than twice that in 2007 (Figure 3.5a). However, under the C1E0 scenario, the primary energy consumption shows a decreasing trend during 2015-2020, and then slight increases to 0.17 EJ in 2025, which is only 41% of that in the reference scenario. The energy intensity in terms of GRP improves at an average annual increase rate of

9.1% in the C1E0 scenario, fulfilling the 30% regional improvement target during 2015-2020.

The trend of CO₂ emissions under C0E0 is in alignment with the primary energy consumption, showing significant growth from 69.7 million tons (Mt) in 2007 to 317.9 Mt in 2025 (Figure 3.5b), equivalent to an annual growth rate of 9.5% and 8.0% for the periods of 2015-2020 and 2020-2025, respectively. However, with the CO₂ emission intensity constraint, the CO₂ emissions show a decreasing trend after 2015. Carbon mitigation strategies have the potential to reduce CO₂ emissions by 172.9 Mt (46%) by 2025, compared with the reference scenario. The carbon intensity (CO₂ emissions per GRP) by 2025 will decrease to 58% of the 2007 level, fulfilling the regional NDC target.

The CO₂ mitigation strategies could substantially reduce energy use and CO₂ emissions and improve energy use efficiency and carbon intensity. The main reason is that with the CO₂ emission intensity constraint under the C1E0 scenario, carbon emission allowance becomes a scarce resource and has a carbon shadow price that could be regarded as the marginal mitigation cost of carbon reduction. The carbon price is an equilibrium price that could balance the supply and demand of the carbon emission allowance. The supply of carbon emissions is implied by the carbon intensity target and future GDP, whereas the demand of the carbon emissions is represented by the emissions required by different industrial sectors and households, which is affected by the industrial output and income level. The carbon price will increase the production prices of all sectors depending on its carbon intensity. On the demand side, consumers will adjust their activities to lower the demand for energy- and carbon-intensive

products. As a result, the output of some typical energy- and carbon-intensive industries such as textile, food production, chemicals, and non-metal will be greatly reduced because of the comparatively high carbon emissions, leading to the industrial structure change (Table B3, Appendix B). For example, compared with C0E0, the proportion of labor-intensive and technology-intensive industries decreases by 4% and 2%, respectively, and the proportion of capital-intensive industries increases by 5%.

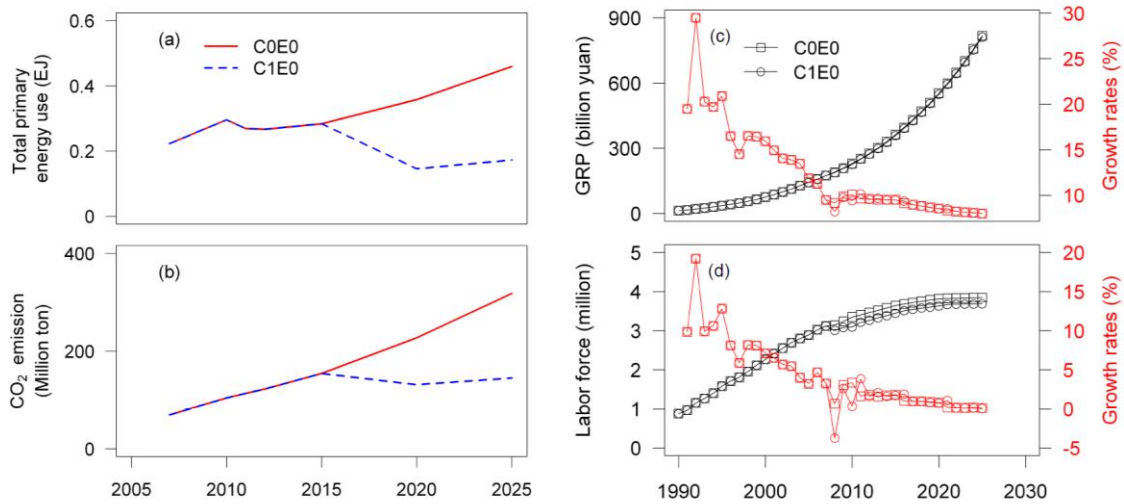


Figure 3.5 Annual variation of (a) total primary energy consumption, (b) CO₂ emission, (c) GRP (with its growth rates), and (d) labor force (with its growth rates) in Shenzhen under the reference scenario (C0E0) and CO₂ mitigation scenario (C1E0).

3.3.2. GRP and Labor Force

CO₂ mitigation strategies will slightly decrease GRP and labor force migration in the catchment due to the change of industrial structure. Because capital-intensive industries have higher labor productivity than the other two industries, e.g., labor productivity of capital-intensive industries is 17 and 5 times of that in technology-

intensive and capital-intensive industries, and thus the total labor productivity improves by 3.6% by 2025 with the increased proportion of capital-intensive industries (Table B4, Appendix B). Less labor force is required to maintain the same GRP growth rate. Under C0E0, it is projected that GRP will increase from 229.6 billion Yuan by 2010 to 818.0 billion Yuan by 2025 (Figure 3.5c). GRP grows very quickly at the early stage of urbanization (1990-2000) with an annual growth rate of 19%, but its growth rate will slow down after 2007 to a nearly constant rate around 8.0% later on. The relatively slow growth rate of GRP after 2007 is mainly attributed to the decreasing return of capital in all administrative areas (PGSZM, 2008). The GRP variation curve under the C1E0 scenario nearly overlaps that under C0E0, and the GRP losses compared with C0E0 by 2025 are 0.7%.

Labor force migration is the primary determinant of the population growth of Shenzhen, and the migration population accounted for nearly 70% of the total population in 2016. The projected labor force demand under C0E0 increases from 3.12 million in 2007 to 3.85 million in 2025, with an average annual growth rate of 1.2% (Figure 3.5d). This average annual growth rate is much smaller than that in the early stage of urbanization (nearly 10% during 1990-2000) due to the slower economic growth rate and improved labor productivity. Under C1E0, the projected labor force demand grows at a lower annual average growth rate of 0.9% (Figure 3.5d). Compared with C0E0, the projected labor force demand decreases by 0.16 million. Constant birth rate and death rates are assumed during 2010-2025, and the projected population decreases by 0.19 million compared with C0E0.

3.3.3. Stress on Water Resources

Water demand under the reference scenario will grow continuously between 2010 and 2025, increasing from 2.38 to 4.08 million m³/d (Figure 3.6a). However, there will be a slight increase in the potential water supply due to the limited increase in reclaimed wastewater reuse for residential and economic activities. Here the water shortage index (WSI) is used, which is defined as the ratio of water demand to potential water supply, to determine the degree of local water stress (Qin et al., 2013), with values greater than one indicating the condition of severe water limitation. Given that the growth of water demand is much greater than the potential water supply, WSI increases quickly to be greater than one after 2015 and reaches as high as 1.46 by 2025 (Figure 3.6b), implying that the study area will suffer severe water deficit in the near future.

By implementing water engineering measures (C0E1), the total water demand will be reduced by 8.1%, and WSI will decrease by 30.7% by 2025 compared with C0E0 (Figure 3.6a,b). Since the WSI value under C0E1 will be close to one when approaching the year 2025 (Figure 3.6b), the water demand and water supply will be nearly in balance even if employing engineering measures alone. With CO₂ mitigation strategies (C1E0), the total water demand by 2025 is expected to decrease by 0.8% relative to C0E0, including a 4.2×10^4 m³/d reduction (4.1%) in the residential sector and a 4.7×10^4 m³/d reduction (16.8%) in labor-intensive industries. However, water demand from capital-intensive industries will increase by 13.9%, and its proportions in sectoral water demand increase from 11% in 2010 to 13% (C0E0) and 15% (C1E0) by 2025, respectively (Figure 3.6c, d, and e). With the combined effects of engineering measures

and CO₂ mitigation strategies, the total water demand by 2025 will be reduced by 12.2% relative to C0E0, and it will be balanced by the water supply.

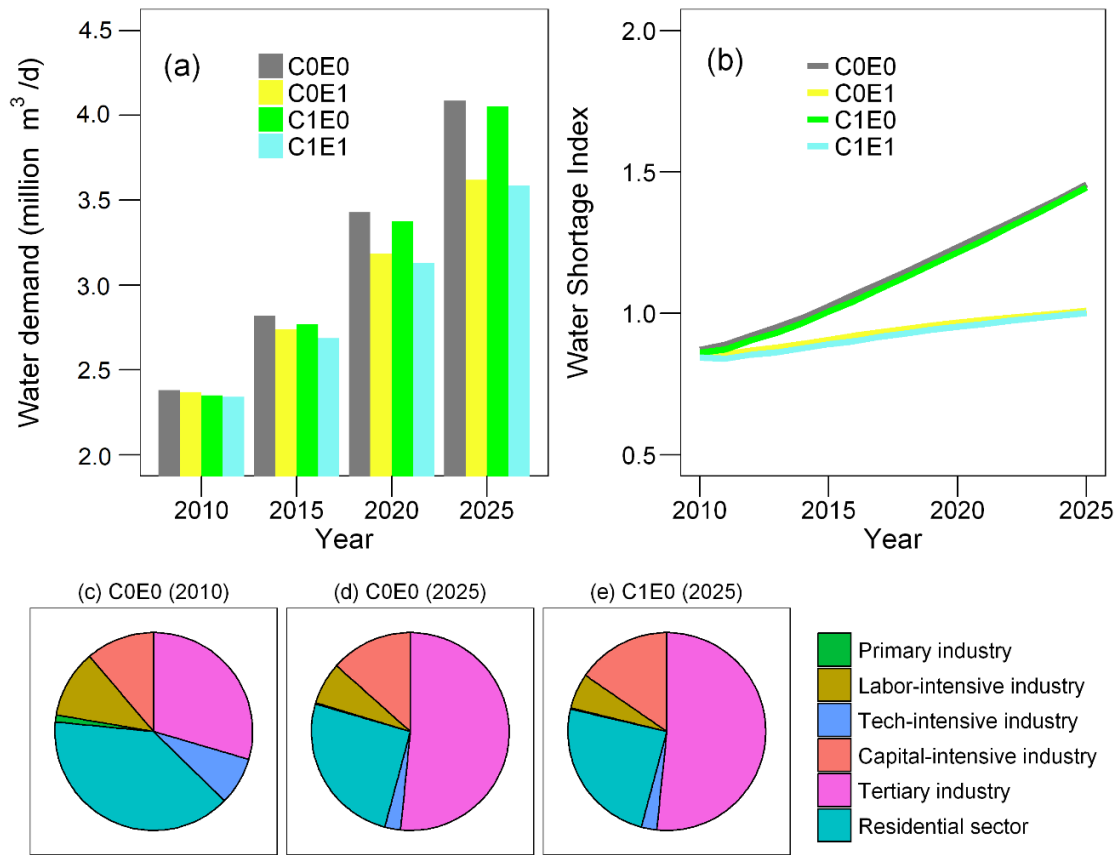


Figure 3.6 Annual variations of (a) total Water demand, (b) WSI and sectoral water demand under different scenarios including (c) current situation (2010) (d) C0E0 (2025) and (e) C1E0 (2025).

3.3.4. Water Quality Change

The current water infrastructure systems cannot provide sufficient service to collect and treat all wastewater. Figure 3.7 shows that under the reference scenario, total BOD₅ and NH₃-N generations from residential and industrial sectors increase by 38.5%

and 27.2% from 2010 to 2025. As a result, the projected BOD₅ and NH₃-N discharges into the river grow greatly from 2010 to 2025 under C0E0, with a total increase of 37.9% and 27.5% in 2025, respectively. CO₂ mitigation strategies (C1E0) have co-benefit on pollutant generation reduction (Figure 3.7c, d), i.e., both BOD₅ and NH₃-N generations by 2025 will decrease by 4.2% and 4.4% compared with C0E0, including a 6.8 t/d (4.1%) and 2.9 t/d (4.1%) decrease in residential sector and a 3.4 t/d (6.8%) and 0.5 t/d (4.7%) decrease in secondary industry, respectively. Water engineering measures can further reduce pollutant discharges. Specifically, the projected BOD₅ and NH₃-N discharges under the C0E1 scenario are reduced by 50.1% and 53.5% in 2025 compared with C0E0, respectively. The combined effects of CO₂ mitigation strategies and engineering measures on pollutant discharge evaluated via the C1E1 scenario show that the total BOD₅ and NH₃-N discharges will decrease to 34.2 t/d and 10.9 t/d by 2025, respectively, corresponding to reduction rates of 29.2% and 39.0% based on 2010 level.

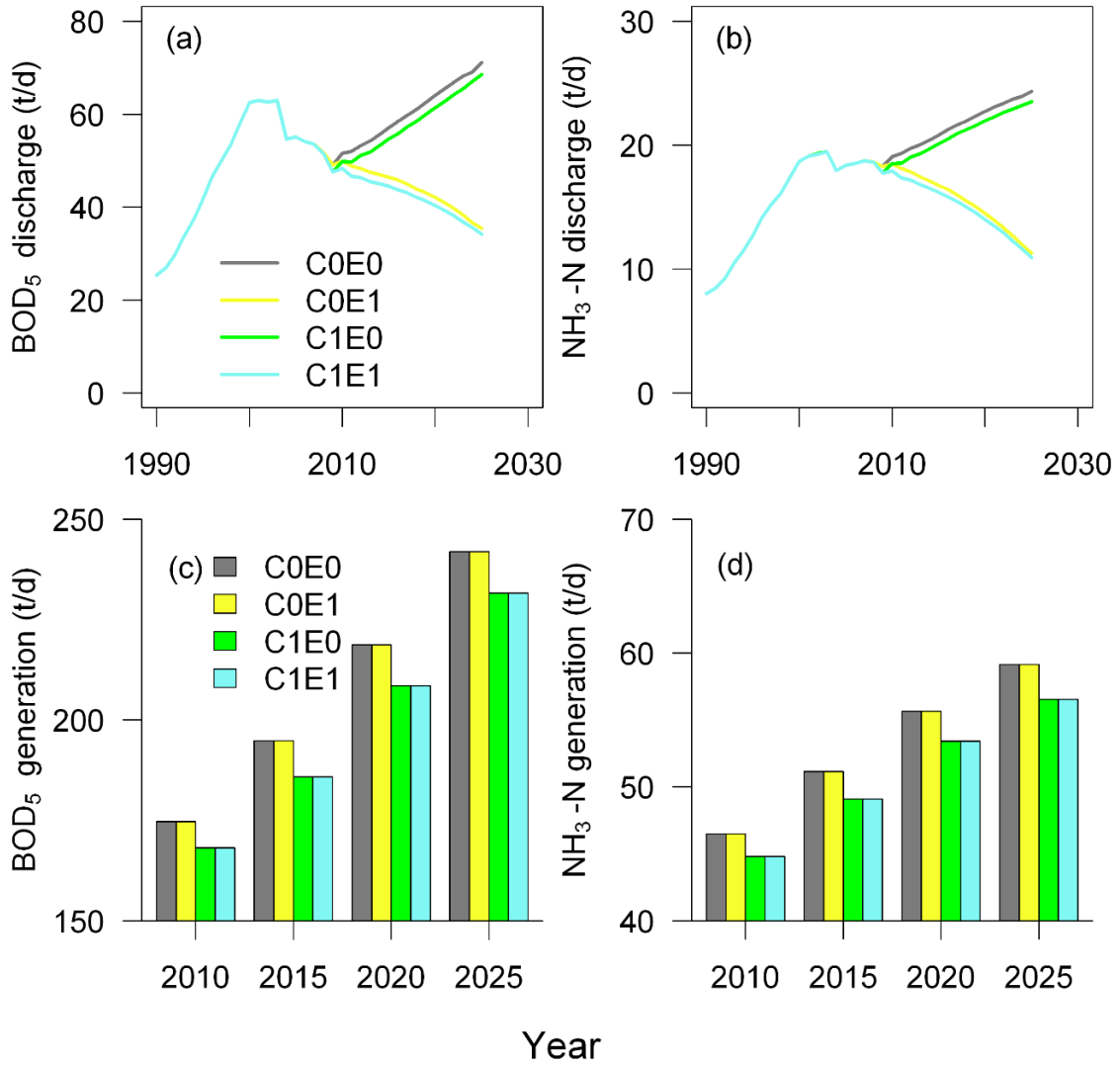


Figure 3.7 Annual variations of BOD₅ loading/discharge (a and c) and NH₃-N loading/discharge (b and d) from 2010 to 2025 under different scenarios.

Figures 3.8 and 3.9 show the temporal and spatial water quality variation in the Shenzhen River estuary under different scenarios. Water quality varies greatly at each station due to the combined effects of the tide and wastewater discharge. At stations S03 and S05, NH₃-N concentration shows a slightly decreasing trend under C0E0. However,

water quality continues to worsen at all other stations from 2010 to 2025, with the average concentration ranges of BOD₅ and NH₃-N in 2025 being 1.1-32.3 mg/L and 1.0-13.1mg/L, respectively.

Under C1E0, water quality is slightly improved at all the four stations relative to C0E0, i.e., the BOD₅ and NH₃-N concentrations at S01, S03, S05, and S06 decrease by 0.7-2.7% and 1.3-5.2%, respectively. Without considering flood or ebb tide, the maximum concentrations of BOD₅ and NH₃-N occur at S01, where most of the untreated wastewater in the study area is discharged into the river. With engineering measures (C0E1), the projected BOD₅ and NH₃-N discharges reduce by 29.0% and 38.8% by 2025 compared with 2010 (Figure 3.8c and d). Thus water quality will be substantially improved between 2010 and 2025. With integrated measures, the average BOD₅ and NH₃-N concentrations at S01 (where the water quality was impaired the worst) will decrease to 13.4 mg/L and 6.0 mg/L in 2025, only 45% and 46% of the 2010 level, respectively. As shown in Figure 3.9, except for some cross-sections in the middle reach of the river, water quality in Shenzhen River Estuary will satisfy the water quality level suggested by Hu (2007) and Su et al. (2014) to eliminate the malodorous-black phenomenon in the river, with average BOD₅ concentration lower than 10 mg/L and NH₃-N concentration lower than 6 mg/L.

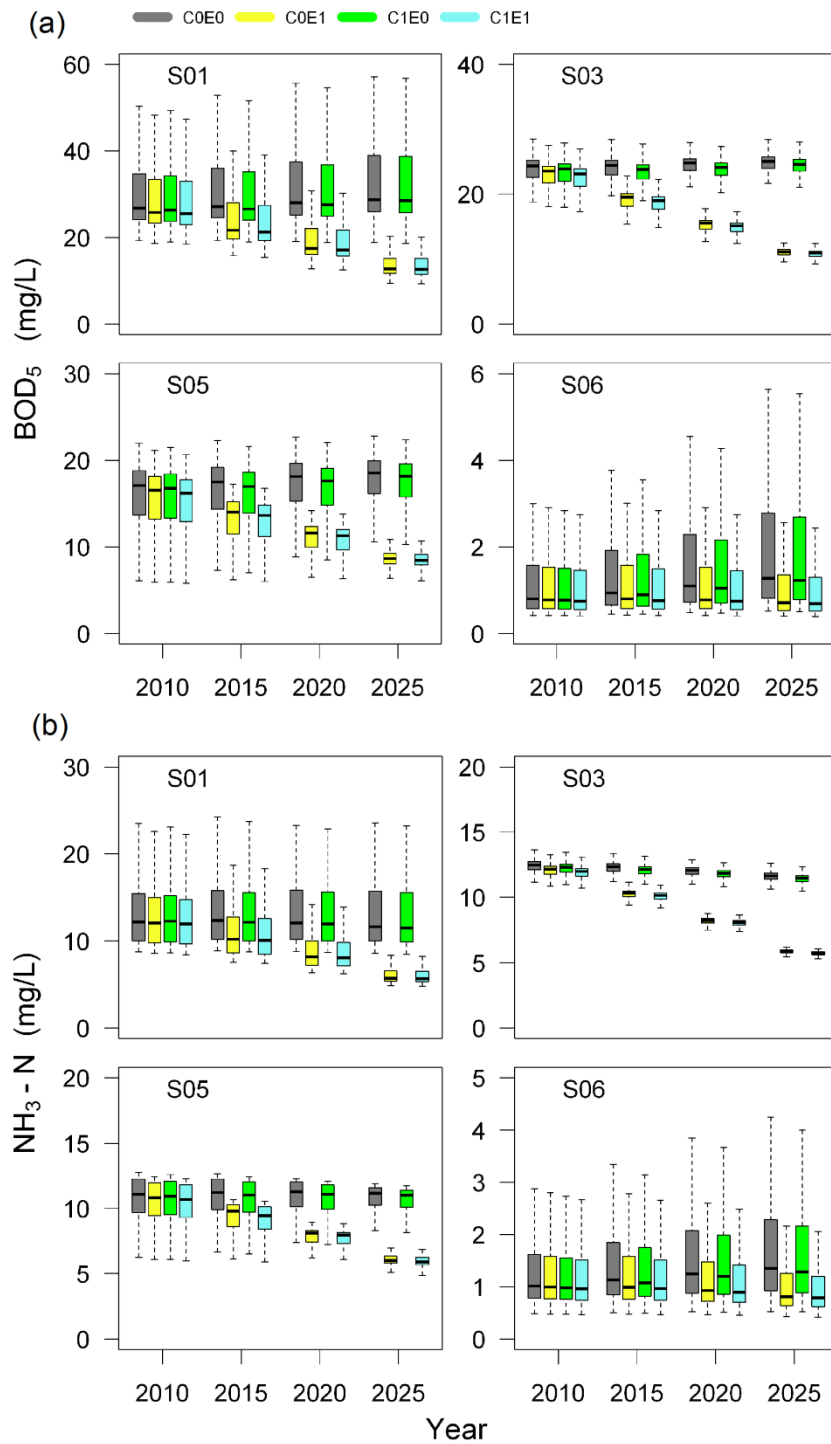


Figure 3.8 Variations of (a) BOD₅ concentration and (b) NH₃-N concentration under different scenarios from 2010 to 2025 at four stations: (a) S01-Buji; (b) S03-Hekou; (c) S05-Tsim Bei Tsui; and (d) S06-Dongjiaotou (n=337).

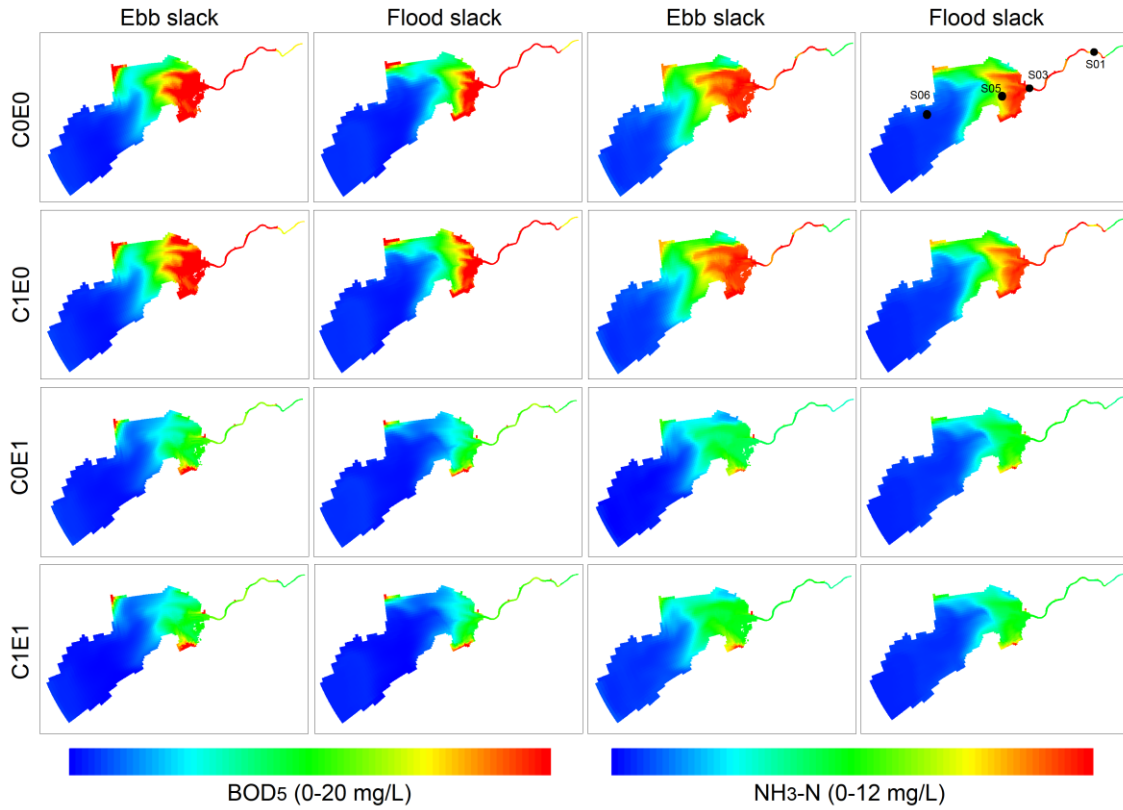


Figure 3.9 Spatial distribution of BOD₅ and NH₃-N concentration during ebb slack and flood slack under different scenarios in 2025.

3.4. Discussion

3.4.1. Effects of CO₂ Mitigation Strategies on Water Use

The co-benefits of carbon mitigation strategies on water demand and pollutant discharge can be captured using the integrated model through the bridge of industrial structure change. For instance, by comparing C0E0 and C1E0 scenarios, the effects of CO₂ mitigation strategies on water saving could be evaluated. Compared with C0E0, economic growth in C1E0 decreases slightly since carbon emissions are not free of

charge anymore. However, it could promote industrial structure adjustment leading to a decreasing proportion of energy- and carbon-intensive industries in the economic system. Since many of those industries are water-intensive, such industrial adjustment has co-benefits for the water system. First, it significantly reduces water demand and pollutant discharge from the domestic sector. The reduction of the labor-intensive industry is beneficial to the acceleration of total labor productivity since its productivity is comparatively lower than other industries. Hence, the projected population growth under the C1E0 scenario decreases by 4.1% compared with C0E0. The residential sector represents the most significant portion of water demand and pollutant discharge, which accounts for 39% (Fig. 3d), 79% (BOD₅), and 91% (NH₃-N) in 2010 under C0E0.

The effects of CO₂ mitigation strategies on residential water demand and pollutant discharge reduction are significant to satisfy future water demand and local water environment standards. Second, it has co-benefits by reducing secondary industry water demand and pollutant generation from labor-intensive and technology-intensive industries. Compared with technology- and capital-intensive industries, the labor-intensive industry has lower water use efficiency and higher pollutant discharge intensity. For example, the projected water use efficiency of the labor-intensive industry is 27% and 96% of technology-intensive and capital-intensive industries in 2025 (Table B4, Appendix B), respectively. Also, the BOD₅ load and NH₃-N load per GRP of the labor-intensive industry are the highest in the three types of industries, e.g., its BOD₅ load and NH₃-N load per GRP is 4 and 6 times of that in capital-intensive industries, respectively (Table B5, Appendix B). Therefore, industrial upgrades away from labor-

intensive to capital-intensive industries could help to save water and reduce water pollutant discharges. However, it should be noted that water demand from some capital-intensive industries, e.g., electricity production and supply, are expected to increase by 14% compared with C0E0 by 2025, which implies that more attention should be paid to water-saving technologies in these industries.

3.4.2. Effects of Engineering Measures

Water engineering measures can greatly alleviate water resource stress and improve water quality. The effects of engineering strategies are evaluated by comparison of C0E0 and C0E1 scenarios. The current water infrastructure systems cannot secure future adequacy of water resources and protect water environment based on the simulations in the reference scenario. From the water demand side, engineering measures can improve water use efficiency, e.g., water use efficiency increases by 16% compared with C0E0, as shown in Table B5, Appendix B, by upgrading industrial water recycling technology and decreasing pipeline leakage. From the water supply side, engineering measures can increase the potential water supply by increasing water transfer quota and wastewater reuse. The water demand and water supply will be nearly in balance even if employing engineering measures alone. However, this balance is very uncertain after 2025 because it is strongly dependent on the available quota of water transferred from other catchments, the increase of reclaimed wastewater reuse, and the improvement of water use efficiency (Qin et al., 2013).

Furthermore, engineering measures can significantly reduce pollutant discharge and improve water quality by building new WWTPs and improving wastewater

treatment capacity and efficiency of the current WWTPs. According to Shenzhen municipal wastewater system planning, three new WWTPs will be built and equipped with tertiary treatment technology with 80% and 90% of $\text{NH}_3\text{-N}$ and BOD_5 removal rates, respectively (PGSZM, 2008; Qin et al., 2014). Engineering measures are more efficient in reducing $\text{NH}_3\text{-N}$ load than BOD_5 load, which is attributed to the relatively lower removal efficiencies for nutrients in the existing WWTPs. For example, the average $\text{NH}_3\text{-N}$ and BOD_5 removal rates of current WWTPs are 60% and 80%, respectively (PGSZM, 2008; Qin et al., 2014). $\text{NH}_3\text{-N}$ loads reduction still has high potential considering the increasing need of using reclaimed wastewater as a potential water resource. However, engineering measures alone cannot meet the water quality improvement target of the study area.

3.4.3. Sensitivity Analysis

Uncertainties associated with all integrated models include (1) uncertainty in the assumptions of the socio-economic system in the CGE model; (2) uncertainty in the estimation of future water demand and pollutant discharge, which is associated with both parameters calibration in the SyDWEM model and the engineering measures settings; and (3) uncertainty in the performance of water quality model. The first uncertainty was analyzed by adding two additional GRP growth rates scenarios to the CGE model, i.e., a higher (10.4%) and a lower annual growth rate (7.7%), and the resulting industrial structure changes and investment changes are fed into the SyDWEM model leading to the changes in energy use, GRP loss, labor force, water demand, and water quality change (Table 3.3). As shown in Table 3.3, energy use, labor force migration, and WSI

are more sensitive to GRP changes than water quality change and GRP losses. For the secondary uncertainty, the calibration of labor productivity, water use efficiency, and pollutant loading in each industry have been analyzed in our previous study (Qin et al., 2011). The predicted GRP, population, and water demand in different districts/towns have been validated with census data. Also, the sensitivity of each engineering measure on water demand and water quality change has been assessed (Qin et al., 2013). The major findings from our previous simulations are as follows. First, increasing water transfer (M3) can significantly alleviate water shortage but has no effects on water quality, e.g., with a 0-20% increase of M3, the water shortage index decreases by 0-15%. Second, measures aimed at increasing the efficiency of wastewater infrastructure system (M5 and M6) can significantly improve water quality in the river but have no impacts on water shortage alleviation, e.g., with 0-10% increase of M5 and M6, water quality (e.g., Chemical Oxygen Demand, COD_{Cr}) at S01 decreases by 0-30% (M5) and 0-23% (M6), respectively. Third, some measures are sensitive to both water demand and water quality change, e.g., water use efficiency increase (M1 and M2) and reclaimed wastewater reuse (M4) can alleviate water shortages but can also decrease water quality (Qin et al., 2013). For example, with water use efficiency and M4 increase by 0-20% and 0-10%, water shortage index decreases by 0-10% and 0-2%, and COD_{Cr} at S01 increases by 0-8% and 0-9%, respectively. Furthermore, their aggregated effects were analyzed by adding two additional engineering measures scenarios, i.e., En_high and En_low, with M1 and M3-M6 increase or decrease 5%, and M2 increase or decrease 2.5% at 2025 compared with C1E1, respectively (Table 3.3). Water quality changes are more sensitive to engineering

measures than WSI, and BOD₅ concentration is more sensitive than NH₃-N. In terms of the uncertainty of the water quality module, two sets of water quality data obtained from water sampling monitoring were used for model calibration and validation. The results show that the water quality model can well capture the spatial and temporal variation of hydrodynamics and water quality in the Shenzhen River estuary.

Table 3.3 Changes from Values in C1E1 in 2025 under Sensitivity Analysis (%).

Scenarios	Energy use	GRP loss	Labor force	WSI	BOD ₅ loads	NH ₃ -N loads	BOD ₅ ^a	NH ₃ -N ^a
S1: GRP_high	23.9	5.1	12.1	12.1	12.8	12.5	4.1	5.6
S2: GRP_low	-17.	-4.5	12.7	-11.5	-11.0	-11.0	-3.2	-4.8
S3: EN_high	0	0	0	-11.7	-47.2	-36.1	-44.6	-29.4
S4: EN_low	0	0	0	14.5	46.7	35.9	40.4	26.1

Note: ^a represents average water quality at water quality station S01 in 2025.

3.4.4. Policy Implications

The aggregated effects of both CO₂ mitigation strategies and engineering measures are evaluated by the C1E1 scenario. The results show that a low-carbon, high-efficiency water and energy use economy and better water environment are potentially achievable. The CGE-SyDWEM integrated model can capture the linkages among socioeconomic, energy use, CO₂ emissions, water resource supply and depletion, as well as changes in the water system and is proved to be capable in analyzing the long-term scenario of rapid urbanization process. The integrated systems presented in this Chapter can be used to aid energy planners to understand the effects of proposed CO₂ mitigation

strategies on energy use efficiency and its co-benefits of water use saving and pollution emission reduction. It can also aid water planners in analyzing if current water engineering measures can support future water security under proposed CO₂ mitigation strategies and socio-economic development. Based on this integrated model, decision-makers across different sectors can consult with each other to design more effective policies and measures to achieve national targets. It also implies that labor-intensive industries should pay more attention to cleaner technologies to reduce energy and water demand as well as pollutant discharge. To promote the use of cleaner technologies, economic incentives such as water tariff adjustment, emissions trading are encouraged (Qin et al., 2014; Su et al., 2009). The local government should also promote water-saving appliances in public and household utilities to reduce residential water demand and seawater cooling in the electricity production and supply industry.

4. ESTIMATION OF GREENHOUSE GAS EMISSIONS FROM INTEGRATED URBAN DRAINAGE SYSTEMS

Although significant efforts have been made to better understand Greenhouse Gas (GHG) emissions in individual sub-systems of an integrated urban drainage system, including sewer, Wastewater Treatment Plants (WWTPs), and receiving water systems, the relative contributions of individual components are still poorly understood. GHG emissions from all these sub-systems have not yet been considered in an integrated manner, leading to considerable uncertainties in the GHG emission estimation of urban drainage systems. In this chapter, a submodule aiming to calculate both the direct and indirect GHG emissions from an integrated urban drainage system is added into the CGE-SyDWEM model developed in Chapter 3. The newly updated CGE-SyDWEM model is used to provide a comprehensive evaluation of both the direct and the indirect GHG emissions from wastewater treatment with the consideration of both carbon mitigation strategies and water engineering measures.

4.1. Introduction

WWTPs have been recognized as one of the largest energy consumers and GHG emitters in urban systems (IPCC, 2014, 2021). The treatment of domestic wastewater alone accounted for 3% of global electricity use and 2% of global carbon dioxide equivalent (CO₂-eq) GHG emissions (IPCC, 2014; Li et al., 2015a; McCarty et al., 2011). WWTPs are also major non-CO₂ GHG emitters, e.g., methane (CH₄) and nitrous oxide (N₂O), accounting for 4.6-5.2% of global non-CO₂ GHG emissions from 2005 to

2030 (USEPA, 2012). The shares of global energy use and GHG emissions from WWTPs are expected to increase in the future due to rapid urbanization and stricter water quality standards enforced in developing countries (Li et al., 2015a; USEPA, 2012). For instance, China has been experiencing rapid urbanization since 1978, and the percentage of its population living in urban areas increased from 18% in 1978 to 60% in 2019 (UN, 2019). This rapid and not well-planned urbanization results in high water use and wastewater discharge, causing risk to local water environmental safety (Dong and Liang, 2014; Gain and Giupponi, 2015; Qin et al., 2013). From 2000 to 2017, wastewater discharge in China increased from 110 to 192 million m³/d, and its treatment capacity increased from 27 to 157 million m³/d. At the same time, the energy use by wastewater treatment industry grew very fast, with an annual growth rate of 6% from 2008 to 2016 (Niu et al., 2019). To reduce water pollutants discharge and improve water quality, the Chinese government has planned to upgrade WWTPs treatment technologies (NPC, 2016), which will further increase energy use and GHG emissions from wastewater treatment industry. The increasing GHG emissions from wastewater treatment may affect China's Nationally Determined Contributions (NDC) targets to reduce the CO₂ emission intensity (CO₂ emissions per unit of GDP) by 60% to 65% by 2030 on the basis of the 2005 level (UNFCCC, 2015) as well as the long-term climate goal of carbon neutral by 2060. Therefore, understanding the energy use and GHG emissions from wastewater treatment plants and their dynamic interactions with socio-economic and water environmental systems in a long-term urbanization process can

assist decision-makers to meet water quality improvement and carbon mitigation targets more efficiently.

GHG emissions occur throughout the process of wastewater collection, treatment, and discharge, including (1) direct GHG emissions from the sewer, WWTPs, and receiving water systems; (2) indirect GHG emissions through electricity use by the sewer and WWTPs systems; and (3) indirect external GHG emissions, i.e., embodied GHG emissions in all materials and resources used outside the WWTPs boundary, e.g., the chemical use in the wastewater treatment process, maintenance of WWTPs machinery, and administration. Figure 4.1 illustrates GHG emissions from integrated urban drainage systems and their dynamic interactions with the socio-economic system. As shown in Figure 4.1, carbon mitigation strategies affect the economic outputs of different industrial sectors and the demand of local labor force, and the associated water demand and wastewater generation from industrial and domestic activities will be changed accordingly. Carbon mitigation strategies may also affect the CO₂ emission intensity in different industrial sectors and influence indirect GHG emissions due to energy consumption, chemical use, maintenance, and administration during the wastewater treatment process. The sewer system collects wastewater from domestic and industrial sectors, which is then pumped and transferred to WWTPs. GHG emissions in these two systems are affected by wastewater quantity, pollutant loading, and wastewater treatment technologies. The treated wastewater is then discharged into nearby water bodies or reused for irrigation and industrial purposes. Receiving water bodies may also receive pollutant loads from untreated wastewater discharge that exceeding the capacity

of the sewer system and non-point pollutants from agricultural production, which can change water quality in the receiving water bodies and associated GHG emissions.

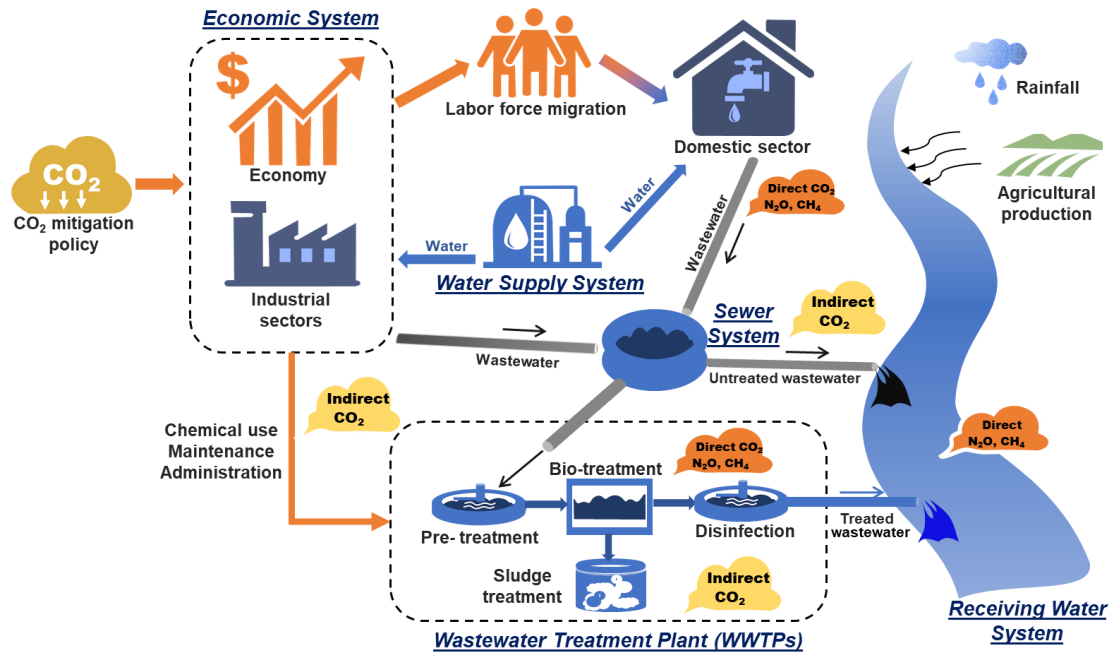


Figure 4.1 Greenhouse gas emissions from integrated urban drainage systems and their interactions with the socio-economic system.

Until now, carbon-energy-water nexus studies in wastewater treatment focused on assessing GHG emissions in an individual component of the integrated urban drainage system, e.g., sewer system, WWTPs, or receiving water bodies. Direct GHG emissions from sewer systems occur during the anaerobic and aerobic biological processes of sewer sediments, including emissions of CH₄ (Guisasola et al., 2008; Gutierrez et al., 2014; Liu et al., 2016b) and CO₂ (Jin et al., 2019), but few studies evaluated its N₂O emissions (Mannina et al., 2018). Direct GHG emissions from WWTPs include CO₂, CH₄, and N₂O emissions during the pre-treatment, biological

treatment, and disinfection, as well as sludge processing and disposal. Although direct CO₂ emission from WWTPs is considered as a biogenic origin and therefore is excluded in the GHG accounting suggested by IPCC (2006), studies show that 10-20% of the CO₂ emission from wastewater can be attributed to fossil origin (Bao et al., 2016; Griffith et al., 2009). The direct on-site CH₄ and N₂O emissions from WWTPs have gained increasing attention recently. However, the reported emission factors (EFs), defined as the amount of GHG emissions per unit of influent load in terms of chemical oxygen demand (COD_{Cr}) and total nitrogen (TN), show considerable variations. For example, the EFs of CH₄ have been found ranging among 0.0005-0.063 kg CH₄/kg COD_{Cr} (Bao et al., 2016; Daelman et al., 2012; Liu et al., 2014; Wang et al., 2011; Yoshida et al., 2014). The reported EFs of N₂O varies among 0.003-0.026 kg N₂O/kg TN, and in some cases, the values are even higher than 0.1 kg N₂O/kg TN in both lab-scale and full-scale WWTPs (Ahn et al., 2010; Bao et al., 2016; Foley et al., 2010; Kampschreur et al., 2009), which were contrasted with the fixed emission factors (i.e., 0.005 kg N₂O/kg TN) suggested by IPCC (2006). These variations in measured EFs can be attributed to the differences in treatment technology, capacity, and influent/effluent wastewater quality (Mannina et al., 2016; Niu et al., 2019). Direct GHG emissions from a receiving water system occur during the biological processes of the receiving water. Beaulieu et al. (2011) reported that N₂O emissions from river and stream networks could contribute 10% of global anthropogenic N₂O emissions. Musenze et al. (2014) quantified CH₄ and N₂O emissions in a sub-tropical estuary in Australia and found that N₂O was the

dominant emitted pollutant and positively correlated with NO_x (oxidized nitrogen, e.g., NO_3^{-1}) concentration.

Indirect GHG emissions stemming from energy consumption in the wastewater treatment process have been widely studied. Wastewater treatment is considered the most energy-intensive process throughout the water sector (Kim and Chen, 2018), and its emissions of GHG depends on electricity intensity (defined as the electricity use per unit of treated wastewater, kWh/m^3) and carbon intensity of electricity generation (defined as the CO_2 emissions per electricity use, $\text{kg CO}_2\text{-eq/kWh}$). Typical electricity intensity varies from 0.06 to 1.5 kWh/m^3 and sometimes can be as high as 3.18 kWh/m^3 (Englehardt et al., 2016; Smith et al., 2018; Wang et al., 2016). The large uncertainties in the reported electricity intensity can be attributed to the variations in treatment technology, WWTPs capacity, and influent/effluent water quality (Wang et al., 2016). Therefore, the field monitoring of electricity use at different treatment stages is usually suggested to improve the accuracy of GHG emissions stemming from electricity consumption. In addition, the electricity use from wastewater collection and discharge are seldom considered in previous studies due to data unavailability (Liao et al., 2020). The carbon intensity of electricity generation is closely related to the local electric power sector's fuel mix, which can be affected by the implementation of carbon mitigation strategies (Xiong et al., 2019). However, few studies have looked at the potential of carbon mitigation strategies for GHG emissions reduction from wastewater treatment.

Indirect external GHG emissions generated from all materials and resources used outside the WWTPs boundary are usually evaluated using life cycle assessment (LCA)

(Racoviceanu et al., 2007). Liao et al. (2020) used a hybrid life cycle analysis (HLCA) and estimated that the indirect GHG emissions from materials use accounted for 5-15% of the total WWTPs emissions, which have been overlooked in previous studies.

Despite the significant progress that has been made to improve the understanding of GHG emissions in individual sub-systems, the relative contributions of individual components in integrated urban drainage systems are still poorly understood. An integrated platform that can capture the cross-sector interactions and feedbacks among social-economic, sewer, WWTPs, and receiving water systems will enable a better understanding of the role of the wastewater sector in global GHG emissions. The specific objectives in this chapter therefore are to (1) quantify the relative contributions of GHG emissions from the sewer, WWTPs, and receiving water systems during 2010-2025 in an integrated manner; (2) assess the impacts of China's NDC on local GHG emissions from the integrated urban drainage system; and (3) evaluate the impacts of upgraded water engineering measures on energy use and GHG emissions.

4.2. Methodology

4.2.1. GHG Emissions Calculation

GHG emissions considered in this study include (1) direct emissions from the sewer (i.e., CO₂ and CH₄ emissions from sewer sediment deposition), WWTPs (i.e., CO₂, CH₄, and NO₂), and receiving water systems (NO₂); (2) indirect internal emissions from electricity consumption during the collection and four wastewater treatment stages, i.e., pre-treatment, biological treatment, disinfection, and sludge treatment; and (3) indirect external emissions from chemicals use, repair and maintenance of WWTPs'

machinery, and administration. Since the treated wastewater in the study area is usually discharged into nearby water bodies, the energy consumption from wastewater discharge is neglected. Emission factors for direct GHG emissions were obtained by averaging available field studies in China to reduce bias. In addition, the EFs for WWTPs emissions consider the differences in wastewater treatment technologies. These technologies include Anaerobic-Anoxic-Oxic (A²/O), Oxidation Ditch (OD), Anaerobic-Oxic (AO), and Sequencing Batch Reactors (SBR), which are the most widely used technologies in China (Zhang et al., 2016). The direct GHG emissions were collected from on-site WWTPs operation data in the study area (Liao et al., 2020).

4.2.1.1. Direct GHG Emissions from Sewer System

CO₂ and CH₄ emissions from sewer sediment deposition is estimated by using sediment deposition rate and the length of sewer pipe as:

$$E_{ti}^{DS} = \alpha_i \times L_t \times EF_i^{DS} \quad (4.1)$$

where t is the time (year); α_i is the 100-year global warming potential (GWP) coefficients used to convert to CO₂-eq GHG emissions, i.e., CO₂=1, N₂O=298, and CH₄=25 (IPCC, 2006); L_t is the length of the sewer pipe in year t ; E_{ti}^{DS} is the i^{th} type direct CO₂-eq GHG emissions from sewer sediment (kg CO₂-eq/year); and EF_i^{DS} is the i^{th} type sewer sediment emission factor (kg CH₄/year/km length of sewer system). Here EF_i^{DS} for CH₄ and CO₂ were adopted from a field study in Xi'an, China (Jin et al., 2019). The averaged EFs for CH₄ and CO₂ with sub-main and main sewer lengths higher than 1 km are used (Table C1, Appendix C). The emissions from wastewater decomposition are neglected in the sewer system.

4.2.1.2. Direct GHG Emissions from WWTPs System

Once the pollutant loads removed by WWTPs under different scenarios are gained from CGE-SyDWEM simulations, the direct CO₂, N₂O, and CH₄ emissions and total CO₂-eq GHG emissions from individual WWTP can be estimated by using equations (4.2) and (4.3).

$$E_t^{DO} = \sum_i \alpha_i EF_{ti}^{DO} \quad (4.2)$$

$$EF_{ti}^{DO} = P_{ti} \times EF_i^{DO} \quad (4.3)$$

where P_{ti} and EF_i^{DO} are the pollutant loads (kg) removed in year t and emission factors (GHG emissions per unit of pollutant treated) of the three types GHGs, respectively. In the calculation, 10% of the direct CO₂ emission is considered from fuel origin. The CH₄ emission is associated with organic matter decomposition in the anaerobic consideration. The EF_{ti}^{DO} of CO₂ and CH₄ are in the units of kg CO₂/kg COD_{removed} and kg CH₄/kg COD_{removed}, respectively (Table 4.1). Although the complete production mechanism of N₂O in WWTPs is not fully understood, it is found that the N₂O emission is associated with nitrogen removal, e.g., aerobic ammonium and nitrate oxidations. Here the N₂O emission factor (kg NO₂/kg TN_{removed}) was obtained from recent field studies in China (Table 4.1).

Table 4.1 GHG Emission Factors of Different Treatment Technologies in WWTPs from Recent Field Studies in China (mean \pm standard deviation).

Technology	CO ₂ *	N ₂ O	CH ₄
	kg CO ₂ /kg COD _{removed}	kg N ₂ O/kg TN _{removed}	kg CH ₄ /kg COD _{removed}
A ² O	0.0424 \pm 0.0261	0.0020 \pm 0.0006	0.0016 \pm 0.0003
OD	0.0550 \pm 0.0410	0.0028 \pm 0.0011	0.0057 \pm 0.0050
Average	0.0517 \pm 0.0322	0.0027 \pm 0.0013	0.0038 \pm 0.0033

Note: *10% of CO₂ is considered from fossil origin. More detailed data is provided in Table C2, Appendix C.

4.2.1.3. Direct GHG Emissions from Receiving Water System

The N₂O emission from receiving water bodies is related to the direct denitrification of NO₃⁻¹ (Beaulieu et al., 2011). The ratios of N₂O emission to NO₃⁻¹ inputs are reported to range from 0.1 to 1% (Beaulieu et al., 2008; Cole and Caraco, 2001). Here, a global mean value of 0.9% of the N₂O/NO₃⁻¹ ratio is used (Beaulieu et al., 2011). The annual NO₃⁻¹ loads in the receiving water bodies are simulated by the water quality module in the CGE-SyDWEM, including sources from the effluent of WWTPs, direct discharge of untreated wastewater, and non-point pollutants caused by agricultural production. The non-point pollutants induced by runoff are not included since this work focuses on only the human-induced GHG emissions from wastewater treatment.

4.2.1.4. Indirect Internal GHG Emissions caused by Electricity Consumption

Electricity consumption (EL_t^{II}) and associated GHG emissions (E_t^{II}) from wastewater collection (pumping), and four treatment stages are calculated using equations (4.4) and (4.5) as:

$$EL_t^{II} = \sum_j \sum_k EL_{tjk}^{II} = \sum_j \sum_k WW_{tk} \times EL_{jk}^G \quad (4.4)$$

$$E_t^{II} = \sum_j \sum_k E_{tkj}^{II} = \sum_j \sum_k EL_{tjk}^{II} \times EF_t^G \quad (4.5)$$

where EL_{tjk}^{II} and E_{tjk}^{II} represent the electricity consumption and associated CO₂ emissions during the j^{th} stage, including pumping, pre-treatment, bio-treatment, disinfection, and sludge treatment, and the k^{th} type of treatment technologies including A²O, OD, biological filter (BF), and Anaerobic-Anoxic-Oxic-Membrane Bio-Reactor (AAO-MBR); WW_{tk} is the wastewater collected and treated using the k^{th} type of treatment technologies in year t (m³); EL_{jk}^G is the electricity intensity of the j^{th} stage and the k^{th} type of treatment technologies (kWh/m³); and EF_t^G is the carbon intensity of electricity generation in year t (kg CO₂/kWh). 30% of Shenzhen City's electricity is supplied locally, whereas the remaining portion is imported from the Southern Power Grid of China. EF_t^G of the local electricity sector is simulated by CGE-SyDWEM, which can be affected by the implementation of carbon mitigation strategies. For the imported electricity, time-evolving EF_t^G values are used considering the historical electric power sector's fuel mix change in China (IEA, 2015). Also, the EF^G of Southern Power Grid in 2013 (0.556 kg/kWh) is used as the base year for the imported electricity (Qu et al., 2017). An annual decreasing rate of 1% is used to calculate the future EF^G of the imported electricity based on the study of electricity fuel structures change in China during 2020-2030 (Xiong et al., 2019). In addition, the EF^G of the imported electricity is assumed not to be affected by the implementation of local carbon mitigation strategies.

To reduce the uncertainty of various data sources, the mean electricity intensity of the existing WWTPs of Shenzhen City is used (Table 4.2). According to the local sewage and WWTPs planning (SZUPLRB, 2011), currently, there are 44 pumping

stations in the study area with an average serving area of 8.8 km². The mean value for pumping 1 m³ of wastewater is 0.0384 kWh.

Table 4.2 Electricity Intensity of Four Treatment Stages using Different Treatment Technologies in WWTPs System.

Technology	Electricity intensity (kWh/m ³)				
	Pre-	Bio-	Disinfection	Sludge	Total
A ² O	0.061±0.021	0.157±0.027	0.019±0.008	0.034±0.014	0.272±0.045
OD	0.069±0.001	0.175±0.092	0.014±0.001	0.031±0.008	0.286±0.112
BF	0.077±0.007	0.156±0.015	0.036±0.003	0.034±0.033	0.302±0.009
AAO-MBR	0.145±0.007	0.582±0.013	0.023±0.009	0.028±0.002	0.776±0.042

Sources: Activity data from 18 WWTPs of Shenzhen (Liao et al., 2020); Sewage and WWTPs system plan of Shenzhen (2011-2020) (SZUPLRB, 2011). The number of WWTPs with different technologies including A²O (n=14), OD (n=2), BF (n=2), and AAO-MBR (n=2).

4.2.1.5. Indirect External GHG Emissions

Once the CO₂ emission intensity of different industrial sectors and the amount of wastewater treated by WWTPs under different scenarios are gained from CGE-SyDWEM simulations, the indirect external GHG emissions from the final demand of WWTPs materials' use can be calculated as:

$$E_t^{IE} = \sum_k \sum_n E_{tkn}^{IE} = \sum_k \sum_n D_{tkn}^{IE} \times CI_{tn}^{IE} \quad (4.6)$$

where E_{tkn}^{IE} and D_{tkn}^{IE} represent the life cycle GHG emissions (kg CO₂) and final demand of WWTPs (RMB) from the n^{th} sector using the k^{th} type of treatment technologies in year t ; CI_{tn}^{IE} is the CO₂ emissions intensity from the n^{th} sector in year t (kg CO₂/10³ RMB), which is simulated by the CGE model. The chemicals use, repair, and maintenance of WWTPs' machinery, and administration refer to the chemical,

machinery, and service sectors, respectively, in the CGE model. D_{tkn}^{IE} can be calculated as:

$$D_{tkmn}^{IE} = WW_{tk} \times Cost_{nk}^{IE} \quad (4.7)$$

where $Cost_{nk}^{IE}$ is the input cost to treat per unit of wastewater from the n^{th} sector using k^{th} type of treatment technologies (RMB/10³ m³) (Table 4.3).

Table 4.3 Chemical Cost, Maintenance Cost, and Administrative Cost per Unit of Wastewater Treated Using Different Technologies (RMB/10³m³) (2015 price).

Technology	Chemical	Maintenance	Administrative	Total
A ² O	41.48±17.86	82.50±28.57	64.01±16.28	187.99±62.71
OD	53.33±43.88	98.80±26.50	46.46±10.15	198.59±80.53
BF	49.78±22.37	61.06±29.05	54.45±23.27	165.29±74.69
AAO-MBR	62.37±38.27	137.45±10.48	140.67±24.35	340.49±73.10

Sources: Activity data from 18 WWTPs of Shenzhen (Liao et al., 2020); Sewage and WWTPs system plan of Shenzhen (2011-2020) (SZUPLRB, 2011). The number of WWTPs with different technologies including A²O (n=14), OD (n=2), BF (n=2), and AAO-MBR (n=2).

4.2.2. Scenarios

Here, two scenarios are evaluated, including Business as Usual (BaU) and Nationally Determined Contributions (NDC) scenarios (Table 4.4). The BaU scenario simulates GHG emissions changes with upgraded water infrastructure systems in 2025 without the implementation of explicit carbon mitigation strategies. The upgraded water infrastructure systems were set to make sure that the water quality in the receiving water bodies can satisfy the local water quality improvement target, which is detailed in Table 3.2, Chapter 3. There is no CO₂ emission intensity constraint in the BaU scenario. The NDC scenario simulates the impacts of carbon mitigation on local GHG emissions from

the integrated urban drainage system. This scenario differs from the BaU scenario in that it includes a constraint on CO₂ emissions intensity, i.e., the emission intensity needs to be reduced by 40% by 2020 and 65% by 2030, to fulfill China's NDC commitment (Table 4.4).

Table 4.4 Configurations of Scenarios.

Scenarios	Emission constraints	Engineering measures
BaU	No constraints	Upgraded engineering measures to satisfy water quality standards in 2025
NDC	Emission intensity reduced by 40% in 2020 and 65% in 2030	Same as BaU

4.3. Results

4.3.1. Direct GHG Emissions

Direct GHG emissions under the BaU scenario would grow continuously between 2007 and 2025, increasing from 21 to 36 kt per year (Figure 4.2a). However, the direct GHG emissions intensity (CO₂-eq emission/m³ wastewater) would reduce by 15% by 2025 compared to the 2007 level under the BaU scenario (Figure 4.5a). The main reason is that the projected WWTPs influent concentrations will be gradually reduced with socio-economic development. As shown in Figure 4.2b-d, the total wastewater treated in 2025 (2.9 Mt/day) is twice that in 2007 (1.4 Mt/day), but COD_{Cr} and TN treated only increase by 50% and 36%, respectively. With continued industrial structure change, the proportions of wastewater from service and residential sectors are increasing, and they have relatively lower pollutant intensities than other sectors (Su et

al., 2018). Accordingly, the influent concentrations of COD_{Cr} and TN show decreasing trends (Figure C1, Appendix C).

Carbon mitigation can reduce direct GHG emissions from wastewater treatment by decreasing wastewater generation and pollutant discharge. Carbon mitigation accelerates local industrial structure upgrading by restricting carbon- and energy-intensive industries. Since many of these industries are also labor- and water-intensive, carbon mitigation is beneficial for reducing wastewater generation and water-related pollutants discharge. Compared with the BaU scenario, carbon mitigation can reduce total treated wastewater by 1% (0.3 Mt/d) and total COD_{Cr} and TN generation, i.e., treated and discharged, by 4.2% (21.1 t/d) and 4.4% (3.4 t/d), respectively (Figure 4.1c-f). Accordingly, carbon mitigation can contribute to reductions in direct GHG emissions by 4% by 2025, approximately 1.5 kt per year, and direct GHG emissions intensity by 3% by 2025.

WWTPs system contributes the largest direct GHG emissions (78%), followed by receiving water (15%) and sewer systems (7%) in 2007 (Figure 4.1a). With improved water engineering measures, pollutant discharges into the river show a decreasing trend during 2007-2025 (Figure 4.1e and f). Therefore, the proportions of direct GHG emissions from receiving water will decrease to 7% by 2025 under both BaU and NDC scenarios. Among all three types of GHGs, N₂O accounts for 53-58% of total direct CO₂-eq GHG emissions, followed by CH₄ (40-44%) and CO₂ (2-3%) during 2007-2025 under both scenarios.

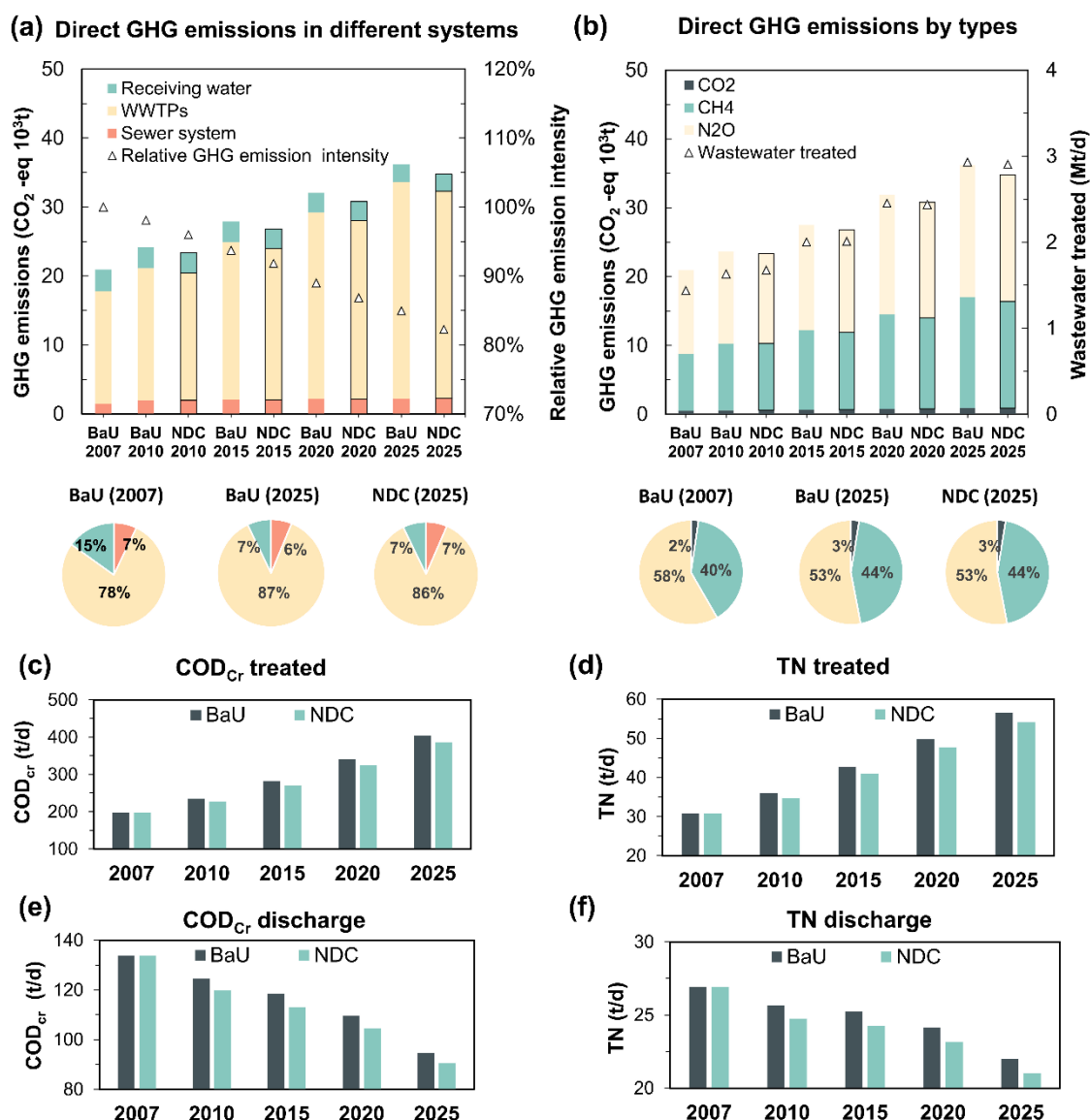


Figure 4.2 Annual variations of (a) direct CO₂-eq GHG emissions in different systems and relative direct GHG emission intensity, (b) direct GHG emissions by types and total wastewater treated, (c) COD_{Cr} treated, (d) TN treated, (e) COD_{Cr} discharge, and (f) TN discharge under BaU and NDC scenarios.

4.3.2. Electricity-related GHG Emissions

On average, 0.32 kWh of electricity is required to treat 1 m³ of wastewater (Figure 4.3a). Among all wastewater collection and treatment processes, biological

treatment consumes the largest amount of electricity, accounting for 49% of the total electricity use, followed by pre-treatment (21%), pumping (12%), sludge treatment (10%), and disinfection (8%). Under the BaU scenario, the total electricity consumption will increase from 170 MWh in 2007 to 349 MWh by 2025 (by 105%), which is in alignment with the trend of total wastewater treatment. Carbon mitigation can slightly reduce electricity consumption by slowing down wastewater generation and water-related pollutant discharges from industrial and domestic sectors.

The projected indirect GHG emissions stemming from electricity consumption show a relatively stable growth rate (1.7% annually) during 2007-2025 under the BaU scenario (Figure 4.3a), increasing from 104 kt in 2007 to 141 kt by 2025, which is much slower than the increase of total wastewater treated (4.0% annually). The reason is that the local electricity sector has a high reduction rate of autonomous GHG emission intensity, since its emissions can be reduced through the use of renewable energy resources and efficient technologies even without the implementation of carbon mitigation strategies (Su et al., 2019). As shown in Figure 4.3b, its GHG emission intensity decreases by 33% by 2025 relative to the 2007 level under the BaU scenario. When the carbon intensity constraint is imposed, carbon abatement cost is generated endogenously, which is the equilibrium price to balance the supply and demand of the carbon emission allowance (Su et al., 2018). The carbon abatement cost is evenly distributed in all industrial sectors and is projected to increase from 56 to 274 USD/t CO₂ from 2020 through 2030 due to higher carbon constraints and adverse endogenous factors, such as increased clean energy prices and less availability of low carbon

technologies in Shenzhen City. The carbon emission supply is implied by future GDP and carbon emission intensity target, and the demand is determined by the emissions from different industrial sectors and households. The carbon abatement cost will increase the production prices of all sectors, which is dependent on their carbon emission intensities. On the demand side, in response to the price change, consumers will adjust their activities to lower the demand for energy- and carbon-intensive products. As a result, carbon emissions from energy- and carbon-intensive industries sectors will be greatly reduced. Under the NDC scenario, carbon emission intensity from most industrial sectors will decrease by 20%-83% by 2025 compared with the BaU scenario. Unlike these sectors, the carbon intensity of the electric power sector shows a limited decrease (1%) by 2025 under the NDC scenario since the local electric power sector can cut emissions through the adoption of non-fossil power, such as nuclear power. In 2007, the GHG emission intensity from the local electricity sector was 0.50 kg/kWh, which was much lower than the imported electricity (0.66 kg/kWh) and the national average (0.84 kg/kWh). Since the imported electricity from South Power Grid accounts for about 70% of the total electricity use, a further decrease in GHG emission intensity is expected if carbon mitigation strategies are applied in other regions in China, especially in the South Power Grid.

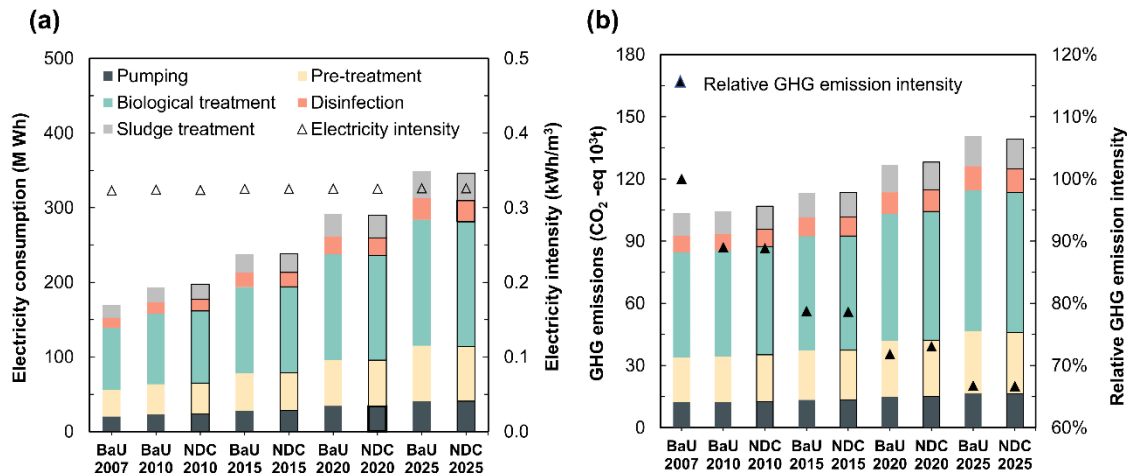


Figure 4.3 Annual variations of (a) electricity consumption and electricity intensity and (b) electricity consumption-induced indirect GHG emissions and relative GHG intensity under BaU and NDC scenarios during 2007-2025.

4.3.3. Indirect External GHG Emissions

Carbon mitigation substantially reduces the indirect external GHG emissions, i.e., by 72% (9.8 kt) by 2025 under the NDC scenario relative to the BaU scenario (Figure 4.4). Chemical use contributes the largest portion of total reductions, i.e., 82% (8.0 kt), followed by administrative (14%) and maintenance (4%). Under the BaU scenario, chemical use in WWTPs accounts for 61-67% of indirect external GHG emissions, and it grows very quickly during 2007-2025, which increases from 2.9 kt in 2007 to 9.1 kt by 2025. The reason is that emission intensity from the chemical sector continues to increase throughout the period under the BaU scenario. Hence, chemical use from WWTPs plays an important role in reducing indirect external GHG emissions from wastewater treatment. Note that the chemical sector is an energy- and carbon-intensive sector, with a carbon intensity of 3.5 and 8.4 times that in the machinery

(maintenance) and service (administrative) sectors in 2007, respectively (Table C3, Appendix C). To meet the carbon mitigation target, the chemical sector relies on minimizing its production, and therefore it suffers economic losses and contributes the largest reductions.

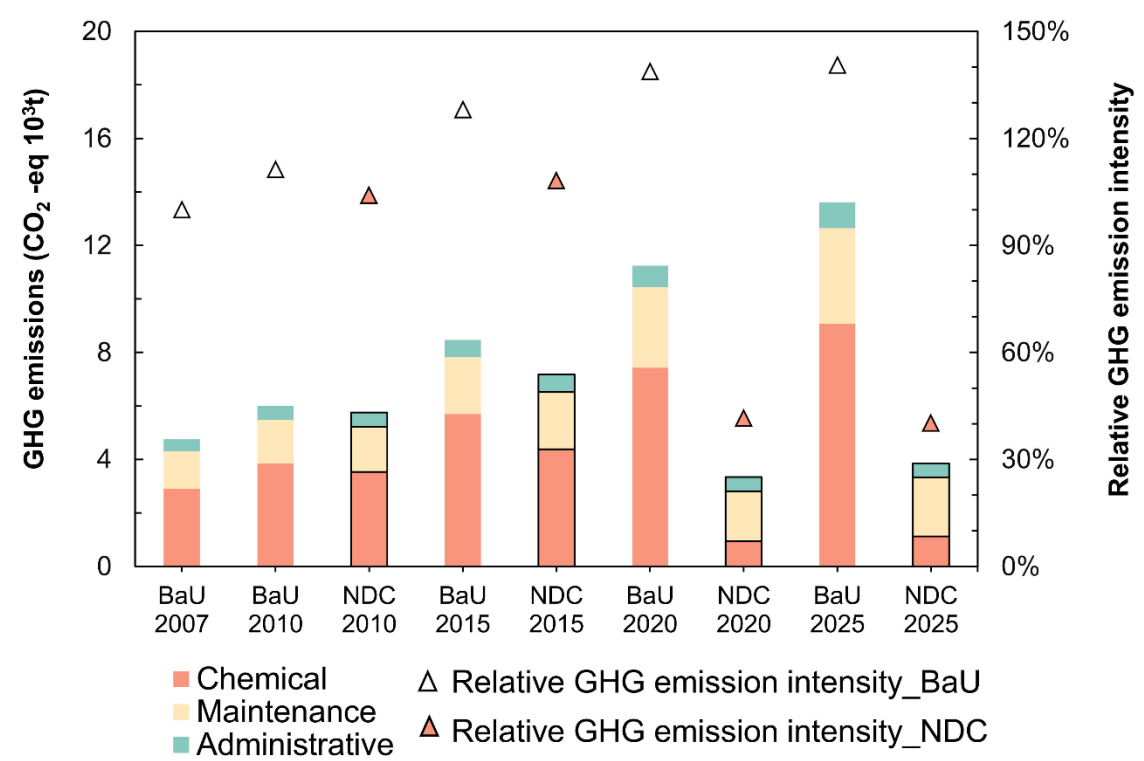


Figure 4.4 Annual variations of indirect external GHG emissions and relative GHG emission intensity from chemical use, maintenance, and administrative of WWTPs under BaU and NDC scenarios during 2007-2025.

On the contrary, carbon mitigation is beneficial to the machinery sector, since it can reduce its carbon intensity by adopting low carbon technology, which is represented in the CGE model by the substitution of energy by capital. Accordingly, the machinery

sector improves production efficiency with low carbon transformation, and therefore, it is affected the least under carbon mitigation. Under the NDC scenario, maintenance of WWTPs contributes more than half of the indirect external GHG emissions (57%) by 2025, while the share of the chemical sector reduces to 29%. The indirect external GHG emissions have been overlooked in previous studies. Liao et al. (2020) estimated that the indirect external GHG emissions accounted for 5-15% of total GHG emissions from WWTPs, depending on the wastewater treatment technologies used.

4.3.4. Integrated Urban Drainage System GHG Emissions

Figure 4.5 shows the annual variations of total GHG emissions and GHG emission intensity under BaU and NDC scenarios during 1990-2025. The trend of GHG emissions under the BaU scenario is in alignment with socio-economic development and wastewater treatment capacity increase, showing a significant increase from 5.1 (95% CI: 4.8-5.5) kt in 1990 to 129.2 (95% CI: 95.9-162.5) kt in 2007 to 190.7 (95% CI: 144.8-236.6) kt in 2025, equivalent to an annual growth rate of 12.2% and 2.0% for the periods of 1990-2006 and 2007-2025, respectively. GHG emission intensity shows a decreasing trend. CO₂-eq emissions from the treatment of 1 m³ wastewater is estimated to be 0.30 (95% CI: 0.22-0.38) kg in 1990, which will decrease to 0.25 (95% CI: 0.18-0.32) kg in 2007 and to 0.16 (95% CI: 0.11-0.21) kg by 2025. Liao et al. (2020) estimated that the GHG emission intensity of wastewater treatment in Shenzhen City was about 0.3 kg/m³ in 2015, larger than our estimations. The reason is that a national average GHG emission intensity (0.861 kg/kWh) was used, which significantly overestimated the electricity-induced GHG emissions.

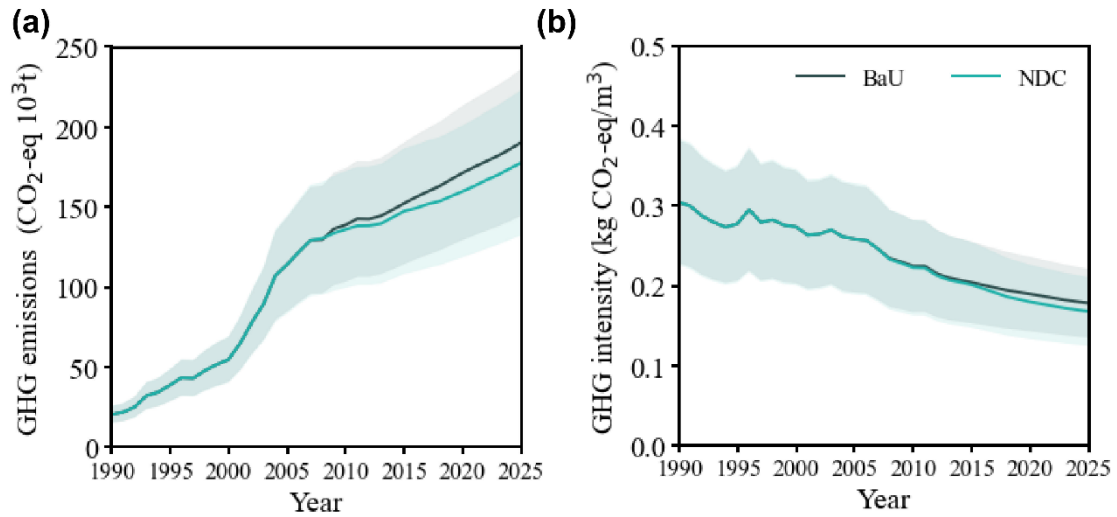


Figure 4.5 Annual variations of (a) total GHG emissions and (b) GHG emission intensity from the integrated urban drainage systems under BaU and NDC scenarios during 1990-2025. Shading indicates the 95% confidential interval.

Figure 4.6a illustrates the wastewater flow and GHG emissions in individual systems under the BaU scenario in 2025. 89% of GHG emissions from the integrated urban drainage system are from WWTPs (direct emissions: 17%; indirect due to electricity use: 65%; and indirect external: 7%), 10% from sewer system (direct emissions: 1%; pumping: 9%) and 1% from receiving water system (direct emission). The indirect GHG emissions due to electricity use contribute 74% of total emissions, including biological treatment process (36%), followed by pre-treatment (15%), pumping (9%), sludge treatment (8%), and disinfection (6%).

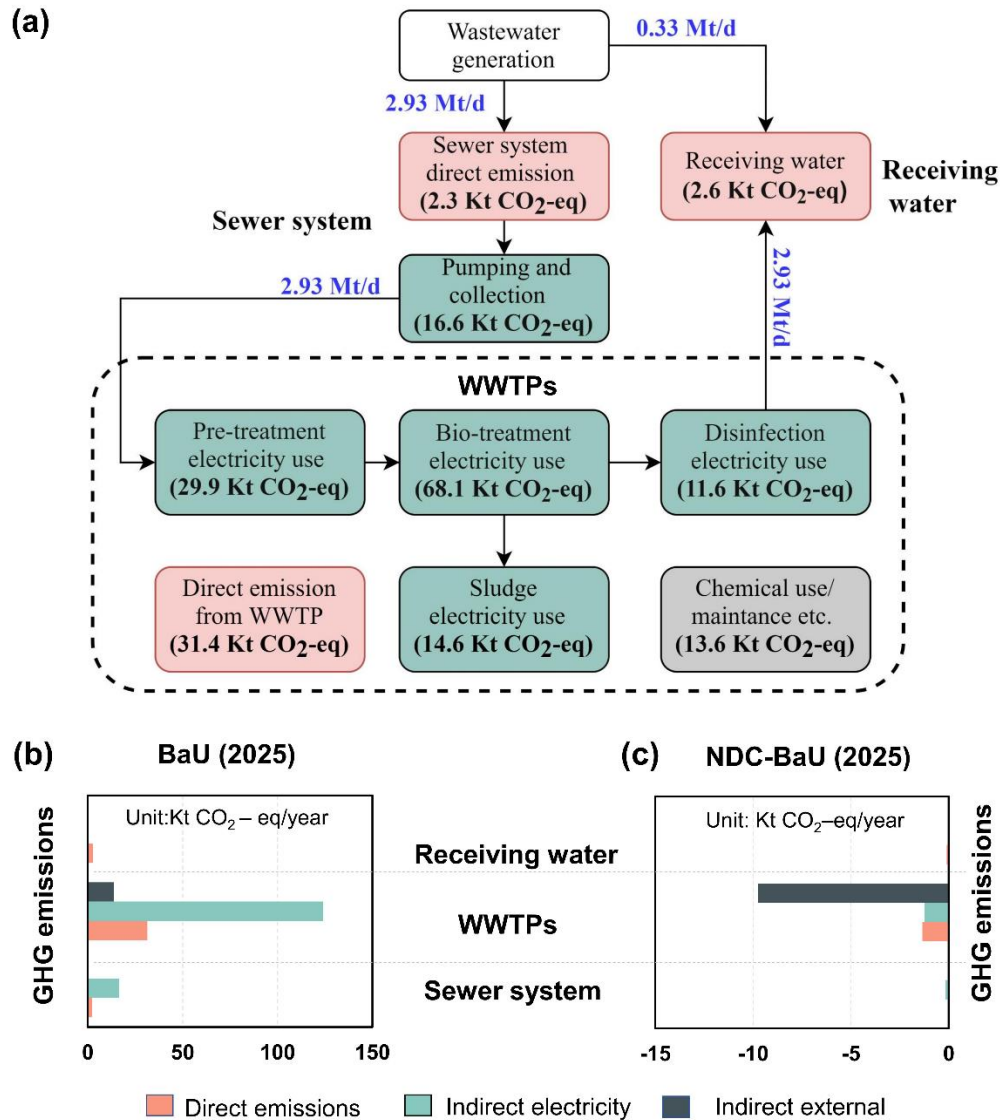


Figure 4.6 (a) Wastewater flow and GHG emissions in individual systems under BaU scenario, (b) comparisons of direct and indirect GHG emissions under BaU scenario, and (c) the difference in GHG emissions between NDC and BaU in 2025.

Carbon mitigation can reduce the total GHG emissions by 6.6% by 2025 under the NDC scenario compared with the BaU scenario (Figure 4.5), including 5.1% from external GHG emissions, 0.8% from direct GHG emissions, and 0.7% from indirect GHG emissions due to electricity use. Compared with the BaU scenario, the GHG

emission intensity under the NDC scenario decreases by 5.8% in 2025 (Figure 4.5b). Carbon mitigation strategies have limited impacts on promoting the adjustment of the local electricity sector's fuel mix since its emissions can be reduced mainly by using renewable energy resources. Given that 70% of the electricity use is purchased from other regions, a scenario with consideration of carbon mitigation is implemented in other regions of China and was analyzed later to gain a better understanding of how electricity fuel structure transformation may potentially change the electricity induced GHG emissions from integrated urban drainage systems.

4.4. Discussion

4.4.1. Sensitivity Analysis

The sensitivities of GHG emissions and GHG intensity to each engineering measure and imported electricity's fuel mix are revealed in Figure 4.7. The electricity fuel structure transformation can significantly reduce GHG emissions from the integrated urban systems and improve GHG emission intensity. For example, with a 0-10% GHG intensity reduction in the imported electricity, both the total GHG emissions and GHG intensity decrease by 29%. Measures aimed at improving the efficiency of wastewater infrastructure systems show negative effects on GHG emissions. For example, with a 0-10% increase of volumetric wastewater treatment rate, GHG emissions increase by 0-10.4%, but the GHG emissions intensity of wastewater treatment shows little change. Increasing the pollutants removal rate of WWTPs can slightly increase GHG emissions assuming that the same treatment technologies are used. For instance, with a 0-10% increase of COD_{Cr} and TN removal rate of the WWTPs,

GHG emissions increase only by 0-0.9% and 0-0.7%, respectively. In order to improve the treatment efficiency of current WWTPs, Anaerobic-Anoxic-Oxic-Membrane Bio-Reactor (AAO-MBR) is usually suggested (Krzeminski et al., 2012). In fact, two newly built WWTPs in Shenzhen City have already been equipped with AAO-MBR, and the operational data of these two WWTPs were used for scenario analysis to evaluate the impact of the updated WWTPs technology on GHG emissions from wastewater treatment.

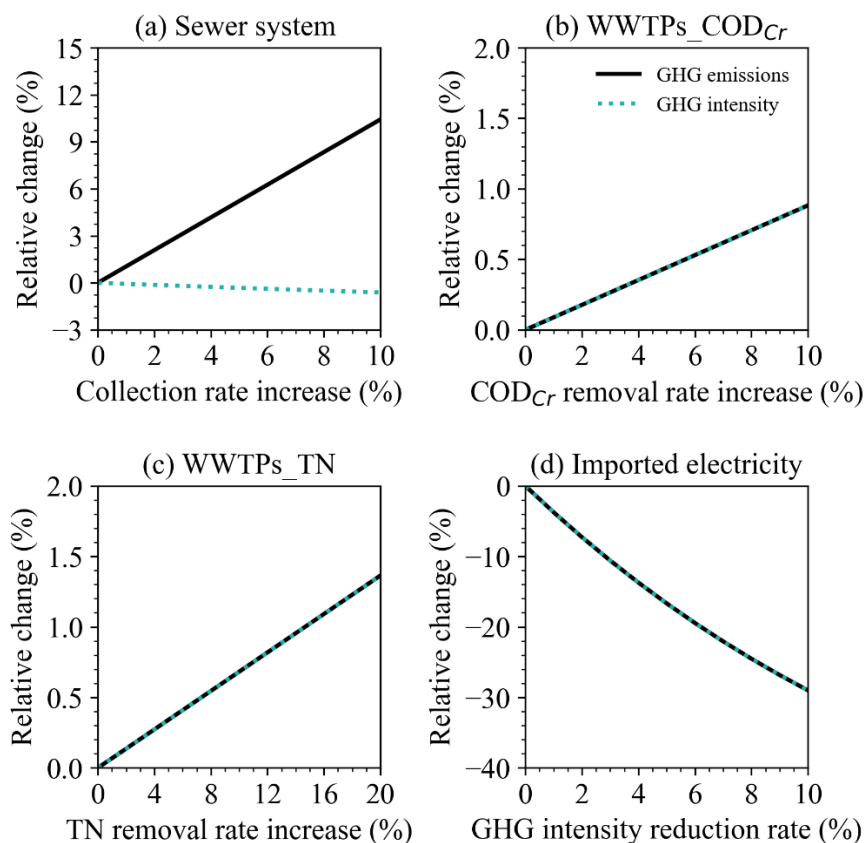


Figure 4.7 Sensitivities of (a) volumetric wastewater treatment rate increase; (b) COD_{Cr} and (c) TN removal rate increase of WWTPs; and (d) GHG intensity reduction of imported electricity on total GHG emissions and GHG emission intensity under the NDC scenario in 2025.

Given that considerable uncertainties may exist in the long-term projections, several additional scenarios are examined. The major uncertainties are from (1) the assumptions of the socio-economic system in the CGE model; (2) the assumptions of future engineering measures, and (3) variations in the imported electricity's fuel mix. The first uncertainty is assessed by examining two additional scenarios of GDP growth rates in the CGE model, i.e., a higher (10.4%) and a lower annual average rate (7.7%) over 2007-2025, corresponding to 22% higher or 18% lower GDP in 2025 than that in the BaU scenario. As shown in Figure 4.8, total GHG emissions increase by 15% (GDP_High) or decrease by 12% (GDP_Low) compared with the NDC scenario in 2025. Regarding the secondary uncertainty, two additional scenarios of engineering measures are analyzed, i.e., En_low and En_high. En_low assumes that the capacity and technology of the water infrastructure system will keep at the 2009 level, and there is no upgrade during the period of 2010-2025. The GHG emissions under the En_low scenario decreases slightly compared with the NDC scenario, but the projected water quality change in the receiving water cannot meet the water quality improvement target of the study area. The En_high scenario evaluates the effects of using AAO-MBR technology on total GHG emissions with the assumption that all WWTPs in the catchment are equipped with AAO-MBR between 1990 and 2025. AAO-MBR is an energy- and carbon-intensive technology, consuming a large amount of energy (0.81 kWh/m^3 wastewater) and has high GHG emission intensity (0.37 , 95% CI: $0.32\text{-}0.42 \text{ kg CO}_2\text{-eq/m}^3$), 2.2 times that in the NDC scenario by 2025. It is found that the projected GHG emission under the En_high scenario is as high as 413.5 (95% CI: $354.9\text{-}472.1$) kt by

2025, which increases by 132% compared with the NDC scenario. The third uncertainty is evaluated by setting a scenario (NDC_all) assuming that carbon mitigation strategies are implemented in other regions of China. A 10% reduction of the carbon intensity of the imported electricity is assumed during the period of 2014-2025. Under the NDC_all scenario, GHG emissions from wastewater treatment reach peak emissions (145.4, 95% CI: 106.7-145.4 kt) by 2015 and gradually decreases to 126.3 (95% CI: 94.1-158.5) kt in 2025. Furthermore, the aggregated effects of En_high and NDC_all scenarios (i.e., En_NDC_all) indicate that electricity fuel structure transformation can offset the increased GHG emissions induced by the improved treatment technology, i.e., AAO-MBR.

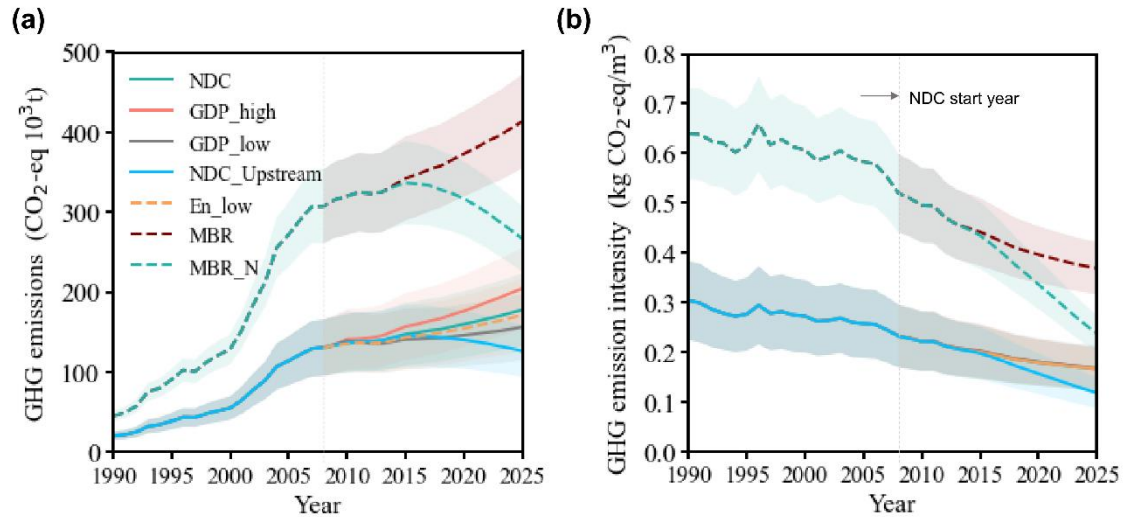


Figure 4.8 Annual variations of (a) total GHG emissions and (b) GHG emission intensity from the integrated urban drainage systems under different scenarios during 1990-2025. Shading indicates the 95% confidential interval.

4.4.2. Policy Implications

The carbon-energy-water nexus has not received much attention in water and energy management in China. The main reason is that the current objective of the wastewater industry is still the removal of nutrients and other contaminants to improve the water environment. Considering the projected increasing trend of wastewater generation under both the BaU and NDC scenarios, the potential contribution of the wastewater industry to meet the goals of China's NDC commitment is significant. The GHG emissions from wastewater treatment are projected to increase in most scenarios, especially under the En_high scenario with all WWTPs equipped with AAO-MBR technology. By reducing the carbon intensity of the electricity sector is the most effective method to minimize the GHG emissions from wastewater treatment. 64% (NDC_all)-88% (En_high) of the GHG emissions from the wastewater industry can be attributed to electricity use. Although both the local and the imported electricity have relatively lower CO₂ intensities than other regions of China (Qu et al., 2017), there is a significant potential to further reduce their CO₂ intensities compared with the levels in other countries (IEA, 2015). Carbon mitigation strategies involving a carbon price can promote the adjustment of the electric power sector's fuel mix to a low-carbon, high-energy efficient one (Dong et al., 2015; Dong and Liang, 2014; Xing et al., 2011). However, simulation studies suggest that carbon mitigation strategies have limited effects in further reducing the carbon intensity of the local electricity sector, but the reduction is expected if carbon mitigation is applied in the imported electricity and other regions of China. Despite the high energy use and CO₂ emission of AAO/MBR, it is an

attractive technology to the water engineering planners because (1) it has high pollutant removal efficiency and can satisfy the high effluent standard required to improve reclaimed wastewater reuse; (2) China's policy to improve the environment quality and local water resources stress are the main driving forces of using AAO/MBR (Liao et al., 2020). To reduce direct GHG emissions, aeration tanks equipped with existing WWTPs would be an easy choice to capture direct emissions. There are also some emerging carbon capture and storage (CCS) technologies that could be integrated with wastewater treatment, such as microbial electrolytic carbon capture (MECC), microbial electrosynthesis (MES), microalgae cultivation, and constructed wetland. These technologies have the potential to contribute to negative emissions with added benefits on water environment protection.

4.4.3. Limitations

In this chapter, the CGE-SyDWEM model is used to provide a comprehensive evaluation of both the direct and the indirect GHG emissions from integrated urban drainage systems with consideration of carbon mitigation strategies and water engineering measures. The superiorities of CGE-SyDWEM in the quantification of GHG emissions from the integrated system are: (1) improving the GHG emissions quantification by including the indirect external emissions, i.e., embodied emissions in all materials and resources used outside the WWTPs boundary and direct emissions from receiving water bodies; and (2) evaluating the potential of carbon mitigation strategies on GHG emissions reduction from wastewater treatment. The impacts of carbon mitigation on wastewater generation and pollutant discharge, the energy intensity of

electricity generation, and embodied GHG emissions in all materials and resources used outside the WWTPs boundary are evaluated. The collection of wastewater is related to the topography and distances of wastewater transfer. Pan et al. (2011) reported that the electricity use for wastewater pumping in Changzhou, China, was about 0.03 and 0.1 kWh/m³ for medium and large WWTPs, respectively, and the shares of electricity use for wastewater pumping can be as high as 20% of the total electricity use. The constant value (0.0384 kWh/m³) used in this study may overestimate or underestimate the electricity use from pumping. In addition, constant electricity intensity is used for the same WWTPs technology due to the data limitation. Studies show that small-scale WWTPs may have lower electricity intensity than large-scale WWTPs (Singh et al., 2012). Therefore, the estimation of electricity use in wastewater treatment can be improved by taking into account the spatial distributions of water infrastructure systems.

5. SELECTION AND IMPLEMENTATION OF REFERENCE EVAPOTRANSPIRATION METHODS FOR ESTIMATION OF REGIONAL IRRIGATION WATER DEMAND

The selection and implementation of reference evapotranspiration (ET_0) methods are vital for estimating irrigation water demand for long-term water resources management, especially in areas with limited weather data. A major limitation of regional ET_0 estimation is that the constant parameters in these methods usually cannot assure the same reliability under different climatic regions. However, the controlling parameters of ET_0 under different climatic conditions and how they are related to the structures of the temperature- and radiation-based methods have not been adequately addressed yet. Here, eight commonly used methods were selected, including three temperature-based methods, i.e., Thornthwaite (Th_T), Blaney-Criddle (BC_T), and Hargreaves and Samani (HS_T), and five radiation-based methods, i.e., Makkink (Ma_R), Priestley-Taylor (PT_R), Jensen and Haise (JH_R), Turc (Tu_R), and Abtew (Ab_R), for the estimation of the ET_0 values which were then compared with estimated using these methods with the values estimated using the reference method of the Penman-Monteith equation in various climate types, including humid, subhumid, semi-arid, and arid, in Texas, United States, using 50 years (1961-2010) of monthly meteorological data from 15 climatological stations. Results indicated that the HS_T method was the best empirical method for estimating ET_0 and is recommended for regional analysis if reliable wind speed and relative humidity data are not available.

However, calibration is suggested in regions with dry and consistently windy conditions. The impact of each climatic variable on the seasonal and spatial variations of ET_0 was further quantified using non-dimensional relative sensitivity coefficients. The radiative component is the driving factor of ET_0 , accounting for 51%-84% of the variability in ET_0 . To accurately reflect the impact of aerodynamic components on the ET_0 estimation under dry and windy conditions, a calibration-free coefficient ($c = 1.47 - 0.0067RH$) with monthly relative humidity (RH) as the only input was found, which should be multiplied with the HS_T or PT_R equations. By doing so, the accuracy of ET_0 under dry and windy conditions considerably improved compared with local calibration methods.

5.1. Introduction

An accurate estimation of ET_0 is important for irrigation water management, water balance studies, and hydrological and crop modeling, which is particularly true given the increasing global irrigation water demand (IWD) owing to growing food demand, higher global mean temperature, and changing precipitation patterns (Florke et al., 2018; Haddeland et al., 2014). The most common method for irrigation water estimation is the crop coefficient approach, i.e., adjusting ET_0 by crop coefficients (Allen, 1998; Doorenbos and Pruitt, 1976). When required meteorological data are available, the Food and Agriculture Organization (FAO) Penman-Monteith equation (FAO-PM) (Allen, 1998) is the recommended standard method for ET_0 estimation, because it is more physically based and can be applied globally without local calibration. However, the FAO-PM method requires a full set of reliable weather data, including

solar radiation, air temperature, relative humidity, and wind speed, which are usually absent or incomplete in many regions. Therefore, less data-intensive methods, e.g., mass-transfer (Hanasaki et al., 2008; Robock et al., 1995), radiation-based (Doll and Siebert, 2002; Rost et al., 2008), and temperature-based methods (Wisser et al., 2008) are still widely used in regional and global IWD studies. Selection of ET_0 methods is one of the major sources of uncertainty in regional and global IWD projections.

Current approaches used for ET_0 estimation are based on (1) empirical relationships, (2) water budget, (3) mass transfer, (4) temperature, (5) radiation, and (6) physical-based combination methods, e.g., Penman (1948) and FAO-PM method (Allen, 1998). Empirical methods, e.g., multiple regression analysis (Kohler et al., 1955), are not suitable for regional and global studies because the variables selected as predictors in the models vary with the empirical method used and thereby could be problematic when applying the same empirical model from one place to another. The water budget methods, e.g., Guitjens (1982), are rarely used in practice due to the difficulty and error accumulation in measuring the required variables, such as deep percolation, subsurface flow, and capillary rise. The mass transfer methods are attractive in estimating the evaporation of free-water bodies, e.g., lakes and reservoirs (Singh and Xu, 1997), but less robust for vegetated surfaces than temperature- and radiation-based methods (Valipour et al., 2017; Xu and Singh, 2002). The use of temperature- and radiation-based methods for ET_0 estimation in regional IWD has two major advantages: (1) easily accessible weather dataset owing to only temperature or radiation-related data required as input; and (2) acceptable accuracy, which was confirmed under various climatic

conditions including humid, subhumid, semi-arid, arid, and high altitude conditions by many studies in which the ET_0 values estimated using temperature- and radiation-based methods were verified against the lysimeter observations or the estimation using the reference method (FAO-PM) (Djaman et al., 2019; Liu et al., 2017).

The performance of various temperature- and radiation-based methods used for ET_0 estimation have been extensively evaluated either at point level or in a specific climate (Amatya et al., 1995; Azhar and Perera, 2011; Djaman et al., 2019; Nandagiri and Kovoov, 2006; Trajkovic and Kolakovic, 2009; Xu and Singh, 2002; Xu et al., 2013). The temperature-based methods like Th_T (Thornthwaite, 1948), HS_T (Hargreaves and Samani, 1985), and BC_T (Blaney and Criddle, 1950), and the radiation-based ones like PT_R (Priestley and Taylor, 1972), Ma_R (Makkink, 1957), and Tu_R (Turc, 1961) are the most commonly used approaches for cross-comparisons (Xu and Singh, 2000, 2001). It has been widely appreciated that the constant parameters in these methods cannot guarantee the same reliability in different climatic regions. In humid climates, radiation-based methods usually perform better than the temperature-based methods, but both of these two methods can provide reasonable estimations (Amatya et al., 1995; Azhar and Perera, 2011; Djaman et al., 2019; Nandagiri and Kovoov, 2006; Trajkovic and Kolakovic, 2009; Xu and Singh, 2002; Xu et al., 2013). In a warmer and drier climate, the aerodynamic component, which is primarily affected by wind speed and relative humidity, becomes more important (Matsoukas et al., 2011), and the warm air advection from unirrigated areas often contributes extra sensible heat energy for evapotranspiration. The advection of sensible heat energy could be reflected

in the temperature-based methods by changing temperature, but the radiation-based methods are not able to adequately compensate for the advection effect and thus are not suggested for semi-arid or arid conditions (Didari and Ahmadi, 2019). For example, the temperature-based methods, e.g., HS_T and BC_T (Allen and Pruitt, 1986), were reported to have better performance than the radiation-based methods in sub-humid (Nandagiri and Koveer, 2006) and semi-arid climates (Bakhtiari et al., 2011; Er-Raki et al., 2010; Gao et al., 2017; Nandagiri and Koveer, 2006; Tabari, 2010). However, inconsistent results were reported in other studies. For example, in an arid climate with light wind conditions in Aksu, China, Gao et al. (2017) reported that the radiation-based method, i.e., the PT_R method shows the best performance, followed by HS_T, Ma_R, Tu_R, BC_T. In a warm, humid climate with moderate to strong wind, Tabari (2010) found that the temperature-based method (HS_T) performed better than the radiation-based methods, including Turc_R, PT_R, and Mk_R. Moreover, the ET_0 estimation in more arid and strong wind conditions usually showed higher uncertainties, and the performance did not improve significantly even after local calibration (Akhavan et al., 2018; Didari and Ahmadi, 2019; Valipour et al., 2017). These studies suggest that the relative contributions of the weather parameters on the ET_0 variation may be different under various climate conditions, leading to inconsistent conclusions regarding the performance of different methods.

However, what the controlling weather parameters of ET_0 under different climatic conditions are and how they relate to the structures of the temperature- and radiation-based methods have not been adequately addressed in previous studies. The

deficiencies in understanding the controlling parameters hinder the effort of applying the less data-intensive methods to predict regional or global irrigation water demand. Herein, eight commonly used methods are selected, including three temperature-based methods, i.e., Thornthwaite (Th_T), Blaney-Criddle (BC_T), and Hargreaves and Samani (HS_T), and five radiation-based methods, i.e., Makkink (Ma_R), Priestley-Taylor (PT_R), Jensen and Haise (JH_R), Turc (Tu_R), and Abtew (Ab_R), for evaluation by comparing them with the reference method (i.e., FAO-PM) for various climate types, including arid, semi-arid, and humid tropical in Texas, United States, using measurements from 15 climatological stations. The objectives of this study were to (1) evaluate the performances of the selected methods with the default, local calibration values for regional ET_0 analysis; (2) identify the controlling weather parameters in the ET_0 estimation under different climatic conditions; and (3) improve the performance of the selected methods in arid, strong wind conditions through adequate consideration of the aerodynamic component.

5.2. Methodology

Theoretical details of the reference method, i.e., FAO-PM, and the selected eight ET_0 methods are described first. Second, the following analysis is performed to evaluate the performance of the selected methods: (1) the ET_0 values estimated using the eight selected methods with default constant parameters are compared with the FAO-PM estimates and then calibrated with an automatic optimization method; (2) the model verification is conducted at the chosen stations to assess the model ability to predict a long-term ET_0 ; and (3) the regional average of parameter values used for each method is

evaluated. Third, sensitivity analysis is conducted to understand the model structure and quantify the contributions of meteorological parameters to ET_0 variations. Last, a simplified method is developed based on the sensitivity analysis results to improve the performance of the selected methods in arid and strong wind climate conditions.

The FAO-PM ET_0 estimation requires high-quality meteorological data (Table 5.1). Elevation is also needed to calculate the psychrometric constant. The eight ET_0 methods ingest much fewer inputs than does the FAO-PM method. For example, the temperature-based methods only require temperature as input, and other parameters, e.g., daytime length and extraterrestrial radiation (R_a), are available from standard tables. The time step, input data, and definition associated with each ET_0 method vary widely. Given the nonlinear nature of ET_0 , the use of daily meteorological data can lead to more accurate estimation than using monthly averages. Nevertheless, daily meteorological data show high uncertainty, since its quality control is more difficult than that of monthly data. Therefore, monthly data is suggested when analyzing long-term trends (Vicente-Serrano et al., 2014). For model comparison, consistent definitions of parameters, time steps (monthly), and units are used.

Table 5.1 Input Data Required by Different Methods.

Methods	Elevation	Temperature			Radiation	Relative humidity	Wind speed
		Max	Min	Mean			
FAO-PM	√	√	√	√	√	√	√
Th_T				√	Daytime length		
BC_T				√	Daytime length		
HS_T		√	√	√	R_a		
Ma_R	√			√	√		
PT_R	√			√	√		
JH_R				√	√		
Tu_R					√	√	
Ab_R		√			√		

5.2.1. FAO-PM Method

The original Penman-Monteith method contains two processes that affect the potential evapotranspiration from a vegetated surface, as shown in equation (5.1). The first process is related to climatic parameters, that determine the evaporative demand ET^* , i.e., evaporation from free water surface. ET^* includes equilibrium evaporation (ET_{eq}) (equation 5.2) and evaporation determined by vapor pressure deficit (ET_D) (equation 5.3). The second process is related to vegetation characteristics, i.e., canopy resistance, r_s , which represents the obstacles of water vapor transfer between crop surface and reference height. ET^* depends on available energy (A), vapor pressure deficit (D), and aerodynamic resistance (r_a), which are driven by four climatic variables, including solar radiation, relative humidity, wind speed, and air temperature. Crop surface can also affect A and r_a , e.g., crop physical characteristics may influence A by regulating albedo, and crop height and roughness may affect r_a .

$$\lambda ET_{PM} = \frac{\lambda ET^*}{1 + \frac{\gamma}{\gamma + \Delta} \times \frac{r_s}{r_a}} = \frac{\frac{\Delta}{\Delta + \gamma} A + \frac{\rho C_p D}{(\Delta + \gamma) r_a}}{1 + \frac{\gamma}{\gamma + \Delta} \times \frac{r_s}{r_a}} = \frac{\frac{\Delta}{\Delta + \gamma} (R_n - G) + \frac{\rho C_p (e_s - e_a)}{(\Delta + \gamma) r_a}}{1 + \frac{\gamma}{\gamma + \Delta} \times \frac{r_s}{r_a}} = \frac{ET_{eq} + \frac{\Delta + \gamma}{\gamma} ET_D}{1 + \frac{\gamma}{\gamma + \Delta} \times \frac{r_s}{r_a}} \quad (5.1)$$

$$\lambda ET_{eq} = \frac{\Delta}{\Delta + \gamma} \frac{R_n - G}{\lambda} \quad (5.2)$$

$$\lambda ET_D = \frac{\rho C_p (e_s - e_a)}{\gamma \times r_a} \quad (5.3)$$

where ET_{PM} is the potential evapotranspiration from well-watered vegetated surfaces (mm d^{-1}); ET^* is the potential evaporation from free water surfaces (mm d^{-1}); λ is the latent heat of vaporization of water (MJ kg^{-1}); $A = R_n - G$, where R_n is the net radiation at the crop surface ($\text{MJ m}^{-2} \text{d}^{-1}$), and G is the soil heat flux ($\text{MJ m}^{-2} \text{d}^{-1}$); $D = e_s - e_a$, in which e_s and e_a are the saturation and actual vapor pressure (kPa), respectively; r_a is the aerodynamic resistance (s m^{-1}); r_s is the surface resistance (s m^{-1}); Δ is the slope of vapor pressure curve ($\text{kPa } ^\circ\text{C}^{-1}$); γ is the psychrometric constant ($\text{kPa } ^\circ\text{C}^{-1}$); ρ_a is the mean air density under constant pressure (kg m^{-3}); and C_p is the specific heat of moist air ($1.013 \text{ kJ kg}^{-1} ^\circ\text{C}^{-1}$). Detailed calculations of each parameter can be found in Appendix D.

To reduce the impact of crop surface, a hypothetical reference grass surface is used by the FAO-PM method (Allen, 1998) with an assumed grass height of 0.12 m, an albedo of 0.23, and a fixed surface resistance ($r_s = 70 \text{ s m}^{-1}$). Equation (5.1) can be rewritten as:

$$ET_0 = \frac{0.408 \Delta (R_n - G) + \gamma \frac{900}{T_a + 273} U_2 (e_s - e_a)}{\Delta + \gamma (1 + 0.34 U_2)} \quad (5.4)$$

where ET_0 is the reference evapotranspiration (mm d^{-1}); T and U_2 are the mean air temperature ($^\circ\text{C}$) and wind speed (m s^{-1}) measured at 2 m height, respectively; $r_a =$

$$208/U_2, \frac{r_s}{r_a} = 0.34 U_2, \text{ and } \frac{\rho_a C_p}{r_a} = \gamma \frac{900}{T_a + 273} U_2.$$

With the use of reference surface, the FAO-PM method depends only on climatic variables, i.e., the available energy (A or Rn if G is small for daily analysis), the vapor pressure deficit (D), and aerodynamic resistance (r_a). Therefore, the change in ET_0 can be attributed to the changes in A , D , and r_a . To better understand the relative contributions of A , D and r_a to the dynamics of ET_0 under different climate conditions, the non-dimensional relative sensitivity coefficients, i.e., S_A , S_D , and S_{r_a} , are calculated as below (Beven, 1979; McCuen, 1974; Rana and Katerji, 1998):

$$S_A = \frac{\partial(\lambda ET_0)}{\partial A} \frac{A}{ET_0} = \frac{1}{1 + \frac{\rho C_p D}{r_a \Delta A}} = \frac{1}{1 + \gamma \frac{900}{T_a + 273} U_2 \frac{D}{\Delta A}} \quad (5.5)$$

$$S_D = \frac{\partial(\lambda ET_0)}{\partial D} \frac{D}{ET_0} = \frac{1}{1 + \frac{r_a \Delta A}{\rho C_p D}} = \frac{1}{1 + \frac{D}{\Delta A \gamma \frac{900}{T_a + 273} U_2}} = 1 - S_A \quad (5.6)$$

$$S_{r_a} = \frac{\partial(\lambda ET_0)}{\partial r_a} \frac{r_a}{ET_0} = S_A - \frac{1}{1 + \frac{\gamma}{\gamma + \Delta} \frac{r_s}{r_a}} = S_A - \frac{1}{1 + \frac{\gamma}{\gamma + \Delta} * 0.34 U_2} \quad (5.7)$$

Since $r_a = 208/U_2$, the relative contributions of U_2 on the dynamics of ET_0 can be evaluated as:

$$S_{U_2} = \frac{\partial(ET_0)}{\partial r_a} \frac{\partial(r_a)}{\partial U_2} \frac{U_2}{ET_0} = -S_{r_a} \quad (5.8)$$

Temperature is highly correlated with solar radiation and vapor pressure deficit. In the FAO-PM method, both Δ and D are functions of mean temperature. Therefore, the relative sensitivity coefficient of T is derived as:

$$S_T = \frac{\partial(ET_0)}{\partial T} \frac{T}{ET_0} = T \left[\frac{r_a A}{r_a \Delta A + \rho C_p D} - \frac{1}{\Delta + C_p (1 + \frac{r_s}{r_a})} \right] \frac{\partial \Delta}{\partial T} + T \frac{\rho C_p}{r_a \Delta A + \rho C_p D} \frac{\partial D}{\partial T} \quad (5.9)$$

$\frac{\partial \Delta}{\partial T}$ and $\frac{\partial D}{\partial T}$ can be found in Appendix D. As shown in equations (5.5-5.9), $S_A, S_D,$

S_{r_a}, S_{u_2} and S_T depend on all the parameters, including available energy, vapor pressure deficit, wind speed, and temperature.

5.2.2. Temperature- and Radiation-based Methods

Most temperature-based methods are developed based on the empirical relationships of air temperature or day length with field measurements (Table 5.2). Typical temperature-based methods can be formulated as equations (5.10) or (5.11) (Xu and Singh, 2001):

$$ET_0 = cT^n \quad (5.10)$$

$$ET_0 = c_1 p (c_2 T + c_3) h \quad (5.11)$$

where T is the mean air temperature; p is the daytime length; h is a humidity term; and $n, c, c_1, c_2,$ and c_3 are constants. Th_T method has a form similar to equation (5.10), and BC_T and HS_T show a similar form as equation (5.11). The Thornthwaite method correlates mean temperature with ET_0 based on water balance. R_s can be estimated by R_a using the terms in the Hargreaves and Samani method, i.e., $R_s = \alpha R_a (T_{max} - T_{min})^{\frac{1}{2}}$, where α is an adjustment coefficient (0.16 for interior locations or 0.19) (Allen, 1998). The temperature difference ($T_{max} - T_{min}$) is related to cloudiness and relative humidity. The daytime length in the Blaney and Criddle method is an indicator of solar radiation. The constants in each method are usually subject to recalibration against the FAO-PM estimates when the temperature-based methods are used in different locations.

Radiation-based methods are based on the energy balance equation using net (R_n)

or solar radiation (R_s) as the primary parameter (Jensen et al., 1990). The available energy for evapotranspiration includes R_n , G , and sensible energy (H). H may be increased or decreased due to the advection effect when strong winds provide significant heating or cooling to the reference surface. This advection of sensible heat energy is treated in the PM method by introducing an aerodynamic term. However, radiation-based methods cannot adequately compensate for the advection effect, since they assume the relative contribution of solar radiation to ET_0 is a constant, i.e., S_A in equation (5.5). Radiation-based methods can be formulated as:

$$ET_0 = \frac{1}{S_A} (ET_{eq}) = \frac{1}{S_A} \frac{\Delta}{\Delta + \gamma} \frac{R_n - G}{\lambda} \quad (5.12)$$

where S_A represents the relative contribution of available energy to ET_0 , with the wind having a negligible effect, i.e., $S_{r_a} = 0$. It is similar to the decoupling coefficient introduced by Jarvis and McNaughton (1986) to analyze the relative contribution of solar radiation and aerodynamic terms to the evapotranspiration process. By replacing $\frac{1}{S_A} = 1.26$, equation (5.12) is transferred to the Priestley-Taylor method (equation 5.17 in Table 5.2). It also indicates that solar radiation accounts for 79.4% ($S_A = \frac{1}{1.26}$) of the ET_0 variation in the PT_R method. The Makkink, Jensen-Haise, Turc, and Abtew methods use R_s instead of R_n , since R_s can be linearly associated with R_n with $G=0$ and an albedo of 0.23. The Ma_R method can be considered as a special form of equation (5.12) when disregarding the aerodynamic term and compensating with two empirical coefficients (equation 5.16 in Table 5.2). $\frac{\Delta}{\Delta + \gamma}$ is a function of temperature with given atmospheric pressure, and therefore, it can be replaced with different forms related to

temperature, e.g., $T+3$ in Jensen-Haise, $\frac{T}{T+15}$ in Turc, and T_{max} in Abtew method.

Because of the empirical character, the default values in each method usually represent certain climatic conditions, and as a consequence, calibration is usually required when applying radiation-based methods in different climatic regions.

Table 5.2 Summary of Selected Models with Default Constant Values.

Method	Equation No.	Generalized equation	Parameters
		$ET_0 = \alpha \left(10 \frac{T}{I} \right)^n$	
Th_T	5.13	$I = \sum_{i=1}^{12} (0.2T_i)^{1.514}$ $n = 6.75 \times 10^{-7} I^3 - 7.71 \times 10^{-5} I^2 + 1.7912 \times 10^{-2} I + 0.4923$	$\alpha = 16$
BC_T	5.14	$ET_0 = kp(0.46T + 8.13)$	$k = 1$
HS_T	5.15	$ET_0 = \alpha(T + 17.8)R_a(T_{max} - T_{min})^{\frac{1}{2}}$	$\alpha = 0.0023$
Ma_R	5.16	$ET_0 = \alpha \frac{\Delta}{\Delta + \gamma} \frac{R_s}{\lambda} + \beta$	$\alpha = 0.61$ $\beta = -0.12$
PT_R	5.17	$ET_0 = \alpha \frac{\Delta}{\Delta + \gamma} \frac{R_n - G}{\lambda}$	$\alpha = 1.26$
JH_R	5.18	$ET_0 = \alpha(T + 3) \frac{R_s}{\lambda}$	$\alpha = 0.025$
Tu_R	5.19	$ET_0 = \alpha(R_s + 50) \frac{mT}{T + 15}$ $m=1$ for $RH \geq 50$; $m=1+\frac{50-RH}{70}$ for $RH < 50$	$\alpha = 0.0133$
Ab_R	5.20	$ET_0 = \frac{1}{K} \frac{R_s T_{max}}{\lambda}$	$K = 56^\circ C$

Note: I is the annual heat index, varying among 0-160; T_i is the i th monthly mean temperature ($^\circ C$). The Th_T method is based on a standard month of 30 days and 12-hour sunlight per day and is adjusted by the length of day (For $T < 0^\circ C$, $ET_0 = 0$); k depends on sunshine hours, daytime wind estimates, and minimum relative humidity and varies among 0.5-1.2; p is the mean daily percentage of annual daytime hours; T_{max} and T_{min} are the maximum and minimum air temperature ($^\circ C$), respectively; RH is the average relative humidity (%); and other parameters have the same definition as in equations (5.1-5.5).

5.2.3. Model Evaluation

Root-mean-square error (RMSE) and relative error (RE) are used to evaluate the model performances, as shown in equations (5.21) and (5.22):

$$RMSE = \sqrt{\frac{\sum_{i=1}^n (X_i - ET_{0i})^2}{n}} \quad (5.21)$$

$$RE (\%) = \frac{(X_i - ET_{0i})}{ET_{0i}} \times 100 \quad (5.22)$$

where X_i and ET_{0i} are the i th calculated ET_o using the selected method and the FAO-PM method, respectively, and n is the sample number of sample observations. The method with the best performance should have RMSE and RE values equal to 0. Here, an RE of $\pm 20\%$ is used as an arbitrary measurement of the acceptance of each model.

The monthly ET_0 values calculated with each model are correlated with the FAO-PM estimates using linear regression:

$$Y = aX + b \quad (5.23)$$

where Y represents FAO-PM ET_0 , and X is the ET_0 calculated in each model; a and b are the slope and intercept, respectively. The best method has the highest model coefficient of determination (R^2), with a close to 1 and b close to 0. To better compare model performance, the intercept was set as 0, and the corresponding slope and R^2 were recalculated.

An automatic optimization method was used to obtain the best parameters involved in each method, suggested by Singh and Xu (1997). Optimization of the model parameters can be obtained by minimizing the residual sum of squares (RSS), as shown in equation (5.24):

$$\text{Minimum RSS} = \sum_{i=1}^n (X_i - ET_{0i})^2 \quad (5.24)$$

The criteria used in selecting ET_0 methods for regional analysis are described as follows: (1) it can be used to accurately estimate ET_0 under different climatic and locations; (2) it can capture both the peak and seasonal variations of ET_0 ; (3) if the original default parameter in a method overestimates/underestimates in a specific climate, then the error should be systematic and correctable; (4) it can be used to evaluate the long-term variation of ET_0 ; and (5) for methods that satisfy all the criteria, the one with fewer inputs is selected.

5.2.4. Study Area

Texas has the largest cropland area in the United States, located in the south-central region and borders with the Gulf of Mexico to the southeast (<https://www.ers.usda.gov/data-products/major-land-uses/major-land-uses/#Cropland>).

As shown in Figure 5.1, there are ten climate divisions in Texas (<https://texas.resiliencesystem.org/texas-climate-divisions>), including humid subtropical (Cfa), semi-arid (BSh and BSk), and arid (BWh and BWk) conditions based on the Köppen-Geiger classification (Beck et al., 2018). Most of the cropland is in semi-arid regions, e.g., High Plains (region 1) and Rolling Plains (region 2), which have dry, high radiation, and windy environment.

The monthly averages of meteorological data between 1961 and 2010 from total 15 stations covering most of the ten regions were downloaded from Climate Data Online provided by National Oceanic and Atmospheric Administration (<https://www.ncdc.noaa.gov/cdo-web/>). To reduce the calculation uncertainty, solar

radiation data, including R_s and R_a , were obtained from direct radiation measurement, which was downloaded from the National solar radiation database (https://rredc.nrel.gov/solar/old_data/nsrdb/). R_n was calculated according to Allen (1998). Wind speeds from climate stations are generally measured at a 10 m height, and they were converted to 2 m wind speeds using the method suggested by (Allen, 1998).

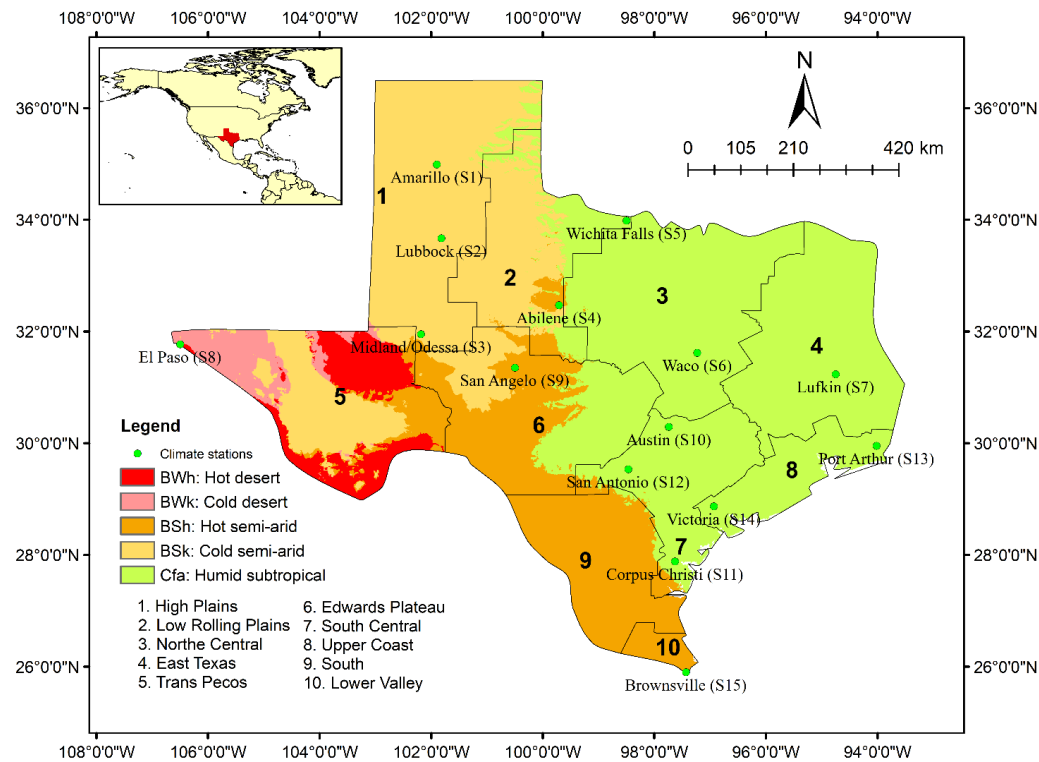


Figure 5.1 Geographical locations of selected stations and climatic regions in Texas, United States. (The climate classifications were adopted from Beck et al., 2018, and region 10 and part of region 9 at southeast corner should belong to humid subtropical climate. These errors are due to the resolution of the dataset used in Beck et al., 2018).

The annual means of main meteorological variables during 1961-2010 are shown in Table 5.3, and their seasonal and annual variations were detailed in Figure D1,

Appendix D. Here, three seasons were identified, i.e., warm season (May through Sep.), transition season (March, April, and October), and cool season (Jan, Feb, Nov, and Dec.), based on air temperature variation. The warm season is of particular interest since this is the growing season with high irrigation requirements. Moderate to strong advection are observed in both arid and humid climates (wind speed among 3-5 m s⁻¹), and the wind speed has no apparent seasonal variation (Figure D1, Appendix D).

Table 5.3 General Information and Monthly Average of the Main Climatic Variables of Selected Stations in Texas, United States (1961-2010).

Climate region	Stations	Elevation (m)	Temperature (°C)			Wind (m/s)	RH (%)	Rs (MJ m ⁻² d ⁻¹)
			Max	Min	Mean			
Semi-arid climate								
1	S1	1098	21.35	6.59	13.85	4.47	56.39	18.27
1	S2	988	23.11	8.51	15.72	4.01	55.75	18.52
1	S3	871	25.02	10.09	17.50	3.74	53.70	19.21
2	S4	534	24.44	11.74	18.00	3.79	59.09	18.24
6	S9	582	25.58	11.32	18.39	3.34	59.50	18.41
Arid climate								
5	S8	1194	25.26	10.34	17.89	2.69	40.24	20.63
Subhumid subtropical climate								
2	S5	314	24.02	10.84	17.36	3.87	63.22	17.44
3	S6	155	25.39	13.32	19.30	3.53	67.69	17.34
7	S10	189	25.02	12.85	18.76	3.27	63.34	17.67
7	S12	242	26.45	14.70	20.47	2.96	66.99	17.39
Humid subtropical climate								
4	S7	96	25.39	13.17	19.16	2.26	73.65	16.53
7	S11	13	27.26	17.01	22.05	4.00	76.10	16.66
8	S13	7	25.47	15.30	20.28	3.04	78.13	16.23
8	S14	32	26.63	15.67	21.01	3.25	75.21	16.48
10	S15	6	28.28	18.49	23.24	3.64	76.39	17.08

Note: Monthly RH_{mean} is used for climatic classification, with arid (<45%), semi-arid (45%-55%), sub-humid (55%-70%), humid (70%-85%), and very humid (>85%) (Allen, 1998).

5.3. Results

5.3.1. Comparison of Each Method with Original Constant Values

Using the original constant values in each method to different locations leads to large errors in estimating monthly ET_0 , with the highest average RMSE of all methods in arid climate (0.62-2.66 mm d⁻¹), followed by semi-arid (0.78-1.62 mm d⁻¹), subhumid (0.56-1.52 mm d⁻¹), and humid (0.34-1.14 mm d⁻¹) climates (Tables 5.4 and 5.5). When concerning the mean RMSE of all 15 stations, the best method is HS_T (0.64 mm d⁻¹), followed by Tu_R (0.76), Ab_R (0.82), PT_R (0.90), JH_R (1.03), BC_T (1.05), Ma_R (1.37), and Th_T (1.68). HS_T is the only method showing comparable reliability across all climate types, i.e., the RE of annual mean ET_0 at all stations was within $\pm 20\%$. Also, it had the lowest RMSE at one station in arid and semi-arid regions and five stations in humid regions (Table 5.4). One possible explanation is that $(T_{max} - T_{min})^{\frac{1}{2}}$ in the HS_R method was highly correlated with relative humidity ($R^2 = 0.96$ with $RH \geq 50\%$, $n = 7738$), in which T_{min} was used to approximate dew point temperature (T_{dew}). In arid regions, assuming $T_{min} \approx T_{dew}$ would lead to an overestimation of T_{dew} , since the difference between T_{min} and T_{dew} increases with higher vapor pressure deficit (Jensen et al., 1997). Therefore, an underestimation of $(T_{max} - T_{min})^{\frac{1}{2}}$ would be expected in arid and semi-arid climates, as illustrated in the underestimation of $(T_{max} - T_{min})^{\frac{1}{2}}$ when $RH < 50\%$ (Figure D2, Appendix D). However, the mean temperature is also used in HS_T, which is computed as the average of T_{max} and T_{min} . If T_{min} is assumed overestimated, then the mean temperature will increase, which can slightly compensate for the underestimation

of $(T_{max} - T_{min})^{\frac{1}{2}}$. Hence, the HS_T method shows comparable reliability across different climate types. The three radiation-based methods, i.e., PT_R, Tu_R, and Ab_R, worked quite well for annual ET₀ estimates in humid climates, but ET₀ was substantially underestimated in arid and semi-arid climates, e.g., by 14-18% in warm, 19-31% in transition, 43-48% in cool seasons (Table D1 and D2, Appendix D). The Tu_R method performed well in arid climate (Table 5.5), since an adjustment was made when RH<50. For methods originally developed in a relatively dry environment, e.g., BC_T and JH_R, they also underestimated by 7% and 12% the mean annual ET₀ in arid and semi-arid regions but significantly overestimated ET₀ in humid regions. Ma_R method had high R^2 , but systematically underestimated at all stations, indicating that the default value was too small. Of all the methods evaluated, the Th_T method performed the poorest in estimating monthly ET₀, but it still showed acceptable accuracy.

The peak and seasonal variations of mean monthly ET₀ from all methods were compared with the FAO-PM estimates, which is further illustrated in Figure 5.2. HS_T, PT_R, and Ab_R well simulated the peak and warm season ET₀ across all the stations with RE within $\pm 20\%$. All methods captured the warm season ET₀ variations, except that the BC_T and JH_T methods overestimated ET₀ under very humid conditions. JH_R overestimated peak values at all stations, ranging between 5% (S1) and 43% (S13). Overall, both the temperature- and radiation-based methods better performed in the warm season than in the transition and cold seasons. HS_T showed less seasonal difference than did other methods.

Table 5.4 Regression Relationships (Y=mx) between FAO-PM ET_o and the Temperature-based Methods using Original Constant Values.

Stations	Thornthwaite_T			Blaney-Criddle_T			Hargreaves and Samani_T		
	S	R ²	E	S	R ²	E	S	R ²	E
<i>Semi-arid climate</i>									
S1	1.82	0.74	2.27	<i>1.11</i>	<i>0.84</i>	<i>0.77</i>	1.17	0.94	0.83
S2	1.69	0.71	2.28	<i>1.09</i>	<i>0.79</i>	<i>0.80</i>	1.16	0.94	0.82
S3	1.67	0.72	2.41	<i>1.13</i>	<i>0.76</i>	<i>0.95</i>	1.17	0.94	0.90
S4	1.47	0.73	1.94	<i>1.03</i>	<i>0.80</i>	<i>0.70</i>	1.16	0.93	0.81
S9	1.45	0.73	1.88	1.01	0.74	0.74	<i>1.07</i>	<i>0.94</i>	<i>0.54</i>
<i>Arid climate</i>									
S8	1.73	0.66	2.66	1.17	0.74	1.10	<i>1.20</i>	<i>0.91</i>	<i>1.09</i>
<i>Subhumid subtropical climate</i>									
S5	1.37	0.78	1.67	0.99	0.75	0.78	<i>1.09</i>	<i>0.93</i>	<i>0.63</i>
S6	1.21	0.78	1.37	0.92	0.67	0.94	<i>1.05</i>	<i>0.92</i>	<i>0.51</i>
S10	1.33	0.69	1.67	0.94	0.59	0.94	<i>1.09</i>	<i>0.87</i>	<i>0.69</i>
S12	1.16	0.74	1.36	0.87	0.69	0.99	<i>1.03</i>	<i>0.94</i>	<i>0.39</i>
<i>Humid subtropical climate</i>									
S7	1.06	0.76	1.05	0.74	0.76	1.41	<i>0.86</i>	<i>0.97</i>	<i>0.66</i>
S11	1.04	0.71	1.21	0.80	0.59	1.31	<i>0.99</i>	<i>0.91</i>	<i>0.37</i>
S13	1.00	0.73	1.11	0.71	0.76	1.57	<i>0.90</i>	<i>0.95</i>	<i>0.49</i>
S14	1.05	0.73	1.18	0.77	0.65	1.36	<i>0.94</i>	<i>0.94</i>	<i>0.42</i>
S15	1.01	0.76	1.16	0.80	0.42	1.33	<i>1.02</i>	<i>0.88</i>	<i>0.39</i>
<i>Arid</i>	1.73	0.66	2.66	1.17	0.74	1.10	<i>1.20</i>	<i>0.91</i>	<i>1.09</i>
<i>Semi-arid</i>	1.62	0.73	2.16	1.07	0.79	0.79	<i>1.15</i>	<i>0.94</i>	<i>0.78</i>
<i>Subhumid</i>	1.27	0.75	1.52	0.93	0.68	0.91	<i>1.07</i>	<i>0.92</i>	<i>0.56</i>
<i>Humid</i>	1.03	0.74	1.14	0.76	0.64	1.40	<i>0.94</i>	<i>0.93</i>	<i>0.47</i>
<i>All regions</i>	1.34	0.73	1.68	0.94	0.70	1.05	<i>1.06</i>	<i>0.93</i>	<i>0.64</i>

Note: Bold and italic values indicate the method with the best performance.

Table 5.5 Regression Relationships (Y=mx) between FAO-PM ET₀ and the Radiation-based Methods using Original Constant Values.

Stations	Makkink_R			Priestley and Taylor_R			Jensen-Haise_R			Turc_R			Abtew_R		
	S	R ²	E	S	R ²	E	S	R ²	E	S	R ²	E	S	R ²	E
<i>Semi-arid climate</i>															
S1	1.52	0.93	1.67	1.29	0.87	1.27	1.12	0.85	1.10	1.32	0.91	1.29	1.30	0.91	1.27
S2	1.51	0.94	1.71	1.28	0.86	1.29	1.07	0.84	1.06	1.28	0.94	1.18	1.28	0.90	1.21
S3	1.55	0.95	1.92	1.32	0.87	1.45	1.06	0.88	0.95	1.28	0.95	1.21	1.25	0.93	1.20
S4	1.51	0.94	1.69	1.25	0.88	1.17	0.99	0.88	0.90	1.26	0.94	1.09	1.23	0.91	1.08
S9	1.47	0.95	1.59	1.21	0.88	1.05	0.97	0.89	0.85	1.23	0.95	0.97	1.17	0.93	0.88
<i>Arid climate</i>															
S8	1.48	0.96	1.83	1.36	0.86	1.63	1.02	0.87	0.99	1.07	0.95	0.62	1.21	0.91	1.15
<i>Subhumid subtropical climate</i>															
S5	1.51	0.93	1.61	1.23	0.89	1.05	0.98	0.90	0.86	1.25	0.93	1.06	1.20	0.93	0.94
S6	1.43	0.94	1.40	1.13	0.91	0.75	0.90	0.91	0.92	1.18	0.93	0.80	1.13	0.94	0.72
S10	1.44	0.92	1.44	1.17	0.85	0.96	0.93	0.86	1.01	1.19	0.92	0.85	1.16	0.89	0.89
S12	1.38	0.96	1.24	1.08	0.92	0.59	0.87	0.90	1.01	1.14	0.96	0.61	1.10	0.93	0.62
<i>Humid subtropical climate</i>															
S7	1.23	0.97	0.71	0.94	0.94	0.46	0.79	0.91	1.20	1.01	0.97	0.24	0.98	0.94	0.44
S11	1.34	0.93	1.08	1.01	0.90	0.51	0.82	0.88	1.13	1.08	0.94	0.44	1.08	0.91	0.56
S13	1.22	0.96	0.69	0.92	0.93	0.51	0.77	0.90	1.24	0.99	0.97	0.23	1.01	0.92	0.44
S14	1.32	0.94	0.98	1.00	0.92	0.47	0.82	0.90	1.12	1.06	0.95	0.38	1.05	0.92	0.50
S15	1.33	0.96	1.07	1.00	0.94	0.38	0.81	0.93	1.18	1.08	0.96	0.39	1.06	0.94	0.44
<i>Arid</i>	1.48	0.96	1.83	1.36	0.86	1.63	1.02	0.87	0.99	1.07	0.95	0.62	1.73	0.66	2.66
<i>Semi-arid</i>	1.51	0.94	1.72	1.27	0.87	1.25	1.04	0.87	0.97	1.27	0.94	1.15	1.62	0.73	2.16
<i>Subhumid</i>	1.44	0.94	1.42	1.15	0.89	0.84	0.92	0.89	0.95	1.19	0.94	0.83	1.27	0.75	1.52
<i>Humid</i>	1.29	0.95	0.91	0.97	0.93	0.47	0.80	0.90	1.17	1.04	0.96	0.34	1.03	0.74	1.14
<i>All regions</i>	1.42	0.95	1.37	1.15	0.89	0.90	0.93	0.89	1.03	1.16	0.94	0.76	1.15	0.92	0.82

Note: Bold and italic values indicate the method with the best performance.

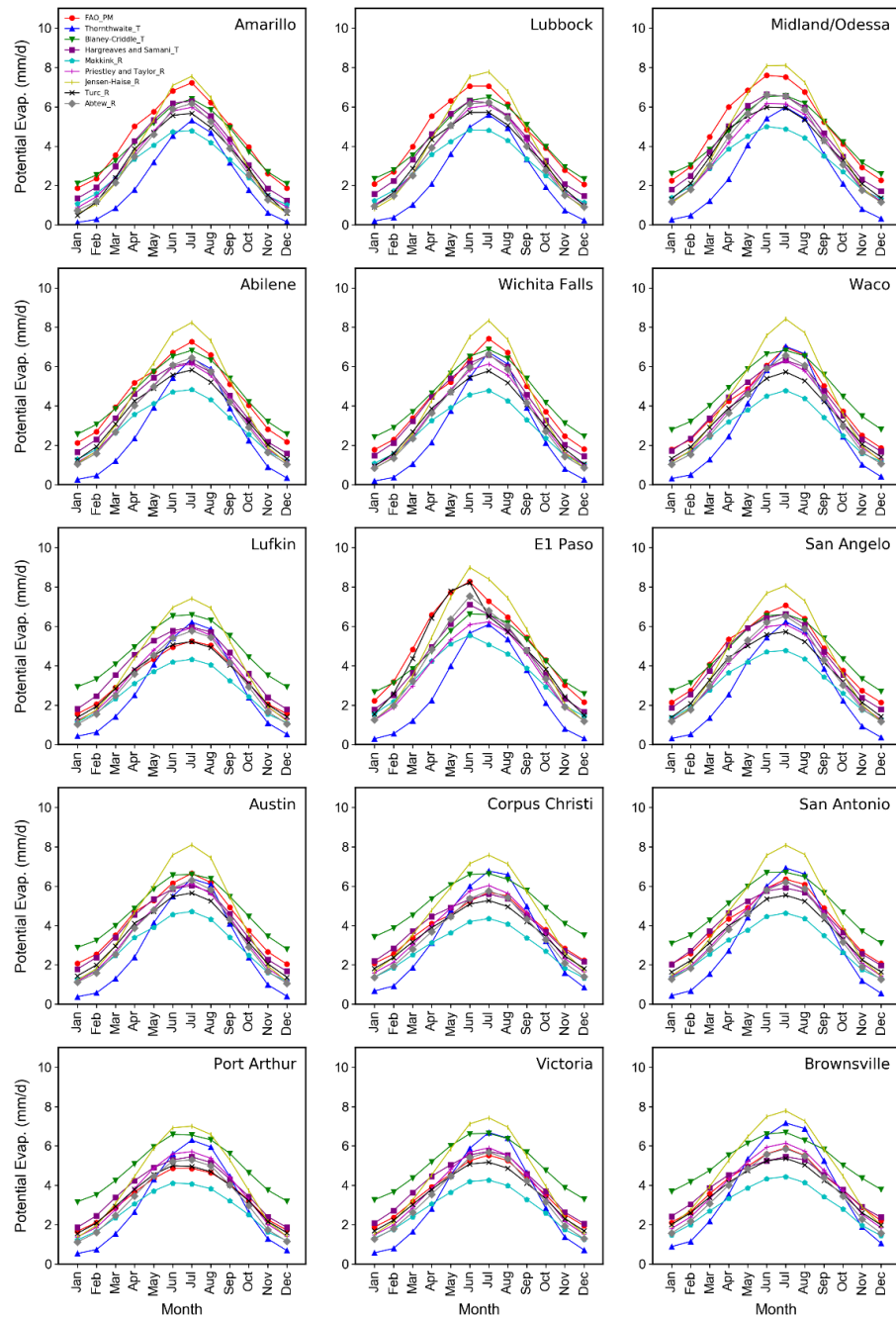


Figure 5.2 Comparison of mean monthly ET_0 simulated by different models using the original constants.

5.3.2. Calibration of Constant Values

The values of recalibrated parameters for each station and method are shown in Tables 5.6 and 5.7. Expected differences are found at different stations for the same method. The differences between climate regions were larger than that between stations in the same climate regions, and, in general, higher parameters values were observed in more arid climates, indicating that relative humidity significantly affected the parameters. Spatial variabilities of the parameters in the subhumid subtropical and semi-arid climates were significant.

All the methods performed better after calibration with the mean annual RE kept within 10% except the Th_T and JH_R methods (Figure 5.3). The Ma_R method performed the best (with the lowest RMSE) at most stations after calibration, followed by the Tu_R and HS_T methods (Figure D2, Tables D3, and D4, Appendix D). The great improvement of the Ma_R method is attributed to the two empirical coefficients used, which can be easily adjusted to reflect the impact of both radiative and aerodynamic components on ET_0 changes. One drawback is that the Ma_R method should be properly calibrated using local weather data, which limits its use in regional analysis. After calibration, the radiation-based methods, e.g., PT_R, JH_R, and Ab_R, still show large underestimation in arid and semi-arid climates, which indicate the relative contribution of solar radiation to ET_0 is not a constant. Moreover, the underestimation is more significant during cool and transition seasons, suggesting that the radiative components play a less role in driving changes in ET_0 in a relatively cold environment.

Table 5.6 Comparison of the Temperature-based Methods Parameters before and after Calibration.

Stations	Thornthwaite_T		Blaney-Criddle_T		Hargreaves and Samani_T	
	Original	Calibrated	Original	Calibrated	Original	Calibrated
<i>Semi-arid climate</i>						
S1	c=16	<u>25.27±0.70</u>	k=1	1.09±0.01	a=0.0023	0.0027±0.0000
S2		23.94±0.70		<u>1.07±0.01</u>		<u>0.0026±0.0000</u>
S3		<u>23.81±0.67</u>		1.10±0.01		0.0027±0.0000
S4		<u>20.97±0.58</u>		<u>1.01±0.01⁺</u>		<u>0.0026±0.0000</u>
S9		<u>20.84±0.56</u>		<u>0.99±0.01⁺</u>		<u>0.0024±0.0000</u>
Average		22.97		1.05		0.0026
<i>Arid climate</i>						
S8		24.16±0.75		<u>1.14±0.01</u>		0.0027±0.0000
<i>Subhumid subtropical</i>						
S5		<u>19.88±0.51</u>		<u>0.96±0.01</u>		<u>0.0025±0.0000</u>
S6		<u>17.74±0.43</u>		<u>0.89±0.01</u>		<u>0.0024±0.0000</u>
S10		<u>18.89±0.54</u>		<u>0.91±0.01</u>		<u>0.0025±0.0000</u>
S12		16.82±0.43		0.85±0.01		0.0023±0.0000 ⁺
Average		18.33		0.90		0.0024
<i>Humid subtropical</i>						
S7		15.62±0.38 ⁺		<u>0.73±0.01</u>		<u>0.0020±0.0000</u>
S11		<u>15.23±0.37</u>		<u>0.77±0.01</u>		0.0023±0.0000 ⁺
S13		<u>14.68±0.37</u>		<u>0.70±0.01</u>		<u>0.0021±0.0000</u>
S14		<u>15.28±0.38</u>		<u>0.76±0.01</u>		<u>0.0021±0.0000</u>
S15		<u>14.71±0.32</u>		<u>0.78±0.01</u>		0.0023±0.0000 ⁺
Average		15.10		0.75		0.0022
All stations mean		19.18		0.92		0.0024

Note: (1) + indicates the original value lies in the 95% confidence interval of the parameter values. (2) underline means there is a significant difference from the regionally mean value, i.e., the mean value does not lie in the 95% confidence interval of the parameter for that station.

Table 5.7 Comparison of the Radiation-based Methods Parameters before and after Calibration.

Stations	Makkink_R		Priestley Taylor_R		Jensen-Haise_R		Turc_R		Abtew_R	
	O	C	O	C	O	C	O	C	O	C
<i>Arid or semi-arid area</i>										
S1	a=0.61	a=0.86±0.02; b=0.14±0.10	1.26	1.58±0.02	0.025	0.027± 0.000	0.0133	0.0172±0 .0002	56	44.1±0.6
S2	b=-0.12	a=0.86±0.02; b=0.17±0.10		1.56±0.02		0.026± 0.000		0.0169±0 .0002		45.2±0.6
S3		a=0.93±0.02; b=-0.11±0.10		1.62±0.02		0.026± 0.000		0.0169±0 .0001		45.6±0.5
S4		a=0.86±0.02; b=0.10±0.10*		1.53±0.02		0.024± 0.000		0.0166±0 .0001		46.5±0.5
S9		a=0.87±0.02; b=-0.06±0.09*		1.50±0.02		0.024± 0.000		0.0162±0 .0001		48.7±0.5
Average		a=0.88; b=0.04		1.56		0.025		0.0167		46.0
S8		a=0.91±0.01; b=-0.22±0.09		1.67±0.02		0.025± 0.000 ⁺		0.0142±0 .0001		47.4±0.5
<i>Subhumid subtropical</i>										
S5		a=0.89±0.02; b=-0.05±0.10*		1.51±0.02		0.024± 0.000		0.0165±0 .0001		47.8±0.5
S6		a=0.85±0.02; b=-0.11±0.09		1.40±0.02		0.022± 0.000		0.0156±0 .0001		50.4±0.5
S10		a=0.81±0.02; b=0.19±0.10		1.43±0.02		0.022± 0.000		0.0156±0 .0001		49.6±0.6
S12		a=0.79±0.01; b=0.11±0.07		1.34±0.01		0.021± 0.000		0.0151±0 .0001		51.5±0.5
Average		a=0.84; b=0.04		1.42		0.022		0.0157		49.8
<i>Humid subtropical</i>										
S7		a=0.70±0.01; b=0.12±0.05		1.18±0.01		0.019± 0.000		0.0133±0 .0001 ⁺		57.6±0.5
S11		a=0.71±0.01; b=0.38±0.08		1.25±0.01 ⁺		0.020± 0.000		0.0143±0 .0001		52.9±0.5
S13		a=0.67±0.01; b=0.24±0.05		1.15±0.01		0.019± 0.000		0.0131±0 .0001		56.5±0.6 ⁺
S14		a=0.73±0.01; b=0.19±0.07		1.24±0.01		0.020± 0.000		0.0141±0 .0001		54.0±0.5
S15		a=0.75±0.01; b=0.16±0.07		1.24±0.01		0.020± 0.000		0.0142±0 .0001		53.3±0.4
Average		a=0.71; b=0.06		1.21		0.020		0.0138		54.9
All regions mean		a=0.81; b=0.08		1.41		0.023		0.0153		50.0

Note: O indicates original parameters, and C indicates calibrated parameters.

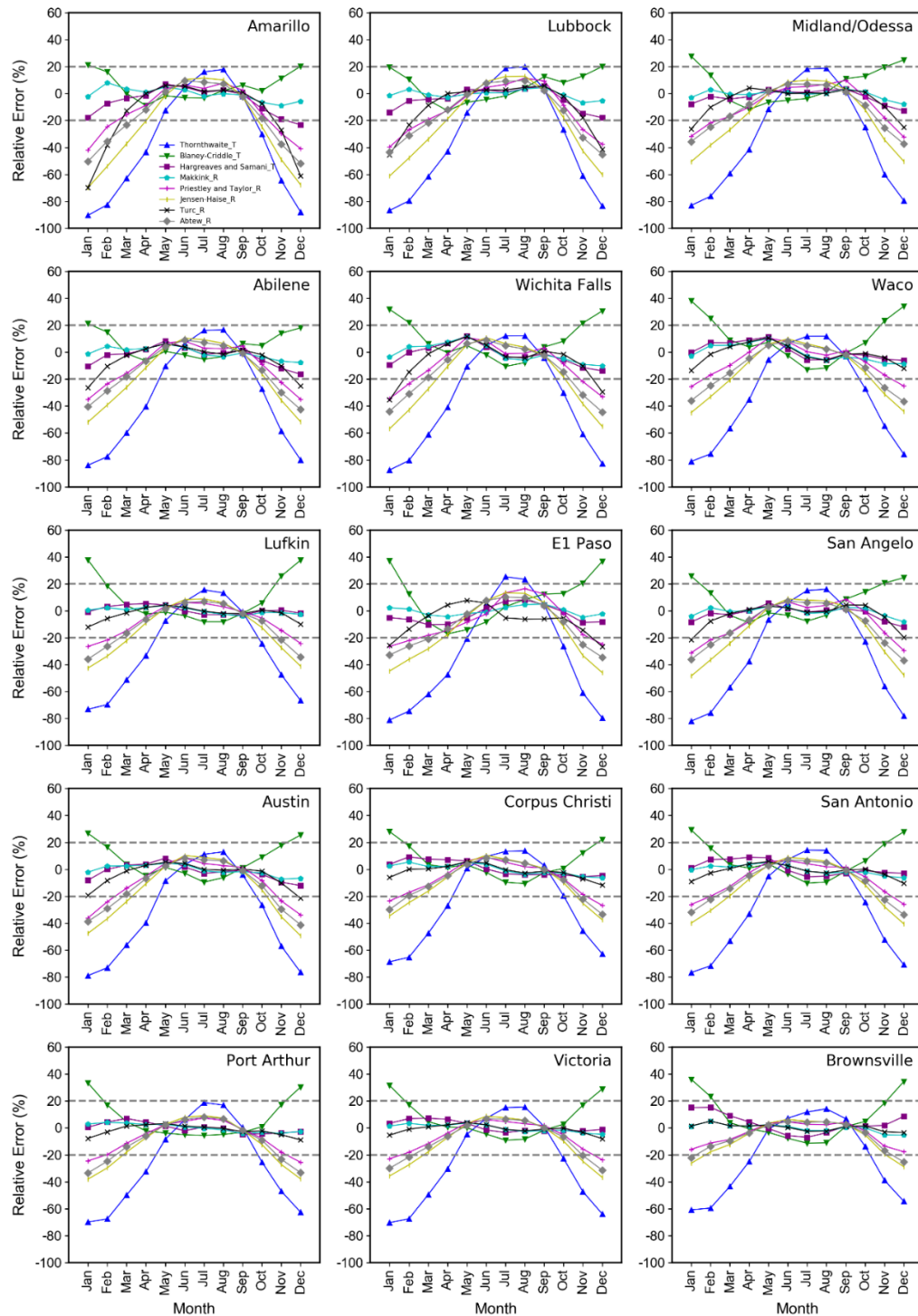


Figure 5.3 Comparison of mean monthly potential evapotranspiration simulated by different methods using the calibrated constant values.

5.3.3. Method Verification

The method verification was carried out at three stations, i.e., S3, S6, and S14, representing different climatic conditions. The split record method was used to analyze the sensitivity of the parameters to model performance (Klemes, 1986; Singh and Xu, 1997). The data set was split into two periods, i.e., 1961-1990 and 1991-2010. The eight selected methods were calibrated separately for these two periods. The calibrated parameters for one period were used as the prediction of the other period. The purpose was to test the method's ability to the monthly prediction of ET_0 for an independent period. As shown in Figure 5.4, the performance of the method in estimating ET_0 in an independent period was acceptable, except for the Th_T method. For the months with higher ET_0 (April to September), the relative errors were all within $\pm 20\%$. In contrast, the radiation-based methods had high relative errors, which was close to -40% in cool months. In general, once the method was calibrated using historical data of a station, it can be used to predict ET_0 in the future for the same station with sufficient confidence.

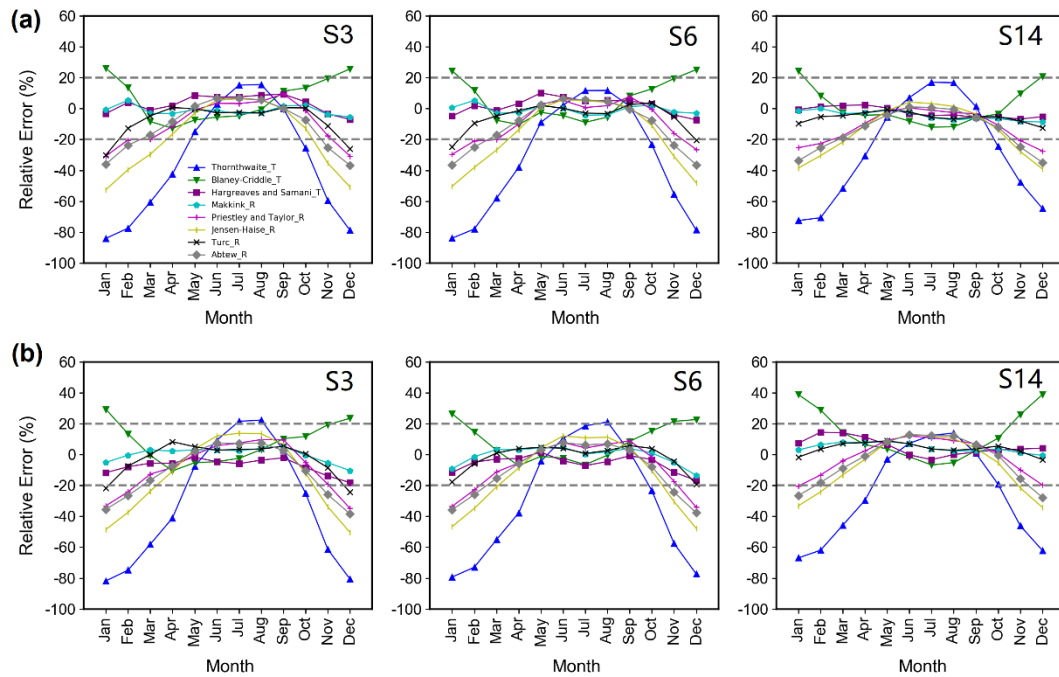


Figure 5.4 Relative errors of mean monthly reference evapotranspiration estimates of each model at three stations. The top panel shows the simulation from 1991 to 2010, and the bottom panel shows the simulation from 1961 to 1990.

5.3.4. Regionalization

The calibrated regional average of parameter values for the eight models was used for ET_0 estimation at the fifteen stations. Figure 5.5 shows a comparison of using one set of parameters for all climates (one region) and two different sets of parameters (two regions), including one for arid/semi-arid climates (stations in climate division 1 and 5, Figure 5.1) and one for humid/subhumid climates (stations in other climate divisions, Figure 5.1). It is obvious that more accurate estimates can be obtained if calibration can be done for each climate type, and the lowest mean relative error was observed when three regions were considered, including humid climate, subhumid, and

arid/semi-arid climates, as shown in Figure D3, Appendix D. Even with the calibrated mean of all stations (one region), the HS_T ($a=0.024$) and Ma_R ($a= 0.81$, and $b=0.09$) methods can produce acceptable levels of confidence in all climates types in all seasons. Tu_R worked well for regional analysis in humid, subhumid, and warm seasons in arid and semi-arid climates. All calibrated methods showed better performance in the warm season than in the transition and cool seasons for regional analysis, and larger errors were found under dry and windy conditions. Generally, air temperature measurements are more reliable than the other three parameters required by the FAO-PM method. Moreover, the default value of the HS_R method is more stable than the Ma_R method. Taken together, the Hargreaves-Samani (HS_T) method is recommended for regional analysis if reliable wind speed and relative humidity data are not available. Calibration with the FAO-PM method is suggested in regions with dry and consistently windy conditions.

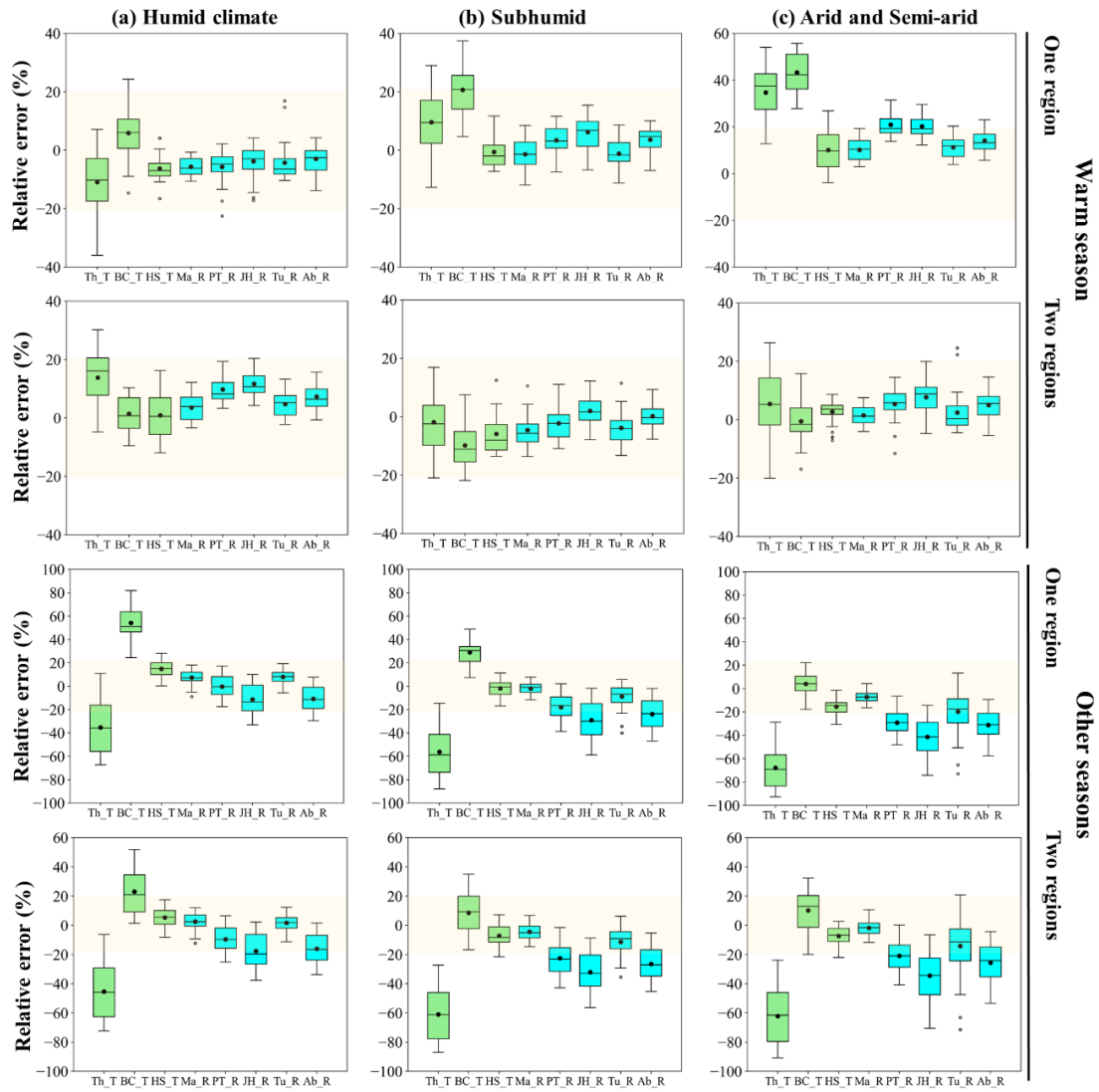


Figure 5.5 Relative error of mean monthly reference evapotranspiration estimates of each model using regional average parameters in (a) humid (b) subhumid and (c) semiarid/arid climates from 1961 to 2010. Boxplots show the 25th, 50th, 75th percentiles, and extremes. Shading is the relative error within 20%. One region indicates that the parameters are the same for (a), (b), and (c), and two regions indicate that (a) and (b) use the same parameters and (c) uses another parameter.

5.4. Discussion

5.4.1. Sensitivity Analysis

The contributions of available energy (A), vapor pressure deficit (D), and aerodynamic resistance (r_a) to the variations of ET_0 at each station in different seasons are shown in Figure 5.6. The available energy is the driving factor of ET_0 , accounting for 51%-84% of the variability in ET_0 (Figure 5.6a). The contribution of available energy to ET_0 varies greatly in different climate regions, and the seasonality difference is more significant than the spatial differences. In warm season, available energy accounted for 84%, 77%, 72%, and 73% of the variability in ET_0 in humid, subhumid, semiarid, and arid climates, respectively. The contributions of available energy to ET_0 were smaller during the cool season as compared with the warm season in all climates, e.g., 68% (humid), 58% (subhumid), 51% (semiarid), and 57% (arid), indicating that a general increase in S_A when air temperature increases. Remember that the PT_R method assumes $S_A = 79.4\%$, $S_D = 1 - S_A = 20.6\%$, and $S_{ra} = 0$. With this assumption, the radiative component was about four times the aerodynamic component. As shown in Figure 5.6b, the vapor pressure deficit had relatively higher impacts on the ET_0 variation in more dry regions and cool seasons, e.g., S_D was 27-28% in the warm season in semiarid and arid climates and can be as high as 43-49% in the cool season in subhumid, semiarid, and arid climates. Hence, methods linking ET_0 with the available energy performed well in the warm season in humid and subhumid climates, and local calibration was usually required under other conditions.

The assumption of the aerodynamic resistance impacts on ET_0 variations was equal to zero, i.e., $S_{ra} = 0$, which is invalid for most stations, leading to the underestimation in most methods even after calibration, especially in the semi-arid and arid climates under strong wind conditions. The effect of wind on ET_0 is not unique due to the differences in the interaction of wind with other climatic factors under different climate conditions. The energy, heat, and vapor transfer rate of the grass reference surface and the surrounding environment are more similar in humid and subhumid climates than in semiarid and arid climates. Accordingly, the effect of regional advection on ET_0 was usually minor under humid conditions. For example, S_{ra} in humid climate was only 4%, 3%, and -2% in warm, transition, and cool seasons, respectively. The negative value in S_{ra} indicated that increasing r_a (or decreasing wind speed) led to a reduction in ET_0 . As shown in Figure 5.6c, wind speed had negative impacts on ET_0 in warm and transition seasons in humid climates due to cool air advection, and the impacts were slightly enhanced with increased wind speed. However, drier air generally had a higher vapor pressure gradient. In addition, wind speed affected the sensible heat transfer from the vast dry, unirrigated area and contributed part of the energy required for evapotranspiration through warm air advection. Hence, S_{ra} in arid climate showed consistently high values (10%-16%) in all seasons even under moderate wind conditions. In semiarid climate, S_{ra} can keep at 4%-6% in warm and transition seasons and rise to 12% in the cool season under strong wind conditions.

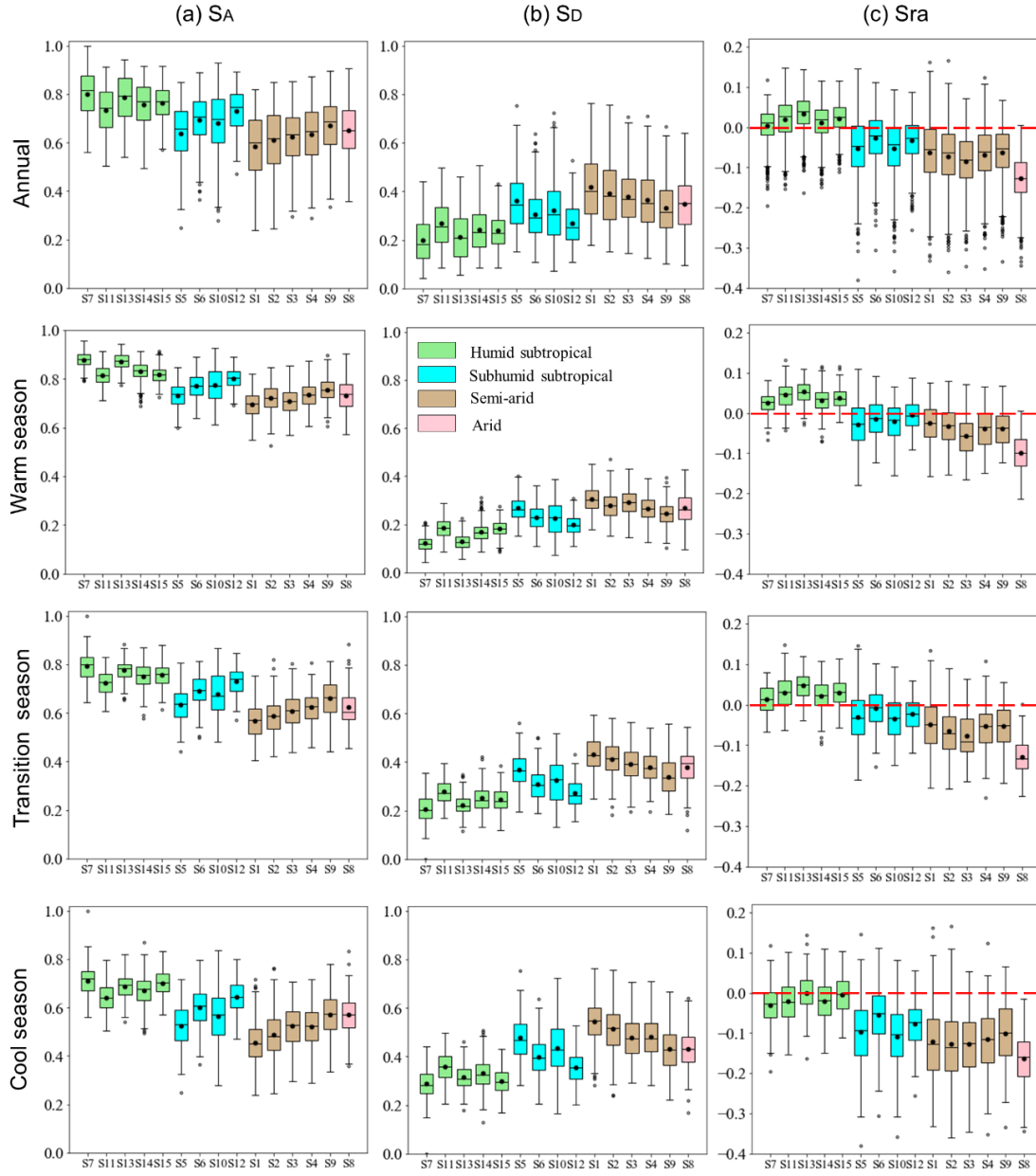


Figure 5.6 Variations of sensitivity coefficients for monthly potential evapotranspiration for (a) available energy (A), (b) vapor pressure deficit (D), and aerodynamic resistance (r_a) at each station from 1961 to 2010. Boxplots show the 25th, 50th, 75th percentiles, and extremes.

Sensitivity analysis of S_A and S_{u2} to changes in meteorological variables was performed by increasing or decreasing an individual variable while holding the other variables constant (Figures 5.7 and 5.8). The ranges of different variables were selected according to their maximum and minimum values recorded during the period of 1961–2010 in the study area. An exponential relationship between mean air temperature and available energy was developed, i.e., $A = 3.4635e^{0.0509T}$, using the data during the period of 1961–2010 with $R^2 = 0.81$. Based on the mean air temperature and relative humidity, four climate regions were classified, including humid/cold, humid/warm, dry/cold, and dry/warm. S_A was sensitive to RH , mean temperature, and wind speed. S_{u2} was more sensitive to RH and wind speed within 0–4 m/s. Stronger wind conditions ($U_2 > 4$ m/s) did not necessarily lead to an increase in the wind speed impact on S_{u2} variations. The equilibrium or quasi-equilibrium evaporation condition, i.e., $S_{u2}=0$, existed within RH between 65% and 75%, and RH under the equilibrium condition showed a decreasing trend with the increase of air temperature (Figure 5.8). At 20°C, the relative humidity under equilibrium or quasi-equilibrium evaporation condition (RH^*) was about 70%, which is consistent with the value ($RH^* = 70\% \pm 6\%$, $n=437$) calculated by selecting the weather variable during 1961–2010 that satisfied the equilibrium or quasi-equilibrium evaporation condition, i.e., S_{ra} is close to 0. With $RH^* = 70\%$, $T = 20^\circ\text{C}$, and $U_2 = 2$ m/s, a S_A value of 0.8 was obtained from Figure 5.7, which is the same as the value suggested by McNaughton and Jarvis (1983) to analyze the relative effects of the radiative component on the evapotranspiration process with advection having the least effect.

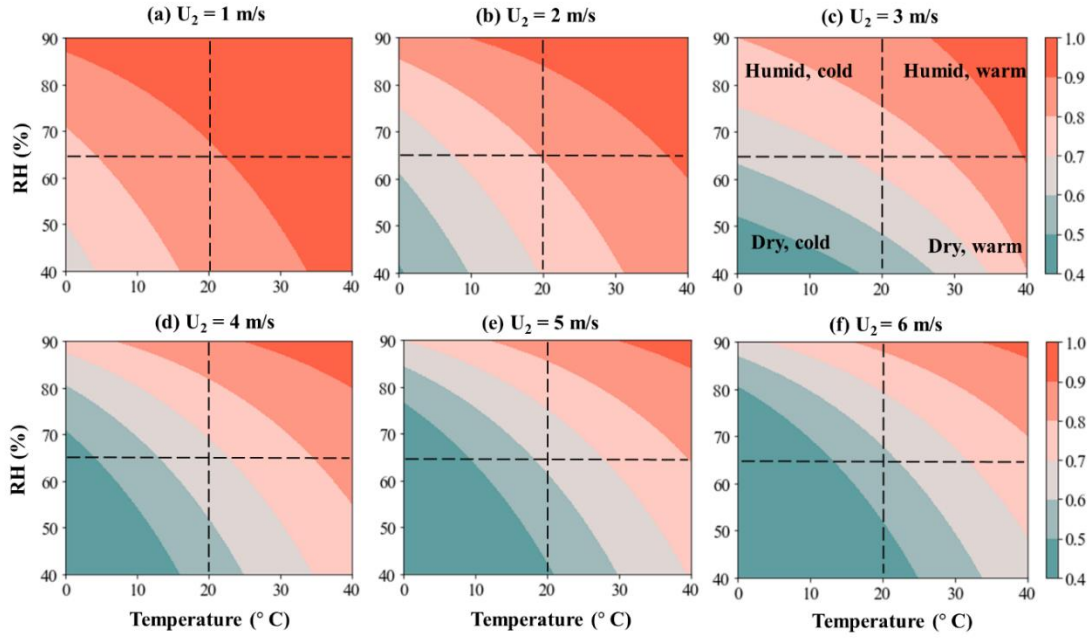


Figure 5.7 Variations of sensitivity coefficient of available energy to the reference evapotranspiration under different climate conditions.

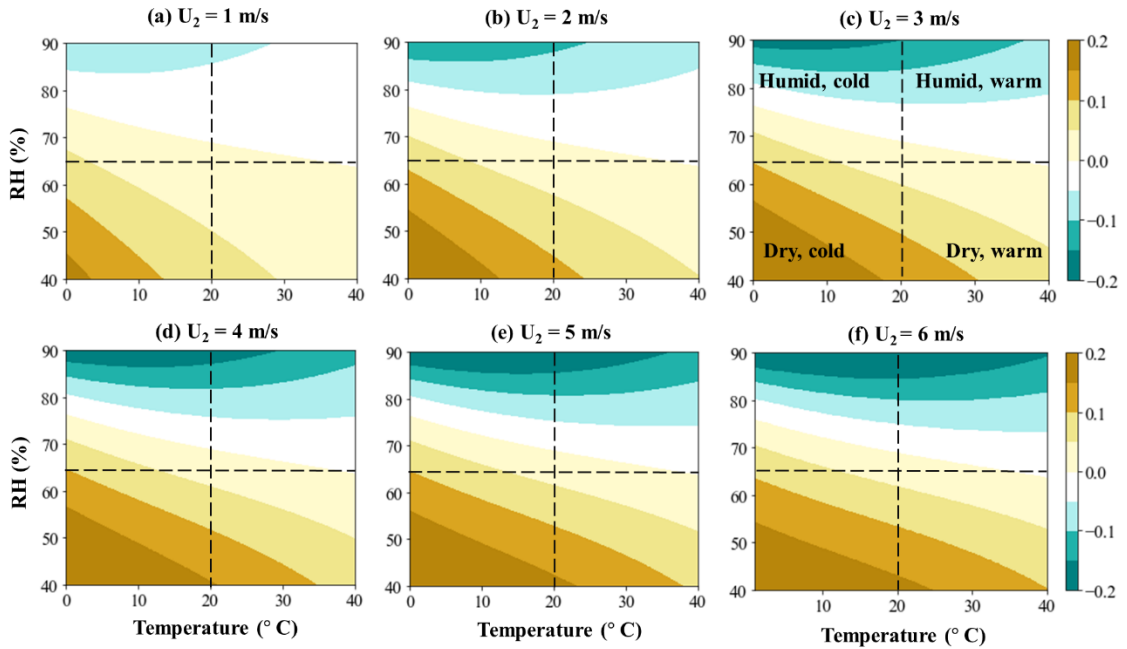


Figure 5.8 Variations of the sensitivity coefficient of wind speed to the reference evapotranspiration (S_{u2}) under different climate conditions. Note $S_{u2} = -S_{ra}$.

5.4.2. Temperature Impacts on ET_0 Variations

In the FAO-PM method, mean air temperature has an indirect impact on ET_0 , considering temperature affects the slope of the vapor pressure curve and the vapor pressure deficit. As shown in Figure 5.9, temperature is very sensitive to ET_0 variations, and a 10% increase in temperature can lead to about a 13-14% increase in ET_0 in the warm season, 9-12% in the transition season, and 5-9% in the cool season. The relative sensitivity coefficient of temperature on ET variation has a significant positive linear trend of $0.05/^\circ\text{C}$, with $R^2 = 0.99$. Results indicated that the temperature impact on ET_0 variations would be intensified in a warming climate, resulting in greater atmospheric demand.

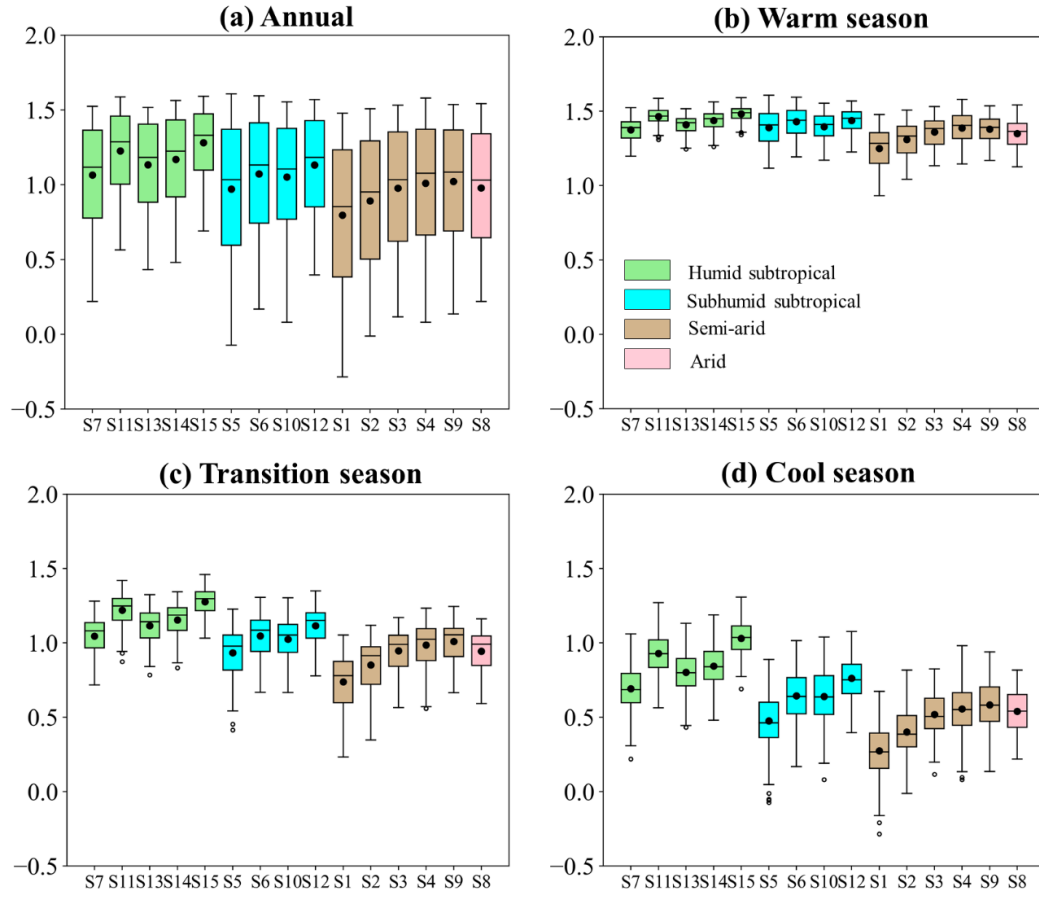


Figure 5.9 Sensitivity coefficients for the monthly reference evapotranspiration for mean temperature at each station from 1961 to 2010. Boxplots show the 25th, 50th, 75th percentiles, and extremes.

5.4.3. Adjustment for Dry and Windy Conditions

Since HS_T is the best method selected for regional analysis and PT_R is the most theoretically based radiative method, these two methods were adjusted to improve their performance under arid, high wind conditions. The impact of vapor pressure deficit change on the ET_0 can be estimated by assuming there were no changes in other parameters, then $ET_{adjust} = ET_0 [1 + (S_D) \frac{D-D^*}{D^*}]$, where D^* is the vapor pressure deficit

under the equilibrium condition. Since vapor pressure deficit can be calculated by $(1 - RH) e_s$. The term $\frac{D-D^*}{D^*}$ can be approximated by $\frac{RH^*-RH}{100-RH^*}$ assuming that there is little change in the mean temperature under the two conditions. RH^* is the relative humidity at the equilibrium value in percentage. Then, one gets $ET_{adjust} = ET_0 [1 + (S_D) \frac{RH^*-RH}{100-RH^*}]$. Under the equilibrium condition, $S_D = 1 - S_A = 0.2$, $RH^* = 70\%$, then $ET_{adjust} = ET_0 [1.47 - 0.0067RH]$. Under strong wind conditions ($u > 3$ m/s), the impact of wind effect on S_D can be approximated as $\frac{\partial(S_D)}{\partial\Omega} \frac{\partial(\Omega)}{\partial U_2} \frac{U_2}{S_D} = (-1)(S_A^2 - S_A) \frac{1}{(1-S_A)} = S_A$, then $ET_{adjust} = ET_0 [1 + (S_D)(1 + S_A) \frac{RH^*-RH}{1-RH^*}] = ET_0 [1.84 - 0.012RH]$.

Figure 5.10 shows the results of using adjustment coefficient for strong wind conditions $c = 1.84 - 0.012RH$. Both methods showed better performance than the local calibration and original methods, especially for the stations under dry and strong windy conditions, including S1, S2, S3, and S9. It was noted that S8 (the station with the lowest RH, i.e., 40%) had a relatively higher RMSE (0.82 mm/d) than the local calibration method (0.66 mm/d). Considering that S8 had light to moderate wind (2.7 ± 0.6 m/s), the adjustment coefficient without the correction for strong wind conditions, i.e., $c = 1.47 - 0.0067RH$, was also tested, and the RMSE was reduced to 0.40 mm/d.

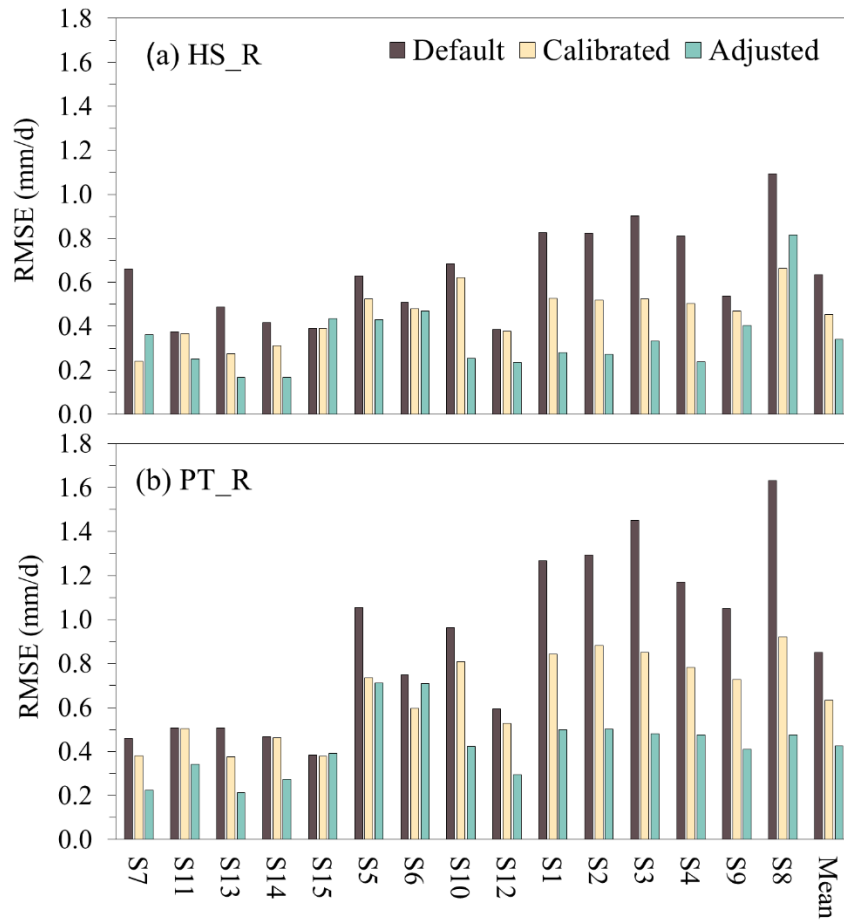


Figure 5.10 Comparison of mean monthly RMSE of ET_0 using (a) HS_T and (b) PT_R at 15 stations with the default method, calibrated method, and adjusted method.

5.5. Conclusions

In this chapter, the eight commonly used ET_0 methods were selected, including three temperature-based methods, i.e., Thornthwaite, Blaney-Criddle, and Hargreaves and Samani, and five radiation-based methods, i.e., Makkink, Priestley-Taylor, Jensen and Haise, Turc, and Abtew, to compare with the FAO-PM reference method in humid, subhumid, with various climatic types including arid, semi-arid, and humid tropical in

Texas, United States using 50 years (1961-2010) monthly meteorological data from 15 climatological stations. The impact of each climatic variable on the seasonal and spatial variations of ET_0 were further quantified to help understand the model structure and improve its performance under dry and windy conditions. The major findings of this study are: (1) HS_T is the most accurate empirical method used to estimate ET_0 with the default value and is suggested for regional analysis; (2) radiative component is the driving factor of ET_0 , accounting for 51%-84% of the variability in ET_0 ; and (3) to correctly reflect the impact of aerodynamic components on the ET_0 estimation under dry and windy conditions, a calibration-free coefficient ($c = 1.47 - 0.0067RH$) with only month relative humid (RH) as input is suggested to multiply the HS_T and PT_R equations and improved accuracy was obtained compared with the local calibration methods. This study has implications for understanding the ET_0 variation under a changing climate.

6. A CALIBRATION-FREE PRIESTLEY-TAYLOR METHOD FOR REFERENCE EVAPOTRANSPIRATION ESTIMATION

The Priestley-Taylor (PT) method represents the equilibrium rate of potential evapotranspiration (PET) from an extensive water surface or well-watered crop surface without considering the impact of advection. It has been widely applied in hydrological and crop models to calculate the atmospheric demand for water or reference evapotranspiration (ET_0). However, the current use of the default value of PT coefficient (*i.e.*, $\alpha = 1.26$) cannot assure reliability under different climatic regions without local calibration using the Penman-Monteith method. In addition, the spatial and temporal evolution of the PT coefficient at a global scale and how meteorological variables affect its change have not been elucidated in previous studies. In this chapter, an analytical expression for the PT coefficient (PT_a) is derived following the Penman-Monteith method, *i.e.*, $PT_a = \frac{1}{S_A} (1 + S_{U_2})$, where S_A represents the radiative component impact on ET_0 and S_{U_2} is wind speed impact on ET_0 . The daily Princeton Global Forcing (PGF) dataset with a spatial resolution of 0.25° by 0.25° and temporal coverage from 1948-2016 was used to validate the derived PT coefficient, indicating that using PT_a well simulates the spatial distribution and temporal variations of global reference evapotranspiration. The global mean PT_a from 1948 to 2016 was 1.37, with a temporal standard deviation of 0.02 and a spatial standard deviation of 0.42. Under equilibrium conditions, PT_a , however, was very close to the default value, *i.e.*, 1.26 ± 0.04 . The use of the simplified PT coefficients with relative humidity (RH, in fraction) as the only input

under slight to moderate ($PT_a = 1.87 - 0.87RH$) and strong wind ($PT_a = 2.35 - 1.55RH$) conditions also showed good performance. The radiative component is the driving factor of ET_0 changes and tends to be intensified in a warming climate. Although aerodynamic components show reinforced impacts on global reference evapotranspiration, the widely declined wind speed slightly counteracts the ET_0 increase caused by the increased radiative components.

6.1. Introduction

The Priestley-Taylor (PT) method represents the equilibrium rate of potential evapotranspiration (PET) from an extensive water surface or well-watered crop surface without considering the impact of advection. The PT method has been widely used in hydrological models, e.g., Soil and Water Assessment Tool (SWAT) (Arnold et al., 2012) and Soil Water Atmosphere Plant (SWAP) (van Dam et al., 2008), representing the upper limit of evapotranspiration (ET). The PT method has numerous applications in crop models to estimate reference ET (ET_0) and irrigation water demand by multiplying crop coefficients (Constantin et al., 2015; Deryng et al., 2011; Dzotsi et al., 2015; Hoogenboom et al., 2019; Jones et al., 2003; Keating et al., 2003). The PT coefficient ($\alpha = 1.26$) represents the ratio of potential evapotranspiration to equilibrium evaporation (the radiative term of the Penman method), which is obtained by averaging several field measurements over vegetated and water surfaces (Priestley and Taylor, 1972). The default value has been adopted in many crop models, e.g., Aqyield (Constantin et al., 2015), DSSAT (Hoogenboom et al., 2019; Jones et al., 2003), PEGASUS (Deryng et al., 2011), and SALUS (Dzotsi et al., 2015), and global PET

products like the Priestly-Taylor Jet Propulsion Laboratory algorithm (PT-JPL) (Fisher et al., 2008). A changing PT coefficient is also used. For example, in APSIM, α ranges from 0.3 at 0°C to 2.1 at 55°, while $\alpha = 1.1$ is for temperature between 6 and 35.6°C (Keating et al., 2003). The Global Land Evaporation Amsterdam Model (GLEAM) (Miralles et al., 2011) assumes that the PT coefficient varies with land cover. Kimball et al. (2019) compared actual ET from 29 maize models and indicated that ET_0 estimation was one of the major sources of uncertainties in estimating irrigation water demand.

Numerical field observations and analytical expressions have reported that the PT coefficient is very close to 1.26 under wet or well-watered grass surface conditions (Davies and Allen, 1973; Eichinger et al., 1996; Parlange and Katul, 1992). Jarvis and McNaughton (1986) introduced the decoupling coefficient (Ω), which was equal to α^{-1} , to analyze the relative contribution of solar radiation and aerodynamic terms to the evapotranspiration process, with $\Omega=0.8$ ($\alpha=1.25$) on average (McNaughton and Jarvis, 1983). Eichinger et al. (1996) derived an analytical expression of α using Bowen ratio and found that $\alpha = 1.26$, which was insensitive to small variations in temperature or humidity. Field observations from irrigated grass suggested that the value of a was typically ranging from 1.20 to 1.27 in the absence of advection under different climate types (Katerji et al., 1990; Pereira, 2004).

On the other hand, Lhomme (1997) used the closed-box model of the convective boundary layer and demonstrated that α was a function of atmosphere conditions and aerodynamic resistance rather than a constant. He also reported that $\alpha = 1$ for saturated surface surrounded by water and $\alpha = 1.3$ for saturated grass surrounded by well-watered

grass. In semi-arid or arid regions, as the wet surface requirement, i.e., the surface is extensive and continually saturated, usually cannot be satisfied, the aerodynamic component is relatively important (Matsoukas et al., 2011), and warm air advection from unirrigated areas often contribute sensible heat energy to evapotranspiration. Consequently, the use of the default value usually underestimates the ET_0 calculation in sub-humid (Nandagiri and Kovoov, 2006), semi-arid (Bakhtiari et al., 2011; Er-Raki et al., 2010; Gao et al., 2017; Nandagiri and Kovoov, 2006; Tabari, 2010) and arid (Didari and Ahmadi, 2019) climates, since it does not adequately consider the aerodynamic term. Although local calibration with the Food and Agriculture Organization (FAO) Penman-Monteith method (FAO-PM) is usually suggested, the reported values after calibration always show significant spatial and seasonal variability. For example, Shiri et al. (2019) reported that the calibrated PT coefficient ranged between 1.01-1.13, 1.25-1.78, and 1.18-1.75 in humid, semi-arid, and arid climates, respectively, according to the evaluation on 29 weather stations in Iran. A recent global calibration of the PT coefficient, which used monthly weather data from 1948 to 2006 at 0.5° horizontal resolution, showed that the global PT coefficient ranged from 0.52 to 2.96, with a mean value of 1.26 (Aschonitis et al., 2017). Therefore, a calibration-free PT method for ET_0 estimation is of special interest given its ubiquitous use in global PET products, hydrological, and crop models which use the PT method for ET_0 estimation. In addition, the spatial and temporal evolutions of the PT coefficient at global scales and how meteorological variables affect its change have not been elucidated in previous studies.

The objectives of this study aimed to (1) derive an analytical expression for the PT coefficient based on the Penman-Monteith method; (2) reveal the spatial and temporal evolutions of the PT coefficient at global scales; and (3) provide a simplified calibration-free PT coefficient with relative humidity as the only input. The daily Princeton Global forcing (PGF) dataset with a spatial resolution of 0.25° and temporal coverage from 1948-2016 was used to validate the derived PT coefficient and characterize its spatial and temporal variations.

6.2. Methodology

6.2.1. Derivation of the Priestley-Taylor Method Following the Penman-Monteith Method

The original Penman-Monteith method can be rearranged as:

$$ET_{PM} = \frac{1}{\lambda} \frac{\frac{\Delta}{\Delta+\gamma} A + \frac{\gamma}{\gamma+\Delta} \frac{\rho_a C_p D}{r_a}}{1 + \frac{\gamma}{\gamma+\Delta} \times \frac{r_s}{r_a}} \quad (6.1)$$

where ET_{PM} is the potential evapotranspiration from well-watered vegetated surfaces (mm d^{-1}); λ is the latent heat of vaporization of water (MJ kg^{-1}); $A = R_n - G$, where R_n is the net radiation at the crop surface ($\text{MJ m}^{-2} \text{d}^{-1}$), and G is the soil heat flux ($\text{MJ m}^{-2} \text{d}^{-1}$); $D = e_s - e_a$, in which e_s and e_a are the saturation and actual vapor pressure (kPa), respectively; r_a is the aerodynamic resistance (s m^{-1}); r_s is the surface resistance (s m^{-1}); Δ is the slope of vapor pressure curve ($\text{kPa } ^\circ\text{C}^{-1}$); γ is the psychrometric constant ($\text{kPa } ^\circ\text{C}^{-1}$); ρ_a is the mean air density under constant pressure (kg m^{-3}); and C_p is the specific heat of moist air ($1.013 \text{ kJ kg}^{-1} ^\circ\text{C}^{-1}$). Detailed calculations of each parameter can be found in Appendix D.

As shown in equation (6.1), two processes affect potential evapotranspiration from a vegetated surface. The first process is related to the climatic parameters, determining the evaporative demand ET^* , i.e., evaporation from free water surface or saturated crop surface. ET^* is calculated based on the combination of energy balance and water vapor transfer, where ET_{eq} represents the equilibrium evaporation, mm/d, and ET_D is the aerodynamic terms determined by D and r_a .

$$ET_{PM} = \frac{ET^*}{1 + \frac{\gamma}{\gamma + \Delta} \times \frac{r_s}{r_a}} = \frac{ET_{eq} + \frac{\gamma}{\Delta + \gamma} ET_D}{1 + \frac{\gamma}{\gamma + \Delta} \times \frac{r_s}{r_a}} \quad \text{with } ET_{eq} = \frac{1}{\lambda} \frac{\Delta}{\Delta + \gamma} A \quad \text{and } ET_D = \frac{\rho C_p D}{\lambda \gamma r_a} \quad (6.2)$$

The second process is related to vegetation characteristics, i.e., canopy resistance, r_s , which represents the obstacles of water vapor transfer between the surface and the reference height. The term $\frac{1}{1 + \frac{\gamma}{\gamma + \Delta} \times \frac{r_s}{r_a}}$ is defined as the decoupling coefficient (Ω) introduced by Jarvis and McNaughton (1986). Equation (6.1) can be rewritten as:

$$ET_{PM} = \Omega \times ET^* = \Omega \times ET_{eq} + (1 - \Omega) \times ET_D \quad \text{with } \Omega = \frac{1}{1 + \frac{\gamma}{\gamma + \Delta} \times \frac{r_s}{r_a}} \quad (6.3)$$

Crop surfaces can both affect A and r_a , e.g., the crop physical characteristics may influence A by regulating albedo and crop height and roughness may affect r_a , respectively. A hypothetical reference grass surface is used to reduce the impact of crop surface in the FAO-PM method. The reference grass has a height of 0.12 m, an albedo of 0.23, and a fixed surface resistance ($r_s = 70 \text{ s m}^{-1}$). Equation (6.1) can be rewritten as the FAO-PM method:

$$ET_0 = \frac{0.408 \Delta (R_n - G) + \gamma \frac{900}{T + 273} U_2 (e_s - e_a)}{\Delta + \gamma (1 + 0.34 U_2)} \quad (6.4)$$

where ET_0 is the reference evapotranspiration (mm d^{-1}); T and U_2 are the mean air temperature ($^{\circ}\text{C}$) and wind speed (m s^{-1}) measured at 2 m height, respectively; $r_a = 208/U_2$, $\frac{r_s}{r_a} = 0.34U_2$, and $\frac{\rho_a c_p}{r_a} = \gamma \frac{900}{T_a + 273} U_2$.

6.2.2. Sensitivity of Different Terms in the FAO-PM Method

In general, ET_0 can be written as:

$$ET_0 = f(p_1, p_2, p_3, \dots p_n) \quad (6.5)$$

where p_n is the n th model parameter. Then, the change in ET_0 can be attributed to the change in each parameter:

$$ET_0 + \Delta ET_0 = f(p_1 + \Delta p_1, p_2 + \Delta p_2, p_3 + \Delta p_3, \dots p_n + \Delta p_n) \quad (6.6)$$

Applying Taylor's theorem in equation (6.6) and ignoring the second-order terms, we can get:

$$\Delta ET_0 = \frac{\partial(ET_0)}{\partial p_1} \Delta p_1 + \frac{\partial(ET_0)}{\partial p_2} \Delta p_2 + \frac{\partial(ET_0)}{\partial p_3} \Delta p_3 + \dots \frac{\partial(ET_0)}{\partial p_n} \Delta p_n \quad (6.7)$$

The impact of changes in one parameter, e.g., p_i , on ET_0 changes can be estimated by assuming no changes in other parameters. Then

$$\frac{\Delta ET_0}{ET_0} = \frac{\partial(ET_0)}{\partial p_i} \frac{\Delta p_i}{ET_0} = \left(\frac{\partial(ET_0)}{\partial p_i} \frac{p_i}{ET_0} \right) \frac{\Delta p_i}{p_i} = S_i \frac{\Delta p_i}{p_i} \quad \text{with } S_i = \frac{\partial(ET_0)}{\partial p_i} \frac{p_i}{ET_0} \quad (6.8)$$

where S_i is defined as the non-dimensional relative sensitivity coefficient (McCuen, 1974). S_i can be used to evaluate the relative contributions of weather parameters on the dynamics of ET_0 , e.g., $S_i = 0.1$ means that a 10% increase in p_i leads to a 1% increase in ET_0 . The negative value of S_i indicates that increasing p_i leads to a decrease in ET_0 . The

sensitivity analysis of Penman and Penman-Monteith methods has already been provided (Beven, 1979; McCuen, 1974; Rana and Katerji, 1998). Here, the sensitivity coefficients of A , D , and r_a were evaluated based on the FAO-PM method as:

$$S_A = \frac{\partial(ET_0)}{\partial A} \frac{A}{ET_0} = \frac{1}{1 + \frac{\rho C_p D}{r_a \Delta A}} = \frac{1}{1 + \frac{\gamma}{\Delta} \frac{900}{T+273} U_2 \frac{D}{A}} \quad (6.9)$$

$$S_D = \frac{\partial(ET_0)}{\partial D} \frac{D}{ET_0} = \frac{1}{1 + \frac{r_a \Delta A}{\rho C_p D}} = \frac{1}{1 + \frac{D}{\Delta A \frac{900}{T+273} U_2}} = 1 - S_A \quad (6.10)$$

$$S_{r_a} = \frac{\partial(ET_0)}{\partial r_a} \frac{r_a}{ET_0} = S_A - \frac{1}{1 + \frac{\gamma}{\Delta} \frac{r_s}{r_a}} = S_A - \Omega \quad (6.11)$$

Since $r_a = 208/U_2$, the relative contributions of U_2 on the dynamics of ET_0 can be evaluated as:

$$S_{U_2} = \frac{\partial(ET_0)}{\partial r_a} \frac{\partial(r_a)}{\partial U_2} \frac{U_2}{ET_0} = -S_{r_a} = \Omega - S_A \quad (6.12)$$

As shown in Eq. (6.3-6.7), S_A , S_D , S_{r_a} and S_{u_2} depend on all the parameters, including the available energy, vapor pressure deficit, wind speed, and temperature.

6.2.3. Equilibrium Rate of Potential Evapotranspiration

The PT method estimates ET_0 based on the concept of equilibrium evaporation as:

$$ET_{PT} = \alpha ET_{eq} = \alpha \frac{\Delta}{\Delta + \gamma} \frac{R_n - G}{\lambda} \quad (6.13)$$

where ET_{PT} is the reference evapotranspiration calculated using the PT method (mm d^{-1}); α is the PT coefficient. To derive ET_{PT} from the FAO-PM method, we assume that the surface is extensive and continually saturated, and evapotranspiration is independent

of the aerodynamic component, i.e., $\frac{\partial \lambda ET_{PM}}{\partial r_a} = 0$. Imposing this condition in equation

(6.1), we get the “critical resistance”, γ^* :

$$\frac{\partial \lambda ET_{PM}}{\partial r_a} = \frac{\Delta \gamma A r_s - \rho_a C_p D (\Delta + \gamma)}{[r_a (\Delta + \gamma) + r_s \gamma]^2} = 0 \gg r_s = \frac{\rho_a C_p D (\Delta + \gamma)}{\Delta \gamma A} = \gamma^* \quad (6.14)$$

Equation (6.1) can now be rewritten as:

$$ET_{PM} = \frac{\Delta}{\Delta + \gamma} \frac{R_n - G}{\lambda} \frac{1 + \frac{\gamma}{\gamma + \Delta} \frac{\gamma^*}{r_a}}{1 + \frac{\gamma}{\gamma + \Delta} \frac{r_s}{r_a}} \quad (6.15)$$

Under saturated grass conditions, r_s is close to 0. Replacing γ^* using equation (6.14), the FAO-PM method can be approximated as:

$$ET_{PM} = \left(1 + \frac{\rho C_p D}{r_a \Delta A}\right) \frac{\Delta}{\Delta + \gamma} \frac{R_n - G}{\lambda} = \frac{1}{S_A} \frac{\Delta}{\Delta + \gamma} \frac{R_n - G}{\lambda} \quad \text{or} \quad ET_{PM} = \frac{1}{S_A} ET_{eq} \quad (6.16)$$

When wind effect is considered, equation (6.16) can be replaced by a more general form (ET_PT_Su) as:

$$ET_{PM} = \frac{1}{S_A} \frac{\Delta}{\Delta + \gamma} \frac{R_n - G}{\lambda} (1 + S_{U_2}) \quad \text{or} \quad ET_{PM} = \frac{(1 + S_{U_2})}{S_A} ET_{eq} \quad (6.17)$$

where the new PT coefficient (PT_a) can be expressed as:

$$PT_a = \frac{1}{S_A} (1 + S_{U_2}) = \frac{1}{S_A} (1 + \Omega - S_A) \quad (6.18)$$

With the assumption of $\frac{\partial \lambda ET_{PM}}{\partial r_a} = 0$, we can get $S_{r_a} = 0$, and then $S_A = \Omega$,

equation (6.16) can be replaced with the saturated or well-watered grass conditions as:

$$ET_{PM} = \frac{1}{\Omega} \frac{\Delta}{\Delta + \gamma} \frac{R_n - G}{\lambda} \quad (6.19)$$

Equation (6.19) represents potential evaporation at equilibrium, and it is only valid for equilibrium or quasi-equilibrium evaporation, a condition that the evaporative surface is close to saturated state and wind effect is independent of evapotranspiration. Equation (6.19) is the same as the potential evaporation equation at equilibrium derived by Lhomme (1997) using a convective boundary layer model. However, in arid or semi-arid regions, the actual environment cannot satisfy the wet surface assumption, and thus there is a departure of the actual saturation deficit from the equilibrium condition (D^*). Based on equation (6.8), the impact of saturation deficit change on ET_0 can be estimated by assuming no changes in other parameters. Then, equation (6.19) becomes:

$$ET_{PM} = \frac{1}{\Omega} \frac{\Delta}{\Delta + \gamma} \frac{R_n - G}{\lambda} \left[1 + (1 - \Omega) \frac{D - D^*}{D^*} \right] \quad \text{with } S_D = 1 - \Omega \quad (6.20)$$

where D^* is the vapor pressure deficit under the equilibrium condition. Since vapor pressure deficit can be calculated by $(1 - RH) e_s$, the term $\frac{D - D^*}{D^*}$ can be approximated by $\frac{RH^* - RH}{1 - RH^*}$, assuming that there is little change in the mean temperature under the two conditions. RH^* is the relative humidity at the equilibrium in the unit of fraction. Then, equation (6.20) becomes:

$$ET_{PM} = \frac{[1 + (1 - \Omega) \frac{RH^* - RH}{1 - RH^*}]}{\Omega} \frac{\Delta}{\Delta + \gamma} \frac{R_n - G}{\lambda} \quad (6.21)$$

Under high wind conditions, the impact of wind effect on S_D can be approximated as:

$$\frac{\partial(S_D)}{\partial \Omega} \frac{\partial(\Omega)}{\partial U_2} \frac{U_2}{S_D} = (-1)(\Omega^2 - \Omega) \frac{1}{(1 - \Omega)} = \Omega \quad (6.22)$$

$$\text{with } \frac{\partial(\Omega)}{\partial U_2} U_2 = (-1) \frac{\frac{\gamma}{\gamma+\Delta} 0.34}{(1+\frac{\gamma}{\gamma+\Delta} 0.34 U_2)^2} = \Omega^2 - \Omega \quad (6.23)$$

In regions with high wind conditions, equation (6.20) becomes:

$$ET_{PM} = \frac{[1+(1-\Omega^2)\frac{RH^*-RH}{1-RH^*}]}{\Omega} \frac{\Delta}{\Delta+\gamma} \frac{R_n-G}{\lambda} \quad (6.24)$$

6.2.4. Data

Available global grid weather datasets can be categorized into three types, including interpolated datasets based on ground observations, reanalysis datasets by merging observation with model outputs, and satellite-based observations. In this study, the daily Princeton Global forcing (PGF) dataset with a spatial resolution of 0.25° and temporal coverage from 1948-2016 was used (<http://hydrology.princeton.edu/data/pgf/>). The PGF dataset was generated by merging several observational datasets, e.g., NASA Langley monthly surface radiation budget, Climate Research Unit Time-Series (CRU-TS), Global Precipitation Climatology Project (GPCP), and Tropical Rainfall Measurement Mission (TRMM) (Sheffield et al., 2006). The dataset includes daily weather parameters such as solar radiation, wind speed at 10 m height, maximum, minimum, and mean air temperature, specific humidity, and air pressure. Wind speed was converted to 2 m wind speeds following the method suggested by (Allen, 1998). Specific humidity was used to calculate actual vapor pressure following equation (E1) in Appendix E.

6.2.5. Statistical Analysis

Trend significance testing of the monthly series of ET_0 and major meteorological parameters was based on a Mann-Kendall significance test with a significance level p at 0.05 (Kendall, 1955; Mann, 1945). The Mann-Kendall significance test is a nonparametric test and does not assume normality of data, which is popular in trend significance tests in climatologic and hydrologic time series (Pascolini-Campbell et al., 2021; Vicente-Serrano et al., 2014). An advantage of this method is that it is insensitive to abrupt changes, i.e., a small and consistent change has a higher coefficient than a more significant and abrupt change. In addition, the Theil-Sen estimator was used to identify the magnitude of the rates of changes (Sen, 1968; Theil, 1950). Regression analysis was also used to identify the relationship between ET_0 (dependent variable) and other variables (independent variable), i.e., $y = ax + b$. The slope (a) and intercept (b) and were obtained using a least-square fit.

The relative error (RE) was used to evaluate the model performances, as shown in equations (6.25):

$$RE (\%) = \frac{(X_i - ET_{0i})}{ET_{0i}} \times 100 \quad (6.25)$$

where X_i and ET_{0i} are the i th calculated ET_0 using the selected methods, e.g., the PT method and ET_PT_Su method, and the FAO-PM method, respectively.

6.3. Results

6.3.1. Comparison of Reference Evapotranspiration by Different Methods

The global long-term mean ET_0 calculated using the FAO-PM method for 1948-2016 was 1066 mm yr^{-1} (temporal standard deviation of 15 mm yr^{-1}), comparable to the studies from a global monthly ET_0 product at 0.5° using the FAO-PM, PT, and Hargreaves-Samani methods for the period of 1950-2000 ($1092\text{-}1219 \text{ mm yr}^{-1}$) (Aschonitis et al., 2017), the Climate Research Unit (CRU) Time-Series (TS) Version 4.03 (CRU_TS4.03) PET dataset (1901-2018) derived from gridded stations at 0.5° spatial resolution (Harris et al., 2020), the Moderate Resolution Imaging Spectroradiometer (MODIS)/Terra Net (MOD16) PET dataset (2001-2020) 8-day ET_0 at 0.5° , and an hourly PET product using the ERA5-Land reanalysis data (1981–2019) (Singer et al., 2021). The estimated geographical patterns agreed well with the hourly PET product from Singer et al. (2021), characterized by ET_0 hotspots located in the deserts of Northern Africa, Western Asia, and Western Australia (Figure 6.1a). However, the PT method greatly underestimated ET_0 in these regions (Figure 6.1b) due to the assumption that the radiative component and aerodynamic component account for 79.4% ($S_A = \frac{1}{1.26}$) and 20.6% of the ET_0 variations, respectively. On average, the PT method underestimated ET_0 by 6% ($1000 \pm 15 \text{ mm yr}^{-1}$) when compared to the FAO-PM method.

The theoretical PT coefficient (hereafter ET-PT-Su) can significantly improve the performance of the original PT method, given that it showed high consistency with the FAO-PM method (Figure 6.1c). The global long-term mean ET_0 calculated using the

ET_PT_Su method was $1038 \pm 14 \text{ mm yr}^{-1}$, with less than 3% underestimation, smaller than using the PT method. The latitudinal profile showed that the highest ET_0 was at low latitudes ($\sim 20^\circ$ to 30°N and S) and declined steeply towards both the pole and equator (FAO-PM method) (Figure 6.1d). The ET_PT_Su showed a similar pattern as the FAO-PM method, only with a slight underestimation at low latitudes ($\sim 20^\circ$ to 30°N and S). Nevertheless, the PT method overestimated ET_0 in the inner tropic ($<10^\circ\text{N}$ and $<15^\circ\text{S}$) and mid-high latitude ($>45^\circ\text{N}$ and $>50^\circ\text{S}$) but underestimated ET_0 at low-latitudes ($\sim 10^\circ$ to 30°N and 20° to 30°S). The longitudinal differences were comparatively small in the PT method as expected since the PT method only considers the variation of available energy. The relative error (%) of mean annual ET_0 derived by the PT and ET_PT_Su methods was compared with the FAO-PM method (Figure 6.1e-f). The PT method showed a large positive relative error (20%-50%) in Canada, Russia, Europe, southern China, Amazonia, and Central Africa and large negative relative error in Northern Africa, Western Asia, and Western Australia (-30%-50%). In contrast, the relative errors between the ET_PT_Su method and the FAO-PM method were less than $\pm 10\%$ over the entire continental domain, again suggesting that it matched well with the FAO-PM method.

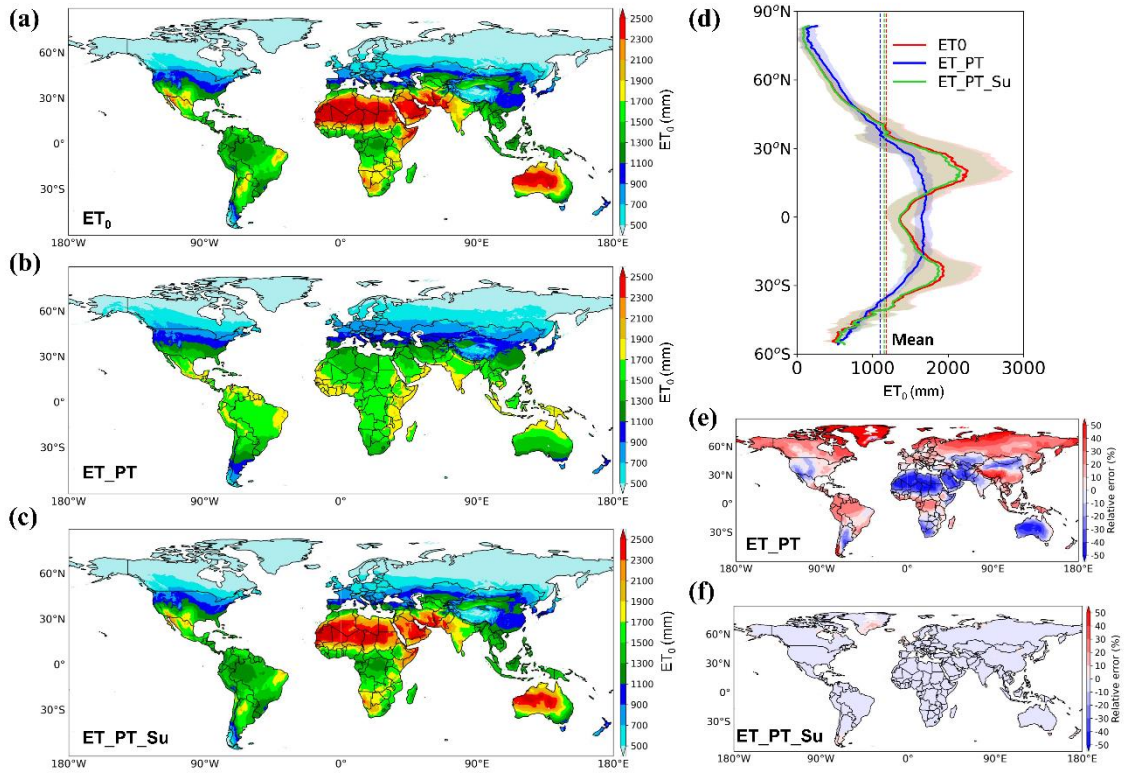


Figure 6.1 Comparison of reference evapotranspiration using different methods. Mean annual reference evapotranspiration using (a) FAO-PM method (ET_0), (b) Priestley-Taylor method (ET_{PT}), and (c) adjusted Priestley-Taylor (ET_{PT_Su} , newly developed in this study); and (d) latitudinal profiles of ET_0 . Color lines indicate the mean value per degree latitude for ET_0 from the three different methods. Shading denotes the standard deviation. Relative errors (%) of mean annual ET_0 for (e) Priestley-Taylor method (ET_{PT}) and (f) adjusted Priestley-Taylor (ET_{PT_Su}) relative to the FAO-PM method (ET_0). Antarctica is excluded since there is no available PGF data over there.

6.3.2. Trends in Reference Evapotranspiration

The seasonal cycle characteristics of long-term ET_0 (1948-2016) are shown in Figure 6.2a. Both the PT and ET_{PT_Su} methods captured the seasonality of ET_0 using the FAO-PM method, all of which peaked in July. The ET_{PT_Su} method performed better than the PT method in all months except in July. Although the ET_{PT_Su} method

(versus the FAO-PM method) showed much smaller relative errors in July compared to that of the PT method (Figure E1-E3, Appendix E), the large positive and negative deviations from the FAO-PM method shown in the ET_0 estimation using the PT method seemed compensate each other in July, leading to the smaller discrepancy between the PT method and the FAO-PM method than that for the ET_PT_Su method in this month. The long-term annual mean ET_0 is removed from the time series by subtracting the mean ET_0 from 1948 to 2016. The mean annual variability of ET_0 (FAO-PM) increased from 1948 to 2016 with a significant positive annual rate of 0.57 mm yr^{-1} , corresponding to an increase of 0.5% per decade above the global mean (Figure 6.2b and c). The mean annual variability of ET_0 using the ET_PT_Su method was very similar to the FAO-PM method (0.55 mm yr^{-1}). In contrast, the PT method showed a more significant increase (0.70 mm yr^{-1}), since it only treats the radiative component impact on ET_0 trends (S_A). As such, the difference between the FAO-PM method and the PT method can be attributed to the impact of the aerodynamic component, i.e., the combined effect of S_D and S_{ra} . As shown in Figure 6.3, S_A can explain 96% of the variance in ET_0 using the PT method ($R^2=0.96$), and S_{ra} alone explained 86% when using the FAO-PM method ($R^2=0.86$). Of the 0.57 mm yr^{-1} trend of global mean ET_0 from 1948 to 2016, the radiative component contributed to 0.70 mm yr^{-1} , but the aerodynamic component compensated for the expected increase in ET_0 by -0.13 mm yr^{-1} ,

The Mann-Kendal trend tests on monthly ET_0 annual variations for the three methods are detailed in Figures E4-6, Appendix E. The percentages of the global land with positive and negative trends are summarized in Figure E7, Appendix E. Positive

trends were dominant in all months (60% globally on average), with 20% of trends were statistically significant ($p < 0.05$). The increasing trends were more significant from April to October, with a mean percentage of 71%. More regions showed negative trends from May to October (23%) than other months (14%), but regions with significant negative trends did not show seasonal variability ($5\% \pm 1\%$). Therefore, there was a general increase in global ET_0 from 1948 to 2016, particularly in warm seasons with relatively high ET_0 . Several hotspots were also observed. For example, Sub-Saharan Africa showed consistent positive trends in all seasons, and the increasing rate from March to April can be as high as 0.6 mm per month. From March to June, Europe, northern China, Western and Central Asia, and the western United States also presented significant increasing trends ($0.4 \text{ mm month}^{-1}$). On the contrary, the Amazonia region showed consistent negative trends through all seasons, and the decreasing rate can be as high as 0.6 mm per month in warm seasons. Northern Australia exhibited a significant decreasing trend in warm seasons. The annual trends of each month simulated by the ET_PT_Su method geographically agreed well with the FAO-PM method, but the increasing trend simulated by the PT method was stronger and more prevalent.

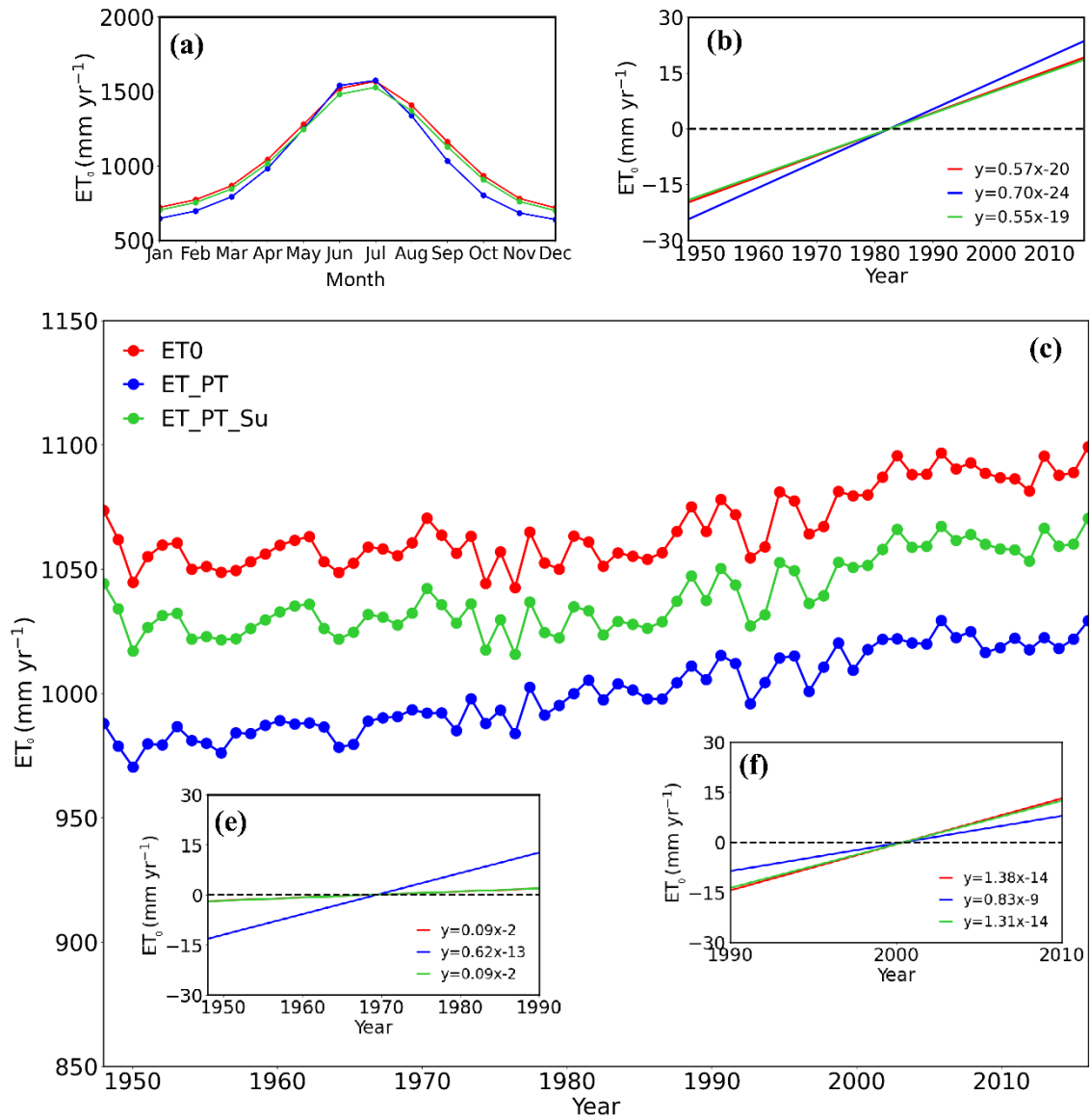


Figure 6.2 Trends in the reference evapotranspiration using different methods. (a) Long-term mean (1948-2016) seasonal cycle of ET_0 ; (b) the trends in global mean ET_0 with long-term mean removed (1948-2016); (c) time series of global mean ET_0 (excluding Antarctica); and the trends in global mean ET_0 with long-term mean removed for the time periods of (e) 1948-1990 and (f) 1990-2016.

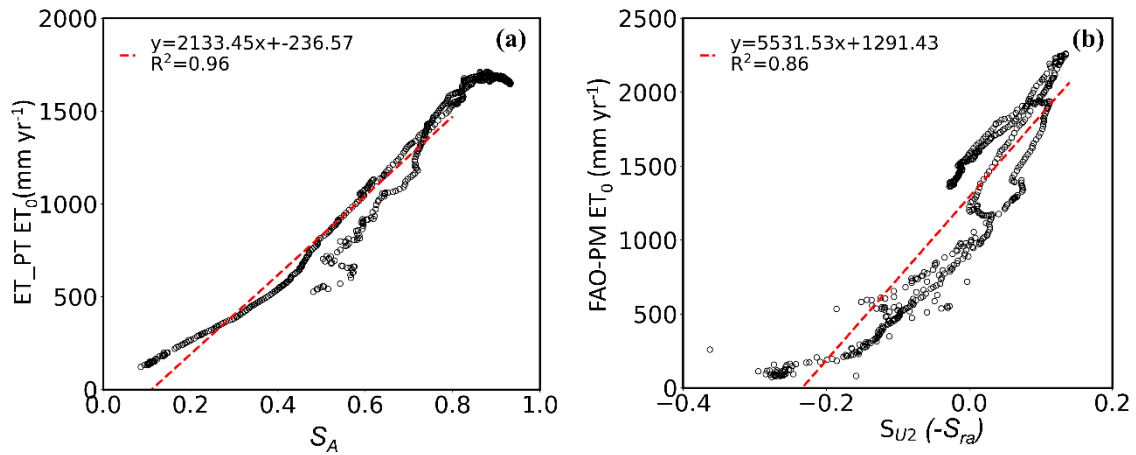


Figure 6.3 Linear regressions of ET₀ and the sensitivity coefficient. (a) The PT method and sensitivity coefficient of available energy and (b) the FAO-PM method and sensitivity coefficient of wind speed (or aerodynamic resistant). The latitudinal means from 1948 to 2016 were used for regression. Each grid cell is an independent scatter point.

The ET₀ estimated using the FAO-PM method and ET-PT-Su method both displayed little variations from 1948 to 1990. As such, the studying time period was split into two sub-periods, i.e., 1948 to 1990 (Figure 6.2e) and 1990-2016 (Figure 6.2f). From 1948 to 1990, the radiative component alone resulted in a 0.62 mm yr⁻¹ increase of global mean ET₀, but the increase was offset by the aerodynamic component variation (-0.53 mm yr⁻¹), leading to a relatively low increasing rate of 0.09 mm yr⁻¹. A positive linear trend (1.39 mm yr⁻¹) was observed from 1990 to 2016, corresponding to an increase of 2.2% per decade above the global mean during this period. As shown in Table 6.1, of the 1.39 mm yr⁻¹ from 1990 to 2016, the radiative component accounted for 60% (0.83 mm yr⁻¹ from the PT method), while the aerodynamic component contributed by 40% (0.55 mm yr⁻¹). Therefore, the main driver of the global mean ET₀ trend from 1948 to 2016 is the radiative component, while the aerodynamic component

counteracted the increase from 1948 to 1990 and accelerated the increase from 1990-2016.

Under equilibrium or quasi-equilibrium evaporation conditions, wind speed has a limited impact on ET_0 variation, and $S_{U_2} = 0$. However, increasing wind speed may increase (decrease) ET_0 in dry (humid) climate regions. Hence, the trends of ET_0 under different climatic regimes are further analyzed in Figure 6.4. The climatic regime was classified based on the mean annual RH from 1948 to 2016 (Figure E8, Appendix E). The RH at the equilibrium or quasi-equilibrium evaporation condition (RH^*) was calculated by averaging the RH from 1948 to 2016 that can satisfy $S_{U_2} \approx 0$. Then, one gets $RH^* = 70\% \pm 6\%$. Based on RH at the equilibrium condition (64%-76%), three regimes, i.e., $RH \leq 64\%$, $64\% < RH < 76\%$, and $RH \geq 76\%$, were divided, accounting for 36%, 35%, and 29% of the global land surface (exclude the Antarctic), respectively. As shown in Figure 6.4a, the ET_0 long-term means and trends using the ET_PT_Su method matched well with the FAO-PM method in all three RH regimes, with slight underestimation (by 1-4%). However, the PT method significantly underestimated global ET_0 (by 24%) in the drier climate regime ($RH \leq 64\%$) and overestimated it in the other two regimes (10-21%). From 1948 to 1990, the drier climate regime ($RH \leq 64\%$) and the region with equilibrium RH ($64\% < RH < 76\%$) showed a similar increasing rate (0.16 mm yr^{-1}), but a decreasing trend was observed in the humid regime (-0.08 mm yr^{-1}), derived by the aerodynamic component (accounted for 56%) (Table 6.1). From 1990 to 2016, the increasing trend rates were significantly reinforced in humid ($RH \geq 76\%$, 0.89 mm yr^{-1})

and drier climate regimes ($RH \leq 64\%$, 1.94 mm yr^{-1}), while in the region with equilibrium RH ($64\% < RH < 76\%$), the trend rate kept stable.

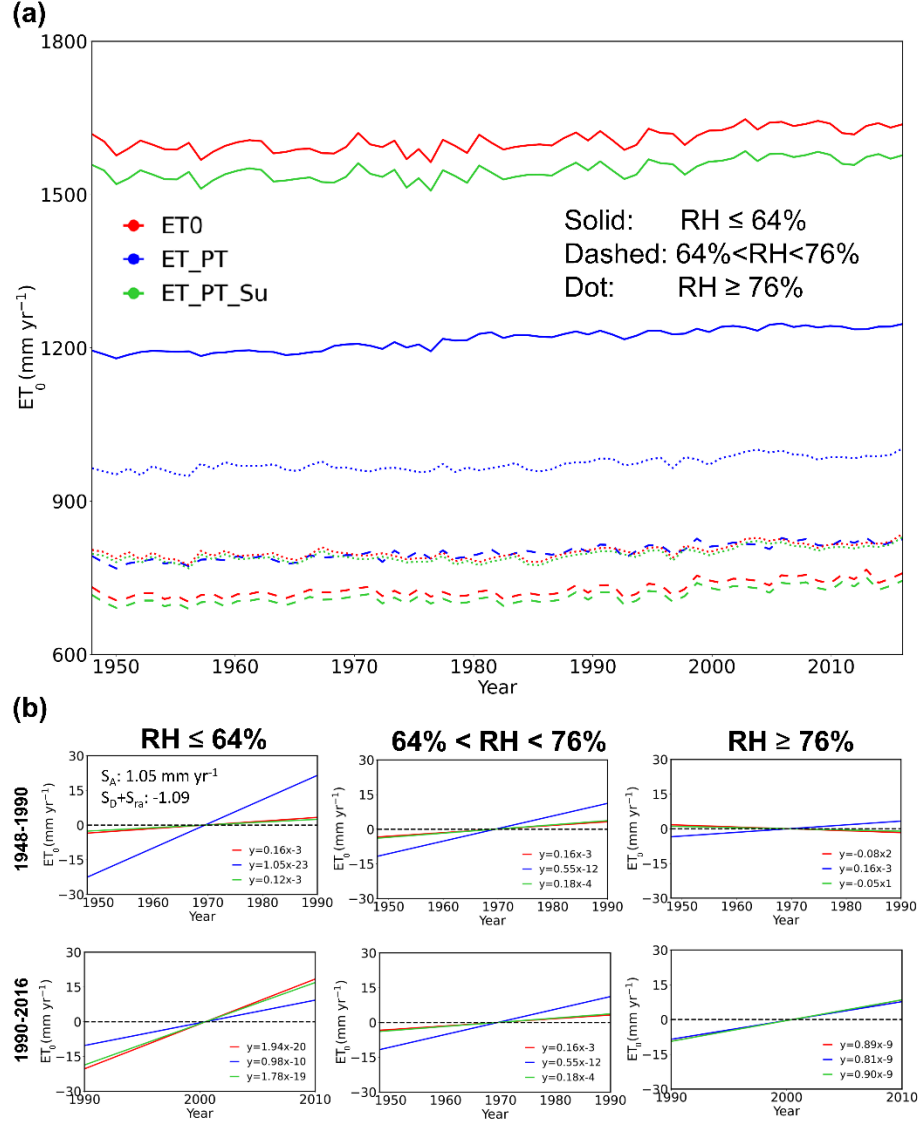


Figure 6.4 Annual variations and trends in the reference evapotranspiration in different RH regimes. (a) Long-term mean (1948-2016) seasonal cycle of ET_0 ; (b) the trends in global mean ET_0 with long-term mean removed (1948-2016); (c) time series of global mean ET_0 (excluding Antarctica); and the trends in global mean ET_0 with long-term mean removed for time periods of (e) 1948-1990 and (f) 1990-2016.

Table 6.1 ET₀ Long-term Means and Trends under Different RH Regimes.

Regimes	1948-1990				1990-2016			
	Mean (mm)	Trends (mm yr ⁻¹)	Trends_R (mm yr ⁻¹)	%R (%)	Mean (mm)	Trends (mm yr ⁻¹)	Trends_R (mm yr ⁻¹)	%R (%)
RH≤64%	1595	0.16	1.05	54	1625	1.94	0.98	51
64% <RH<76%	719	0.16	0.55	59	739	0.16	0.55	59
RH≥76	793	-0.08	0.16	44	811	0.89	0.81	91
Global	1057	0.09	0.62	54	1082	1.38	0.83	60

Note: Trends-R means that the ET₀ trends if only the radiative component is considered. %R indicates the proportion of the ET₀ trends that can be explained by the radiative component. The mean and trends values are based on the FAO-PM method.

6.3.3. Theoretical PT Coefficient

The global long-term mean (1948-2016) theoretical PT coefficient (PT_a) is 1.37 with a temporal standard deviation of 0.02 and a spatial standard deviation of 0.42 (Figure 6.5a). Our results also demonstrated that the PT_a value was 1.26 ± 0.04 under equilibrium conditions, i.e., $S_{r_a} \approx 0$. The procedure of PT_a calculation is similar to that of RH at the equilibrium condition, i.e., $RH^* = 70\% \pm 6\%$. The long-term mean seasonal variations of PT_a of the Northern Hemisphere (NH) and the Southern Hemisphere (SH) are shown in Figure 6.5b. Global averaged PT_a from April to August showed very similar values (1.18) in NH, since the effect of the radiative component on ET₀ was dominated in warm seasons. The monthly-specific variations of PT_a are detailed in Figure E9, Appendix E.

The spatial variation of annual mean PT_a (Figure 6.5c) resembled that of the calibrated PT coefficient using the FAO PM method (Aschonitis et al., 2017), despite using different temporal and spatial resolutions and focusing on different periods in our study from theirs. In addition to the latitudinal profiles of annual mean PT_a, the inner

tropic ($<10^{\circ}\text{N}$ and $<15^{\circ}\text{S}$) and mid-high latitude ($>45^{\circ}\text{N}$ and $>50^{\circ}\text{N}$) showed low PT_a values (less than 1.26) (Figure 6.5d). In addition, the inner tropic regions exhibited the least variability compared to higher latitude regions. The reason is that the radiative component accounted for more than 90% of the ET_0 variation, i.e., $S_A > 0.9$, and the wind effect showed little impact on ET_0 in hot, and humid climatic types (Figure 6.5e and f). In addition, wind speed is usually less than 2 m s^{-1} . Hence, e.g., S_{U_2} is nearly zero in the inner tropic regions (Figure 6.5g and h). The low value in the mid-high latitude is due to the negative value of S_{U_2} under cold and windy conditions (Figure 6.5h). The highest PT_a value was observed in cold, humid, and windy climatic regions, e.g., the mid-high latitude in SH ($>50^{\circ}\text{S}$). In the low latitude ($\sim 15^{\circ}$ to 30°N and 20° to 35°S), the mean PT_a was relatively stable latitudinally but showed high longitudinally variability due to the highly variable RH (Figure E10, Appendix E).

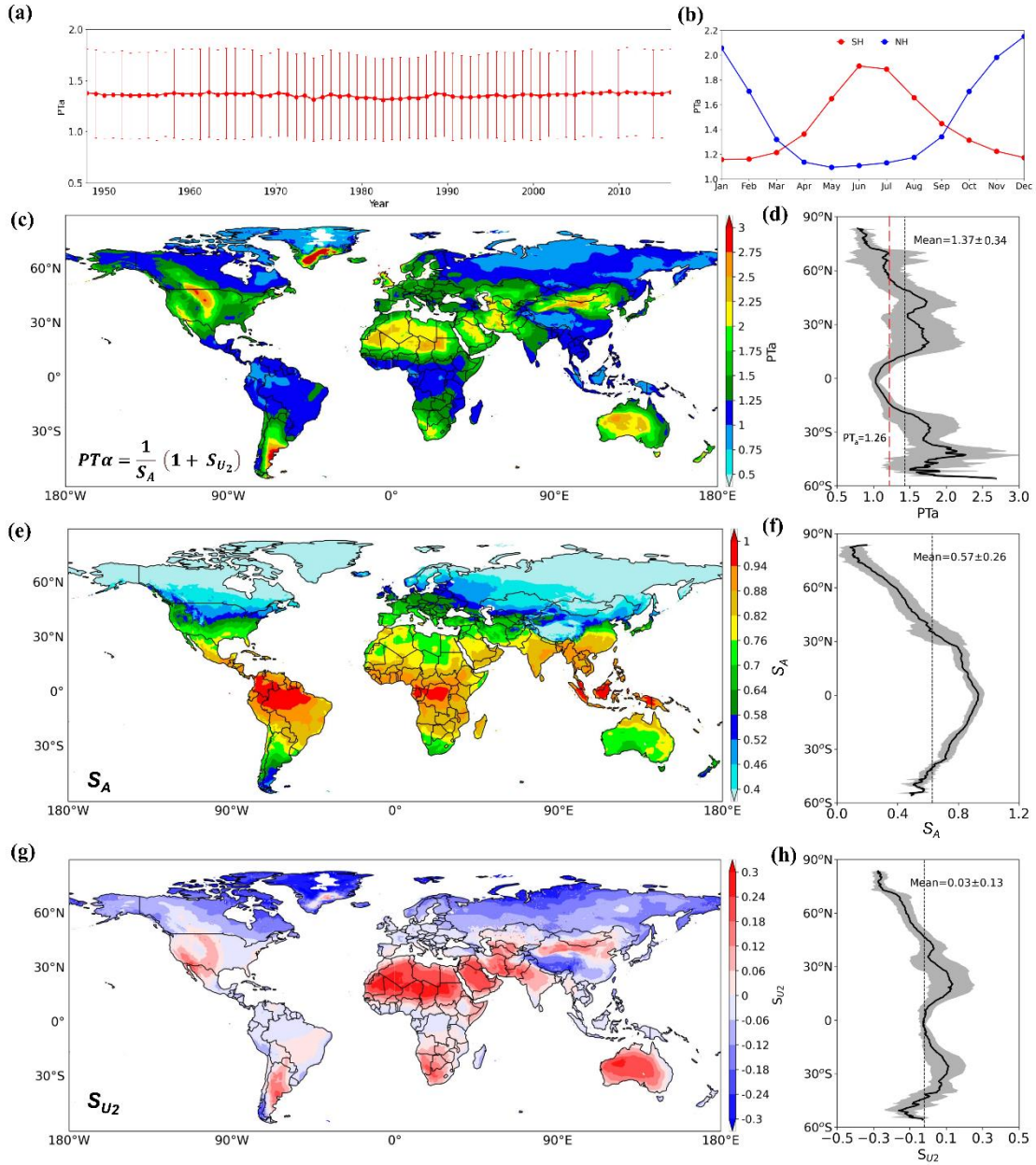


Figure 6.5 The theoretical PT_a and sensitivity coefficients of available energy (S_A) and wind speed (S_{U2}) for ET_0 . (a) Annual global mean PT_a and standard deviation; (b) long-term mean (1948-2016) seasonal cycle of PT_a ; long-term mean (1948-2016) global distributions of (c) PT_a ; (e) S_A ; and (g) S_{U2} ; and latitudinal profiles of (d) PT_a ; (f) S_A ; and (h) S_{U2} . Shading in (d), (f), and (h) denotes standard deviations, and the black dotted lines mark the mean values. Antarctica is excluded since there is no available PGF data.

The changes in ET_0 can be attributed to the changes in available energy (S_A), vapor pressure deficit ($S_D = 1 - S_A$), and aerodynamic resistance (S_{ra}). In the PT method, $S_A = 79.4\%$, $S_D = 1 - S_A = 20.6\%$, and $S_{ra} = -S_{u2} = 0$. With these assumptions, the radiative component contribution to ET_0 is about four times the aerodynamic component. The latitudinal profile showed that S_A was the highest at the equator (92%) and declined poleward (Figure 6.5f). At around 30°N and S , the S_A value can satisfy the assumptions in the PT method. The latitudinal profiles of S_A and air temperature (Figure E10, Appendix E) presented a highly positive correlation ($R^2=0.99$), indicating a strong increase in S_A as air temperature increases. Overall, available energy is the driving factor of global ET_0 variations from 1948 to 2016, accounting for $57\% \pm 26\%$ of the variability in ET_0 (Figure 6.5f). The result is consistent with the estimated global means shown in Table 6.1. Also, the seasonal variations were more significant than the spatial variations. As shown in Figure 6.6, S_A in warm seasons in Northern Hemisphere was higher than 76%, even in the high latitude ($>60^\circ\text{N}$), while in cold seasons, e.g., November and December, S_A can be lower than 50% in the low-latitude regions ($\sim 20^\circ$ to 30°N and S).

The seasonal impact of aerodynamic resistance ($-S_{U2}$) on ET_0 is shown in Figure 6.7. The negative values in S_{U2} indicated that the increasing wind speed (or decreasing aerodynamic resistance) could result in a reduction in ET_0 . The wind effect on ET_0 was not monotonous due to the varying interactions of wind with different climatic factors, e.g., temperature and relative humidity. In warm, arid climate regions, e.g., Northern Africa, Western Asia, and Western Australia, S_{U2} showed consistently high values (18-30%) in all seasons. This is because the drier air over these regions generally has a

higher vapor pressure gradient. Moreover, wind speed can modulate the sensible heat transfer from the vast dry, unirrigated areas and contributes part of the energy required for evapotranspiration through warm air advection. In humid climates, the energy, heat, and vapor transfer rates over grass reference surfaces and their surrounding environment are more similar to each other than in semiarid and arid climates. Hence, PT_a can be simplified to $PT_a = \frac{1}{\Omega} = 1 + \frac{\gamma}{\gamma + \Delta} \frac{r_s}{r_a} = 1 + \frac{\gamma}{\gamma + \Delta} (0.34U_2)$, which is dependent only on temperature and wind speed. As $\frac{\gamma}{\gamma + \Delta}$ varies from 0.45 at 10°C and 0.26 at 25°C, the corresponding calculated PT_a was from 1.18 (25°C) to 1.32 (10°C), with the assumption of $U_2 = 2 \text{ m s}^{-1}$. Therefore, in warm seasons in humid climates, wind speed showed negative impacts on ET_0 under moderate wind speed, e.g., in southern China or the eastern United States, S_{U2} was usually within -6%. In mid-high latitude regions (>45°N and >50°S), S_{U2} showed consistently negative values due to cold, humidity, and windy climates.

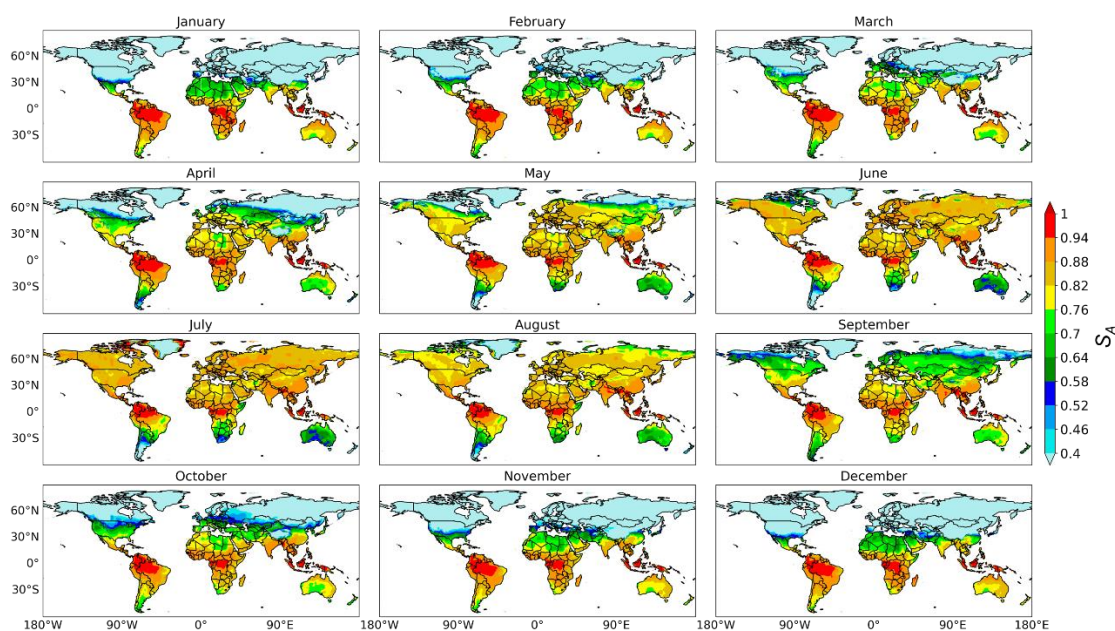


Figure 6.6 Monthly mean of sensitivity coefficients of available energy (S_A) on reference evapotranspiration from 1948 to 2016.

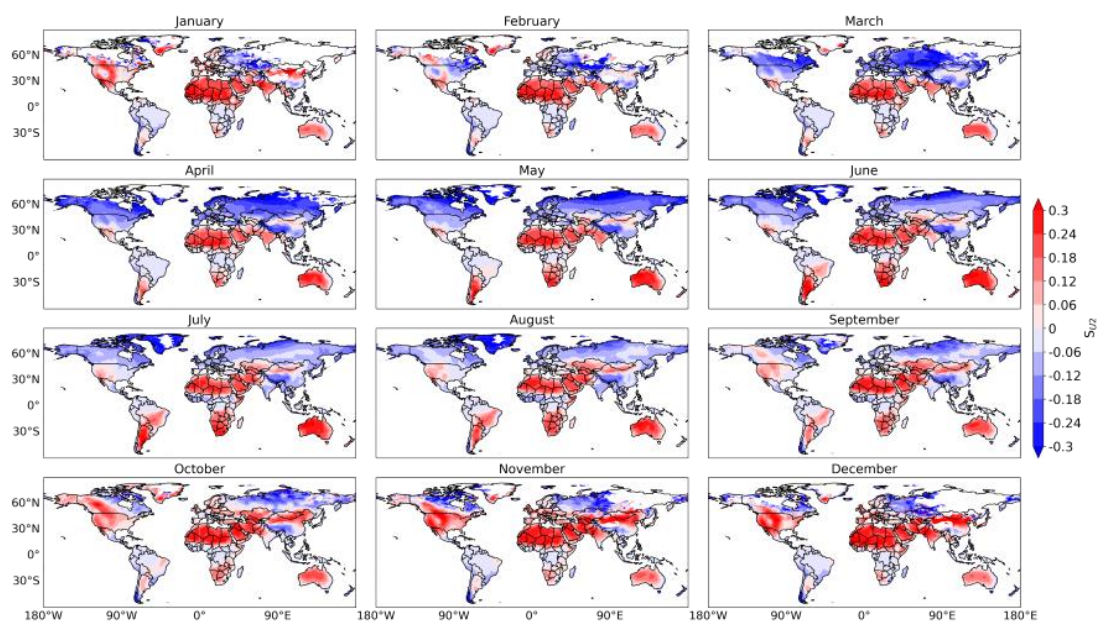


Figure 6.7 Monthly mean of sensitivity coefficients of wind speed S_{U2} ($-S_{ra}$) on reference evapotranspiration from 1948 to 2016.

6.3.4. Validation of PT Coefficients under Different Climate Conditions

The relative humidity at the equilibrium condition, i.e., $RH^* = 70\%$, was used to obtain the simplified PT coefficients based on equations (6.21) and (6.24). Simplified forms for all climatic types with light to moderate winds were derived using equation (6.21), i.e., $PT_a = 1.87 - 0.87 RH$ (1). The simplified form with strong winds was obtained using equation (6.24), i.e., $PT_a = 2.35 - 1.55 RH$ (2). Three scenarios were set to evaluate the performance of these two simplified forms. Scenario 1 (ET1) applies form (1) for all wind conditions, scenario 2 (ET2) applies form (2) for all wind conditions, and Scenario 3 (ET3) applies form (1) when $U_2 \leq 2.0 \text{ m s}^{-1}$, and form (2) when $U_2 > 2.0 \text{ m s}^{-1}$. By doing this, the underestimation (overestimation) was expected in ET1 (ET2). As shown in Figure 6.8, the three adjusted PT methods captured the mean geographical patterns of ET_0 compared with the FAO-PM method, and the relative errors were within 20%. As expected, the global mean ET_0 calculated using ET1 (ET2) was underestimated by 1% (overestimated by 3%). A slight overestimation was observed in ET3 (by 1%). ET3 also performed better than ET1 and ET2 in simulating global mean ET_0 trends. However, these three methods all overestimated ET_0 from May to July (Figure 6.9). Taken together, the general forms of PT coefficients under different climatic types are summarized in Table 6.2. Depending on the weather data availability and climatic conditions, different forms of the PT coefficients can be used. The use of simplified PT coefficients with relative humidity as the only input can improve the performance of the PT method in areas with limited weather data.

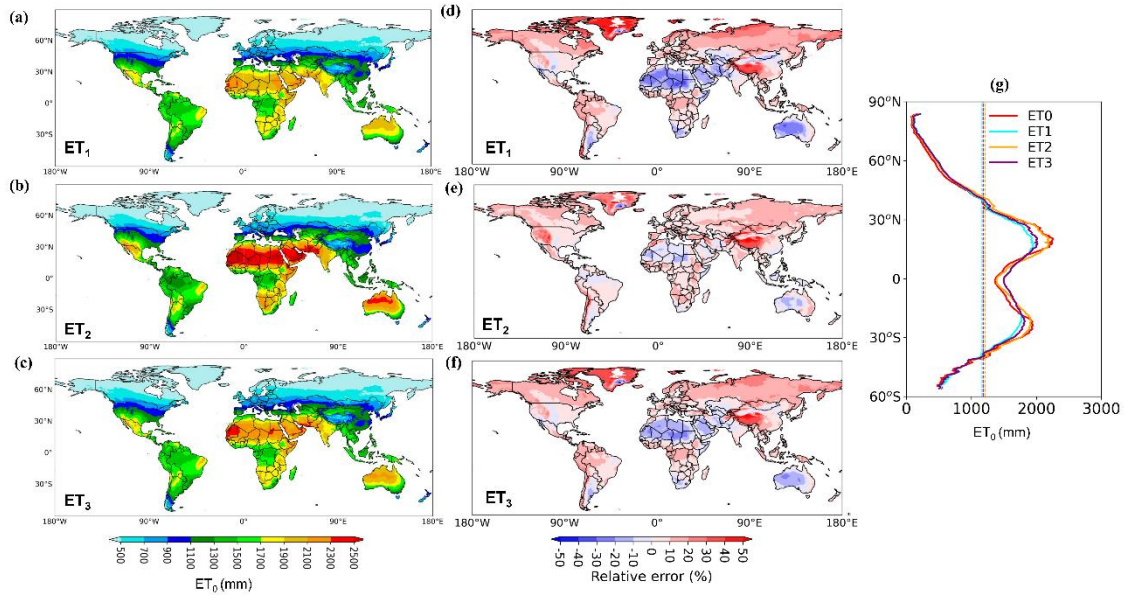


Figure 6.8 Comparison of reference evapotranspiration using the adjusted PT methods. Mean annual reference evapotranspiration using (a) ET_1 , (b) ET_2 , and (c) ET_3 ; relative error (%) of (d) ET_1 , (e) ET_2 , and (f) ET_3 compared with the FAO-PM method; and (g) latitudinal profiles of mean annual ET_0 . Antarctica is excluded since there is no available PGF data over there.

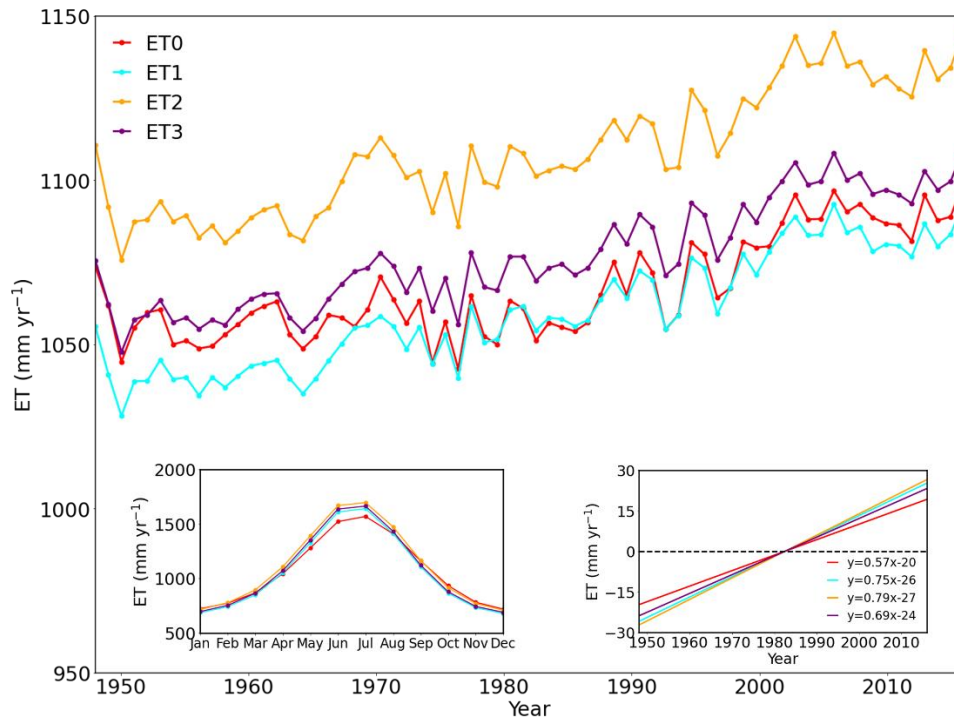


Figure 6.9 Trends in the reference evapotranspiration using the adjusted PT methods. (a) Time series of global mean ET_0 (excluding Antarctica); (b) long-term mean (1948-2016) seasonal cycle; and (c) the trends in global mean ET_0 with long-term mean removed (1948-2016).

Table 6.2 Priestley-Taylor Coefficients for Different Climatic Types and Required Weather Data.

Priestley-Taylor coefficient	Range of α	Applications	Weather data required
$\frac{S_A}{(1 + \Omega - S_A)}$		The general form for all climatic types	same as PM method
$\frac{S_A}{\Omega}$		General form in a humid climate	same as PM method
1.26		Equilibrium evaporation from well-watered grass surface (humid, light to moderate wind)	-
$1.87 - 0.87RH$	(1-1.87)	Simplified form for all climatic types with light to moderate winds ($U_2 \leq 2.0 \text{ m s}^{-1}$)	monthly mean RH in fraction
$2.35 - 1.55RH$	(0.8-2.35)	Simplified form for all climatic types regions with strong wind ($U_2 > 2.0 \text{ m s}^{-1}$)	monthly mean RH in fraction

6.4. Discussion

6.4.1. Sensitivity Analysis

Sensitivity analysis of S_A and S_{u2} to changes in air temperature, RH , and wind speed was performed. Since each year showed a similar pattern, the daily data at each grid in 2015 was illustrated (Figure 6.10). Regression analysis on S_A and S_{u2} against air temperature, RH , and wind speed was also conducted (Figure E11, Appendix E). Temperature can explain 41% of the variance of S_A from 1948 to 2016 ($R^2=0.41$). When air temperature was higher than 20°C , S_{u2} was more sensitive to RH , which explained 42% of the variance of S_{u2} . Variations of the theoretical PT coefficient to changes in air temperature, RH , and wind speed were displayed in Figure 6.11, which can be used to guide the selection of an appropriate PT coefficient for regional use.

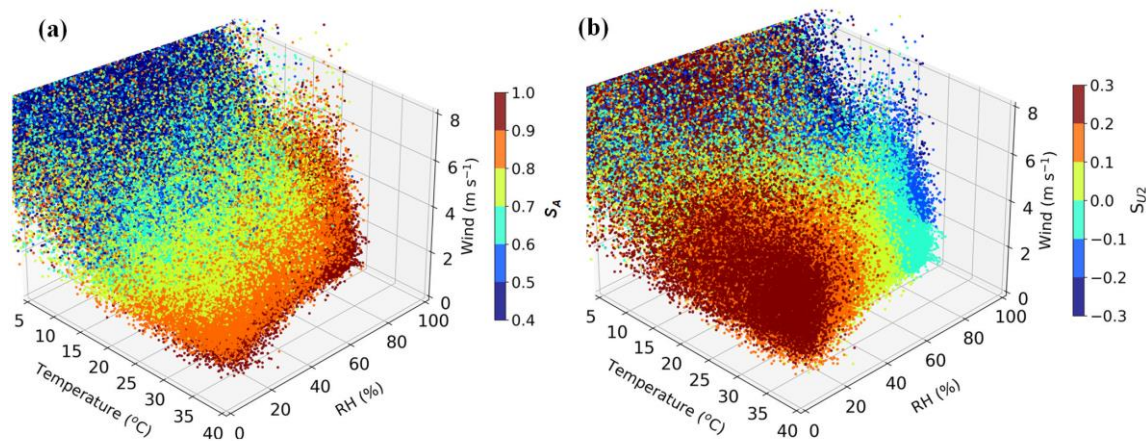


Figure 6.10 Variations of S_A and S_{u2} to changes in meteorological variables. Daily data in 2015 is illustrated.

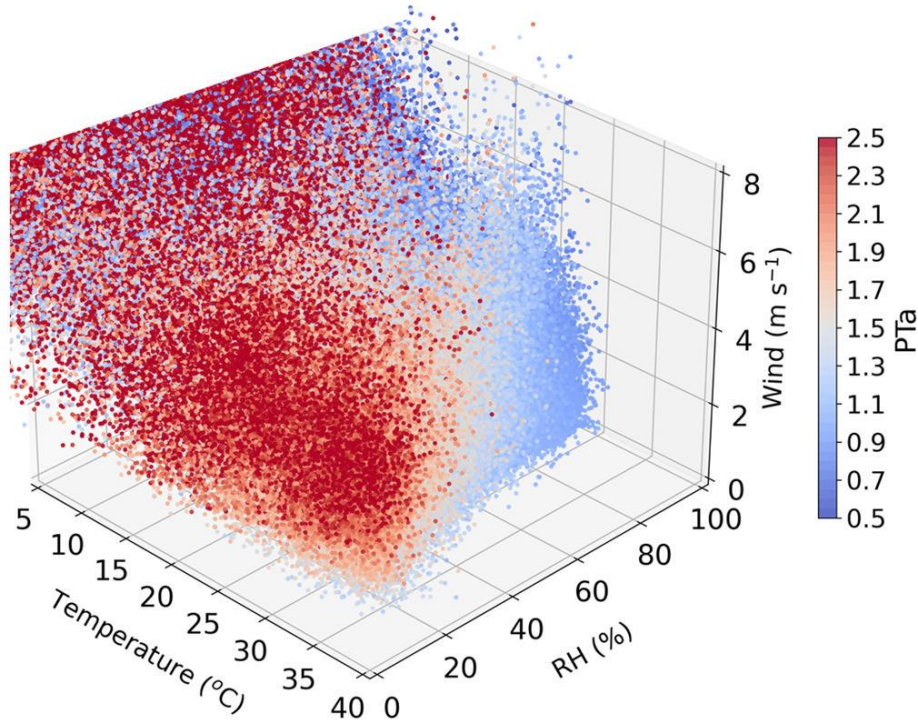


Figure 6.11 Variations of the theoretical PT coefficient to changes in meteorological variables. Daily data in 2015 is illustrated.

6.4.2. Trends in S_A , S_{u2} , and PT_a

The theoretical PT_a derived in this study, i.e., $PT_a = \frac{1}{S_A} (1 + S_{U_2})$, well captured the temporal variations and spatial distributions of global ET_o , as well as its long-term trends, indicating the reliability and robustness of this method. With PT_a rewritten as $PT_a = \frac{1}{S_A} (S_A + S_D + S_{U_2})$, the reciprocal of PT_a , i.e., $\frac{S_A}{S_A + S_D + S_{U_2}}$, could be a useful coefficient to evaluate the relative contribution of the radiative component to the ET_o changes. Given that the global mean PT_a from 1948-2016 was 1.37, the radiative component contributed to 73% of the ET_o changes during this period. In previous studies, the estimations of the relative contribution of radiative or aerodynamic in

driving ET_0 changes were inconsistent with each other and showed opposite conclusions (Matsoukas et al., 2011; Vicente-Serrano et al., 2014; Wang et al., 2012). The theoretical PT_a derived in this study provides a possible way to resolve this important issue. It is noted that wind effect was independent of evapotranspiration saturated under equilibrium or quasi-equilibrium evaporation, i.e., $S_{U_2}=0$. Therefore, PT_a can be simplified to $\frac{S_A}{S_A+S_D+S_{U_2}} = \frac{S_A}{S_A+S_D+0} = S_A$, which indicates that S_A represents the relative contribution of the radiative component to ET_0 under equilibrium or quasi-equilibrium evaporation, the same as the decoupling coefficient (Ω) suggested by Jarvis and McNaughton (1986). Moreover, the trends of PT_a can be used to determine if the relative contribution of the radiative or aerodynamic component is changing or not in a warming climate. A negative (positive) trend of PT_a indicates that the radiative component would contribute more (less) to ET_0 changes. As shown in Figure 6.12, the relative contribution of the radiative component to ET_0 variation did not show a clear trend at global scales from 1948 to 2016. Although there are some regions, e.g., regions with mid-high latitude ($>30^\circ N$ and $>30^\circ S$), showing significant increasing or decreasing trends in cold seasons, these trends were not statistically significant in most regions. For example, the area fraction of regions with positive trends ($45\% \pm 8\%$) on average was slightly larger than with negative trends ($42\% \pm 6\%$), and more regions showed positive trends ($53\% \pm 3\%$) from June to October than in other months ($40\% \pm 3\%$, Figure 6.13). However, the area fraction of regions with statistically significant trends was much smaller and showed an opposite pattern, i.e., more negative trends ($9\% \pm 3\%$) in all months than the positive trends ($6\% \pm 1\%$), particularly from April to September. Most of the significant

decreasing trends were shown in Northern Africa, indicating that the proportion of radiative components in driving ET_0 has been increasing in this region over the past several decades. This is mainly due to the decreasing trend of S_{u2} (Figure E13, Appendix E), driven by the decreasing wind speed in this region (Figure E14, Appendix E).

The significance of monthly S_A and S_{ra} ($-S_{u2}$) trends were further evaluated using the Mann-Kendal trend test to determine if the radiative component and aerodynamic component impacts on global reference evapotranspiration would increase or decrease in a warming climate (Figure 6.13, Figures E12 and 13 in Appendix E). The regions with positive trends of S_A were dominant in all months, accounting for $59\% \pm 13\%$ of total global land surface area, with $36\% \pm 10\%$ of the regions passing the statistical significance test ($p < 0.05$). In addition, the S_A increasing trends were more pronounced in warm seasons, showing similar patterns as the ET_0 changes (Figure E7). The increasing trend of S_A indicated that the radiative component impact on ET_0 variation was reinforced, particularly in warm seasons. The positive trends of S_{u2} were also dominant in all months ($50\% \pm 11\%$), but the trends with statistical significance were only $6\% \pm 8\%$ ($p < 0.05$). Considering the widely declining wind speed, an increase of S_{u2} would lead to a reduced ET_0 . Although both radiative and aerodynamic components showed reinforced impacts on global reference evapotranspiration, the widely declining wind speed slightly compensated for the expected increases driven by the increased contribution of the radiative components to ET_0 increases in a warming climate.

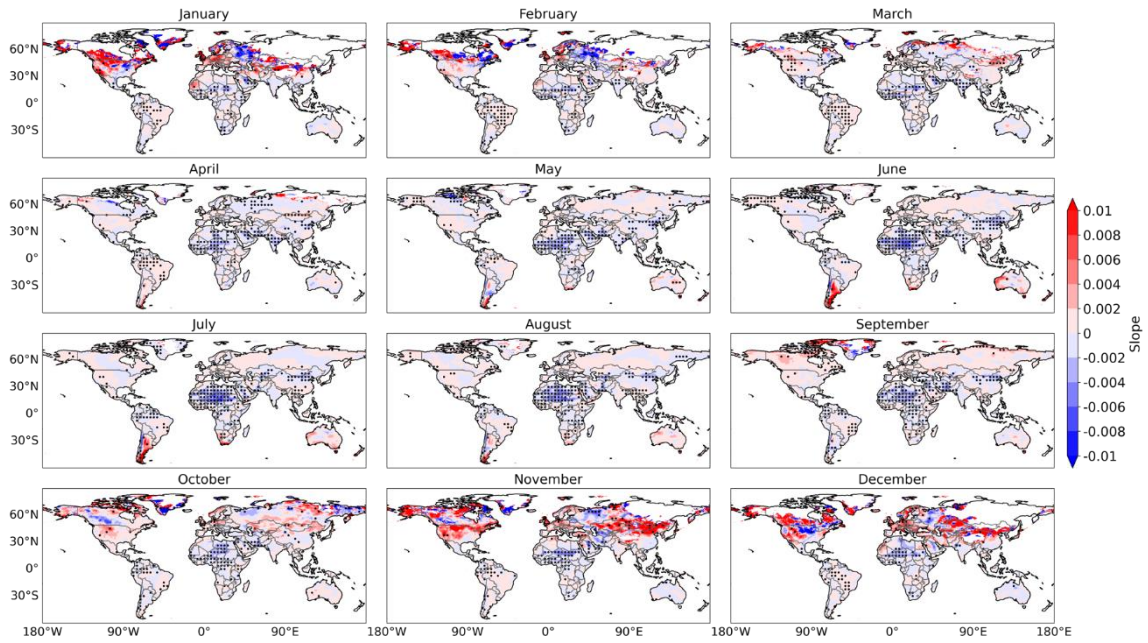


Figure 6.12 Mann-Kendal annual trend tests of monthly PT coefficient (PT_a) from 1948 to 2016. Black dots indicate statistically significant ($p < 0.05$), and shading is the Theil-Sen slope.

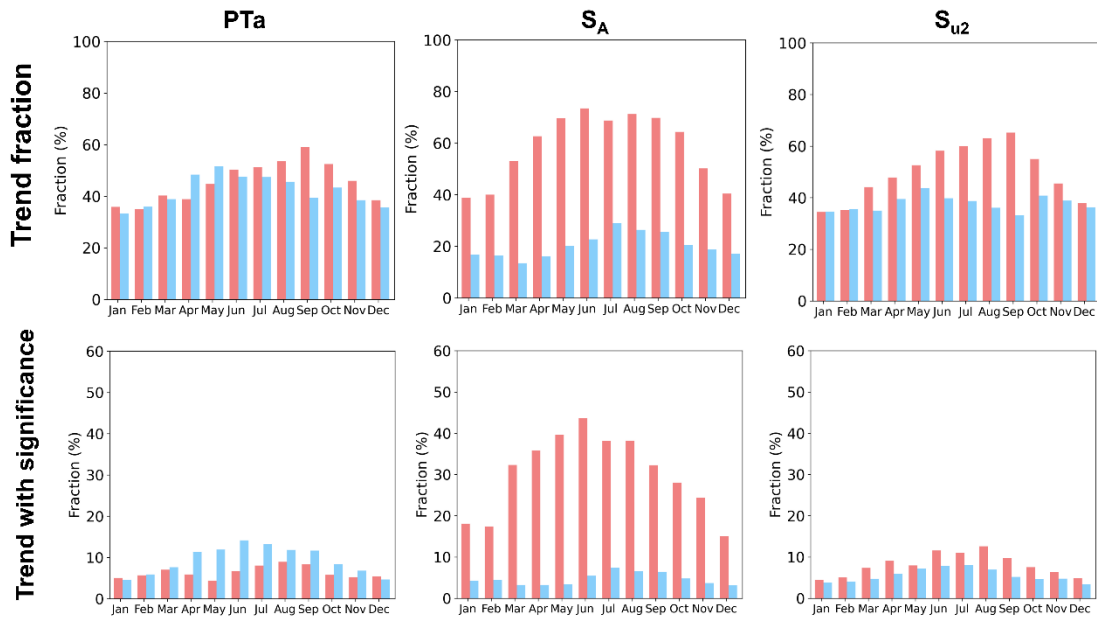


Figure 6.13 Area fractions of global land surface with positive trends and negative trends as well as the trends with statistically significant ($p < 0.05$) for PT_a , S_A , and S_{u2} from 1948 to 2016.

6.5. Conclusions

In this chapter, an analytical expression for the PT coefficient was derived, i.e., $PT_a = \frac{1}{S_A} (1 + S_{U_2})$, following the FAO-PM method using the daily Princeton Global Forcing (PGF) dataset with a spatial resolution of 0.25° and temporal coverage from 1948-2016. PT_a well captures the temporal and spatial distribution of global ET_o as well as its long-term trends. PT_a was 1.26 ± 0.04 under equilibrium conditions. The PT coefficients were further simplified with relative humidity as the only input under slight to moderate wind ($PT_a = 1.87 - 0.87RH$) and strong wind ($PT_a = 2.35 - 1.55RH$), both of which showed improved performance compared with the original PT method. The radiative component is the driving factor of the ET_o changes, and it is controlled by the changes in air temperature. Our finding shows implications of understanding the roles of the radiative and aerodynamic components in the ET_o changes. The major uncertainty in this study is from the variations of the gridded weather dataset used, which may affect the magnitudes and spatial distributions of ET_o , ET_o trends, S_A , S_{u2} , and the PT coefficient at global scales. However, the dataset uncertainties are limited, and thus the reliability and robustness of the theoretical PT coefficient derived in this study are high.

7. CALIBRATION AND BIAS CORRECTION OF SEASONAL WEATHER FORECASTS FOR REAL-TIME REGIONAL CROP MODELING

Reliable monthly and seasonal weather forecasts at regional and local scales are essential for decision-making in irrigation management and predicting future crop production, especially in water-stressed regions with declining water resources. Currently, global and regional climate models that provide intra-seasonal and seasonal weather predictions are limited. The North American Multi-Model Ensemble (NMME) is an experimental real-time seasonal forecast system, which provides 12-month daily global weather forecasts at 1° spatial resolution (roughly 110 km at the equator) based on ensemble simulations of several state-of-the-art coupled general circulation models. However, the coarse resolution of the NMME dataset limits its use in driving regional and local crop models because of the increased bias and uncertainties associated with applying large-scale information at the regional scales. To overcome this issue, an improved downscaling method, namely bias-corrected or ‘nudging’ method, was used to produce 1-km gridded daily weather projections (maximum and minimum air temperatures and precipitation) over the contiguous United States (CONUS) from one representative NMME model, i.e., the Canadian Coupled Climate Model versions 4 (CanCM4). Additionally, the arithmetic means of three NMME model ensembles, including CanCM4, the Community Climate System Model version 4 (CCSM4), and the Goddard Earth Observing System Model version 5 (GEOS-5) were calculated and incorporated into comparisons with the downscaling results.

The recently-released Daily Surface Weather and Climatological Summaries (DAYMET, version 4), a 1-km grid spacing dataset created by interpolating and extrapolating ground-based observations through statistical modeling techniques, was used for calibration of the downscaled hindcast predictions of CanCM4 for 1982-2010. Furthermore, the reliability of the downscaled CanCM4 forecasts for its usage in local crop modeling was evaluated at various lead times using a calibrated CSM-CROPGRO-Cotton module of the Decision Support System for Agrotechnology Transfer (DSSAT) model at an experimental station (i.e., Chillicothe) in the semi-arid Texas Rolling Plains during the 2020 cotton growing seasons. Results indicated that the post-processing of projected data like downscaling of the raw NMME outputs was required before using the data for seasonal irrigation management and crop yield prediction. Our study suggested that the downscaling approach used in this study could considerably improve the performance of CanCM4 in driving regional modeling, and the extent of improvement could vary with time and location. The high-resolution seasonal weather forecasts generated in this study ensured robust and reliable regional or local crop yield prediction over the CONUS region.

7.1. Introduction

Reliable short-term and seasonal weather forecasts at regional and local scales are essential for decision-making in irrigation management and predicting future crop production, especially in water-stressed regions with declining water resources. The short-term climate projections, e.g., the Global Forecast System (GFS), and long-term climate projections, e.g., Global Climate Models (GCMs), have been widely

investigated. However, current uses of global and regional climate models to provide intra-seasonal and seasonal weather predictions are still limited. The North American Multi-Model Ensemble (NMME) is an experimental real-time seasonal forecast system, which provides 12-month daily global weather forecasts at 1° spatial resolution based on ensemble simulations of several state-of-the-art coupled general circulation models, including Community Climate System Model, version 4 (CCSM4) (Danabasoglu et al., 2012), Canadian Coupled Global Climate Model, version 3 (CanCM3) and version 4 (CanCM4) (Merryfield et al., 2013), Goddard Earth Observing System (GEOS-5) (Vernieres et al., 2012), Climate Forecast System, version 2 (CFSv2-2011) (Saha et al., 2006), and Global Environmental Multiscale/Nucleus for European Modeling of the Ocean (GEM/NEMO) (Aumont et al., 2015). However, the coarse resolution of the NMME dataset is always accompanied by increased bias and uncertainties when applying it to the regional scales, which usually limits its use in driving regional and local real-time crop models (Barbero et al., 2017; Barnston and Tippett, 2017; Narapusetty et al., 2018; Yazdandoost et al., 2020).

The limitation of the use of the NMME data is illustrated in Figure 7.1. The maximum temperature (T_{max}) and minimum temperature (T_{min}) simulated by CanCM4 were overall overestimated in July 2019 compared with observations from the Daily Surface Weather and Climatological Summaries version 4 (DAYMET). Precipitation also exhibited considerable bias compared with the observation, particularly over the eastern United States, with many observed details not captured in CanCM4.

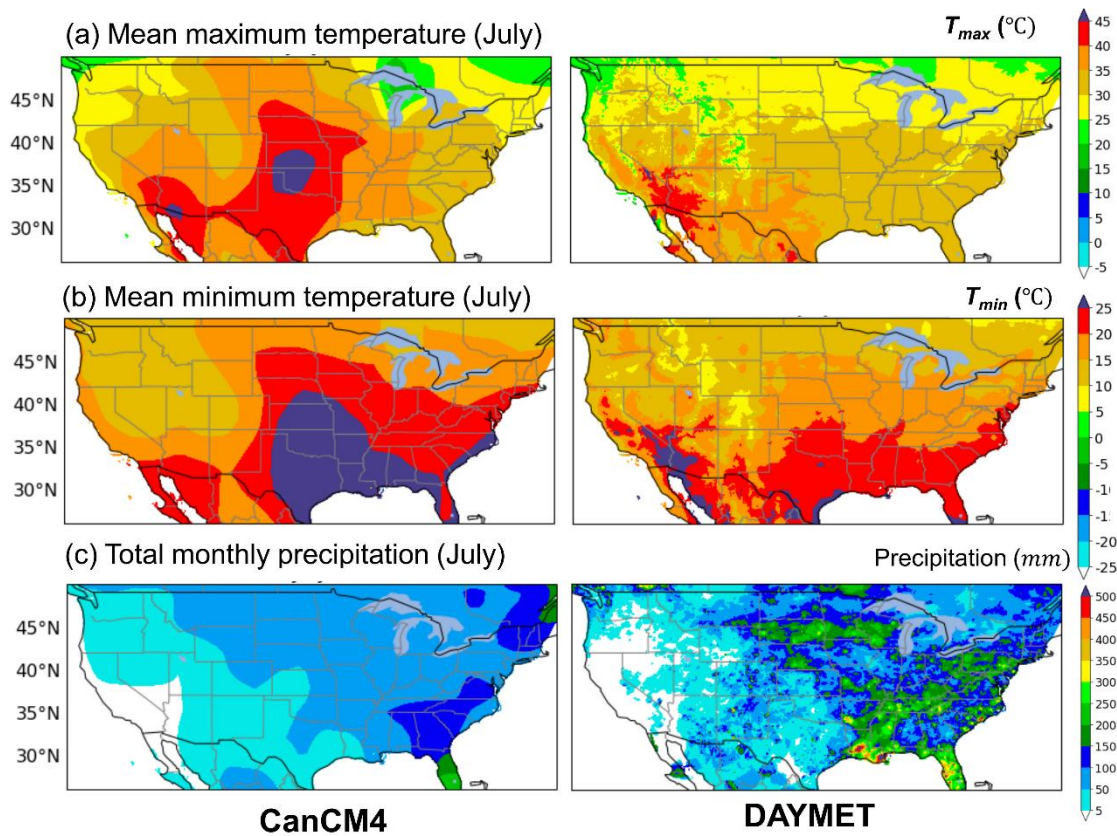


Figure 7.1 Comparison of (a) monthly mean maximum temperature, (b) monthly mean minimum temperature, and (c) monthly total precipitation from NMME dataset (simulated by CanCM4 at 1° spatial resolution) and observations from DAYMET at 1 km spatial resolution in July 2019.

Dynamic and statistical downscaling are the two most commonly used techniques to downscale climate model outputs to the regional scale for use in agricultural impact studies (Gebrechorkos et al., 2019; Gutmann et al., 2012). Dynamic downscaling requires inputs from GCMs to set up boundary and initial conditions, which can explicitly resolve the convective rainfall process. However, dynamic downscaling is computationally expensive and the downscaled data can still have bias and uncertainty from the systematic errors inherent to the use of boundary conditions from GCMs, which

limit its application in local and regional impact analysis and adaptation studies (Adachi and Tomita, 2020). In contrast, statistical downscaling is simple, fast, and effective, and it requires less computational time and expense. Therefore, it is widely used in local and regional crop modeling (Hawkins et al., 2013; Jones and Thornton, 2013) and water management (Madadgar et al., 2016; Yazdandoost et al., 2020).

Typical statistical downscaling includes two steps: (1) to develop a transformation function to represent a statistical relationship between large- and local-scale weather variables using historical data; and (2) to apply the transformation function onto future large-scale outputs to derive future downscaled data. The commonly used statistical downscaling approaches include the delta method, e.g., delta addition and changing factor (Navarro-Racines et al., 2020), bias correction (or nudging), e.g., correction only for mean bias (Huntingford et al., 2005; Ines and Hansen, 2006) or corrections for both mean and variance (Hawkins et al., 2013; Ho et al., 2012), quantile mapping (Kaini et al., 2020), and multiple linear regression (Gebrechorkos et al., 2019). Figure 7.2 illustrates example procedures of the four typical methods, including (a) Delta addition (only mean is corrected) (Figure 7.2a); (b) Delta correction (corrected for variance) (Figure 7.2b); (c) Quantile mapping (Figure 7.2c); and (d) Proposed method (both mean and variance are corrected, Figure 7.2d) (Hawkins et al., 2013; Ho et al., 2012).

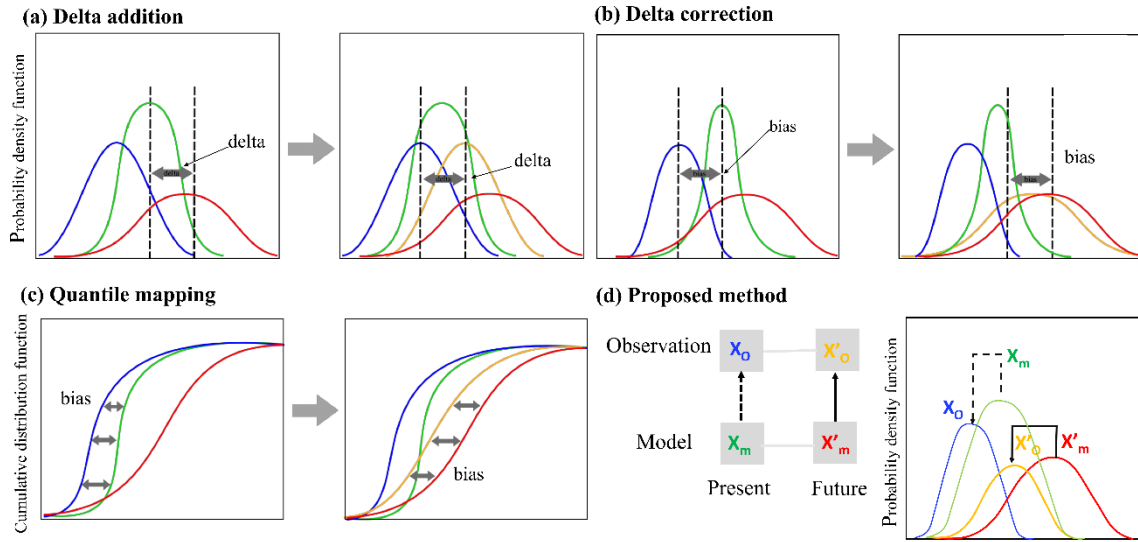


Figure 7.2 Schematic diagrams showing different downscaling methods: (a) delta addition; (b) delta correction; (c) quantile mapping; and (d) proposed method. (a)-(c) are adapted from <https://rcmes.jpl.nasa.gov/content/statistical-downscaling>.

This chapter aimed to improve the skill of seasonal weather forecasts of the CanCM4 GCM, for real-time regional crop modeling over the CONUS by performing bias-corrected statistical downscaling. The specific objectives were to (1) perform an improved bias-corrected downscaling on the original outputs of T_{max} , T_{min} , precipitation, and solar radiation from CanCM4; (2) compare the performance of the downscaled CanCM4 forecast with the ensemble means of multiple models, including CanCM4, CCSM4, and GEOS-5; (3) evaluate the reliability of the downscaled CanCM4 forecasts at different lead times (0-5 month lead); and (4) test the downscaled CanCM4 seasonal forecasts in real-time crop modeling using a calibrated CSM-CROPGRO-Cotton module of the Decision Support System for Agrotechnology Transfer (DSSAT) model at an experimental station in the semi-arid Texas Rolling Plains during the 2020 cotton growing season.

7.2. Methodology

7.2.1. Downscaling Method

The improved bias correction downscaling method with both mean and variability correction (Hawkins et al., 2013; Ho et al., 2012) was used to produce daily weather data at a 1-km resolution from CanCM4 seasonal forecasts. The major assumptions of this method include: (1) stationarity between small-scale and large-scale dynamics, which means that the same relationship holds good when relating future simulations to future observations, and (2) present-day small-scale and large-scale weather data have the same shape of distributions, but with different means and variance. As such, the future small-scale weather data can be calculated as:

$$M(t) = \overline{O_{ref}} + \frac{\sigma_{O,ref}}{\sigma_{M,ref}} (M_{fut}(t) - \overline{M_{ref}}) \quad (7.1)$$

where $M(t)$ is the T_{max} , T_{min} , and precipitation at the field location (1-km resolution) at time t ; $M_{fut}(t)$ is the seasonal forecasts by CanCM4 at time t ; $\sigma_{O,ref}$ and $\sigma_{M,ref}$ represent the standard deviations of the monthly observations and the CanCM4 outputs in the reference period, respectively; and $\overline{O_{ref}}$ and $\overline{M_{ref}}$ are the means of the monthly observations and the CanCM4 outputs, respectively. Since weather variables have a strong seasonal cycle, the calibration was performed for each month individually.

7.2.2. Data

The daily seasonal forecast data was obtained from the NMME forecasting system. NMME is an experimental real-time seasonal forecast system, which provides daily global weather forecasts with an 11-month lead time at 1° spatial resolution

(approximately 110 km at the equator) with 10 ensemble simulations using several state-of-the-art coupled GCMs. In the NMME dataset, CESM1, CanCM3, and CanCM4 GCMs provide all the four weather variables required for crop modeling, i.e., T_{max} , T_{min} , precipitation, and solar radiation, but currently, only CanCM4 has a long-term coverage of dataset accessible for a reliable calibration (<https://www.ncei.noaa.gov/data/north-american-multi-model-ensemble/access/cancm4/>). Therefore, the hindcast predictions (1982-2010) of CanCM4 were used to calibrate the downscale parameters. In addition, for real-time weather forecasts, the multi-model means of CCSM4, GEOS-5, and CanCM4 were calculated and compared with the downscaled data. The CCSM4 and GEOS-5 models were selected because they get updated and have the same time and spatial resolution as CanCM4. Solar radiation is not simulated in CCSM4 and GEOS-5. Hence, solar radiation was derived based on T_{max} , T_{min} , and extraterrestrial solar radiation (R_a).

DAYMET, version 4 (<https://daymet.ornl.gov/>) data, which is available at 1-km grid-level over the CONUS (1982-2019), was used as the reference database for the calibration and validation of the downscaling results. DAYMET provides long-term, continuous daily weather variables (e.g., T_{max} , T_{min} , precipitation, solar radiation, and vapor pressure, etc.) by interpolating and extrapolating ground-based observations, which has been widely applied in agricultural research areas.

7.2.3. Crop Growth Simulation Model

Texas has the largest cropland acreage in the United States. The agricultural production of Texas contributed about \$24 billion in 2015, which is crucial to the local

economy (Gleaton and Robinson, 2016). Texas Rolling Plains (TRP) region accounted for 13% of Texas cotton. Since the TRP region is a semi-arid area with a relatively low annual rainfall of about 460-700 mm (18 to 28 in), cotton production over TRP is highly dependent on irrigation water from the underlying Seymour Aquifer. However, irrigated agriculture here is facing many challenges, including a reduction in well capacities and increased irrigation water demand due to the projected warmer and drier summers in the future (Modala et al., 2017; Nielsen-Gammon et al., 2020). Therefore, reliable seasonal weather forecasts can help develop efficient irrigation management strategies for sustaining crop production in this region.

To test the reliability of the downscaled seasonal weather forecasts in real-time crop modeling, a calibrated CSM-CROPGRO-Cotton module of the Decision Support System for Agrotechnology Transfer (DSSAT) model (Hoogenboom et al., 2019; Jones et al., 2003) was applied to a cotton field at the Texas A&M AgriLife Research Station at Chillicothe in the TPR region (34.25°N, 99.52°W, elevation 447 m) during the cotton growing season of 2020 (May-October). The DSSAT CSM-CROPGRO-Cotton module was previously calibrated and validated by Adhikari et al. (2017) using the measurements of 2011-2015 at the same site, with an average percent error in seed cotton yield prediction of -10.1% and -1.0% for the calibration and validation, respectively.

The evaluated CSM-CROPGRO-Cotton model was used to predict cotton water use and yield using the historical data (i.e., preceding to the growing season) and the forecasted seasonal weather data (i.e., downscaled data) with 0-5 month lead time. The

minimum weather data inputs required for the crop model included daily T_{max} and T_{min} (°C), precipitation (mm), and solar radiation (MJ m⁻²). Historical weather data from an on-site weather station at Chillicothe was used for validation of the downscaled data. Missing weather data was filled with the data recorded at a nearby West Texas Mesonet weather station (Mesonet, 2021) and a National Climatic Data Center (NCDC) weather station. In DSSAT, crop growth was simulated with the assumptions of no water and fertilizer stresses.

7.2.4. Real-time Weather Forecasts Generation

The seasonal weather forecast generation workflow using the multi-model mean and downscaling methods is illustrated in Figure 7.3. For the multi-model mean method, the arithmetic means of the raw model outputs (30 ensembles) of T_{max} , T_{min} , and precipitation were calculated at every grid with daily frequency and at 1°×1° spatial resolution. For the downscale method, the 1°×1° data was first interpolated to 1 km×1 km using bilinear interpolation, which was then bias-corrected using the downscaling parameters derived in Section 7.2.1 to get the final downscaled weather forecast data at a 1 km resolution. The real-time solar radiation was calculated as (Allen, 1998):

$$R_s = 0.16\sqrt{(T_{max} - T_{min})} R_a \quad (7.2)$$

where R_a is the extraterrestrial radiation, MJ m⁻² d⁻¹. An adjustment coefficient of 0.16 is suggested for interior regions, while 0.19 is suggested for coastal regions.

For real-time crop modeling, the seasonal forecast weather file is updated monthly, and the forecasted data is replaced by the newly available real-time weather

data as the growing season progresses and thereby ensuring a more reliable prediction of crop yield and irrigation water requirement. The historical weather data started several months before the planting date, ensuring the start-up of the DSSAT model, and historical data was obtained from three sources: 1) Mesonet data (<http://www.mesonet.ttu.edu/meteograms/>), 2) National Climatic Data Center (NCDC) data (<https://www1.ncdc.noaa.gov/pub/data/ghcn/daily/>), and 3) North American Regional Reanalysis (NARR) data (<ftp.cdc.noaa.gov/Datasets/NARR/Dailies/monolevel/>).

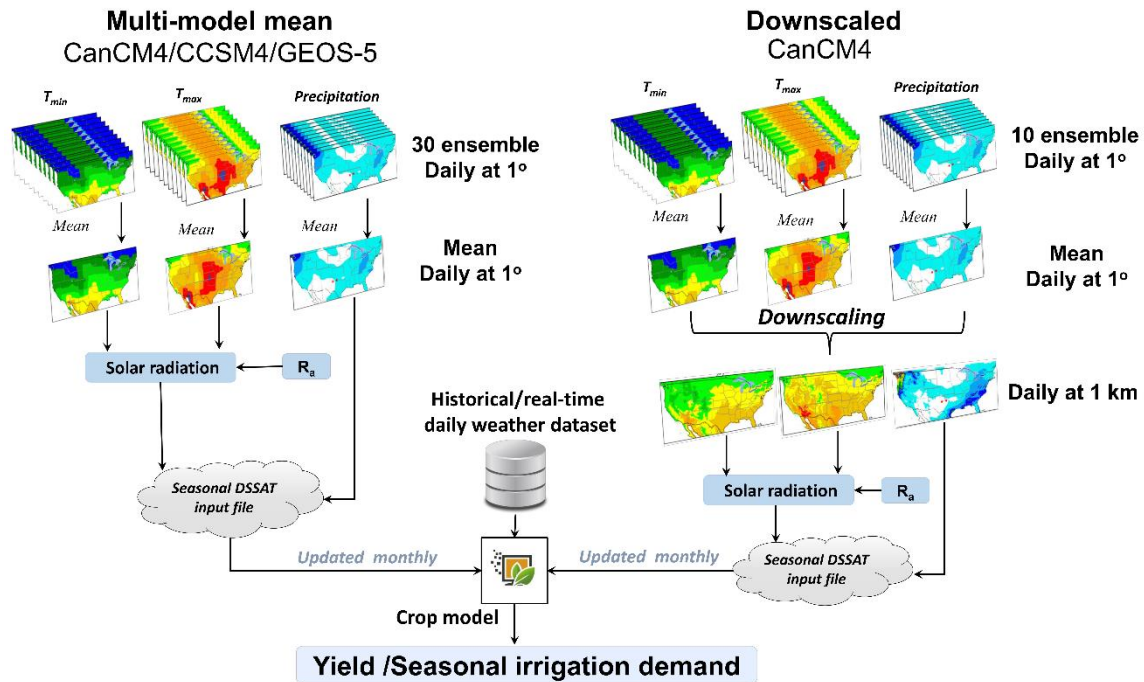


Figure 7.3 Schematic showing weather data inputs and processing.

7.2.5. Model Evaluation

Root-mean-square error (RMSE) and relative error (RE) were used to evaluate the model performance, and they were estimated as per equations (7.3) and (7.4):

$$RMSE = \sqrt{\frac{\sum_{i=1}^n (X_i - X_{oi})^2}{n}} \quad (7.3)$$

$$RE (\%) = \frac{(X_i - X_{oi})}{ET_{oi}} \times 100 \quad (7.4)$$

where X_i and X_{oi} are the i^{th} calculated data using the predicted weather variable using different methods and observations from DAYMET or field data, respectively, and n is the number of observations. The best method has RMSE and RE values equal to 0.

7.3. Results and Discussion

7.3.1. Downscaling Method Evaluation for the Reference Period

The hindcast of the raw CanCM4 output greatly overestimated T_{max} in most regions compared with the DAYMET observations (Figure 7.4a,b). The most significant overestimation was found around the Rocky Mountains (by 50%, Figure 7.4d), followed by Kansas, Nebraska, and Iowa (by 40%). Underestimation was found in the Great Lake regions (by 50%), Washington (by -20%), California (by 20%), and Florida (<10%). From seasonal variation (Figure 7.4e), it was found that the raw CanCM4 output overestimated T_{max} from June to September by as high as 5 °C. Significant overestimation was also noticed for T_{min} (Figure 7.5a-d), with a consistent overestimation of around 3 °C throughout the season (Figure 7.5e). The overestimation of T_{min} by the CanCM4 was more significant in the northern regions (by 50%) than in the southern regions (by 20-30%, Figure 7.5d).

Precipitation from the original hindcast of CanCM4 showed pronounced differences over short distances in regions with complex topography, such as the Rocky Mountains and the Appalachian Mountains (Figure 7.6). The reason for this trend is that the orographic and inversion processes can lead to substantial differences in seasonal weather variability. Excepting overestimation in the northwestern United States (by 50%), most regions showed large negative deviations from the observations. The underestimation was pronounced during the growing season, with an average of around 30 mm per month (Figure 7.6e).

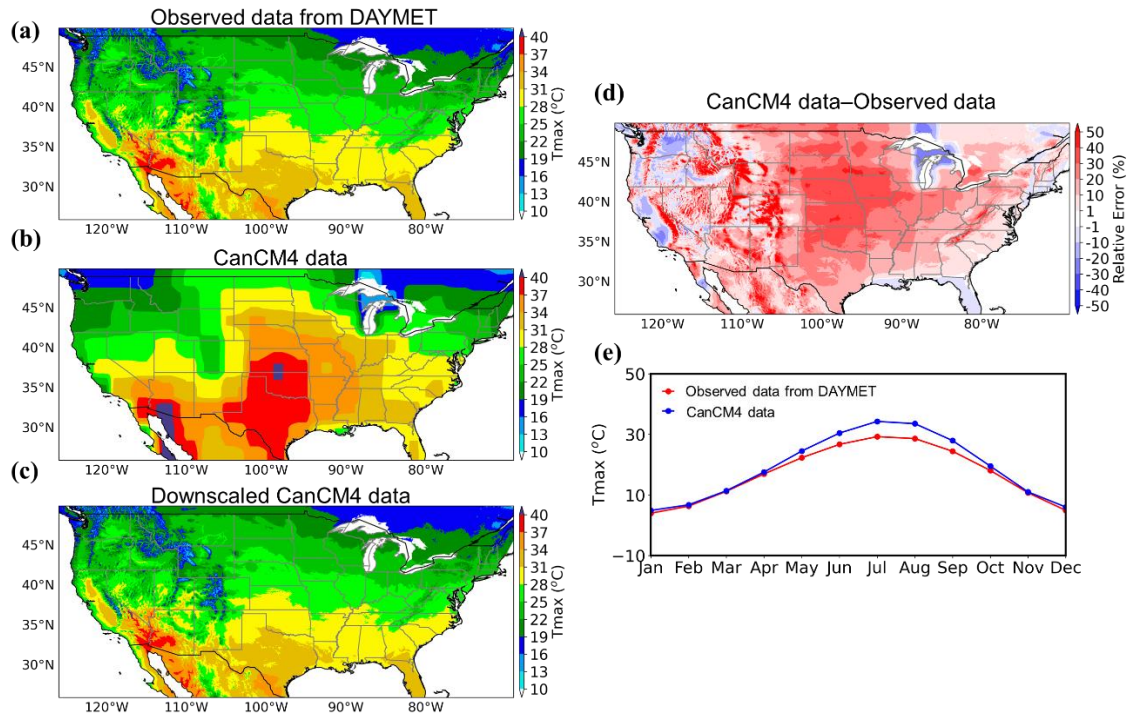


Figure 7.4 Comparison of hindcast predictions of mean maximum temperature in the growing season (May to October) using different methods. Long-term (1982–2010) seasonal mean T_{max} using (a) observed data from DAYMET; (b) CanCM4 data; (c) downscaled CanCM4 data; (d) relative errors (%) of CanCM4 data relative to the observed data; and (e) their mean seasonal variations.

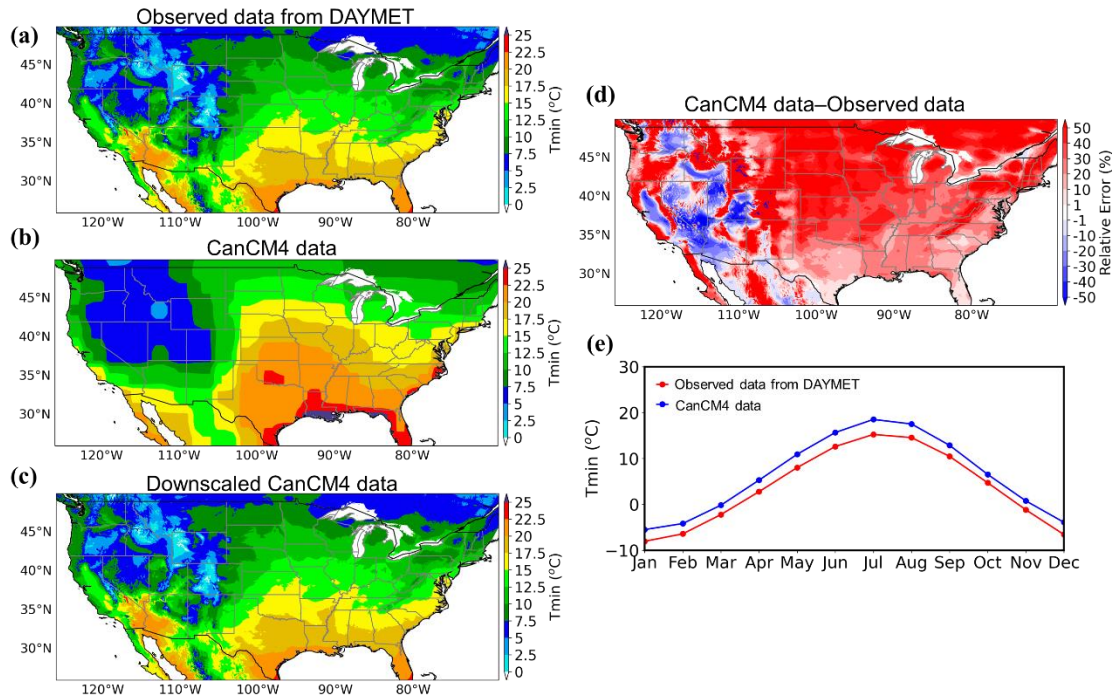


Figure 7.5 Comparison of hindcast predictions of mean minimum temperature in the growing season (May to October) using different methods. Long-term (1982-2010) seasonal mean T_{min} using (a) observed data from DAYMET; (b) CanCM4 data; (c) downscaled CanCM4; (d) relative errors (%) of CanCM4 data relative to the observed data; and (e) their mean seasonal variations.

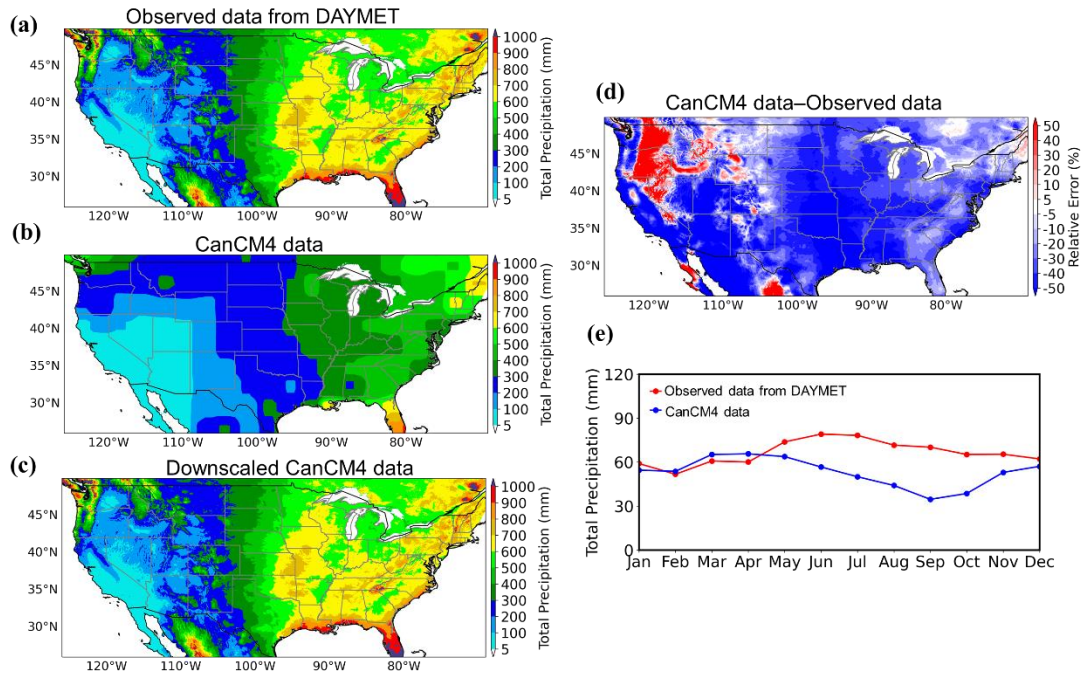


Figure 7.6 Comparison of hindcast predictions of the total precipitation in the growing season (May to October) using different methods. Long-term (1982-2010) mean total seasonal precipitation from (a) observed data from DAYMET; (b) CanCM4 data; (c) downscaled CanCM4; (d) relative errors (%) of CanCM4 data relative to the observed data; and (e) their mean seasonal variations.

Together, T_{max} and precipitation from the raw CanCM4 outputs showed more significant errors in the growing season. Therefore, the post-processing of the raw CanCM4 outputs was required before using them in seasonal irrigation management and crop yield prediction. As shown in Figures 7.4 to 7.6, the downscaled CanCM4 output captured the long-term mean (1982-2010) of the observations very well. The calibration parameters used to downscale the raw CanCM4 outputs of T_{max} , T_{min} , and precipitation at 1 km resolution are documented in NetCDF files, which can be easily applied in other studies. The spatial distribution of these parameters is also detailed in Figures F1-3, Appendix F.

7.3.2. Downscaling Method Versus Multi-Model Mean

To test the seasonal forecast ability at the regional scale, the grid-level comparisons of T_{max} , T_{min} , and total precipitation for the 2019 growing season (August was not included due to data unavailability from the NMME forecasts) of the downscaled CanCM4 and multi-model mean forecasts were compared with the observations from DAYMET (Figures 7.7-7.9). The seasonal mean T_{max} in 2019 was $23.8 \pm 6.2^{\circ}\text{C}$. The downscaled CanCM4 forecast showed high consistency with the observations, with a seasonal mean of $24.1 \pm 5.7^{\circ}\text{C}$. On average, the downscaled method overestimated seasonal mean T_{max} in 2019 by 1.2% compared with the observations. Most of the positive deviation was found in the western regions, except for California, and most of the negative deviation (within 10%) was found in the eastern regions (Figure 7.7e). The relative error for each month is further detailed in Figure F4, Appendix F. The multi-model mean forecast showed a large positive deviation (about 2°C) in most regions (Figure 7.7f), which can also be inferred in the latitudinal profiles (Figure 7.7d).

The overestimation in T_{min} in the multi-model mean forecast was more pronounced (Figure 7.8), with an averaged positive deviation of 2.6°C compared to the observation ($10.6 \pm 5.9^{\circ}\text{C}$). The seasonal mean T_{min} from the downscaled forecast was $10.4 \pm 5.3^{\circ}\text{C}$, with less than 2% underestimation (0.2°C) compared with observation, much smaller than using the multi-model mean (23%). The relative error of the seasonal and monthly mean T_{min} of the downscaled method showed a similar pattern as T_{max} forecast, and the monthly comparison is detailed in Figure F5, Appendix F.

The seasonal total precipitation in 2019 was 309 ± 282 mm (Note that August was not included due to data being unavailable from the NMME forecast) (Figure 7.9). Precipitation from the downscaled CanCM4 forecast (336 ± 292 mm) well captured the geographical patterns of observations, with a slight overestimation by 9% on average (Figure 7.9e). The latitudinal profiles of seasonal total precipitation also matched the observation well, except for a 50 mm overestimation from 35° to 40°N (Figure 7.9d). However, the downscaled CanCM4 forecasts at local scales exhibited high variability, and a significant overestimation in the western regions. This overestimation was also found in the multi-model mean forecast (Figure 7.9f). On average, the seasonal precipitation prediction from the multi-model mean (254 ± 192 mm) was underestimated by 18% relative to the observations, with a more significant underestimation in September and October (Figure F6, Appendix F).

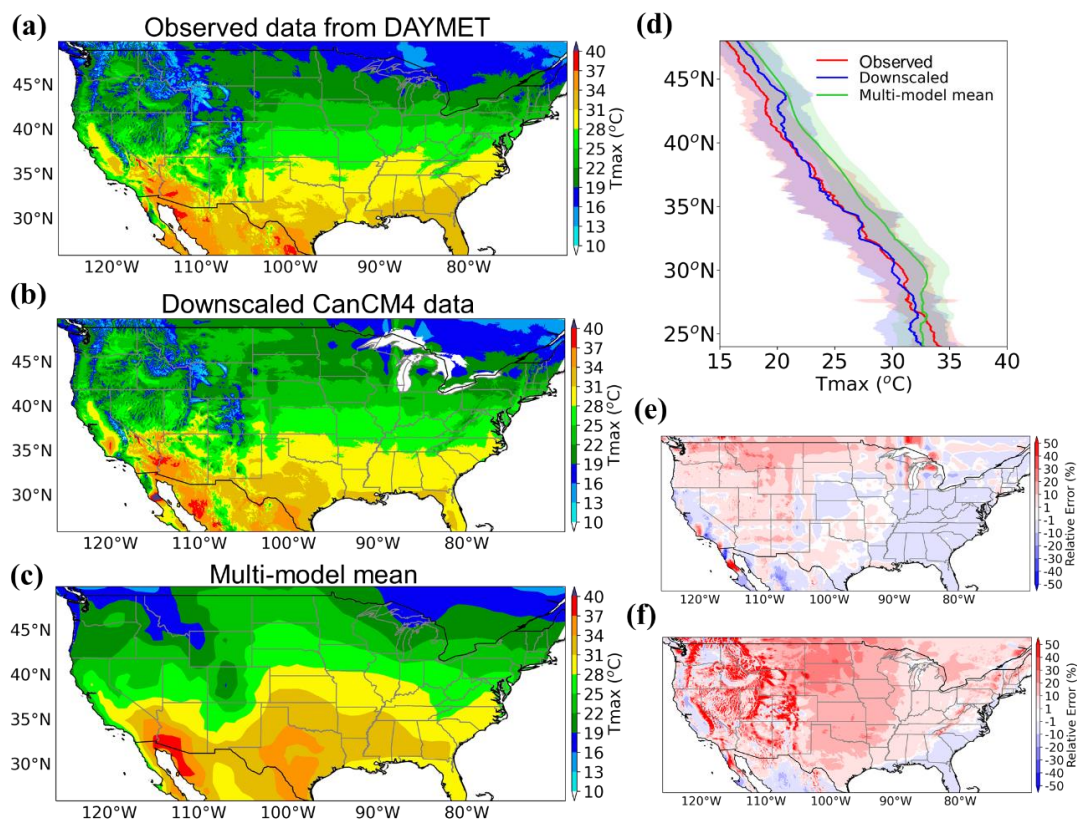


Figure 7.7 Comparison of mean maximum temperature forecast in the growing season (May to October) in 2019 using different methods. Seasonal mean T_{max} using (a) observed data from DAYMET; (b) downscaled CanCM4; (c) multi-model mean; (d) latitudinal profiles of seasonal mean T_{max} . Color lines indicate the mean value per degree latitude for T_{max} from the three different methods. Shading denotes the standard deviation and relative errors (%) of seasonal mean T_{max} of (e) downscaled CanCM4 and (f) multi-model mean relative to the observation. Note that August data is not included due to non-availability.

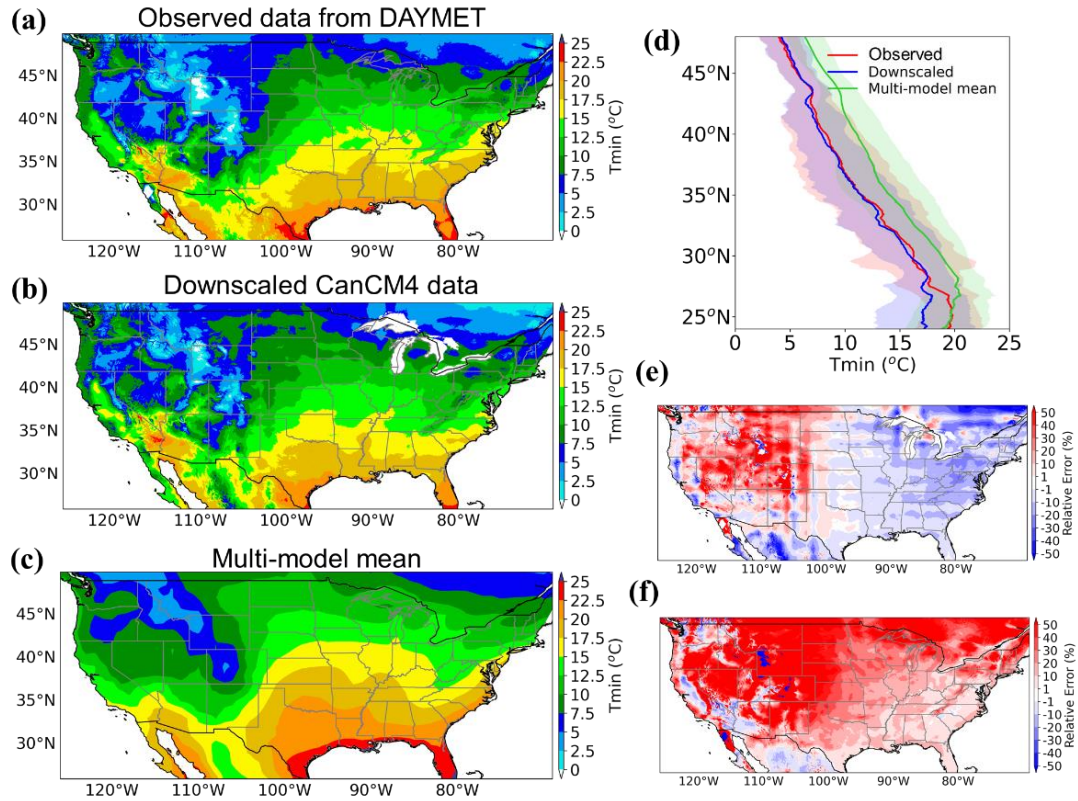


Figure 7.8 Comparison of mean minimum temperature forecast in the growing season (May to October) in 2019 using different methods. Seasonal mean T_{min} using (a) observed data from DAYMET; (b) downscaled CanCM4 data; (c) multi-model mean; (d) latitudinal profiles of seasonal mean T_{min} . Color lines indicate the mean value per degree latitude for T_{min} from the three different methods. Shading denotes the standard deviation and relative errors (%) of seasonal mean T_{min} of (e) Downscaled CanCM4 and (f) multi-model mean relative to the observation. Note that August data is not included due to non-availability.

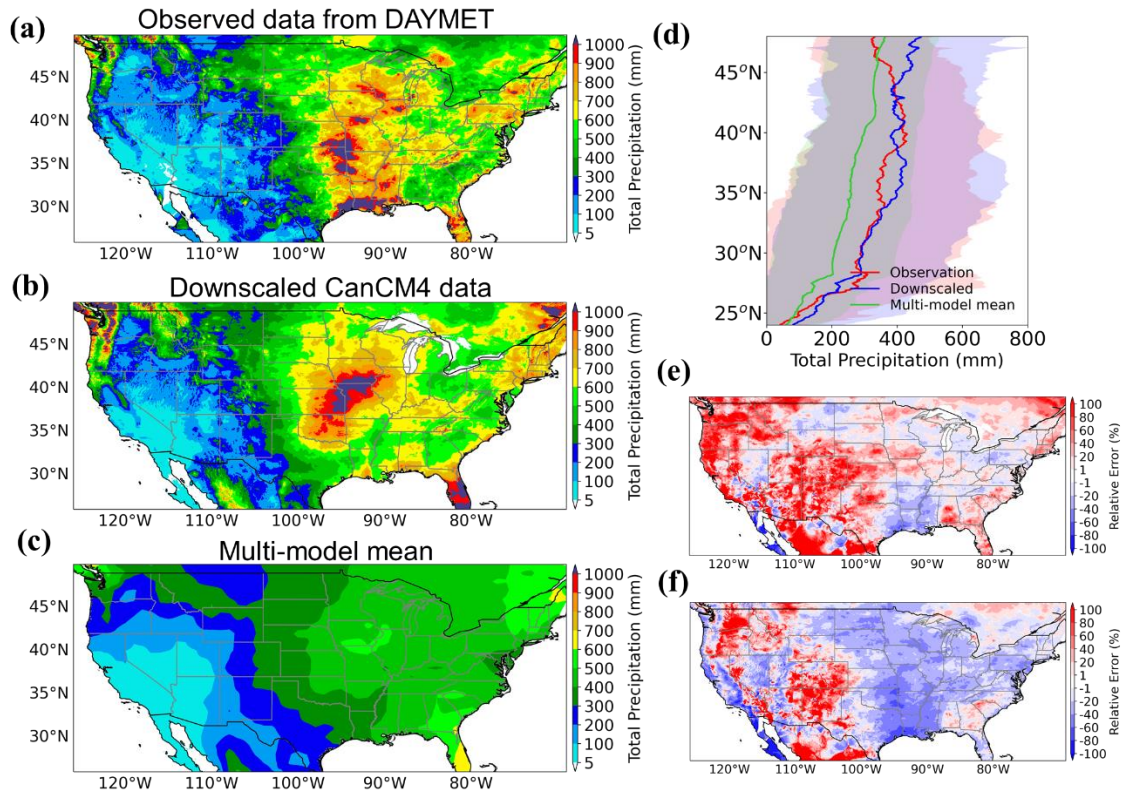


Figure 7.9 Comparison of total precipitation forecast in the growing season (May to October) in 2019 using different methods. Seasonal mean T_{min} using (a) observed data from DAYMET; (b) downscaled CanCM4 data; (c) multi-model mean; (d) latitudinal profiles of seasonal precipitation. Color lines indicate the mean value per degree latitude for precipitation from the three different methods. Shading denotes the standard deviation and Relative errors (%) of seasonal precipitation of (e) downscaled CanCM4 and (f) multi-model mean relative to the observation. Note that August data is not included due to non-availability.

Figures 7.7 to 7.9 revealed that the downscaled CanCM4 data exhibited better performance than the multi-model mean in the forecast of T_{max} , T_{min} , and precipitation at a regional scale and hence this data could be possibly used in regional real-time crop modeling with careful attention to the relatively high variability of the downscaled precipitation forecast at local scales.

7.3.3. Predictions at Different Lead Times

In order to investigate the reliability of the downscaling method at different lead times, predictions with 0 to 5-month lead times were examined. The growing season of cotton in the TRP region usually begins from the planting date in May and continues to October, suggesting a lead time of 5 months. Here, the predictions in June 2019 at different lead times were taken as an example (Figure 7.10). For T_{max} and T_{min} , the downscaling signature can be persistent for a relatively long lead time, as much as 5 months. However, the downscaling signature for precipitation diminished quickly as the lead time increased, which was found primarily in warm seasons (Figure F7, Appendix F). This is because the influence of initial conditions decayed with a longer simulation time (Lavers et al., 2009). In contrast, precipitation in cold months like December showed better performance (Figure 7.11), which is consistent with other studies (Narapusetty et al., 2018; Yazdandoost et al., 2020). Therefore, the decline of the downscaling signature in precipitation was not evident in cold seasons (Figure 7.11).

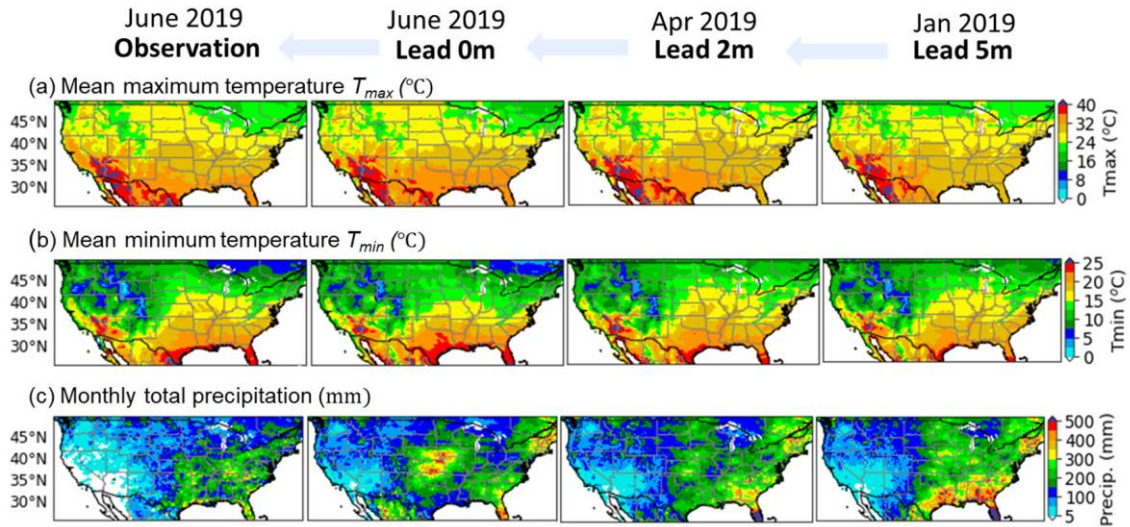


Figure 7.10 Mean maximum/minimum temperature and total precipitation predictions for June 2019 at different lead times using the downscaled method.

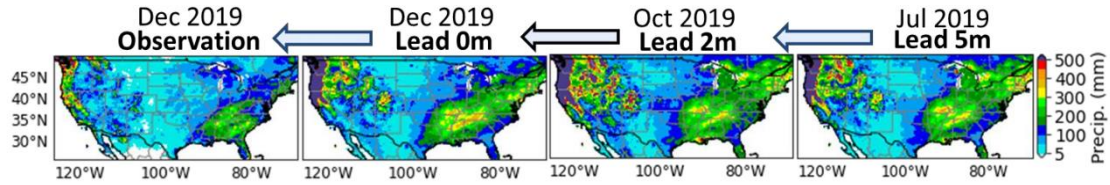


Figure 7.11 Monthly total precipitation predictions for December 2019 at different lead times using the downscaled method.

7.3.4. Cross-validation at Local Scale

To test the forecast skill of the downscaling method at a local scale, cross-validation for both the hindcast and forecast periods was performed at the Chillicothe station (Figure 7.12). During the hindcast period, the downscaling method significantly improved the forecast skill of the raw CanCM4 output. The RMSE of the T_{max} , T_{min} , and seasonal precipitation reduced from 6.3 °C, 4.1 °C, and 290 mm (the downscaled CanCM4) to 2.2 °C, 1.6 °C, and 203 mm (the raw CanCM4), respectively. The

precipitation forecasts showed higher variability than did T_{max} and T_{min} . Daily forecasts of T_{max} and T_{min} , and monthly forecasts of precipitation in 2019 are illustrated in Figure 7.13. Daily T_{max} and T_{min} forecasts exhibited high prediction skills ($R^2=0.72$ for T_{max} and $R^2=0.71$ for T_{min}), while the precipitation in this year was forecasted with poor skill.

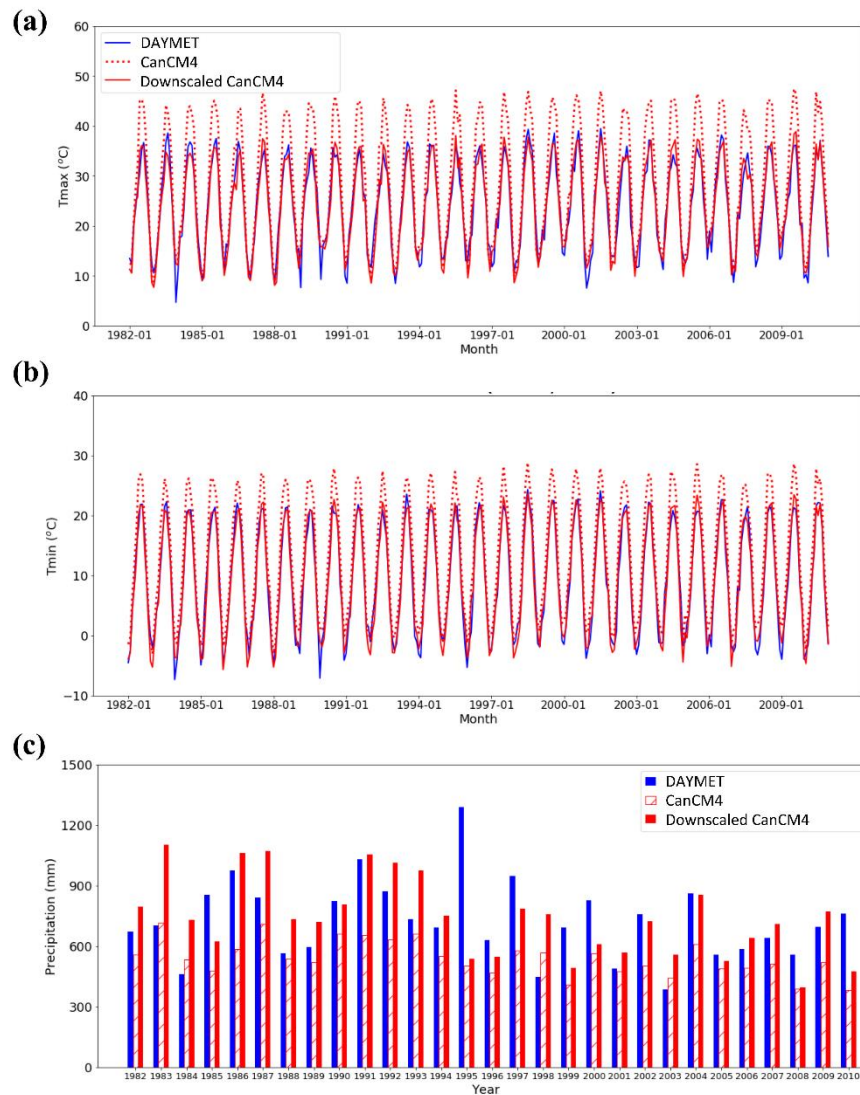


Figure 7.12 Comparison of monthly mean (a) T_{max} and (b) T_{min} , and seasonal total precipitation for the reference period (1982-2010) using DAYMET (Observation), CanCM4, and downscaled CanCM4 data at the Chillicothe station.

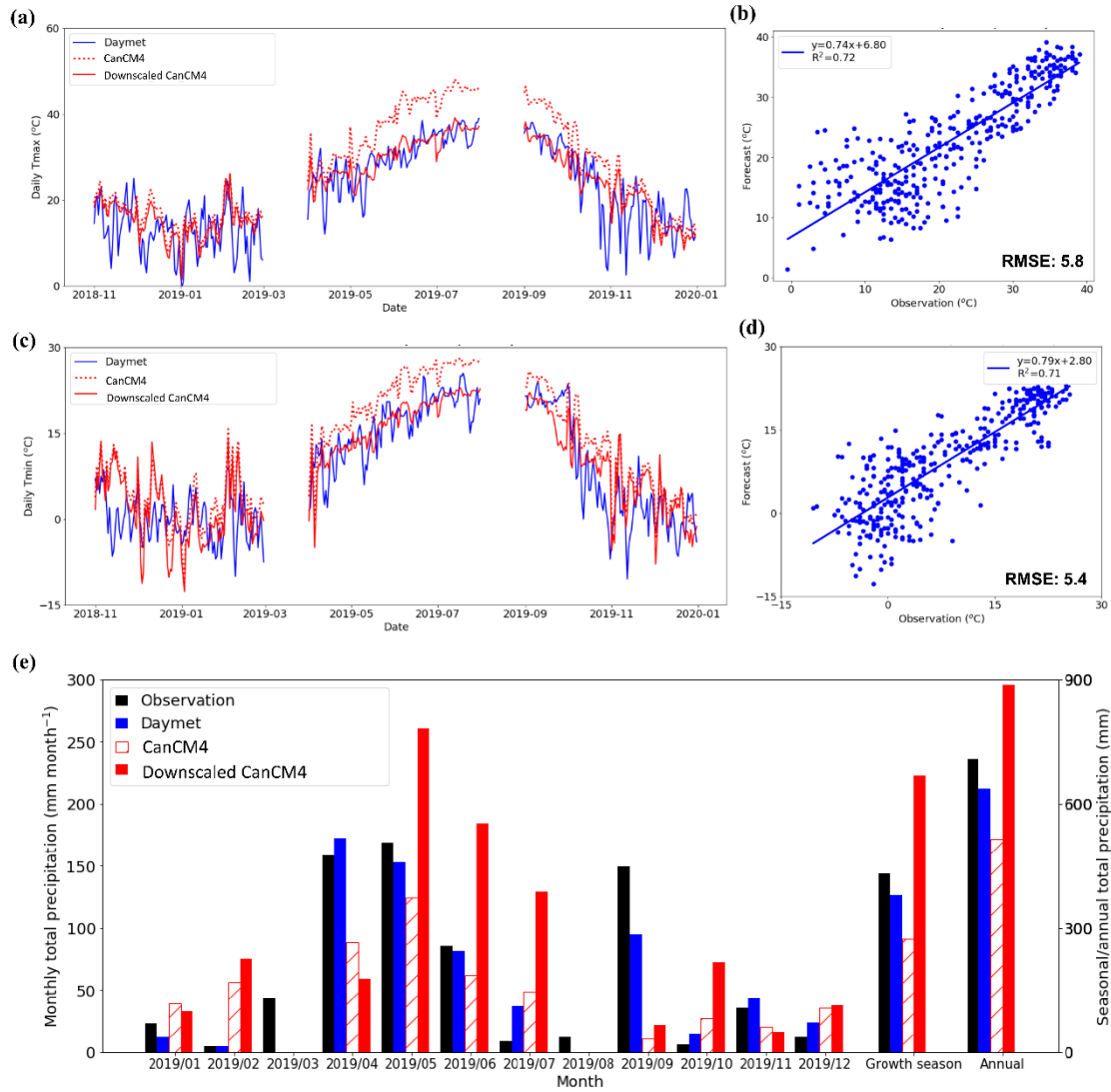


Figure 7.13 Comparison of daily (a) (b) T_{max} , (c)(d) T_{min} , and (e) monthly precipitation from DAYMET (Observation), CanCM4, and downscaled CanCM4 in 2019 at the Chillicothe station. Note that the black bar in (e) represents field observation of rainfall. March and August data were unavailable.

7.3.5. Test for Crop Modeling

To test the usability of high-resolution seasonal weather forecasts generated in this study in local crop modeling, the yield prediction for the 2020 growing season at lead 0 month using different methods at the Chillicothe station was compared (Figure

7.14). The accumulated precipitation of the downscaled forecasts in the 2020 growing season exhibited good performance compared with the field observation, but both the raw CanCM4 output and multi-model mean methods significantly underestimated the accumulated precipitation by 49% and 43%, respectively (Figure 7.14a). The downscaling method also showed the best performance in T_{max} and T_{min} , compared with the other two methods (Figure 7.14b, c). The mean T_{max} and T_{min} forecasted using the downscaling method showed a slight underestimation (about 1-2%) compared with field observations, while appreciable overestimation was found using the raw model outputs and multi-model mean. With the use of multi-model mean, the relative errors of T_{max} and T_{min} reduced from 27-30% (CanCM4) to 15-25% (Multi-model mean).

Seed cotton yields predicted by the three methods were reasonable in the 2020 growing season, with RE within 7-15% relative to the field observations (Figure 7.14d). The downscaling method predicted the irrigation amount closer to the field observations, while the irrigation amounts predicted by the raw CanCM4 and the multi-model mean were more than twice the observations (Figure 7.14e). The unrealistic high irrigation amounts predicted in the latter two methods were likely due to the underestimation of the rainfall and increased crop evapotranspiration due to air temperature overestimation.

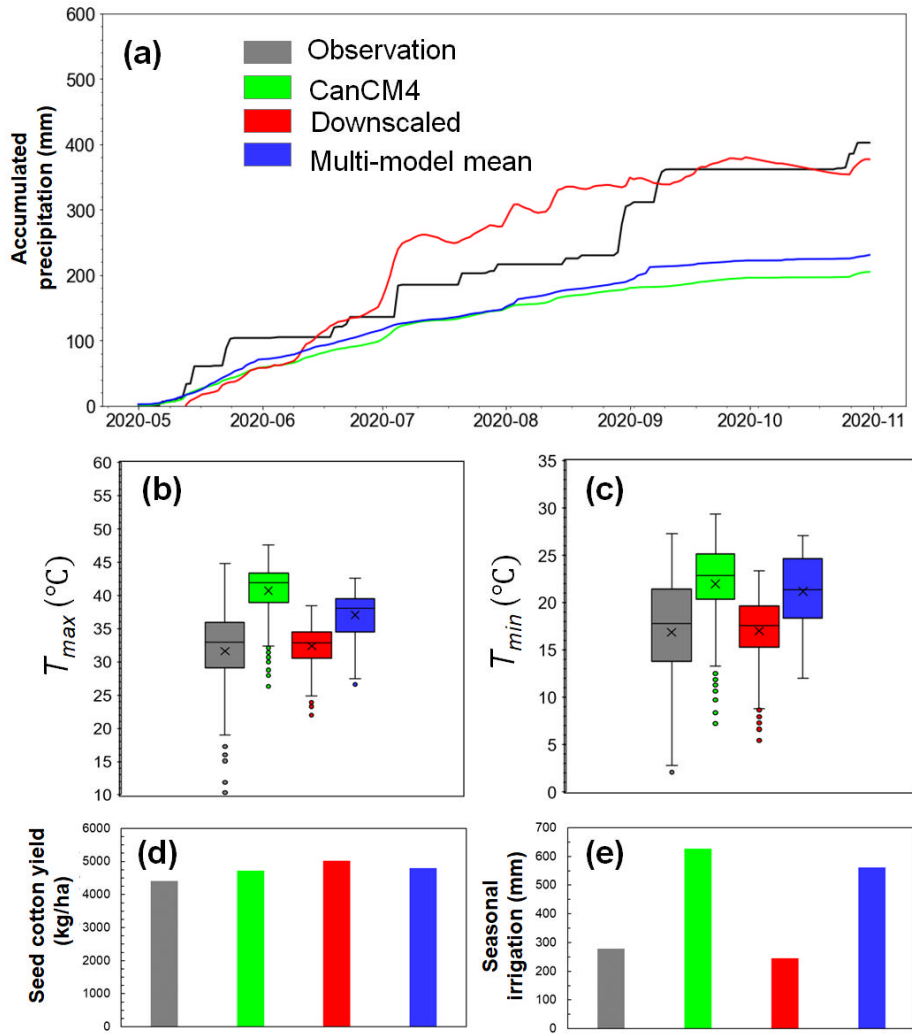


Figure 7.14 Comparisons of 2020 growing season prediction at the Chillicothe station using different weather datasets (lead 0m). (a) Accumulated precipitation; (b) T_{max} ; (c) T_{min} ; (d) seed cotton yield; and (e) seasonal irrigation.

The real-time prediction at different lead times using the downscaling method and multi-model mean were further examined (Figure 7.15). The downscaled method exhibited better forecast skills in the season precipitation, irrigation demand, and seed cotton yield than using the multi-model mean. At the beginning of the season in May 2020 (lead 5-month), the downscaling method also provided reasonable rainfall, yield,

and seasonal irrigation forecasts, within relative errors of 14%-18%. As time proceeds, the prediction would be expected closer to the observations. However, irrigation demand predicted by using the downscaling method showed relatively large variability due to the combined effect of rainfall and temperature predictions, but the variation was still much less significant than that of the multi-model mean.

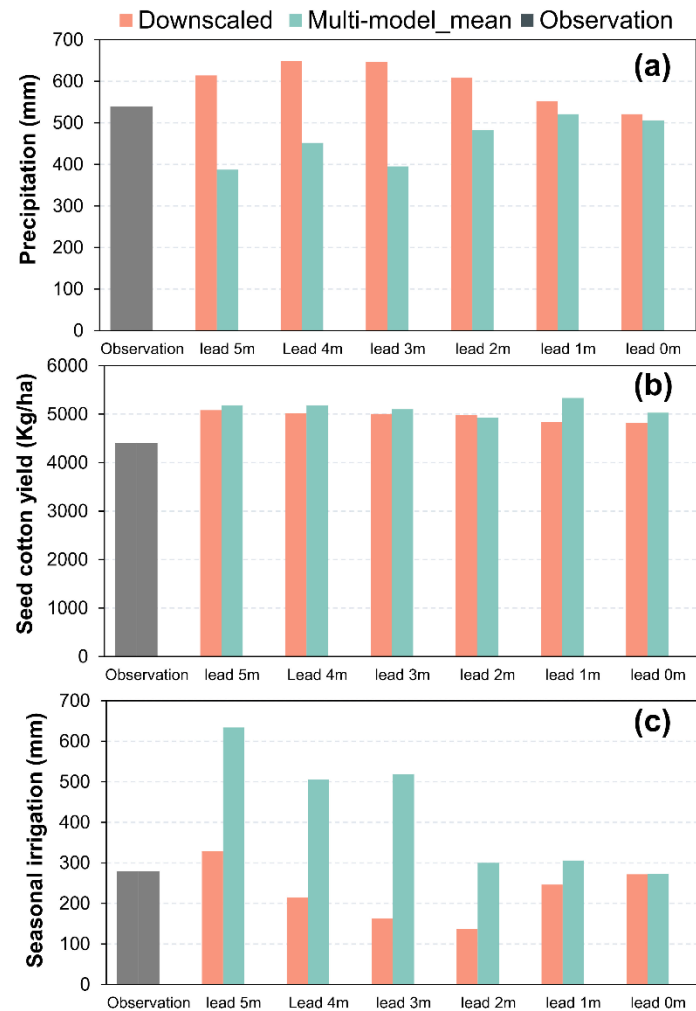


Figure 7.15 Comparisons of (a) seasonal precipitation, (b) seed cotton yield, and (c) seasonal irrigation predictions using the downscaled and multi-model methods in the 2020 growing season at the Chillicothe station at different lead times.

7.4. Conclusions

In this chapter, an improved bias-corrected downscaling method was applied with both mean and variance correction to generate a 1-km grid-level daily weather projection (maximum and minimum air temperatures, and precipitation) over the CONUS using a representative NMME dataset, namely CanCM4. The usability of downscaled seasonal weather forecasts at a regional scale and real-time crop modeling at a local scale were evaluated by comparing with the raw CanCM4 outputs and the multi-model mean of three NMME models (i.e., CCSM4, GEOS-5, and CanCM4). The major findings include: (1) the post-processing like proper downscaling of the raw NMME outputs was required before applying them in seasonal irrigation management and crop yield prediction; (2) the bias correction downscaling method significantly improved the performance of the CanCM4 outputs and overperformed the multi-model mean, but its performance on precipitation prediction varied with time and location; and (3) the high-resolution seasonal weather forecasts generated in this study ensured robust and reliable predictions of regional or local crop yields over the CONUS region.

8. REDUCING THE UNCERTAINTY IN CROP WATER STRESS INDEX (CWSI)

MODELS FOR IRRIGATION SCHEDULING

Improving deficit irrigation management in water-stressed regions requires an accurate estimation of crop water stress. The Crop Water Stress Index (CWSI), determined both empirically and theoretically, has been widely used to indicate crop water stress and schedule irrigation. However, the non-water stress boundary in the original theoretical CWSI model, derived with the assumption of evaporation from a free water surface, cannot accurately represent potential evapotranspiration from a crop surface. Here, we improved the representation of the non-water stress boundary by including the calculation of canopy resistance (r_c) over a saturated crop surface (CWSI-PEc) or a well-watered crop surface (CWSI-PET). In addition, to reduce intensive use of inputs as required in the theoretical models, a novel, semi-empirical CWSI model based on the Priestly-Taylor equation (CWSI-PT) was developed. The CWSI calculated by the original model and three newly developed models in this study were evaluated against a soil moisture-based water stress coefficient simulated using a calibrated CROPGRO-Cotton module of the Decision Support System for Agrotechnology Transfer (DSSAT) Cropping System Model (CSM) at Chillicothe in the Texas Rolling Plains during the 2020 cotton growing season. Results indicated that the CWSI-PET model outperformed the other three methods with less variability and uncertainty. The CWSI-PT model provided CWSI estimates comparable to the other three models, but with less input requirement. Errors were noted when applying the four CWSI methods in the field with

a low percentage of canopy coverage. The water deficit index (WDI), a modification of CWSI, with the consideration of normalized difference vegetation index (NDVI) was then suggested to improve the model performance with incomplete canopy coverage.

8.1. Introduction

Irrigation water demand accounts for nearly 70% of global anthropogenic freshwater demand (FAO, 2016), and it is by far the largest water use sector in the world. Irrigated agriculture is fundamental to global food security. From 1961 to 2018, global irrigated agriculture has doubled and increased to 22% of the total cropland in 2018, contributing to about 40% of global food production (FAO, 2018). At the same time, availability of water resources for irrigated agriculture faces multiple challenges, including growing food demand, increasing global mean temperature, and changing precipitation patterns under climate changes, as well as competition from domestic and industrial users due to population growth, rising standard of living, and economic development (Florke et al., 2018; Haddeland et al., 2014). The situation is exacerbated in semi-arid regions which are experiencing a decline in water supplies. Regulated deficit irrigation can conserve water resources and optimize production, and it has been widely investigated as a sustainable strategy to meet these challenges. The development and optimization of deficit irrigation requires a better understanding of crop responses under water stress. Therefore, developing tools that enable an accurate estimation of crop water stress is critical for deficit irrigation management.

The traditional methods for crop water stress monitoring include soil water measurement (González-Dugo et al., 2006), soil water balance method (Osroosh et al.,

2016), and plant-based method, e.g., sap flow measurement (Han et al., 2018), direct measurement of leaf water potential (Bellvert et al., 2016; Zarco-Tejada et al., 2012), and stomatal conductance (Agam et al., 2013; Ballester et al., 2013). Soil water measurement is time-consuming. In addition, single or several point measurements usually cannot reflect the overall status of the field. The soil water balance approach is an indirect estimation of soil moisture status by calculating crop evapotranspiration, rainfall, runoff, and irrigation amount. It has a relatively high uncertainty due to the accumulation of measurement errors, and therefore requires calibration with actual soil moisture measurements. Plant-based approaches can provide reliable measurements, but they are also time-consuming and unsuitable for automation (Ihuoma and Madramootoo, 2017).

The Crop Water Stress Index (CWSI), which uses the canopy-to-air temperature difference to quantify the crop water stress, has been widely used to indicate crop water status and schedule irrigation. Two CWSI methods have been previously adopted and evaluated, i.e., an empirical method first introduced by Idso et al. (1981) and a theoretical method developed by Jackson et al. (1981). Both methods require the calculation of a non-water stress baseline and an upper boundary representing the canopy-to-air temperature difference for a well-watered crop surface with full transpiration and a dry crop surface with non-transpiration conditions. The empirical method uses invariant lower and upper boundaries by developing a linear relationship between canopy-to-air temperature difference and the vapor pressure deficit (Idso et al., 1981). The empirical method requires less data inputs, but high uncertainty exists due to

the constant baselines used. Since the baselines are dependent on weather variables, e.g., solar radiation and wind speed, substantial errors were reported when constant baselines were used in different climate conditions (Gonzalez-Dugo et al., 2014; Payero and Irmak, 2006) or even in the same field (Gonzalez-Dugo et al., 2014). Compared to the empirical method, the theoretical method is derived based on the energy balance equation and thereby shows more stability under different climate conditions (Han et al., 2018; Jackson et al., 1988; O'Shaughnessy et al., 2012). However, the non-water stress boundary in the original theoretical CWSI model is derived with the assumption of evaporation from a free water surface, which cannot accurately represent potential evapotranspiration from a crop surface. The major uncertainty of the CWSI method is the determination of non-water stress boundary, which could be attributed to the use of different aerodynamic resistance (r_a) and crop resistance (r_c) (Agam et al., 2013; Han et al., 2018). For example, seasonal average r_a was recommended by several studies (Clawson et al., 1989; Han et al., 2018; Jalalifarahani et al., 1993). Also, daily value of r_a and r_c , calculated using the FAO Penman-Monteith method (Allen, 1998), was suggested by O'Shaughnessy et al. (2012).

Here, the representation of the non-water stress boundary was improved by including the calculation of canopy resistance (r_c) over a saturated crop surface (CWSI-PEc) or a well-watered crop surface (CWSI-PET). In addition, to reduce the intensive input requirement as in the theoretical models, a novel, semi-empirical CWSI model based on the Priestly-Taylor equation (CWSI-PT) was developed. The specific objectives were therefore to (1) compare three non-water stress boundary equations

under the assumption of free water surface, saturated crop surface, and well-watered crop surface; (2) derive a new non-water stress boundary equation with the assumption of free water surface using a less data-intensive method, i.e., Priestly-Taylor equation; and (3) evaluate the uncertainty of the four models.

8.2. Methodology

8.2.1. Crop Water Stress Index (CWSI) Calculation

CWSI is defined as:

$$CWSI = \frac{(T_c - T_a) - (T_c - T_a)_L}{(T_c - T_a)_U - (T_c - T_a)_L} \quad (8.1)$$

where T_c is the canopy temperature, °C; T_a is the air temperature, °C; $(T_c - T_a)_U$ is the upper boundary of $(T_c - T_a)$, representing dry surface condition; and $(T_c - T_a)_L$ is the lower boundary of $(T_c - T_a)$, representing the non-water-stressed baselines.

Based on the energy balance equation, the net radiation flux at a crop canopy surface is calculated as:

$$R_n = G + H + \lambda E \quad (8.2)$$

where R_n is net radiation flux, MJ m⁻² d⁻¹; G is soil heat flux, MJ m⁻² d⁻¹; H is the sensible heat flux, MJ m⁻² d⁻¹; and λE is latent heat flux, MJ m⁻² d⁻¹; and λ is the latent heat of vaporization, MJ kg⁻¹.

The sensible heat flux can be expressed as:

$$H = \frac{\rho C_p (T_c - T_a)}{r_a} \quad (8.3)$$

The latent heat flux can be expressed as:

$$\lambda E = \frac{\rho C_p (e_c^* - e_a)}{\gamma (r_a + r_c)} \quad (8.4)$$

where ρ is the density of air approximated as a function of air temperature and pressure, kg m^{-3} ; C_p is the specific heat of moist air, $1.013 \text{ kJ kg}^{-1} \text{ }^\circ\text{C}^{-1}$; γ is the psychrometric constant, $\text{kPa } ^\circ\text{C}^{-1}$; e_c^* is the saturation vapor pressure at the canopy temperature T_c , kPa ; e_a is the actual vapor pressure of the air, kPa ; r_a is the aerodynamic resistance, s m^{-1} ; and r_c is the canopy resistance, s m^{-1} .

If the temperature difference between canopy and air is not large, the slope of saturation vapor pressure curve at the canopy surface can be approximated as (Eichinger et al., 1996):

$$\Delta = \left. \frac{de^*}{dT} \right|_{T_c} \approx \frac{(e_c^* - e_a^*)}{(T_c - T_a)} \quad (8.5)$$

where Δ is the slope of saturation vapor pressure, $\text{kPa } ^\circ\text{C}^{-1}$; and e_a^* is the saturation vapor pressure of the air, kPa .

Substituting (3), (4), and (5) to (1), one obtains:

$$T_c - T_a = \frac{r_a}{\rho C_p} \frac{\gamma(1 + \frac{r_c}{r_a})}{\Delta + \gamma(1 + \frac{r_c}{r_a})} (R_n - G) - \frac{e_a^* - e_a}{\Delta + \gamma(1 + \frac{r_c}{r_a})} \quad (8.6)$$

8.2.2. Derivation of the Upper and Lower Boundary

The upper boundary of $(T_c - T_a)$ is found by assuming the latent heat flux H as zero, which represents evapotranspiration from a completely dry surface. Then equation (8.6) becomes:

$$(T_c - T_a)_U = \frac{r_a(R_n - G)}{\rho C_p} \quad (8.7)$$

Soil heat flux can be considered as 0 for daily analysis. For hourly or shorter duration calculations, $G = 0.1 R_n$ during the daylight period, and $G = 0.5 R_n$ during the nighttime period.

The lower boundary of $(T_c - T_a)$ is a non-water stressed baseline, which represents a fully transporting crop. $(T_c - T_a)_L$ is derived based on different assumptions, i.e., free water surface, saturated crop surface, and well-watered crop surface. Figure 8.1 shows the aerodynamic resistance (r_a) and canopy resistance (r_c) in different non-water stress baseline models, which was adapted from Katerji and Rana (2011). Here, the representation of the non-water stress boundary was improved by including the calculation of canopy resistance (r_c) over a saturated crop surface (CWSI-PEc) or a well-watered crop surface (CWSI-PET). In addition, to reduce the intensive inputs as required in the theoretical models, a novel, semi-empirical CWSI model based on the Priestly-Taylor equation (CWSI-PT) was also developed.

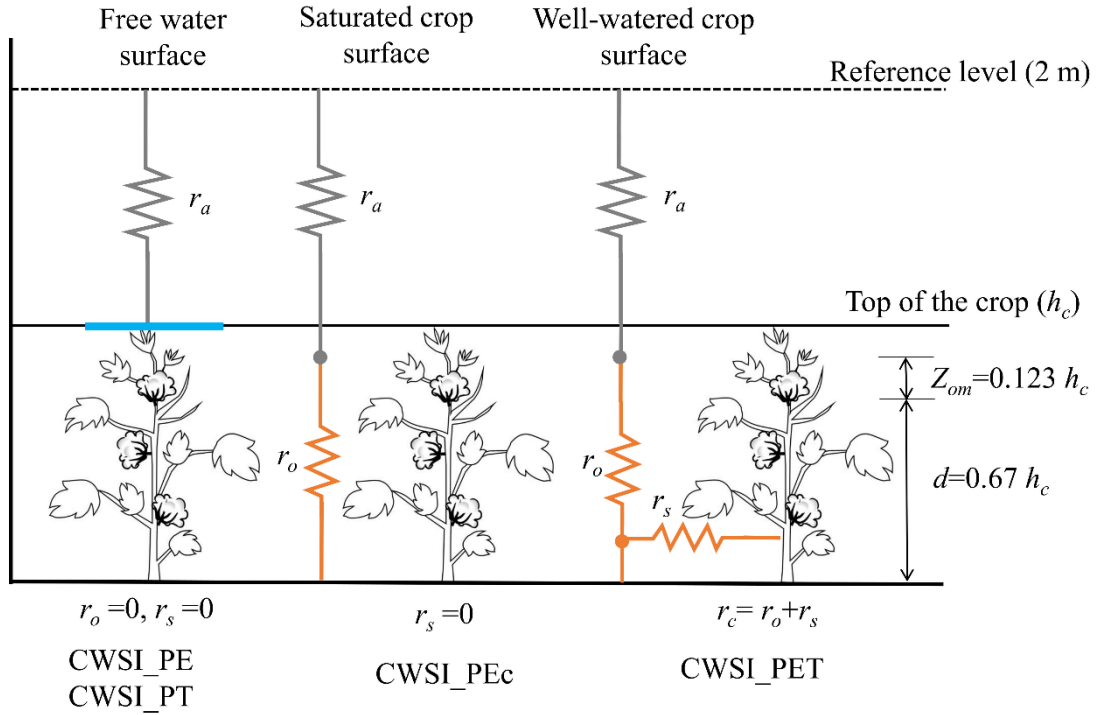


Figure 8.1 Schematic representation of aerodynamic resistance (r_a) and canopy resistance (r_c) in different non-water stress baseline models. r_o is the crop structure resistance, and r_s is the stomatal resistance. After Katerji and Rana (2011).

CWSI_PE (Potential evaporation from free water surface) represents evaporation from a free water surface or on the crop surface with 100% relative humidity. This variable is only theoretical, and it allows the calculation of canopy to air temperature differences due to the evaporation demand of the atmosphere. It is suitable to calculate the air/surface temperature difference for large surfaces of water bodies (e.g., lakes, seas, and oceans), saturated soil, or crop surface with all the hypotheses being met (Figure 8.1). With the assumption of free water surface, and the canopy resistance $r_c = 0$, equation (8.6) becomes:

$$(T_c - T_a)_L = \frac{r_a}{\rho c_p} \frac{\gamma}{\Delta + \gamma} (R_n - G) - \frac{e_a^* - e_a}{\Delta + \gamma} \quad (8.8)$$

The aerodynamic resistance r_a can be calculated as (Allen, 1998):

$$r_a = \frac{\ln \left[\frac{Z_u - d}{Z_{om}} \right] \ln \left[\frac{Z_e - d}{Z_{ov}} \right]}{(0.41)^2 U_Z} \quad (8.9)$$

where Z_u and Z_e are the respective heights for wind speed and humidity measurements (here, $Z_u = 2$ m, $Z_e = 2$ m); d is the zero-plane displacement height, at which the wind speed is considered as zero, $d = 0.67 h_c$; Z_{om} is the roughness height governing the momentum transfer, $Z_{om} = 0.123 h_c$; Z_{ov} is the roughness height governing heat and vapor transfer, $Z_{ov} = 0.0123 h_c$; the value 0.41 is the von Kármán constant; U_Z is the wind speed at 2-m height, and h_c is the mean crop height.

CWSI-Pec (Potential crop evaporation) represents evaporation from a crop surface having all surfaces (including leaves, stems, and soil) saturated. Therefore, there is no biological control of evaporation, i.e., $r_s = 0$, but the water vapor transfer is still resistant to the crop structure (r_o). As such, equation (8.6) becomes:

$$(T_c - T_a)_L = \frac{r_a}{\rho C_p} \frac{\gamma(1 + \frac{r_o}{r_a})}{\Delta + \gamma(1 + \frac{r_o}{r_a})} (R_n - G) - \frac{e_a^* - e_a}{\Delta + \gamma(1 + \frac{r_o}{r_a})} \quad (8.10)$$

where r_o is the crop structure resistance. Mean values of r_o for different crops with various heights and climate conditions can be found in Katerji and Rana (2011).

CWSI-PET (Crop evapotranspiration) represents evapotranspiration from a well-watered crop surface. No saturation can be found on the evaporative surfaces, and equation (8.11) is used here:

$$(T_c - T_a)_L = \frac{r_a}{\rho C_p} \frac{\gamma(1+\frac{r_c}{r_a})}{\Delta + \gamma(1+\frac{r_c}{r_a})} (R_n - G) - \frac{e_a^* - e_a}{\Delta + \gamma(1+\frac{r_c}{r_a})} \quad \text{with} \quad r_c = \frac{r_s^*}{LAI_{active}} \quad (8.11)$$

where r_s^* is the stomatal resistance of a well-illuminated leaf, the value for cotton is about 237.5 (Evenson and Rose, 1976). LAI_{active} is the active leaf area index (LAI), which is about 0.5 LAI (Allen, 1998). LAI of cotton under well-irrigated, non-nutrient limitation is obtained from (Bezerra et al., 2015).

8.2.3. Lower Boundary Derived from the Priestley-Taylor Method

Assuming that a uniform, saturated surface, similar to CWSI-PE, the ratio of the sensible heat flux to the latent heat flux is the Bowen ratio (B):

$$B = \frac{H}{\lambda E} = \frac{\frac{\rho C_p (T_c - T_a)}{r_a}}{\frac{\rho C_p (e_c^* - e_a)}{\gamma(r_a + r_c)}} = \gamma \frac{(T_c - T_a)}{(e_c^* - e_a)} \quad \text{with} \quad r_c = 0 \quad (8.12)$$

Priestley and Taylor (1972) suggested a more straightforward form of the Penman method (Penman, 1948) by recognizing that the first term in the equation is larger than the second term by a factor of about 4.

$$\lambda E = \alpha \frac{\Delta}{\Delta + \gamma} (R_n - G) \quad (8.13)$$

where α is the PT coefficient.

Bowen ratio can be expressed using the PT equation as:

$$B = \frac{1 - \alpha \frac{\gamma}{\Delta + \gamma}}{\alpha \frac{\gamma}{\Delta + \gamma}} \quad (8.14)$$

Combing equations (8.5), (8.12), and (8.14), one gets:

$$(T_c - T_a)_L = \frac{e_a^* - e_a}{\frac{\gamma C}{1-C} - \Delta} \quad (8.15)$$

where

$$C = \alpha \frac{\Delta}{\Delta + \gamma} \quad (8.16)$$

8.2.4. Water Stress Based on Soil Water Balance

The water stress coefficient (K_s) is related to CWSI as:

$$CWSI = 1 - K_s \quad (8.17)$$

K_s can be calculated as (Allen, 1998):

$$K_s = \frac{TAW - D_r}{TAW - RAW} \quad (8.18)$$

where D_r is the root zone depletion in mm, TAW is the total available soil water in the root zone in mm, and RAW is the readily available water in mm.

Soil water content was simulated using a calibrated CSM-CROPGRO-Cotton module of the Decision Support System for Agrotechnology Transfer (DSSAT) model (Hoogenboom et al., 2019; Jones et al., 2003). The DSSAT CSM-CROPGRO-Cotton module was previously calibrated and validated by Adhikari et al. (2017) using the measured data (2011-2015) at the study site, with an average percent error in seed cotton yield prediction of -10.1% and -1.0% during the calibration and validation periods. The minimum weather data required for the crop model includes daily T_{max} and T_{min} (°C), precipitation (mm), and solar radiation (MJ m^{-2}), which was obtained from an on-site weather station.

8.2.5. Field Experiment and Data Collection

A field experiment was conducted at the Chillicothe Research Station in Texas Rolling Plain, Texas, USA (34.25°N, 99.52°W, elevation 447 m) to evaluate the performance of the four CWSI methods (Figure 8.2). Cotton (Pyhtogen 350) was planted on 15 June 2020 with a seeding rate of 4 seeds per ft (40 in rows). Half of the area covered by the center pivot system was utilized for this study, which was divided into pie slices, with each occupying 1/12th of the total area (Figure 8.1c). The broad and even spacing of all treatments allowed for a robust analysis of trends across different levels of water stresses. The experiment was laid out in a randomized complete block design, with three replications of four irrigation scheduling treatments (90%, 60%, 30%, and 0% ET replacements), representing different water stress. During the growing season, irrigation amount was applied based on the reference evapotranspiration and the growth stage-based crop coefficients developed by (Ko et al., 2009) for cotton, which was further multiplied by percent ET replacement treatment values (e.g., 0.60 for 60% ET replacements, Table 8.1). Reference evapotranspiration was calculated using the Penman-Monteith method (Allen, 1998). Irrigation water was applied weekly as prescribed by the treatments.

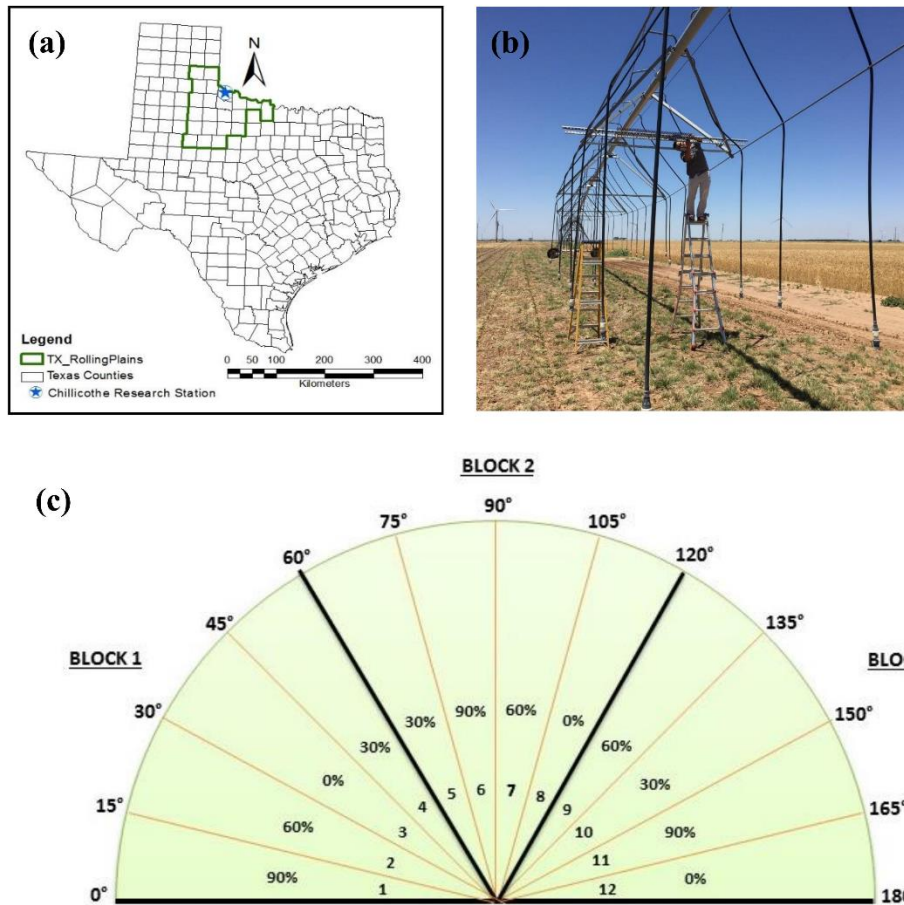


Figure 8.2 Experimental plot plans at the Chillicothe research station. (a) Location of the Chillicothe Research Station; (b) sensor platform setup; and (c) experimental layout on half of a two-tower pivot.

Hourly meteorology was obtained at a nearby weather station, including air temperature, relative humidity, solar radiation, and wind speed. Hourly data from 11:00 to 14:00 was used to estimate CWSI. Canopy temperature was measured by SI-121-SS an infrared radiometer (Apogee Instruments, Logan, UT), which is capable of making non-contact surface temperature measurements of the crop canopy. NDVI, a spectral index that is highly correlated with cotton crop biomass (Gutierrez et al., 2012), was

determined using measurements made by S2-412-SS spectral sensors (Apogee Instruments, Logan, UT). The system included an AtlasLink GNSS device (Hemisphere, Scottsdale, AZ), allowing assignment of plot ID information to the data based on geolocation information of the system within the field. A CR1000X datalogger (Campbell Scientific, Logan, UT) was used to store and export data wirelessly. Sensor systems were placed on platforms mounted in the trusses of the pivot. The canopy temperature and NDVI sensors faced downward at a 45° angle.

Table 8.1 Development Stages and Basal Crop Coefficient K_{cb} of Seed Cotton (Ko et al., 2009).

DAP	Date	Development stage	K_{cb}
7	6/22/2020	Seeding	0.40
8-45	7/30/2020	1st square	0.45
46-65	8/19/2020	1st bloom	0.80
66-86	9/9/2020	Max bloom	1.08
87-110	10/3/2020	1st open	1.23
111-125	111-125	25% open	1.25
126-133	126-133	50% open	1.05
134-151	134-151	95% open	0.60
152-162	152-162	Pick	0.1

Note: DAP, days after planting.

8.2.6. Model Comparison

The differences between the CWSI calculated using the four models and soil water balance method were evaluated by the root-mean-square error (RMSE) and the mean bias difference (MBD), as shown in equations (8.18) and (8.19):

$$RMSE = \sqrt{\frac{\sum_{i=1}^n (X_i - Y_{oi})^2}{n}} \quad (8.18)$$

$$MBD = \frac{\sum_{i=1}^n (X_i - Y_{oi})}{n} \quad (8.19)$$

where X_i and Y_{0i} are the i^{th} calculated CWSI using the soil water balance methods and the four CWSI models, respectively; and n is the number of observations. The best method has RMSE and MBD values equal to 0.

8.3. Results and Discussion

8.3.1. Canopy Cover during the Growing Season

In the experiment, plot-specific NDVI cannot be collected while the pivot was stationary (multiple plots must be covered) or watering (the entire field cannot be watered in the hours surrounding solar noon). Therefore, weekly “dry runs” of the pivot were made to measure NDVI, as well as the canopy temperature, in the hours surrounding solar noon in the time between watering events. The relationships between canopy cover and NDVI were developed based on measurements in the 2021 growing season. Canopy cover and height measurements were collected using UAV flights on four dry run days of July 8, July 31, Aug 22, and Aug 26, 2021. A least-square fit was used to identify the relationship between canopy cover and NDVI, showing *Percent canopy cover* = $0.933 + 0.109 * NDVI$ with $R^2=0.68$ (sample size $n=60$). The canopy cover for each treatment in the 2020 cotton growing season is shown in Figure 8.3. Five measurements for each ET replacement in 2020 were made on July 20, 2020 (Day 35), Aug 6 (Day 52), Aug 19 (Day 65), Aug 27 (Day 73), and Sep 9 (Day 85).

The canopy coverage measured in all treatments was larger than 0.31 (the minimum value was from the 30% ET replacement plot on Day 35). The 90% ET replacement showed more canopy coverage value throughout the growing season, followed by the 60% ET replacement. However, the 30% ET showed a slightly lower

NDVI value than the 0% ET replacement. The reason for this is that irrigation was similar in these two treatments due to the relatively large amount of rainfall received during the growing season. At the end of the season, the 90% ET replacement had the largest seed cotton yield ($2879 \pm 525 \text{ kg ha}^{-1}$), followed by 60% ET replacement ($1877 \pm 525 \text{ kg ha}^{-1}$). The 0% ET replacement had 33% more yield ($1585 \pm 189 \text{ kg ha}^{-1}$) than the 30% replacement ($1195 \pm 309 \text{ kg ha}^{-1}$).

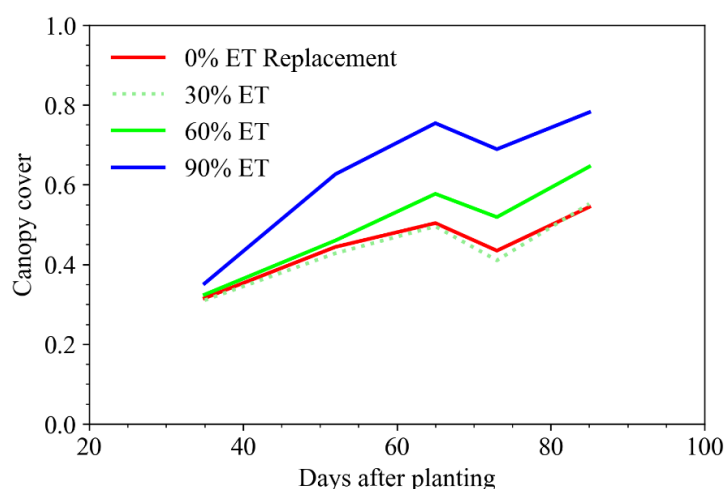


Figure 8.3 Canopy cover changes through the growing season in 2020.

8.3.2. Comparison of CWSI Using the Four Models

To test the differences in the three replications of the four irrigation scheduling treatments, CWSI calculated using the original method (CSWSI_PE) was examined at different plots with various ET replacements (Figure 8.4). The CWSI differences were more considerable when the canopy coverage was small, e.g., the standard deviation of all four treatments ranged from 0.11 to 0.17 at Day 35 and 0.02 to 0.07 at Day 85, respectively. The three plots of the 90% ET replacement showed stable performance

after Day 52 (standard deviation within 0.05). The deviations can be attributed to the influence of surrounding plots and the difference in the soil texture. Although much of the field is Grandfield fine sandy loam soil, the top right of block 3 is primarily Tipton loam soil and the left of block 1 is clay soil. The soil texture influences water holding capacity in the soil, leading to different responses of CWSI to the same treatment.

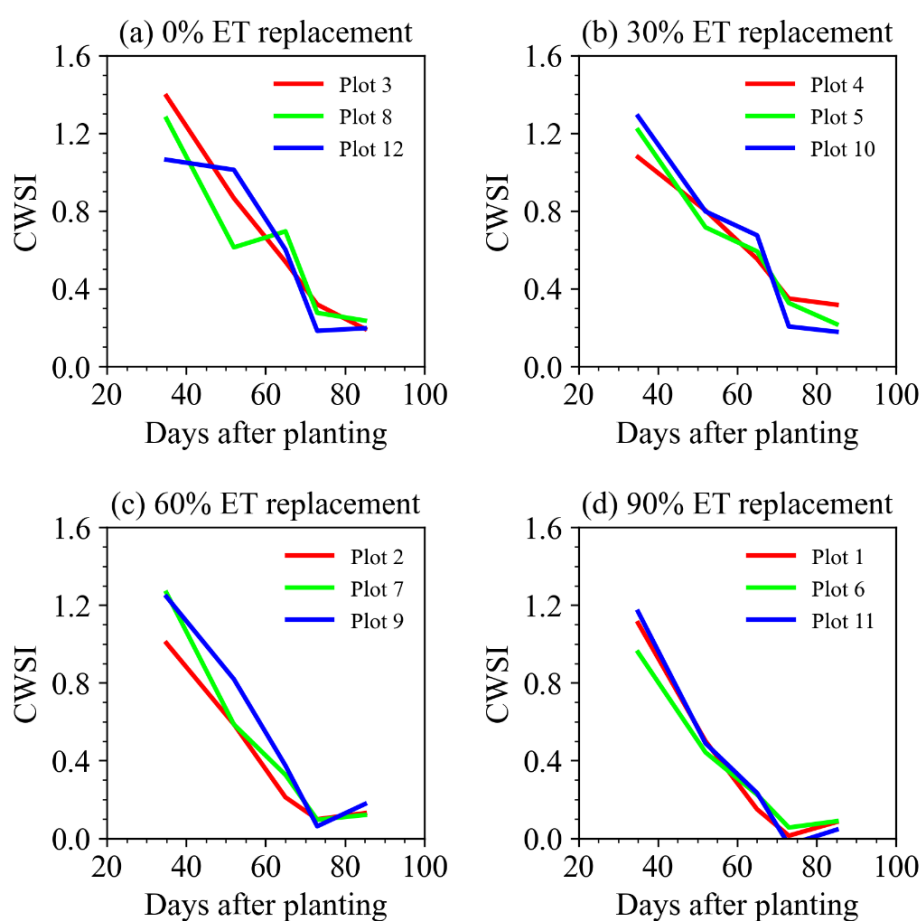


Figure 8.4 Crop water stress comparison using the original method (CWSI_{PE}) at three plots for each ET replacement. Plot numbers are the same as Figure 8.2.

Figure 8.5 shows the daily CWSI values calculated by the four models and DSSAT simulation for different irrigation treatments. The CWSI_PT model provided CWSI estimates comparable to the original CWSI model (CWSI_PE) with lower input requirements, e.g., relative humidity and wind speed were not required. These two methods also showed similar RMSE and MBD (Table 8.2). In the case of 90% ET replacement, the well-water case, i.e., the values of the CWSI-PET model, were relatively stable (around zero) when the soil between crop rows was not visible to the temperature sensor mounted on the phenotyping system (shortly after 50 days of planting). However, the other three methods varied within a range of 0.2-0.5 from Day 52 to Day 65, with high RMSE for the 90% ET replacement (Table 8.2). This indicated that the CWSI-PET model better represented the non-water stress boundary.

Another advantage of using the CWSI-PET method can also be highlighted by comparing the canopy-to-air temperature differences of the four ET replacements (Figure 8.6). Stable temperature differences under 0%/30% (around 6.3 °C), 60% (1.7 °C), and 90% (-0.7 °C) ET replacements were found from 50 days after planting. The CWSI-PET methods exhibited more stable performance, while the simulations of CWSI values for the other three methods showed decreasing trends (Figure 8.5). The canopy-to-air temperature differences for the four ET replacements showed similar values, which were around 12.5 °C at Day 35, indicating high water stress. For example, in the case of 90% ET replacement, the well-water case, the CWSI values simulated by the soil water balance method (DSSAT) still showed water stress around Day 30-35. The reason is that the canopy coverage was relatively low, and the temperature measured under a

partially covered field was a composite temperature of the canopy and soil surface. When the surface cover was sparse, soil temperature dominated the composite temperature measurements. Therefore, the direct use of the crop water stress method in partial crop conditions can lead to substantial errors.

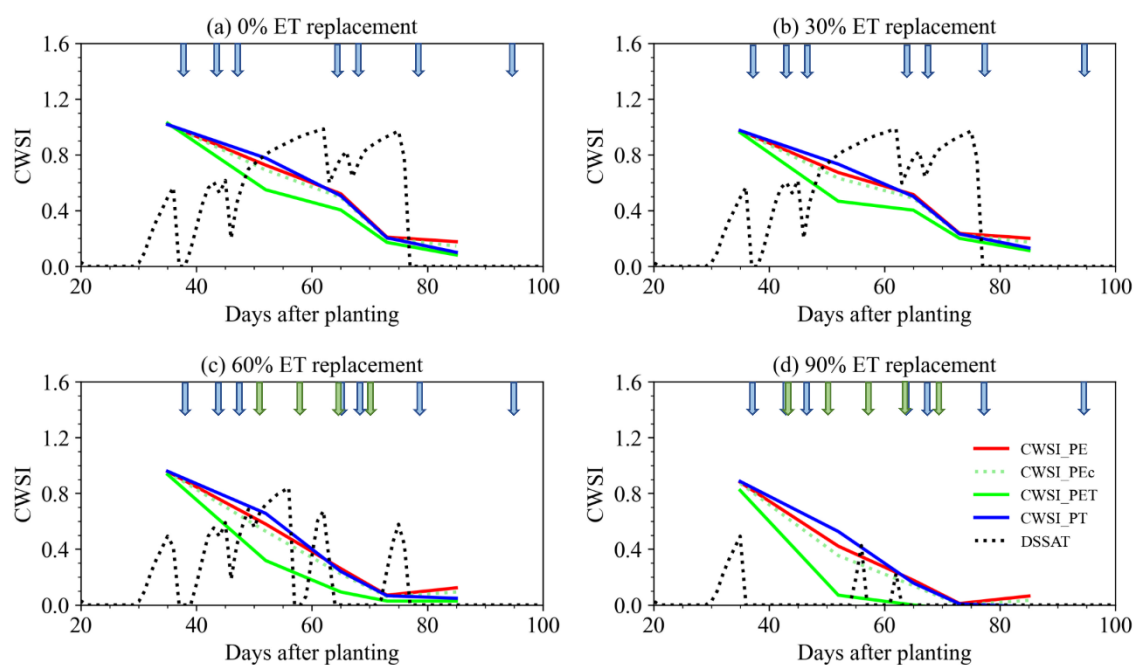


Figure 8.5 Comparison of CWSI values using the four CWSI models and the DSSAT simulation under different ET replacements. The blue arrow indicates rainfall, and the green arrow indicates irrigation.

Table 8.2 Seasonal Error Estimates for CWSI using the Four Models as compared against the DSSAT Simulation.

Model	0% ET		30% ET		60% ET		90% ET		All treatments	
	RMSE	MBD	RMSE	MBD	RMSE	MBD	RMSE	MBD	RMSE	MBD
CWSI_PE	0.39	0.20	0.39	0.22	0.18	-0.02	0.23	-0.17	0.31	0.06
CWSI_PEc	0.40	0.23	0.40	0.25	0.18	0.02	0.19	-0.13	0.31	0.09
CWSI_PET	0.43	0.20	0.45	0.22	0.23	-0.02	0.04	-0.17	0.33	0.06
CWSI_PT	0.39	0.21	0.38	0.23	0.16	-0.01	0.27	-0.17	0.32	0.07

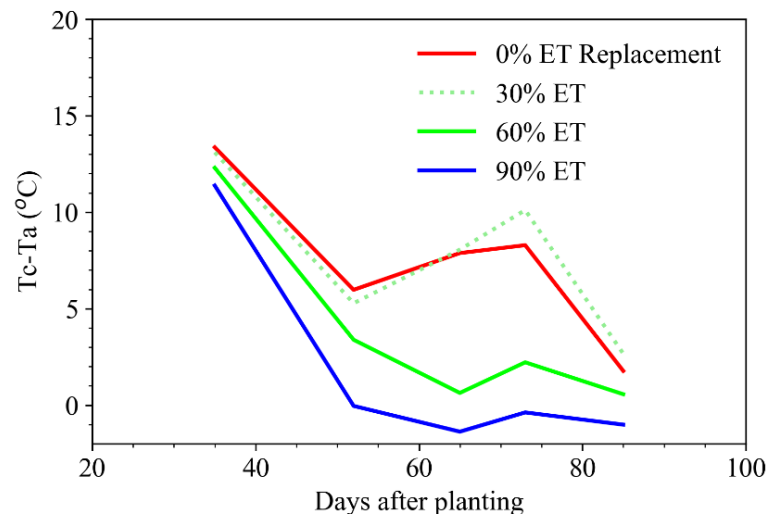


Figure 8.6 Canopy to air temperature differences through the growing season in 2020.

Since the data obtained in the 2020 growing season was very limited (only five days), it was difficult to perform a sufficient and comprehensive evaluation as continuous measurements were not available. The daily CWSI simulation using DSSAT showed that crop water stress varied greatly due to rainfall or irrigation events, as illustrated in the sudden decrease in CWSI in all four treatments (Figure 8.5). Therefore, valid CWSI values from the 0% and 30% ET replacements usually cannot be guaranteed. For example, the CWSI value simulated by DSSAT for all four treatments on Day 85 was zero, indicating no water stress. Therefore, more frequent measurements are required to avoid the influence of rainfall.

8.3.3. Relationship with Crop Yield

The seasonal averaged CWSI (Day 35 excluded) using the four CWSI models was also compared against water stress calculated using DSSAT (Table 8.3). The

averaged CWSI values were used to develop a yield-CWSI linear relationship, as shown in Figure 8.7. All models well captured the yield decrease caused by the elevated crop water stress, with R^2 ranging from 0.85 to 0.87. However, the yield decreasing trends (slopes) were considerably different, depending on the method. The slope of the CWSI-PET method was close to the slope of the DSSAT simulation. However, the CWSI_PE, CWSI_PEc, and CWSI_PT methods had similar slopes but were much higher than the DSSAT simulation. The high slopes of these three methods were mainly due to the underestimation of the lower boundary conditions, i.e., the non-water stress boundary.

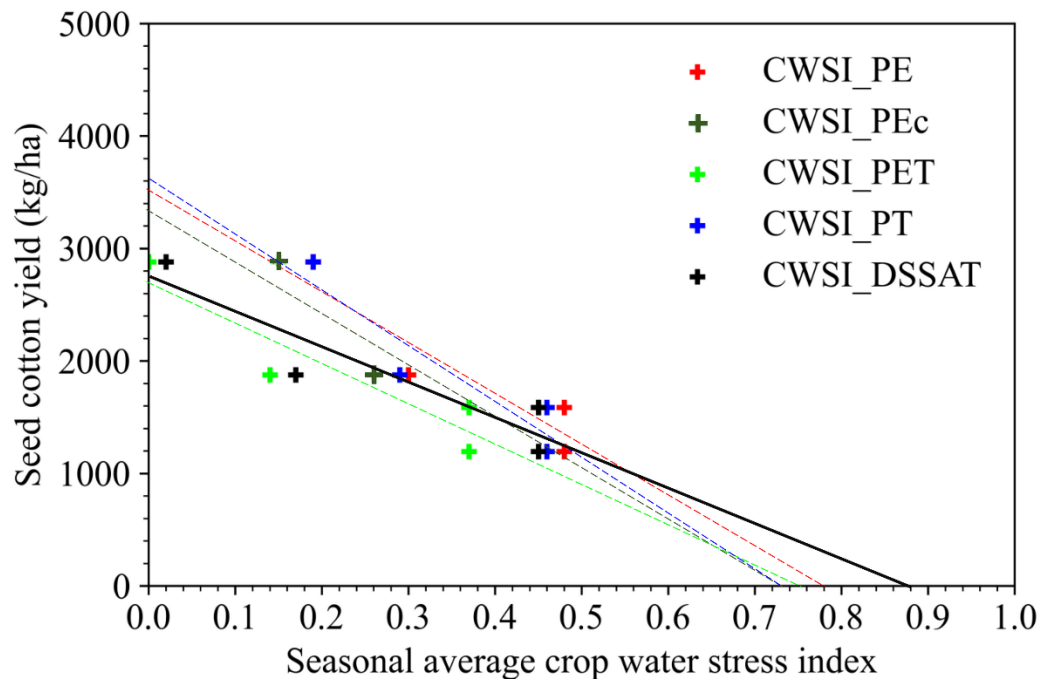


Figure 8.7 Relationships between the seasonal averaged CWSIs and seed cotton yield. Line colors represent the same method as the symbol color.

Table 8.3 Seasonal Averaged CWSI using the Four CWSI Models and the DSSAT Simulation under Different ET Replacements.

ET %	CWSI_PE	CWSI_PEc	CWSI_PET	CWSI_PT	DSSAT
ET_0	0.41	0.38	0.30	0.40	0.45
ET_30	0.41	0.38	0.30	0.40	0.45
ET_60	0.26	0.23	0.12	0.25	0.17
ET_90	0.17	0.13	0.00	0.17	0.02

8.4.4. Improved Method under Low Canopy Coverage

The direct use of the crop water stress method before full canopy closure can incur substantial errors due to the influence of soil heat flux. To overcome this weakness, Moran et al. (1994) developed a water deficit index (WDI), a modification of CWSI, in which the impact of soil heat flux was considered using a linear mixing model of soil and canopy temperature (Figure G1, Appendix G). Colaizzi et al. (2003) used the WDI to trigger irrigation for cotton under high-frequency sprinkler irrigation. In this study, the crop water stress under the four ET replacements in the 2020 growing season was recalculated using the WDI method following Moran et al. (1994) (detailed in Appendix G). As shown in Figure 8.8a, WDI under the 0% and 30% ET replacements was more stable with the consideration of canopy cover. However, the values of WDI for 60% and 90% ET replacements on Day 35, with the lowest canopy coverage, still showed similar water stress as those of the 0% and 30% ET replacements. The reason is that the conditions favoring free evaporation from the soil surface did not exist for a very long period when the surface cover was sparse. Frequent irrigation was required to allow free evaporation from the soil. Our preliminary data in 2021 with nearly bare soil surface showed a relatively stable WDI trend under irrigated conditions (Figure G2, Appendix

G). The average WDI value (0.49) during a 2-week continuous hourly measurement (averaging hourly data of 11:00, 12:00, 13:00, and 14:00h) was similar to the WDI values obtained under no water stress conditions (Figure 8.8a). The relationship between the seasonal average WDI and observed seed cotton yield is shown in Figure 8.8b. According to the yield-CWSI linear relationship, the seed cotton yield under no water stress was obtained as 4296 kg/ha, which was close to the DSSAT yield simulation when assuming there were no water and fertilizer stresses with a relative error of less than 2%. These results lead us to conclude that WDI, a modified CWSI method that accounts for canopy coverage, can be reliably used as an indicator for precision deficit irrigation management.

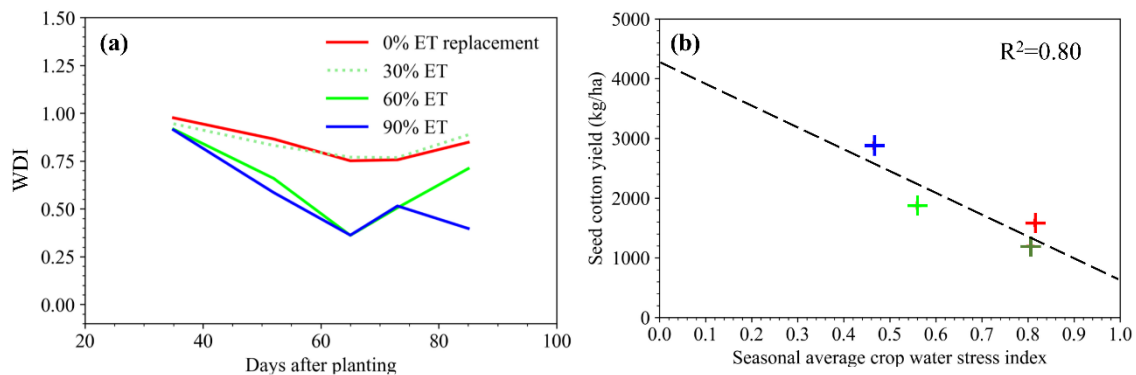


Figure 8.8 (a) Water deficit index (WDI) variation under different water management regimes as a function of time and (b) the relationship between seasonal average WDI and seed yield cotton during the 2020 growing season at Chillicothe, TX.

8.5. Conclusions

In this chapter, the representation of the non-water stress boundary was improved by including the calculation of canopy resistance (r_c) over a well-watered crop surface (CWSI-PET). In addition, to reduce the intensive inputs as required in the theoretical models, a novel, semi-empirical CWSI model based on the Priestly-Taylor equation (CWSI-PT) was developed, which showed comparable performance to the other three models.

Since substantial errors were noted when the field had a low percentage of canopy coverage for all the four CWSI methods, the water deficit index (WDI), a modification of CWSI, with the consideration of normalized difference vegetation index (NDVI), was suggested to improve the model performance when canopy coverage is incomplete. Preliminary examination shows that WDI can be a reliable indicator of precision deficit irrigation management.

9. CONCLUSIONS

9.1. Outcomes

In 2050, globally, there will be 9.7 billion people, and we need 55% more water, 50% more food, and 80% more energy, with 52% more CO₂ emissions with no policy change (OECD, 2012). The situation is exacerbated in developing countries which are experiencing rapid urbanization processes. To mitigate climate change impacts, many countries have announced their Nationally Determined Contributions (NDC) in the Paris Agreement to reduce CO₂ emissions. Water and energy systems are interdependent and have complex dynamic interactions with the socio-economic system and climate change. Policies and measures designed to increase the efficiency in one system might significantly affect that in the other. Therefore, accurate simulation of the dynamic interactions among socio-economic, energy, and water environmental systems is critical to cope with the growing energy and freshwater consumption and greenhouse gas emissions, particularly under long-term urbanization. However, these cross-sector feedbacks have not been fully considered in current water-energy nexus studies. The integrated model developed in this dissertation improved the understanding of the interactions among socioeconomics, energy consumption, water use, water infrastructure, and receiving water systems, which can be used to identify the cost-effective solutions to meet the water and energy demands under different economic development pathways and climate futures.

The dissertation includes two major parts: Part I includes the integration of CGE and SyDWEM model, i.e., CGE-SyDWEM, and evaluation of its ability in simulating the carbon-energy-water nexus in urbanized regions. The integrated model can be used to aid policymakers from energy, carbon, and water sectors to understand the complicated synergistic effects of proposed carbon mitigation strategies and water engineering measures on local/regional energy consumption, CO₂ emissions, water resources balance, and water-environment change and to design more effective policies and measures to ensure energy and water security in future. Chapter 2 showed that the integrated systems could be used to aid energy planners in understanding the effects of the proposed CO₂ mitigation strategies on energy use efficiency and its co-benefits and trade-offs on saving water use and reducing pollutant emissions. In Chapter 3, a CGE-based integrated model (CGE-SyDWEM) for energy, carbon, and water management in a rapidly urbanizing catchment was developed in order to simulate the dynamic interactions among the socio-economic, energy, water environment systems. Sensitivity experiments showed that the integrated model was able to assess the effects of proposed CO₂ mitigation strategies and water-engineering measures on future energy use, carbon emissions, economic and population growth, and water resources stress, as well as water quality change at a watershed level. With this integrated model, decision-makers across different sectors can consult with each other and design more effective policies and measures to achieve the national water and energy management targets. The aggregated effects of both CO₂ mitigation strategies and engineering measures show that a low-carbon, high-efficiency water, and energy use economy and better water environment are

potentially achievable. In Chapter 4, the relative contributions of GHG emissions from the sewer, WWTPs, and receiving water systems were quantified using the integrated model. The result enables a better understanding of the role of the wastewater sector in global GHG emissions reduction.

Part II improved the integrated model in simulating irrigation water demand and agricultural adaptation strategies to climate change. The selection and implementation of reference evapotranspiration (ET_0) methods are vital for estimating irrigation water demand for long-term water resources management, especially in areas with limited weather data. In Chapters 5, the representation of the irrigation water demand module in CGE-SyDWEM was improved by assessing several less data-intensive reference evapotranspiration (ET_0) models used for regional irrigation water demand estimation. In Chapter 6, an analytical expression for the PT coefficient (PT_a) is derived following the Penman-Monteith method, i.e., $PT_a = \frac{1}{S_A} (1 + S_{U_2})$, where S_A represents the impact of the radiative component on ET_0 and S_{U_2} is the impact of wind speed on ET_0 . The new Priestley-Taylor coefficients can be easily applied to existing hydrological and crop models to improve ET_0 estimation performance. In Chapter 7, the seasonal forecast from one representative NMME model, i.e., the Canadian Coupled Climate Model versions 4 (CanCM4) was calibrated and bias-corrected from one representative NMME model, i.e., the Canadian Coupled Climate Model versions 4 (CanCM4). The high-resolution seasonal weather forecasts generated in this study ensured robust and reliable regional or local crop yield prediction over the CONUS region. In Chapter 8, a novel, semi-empirical method to calculate crop water stress was derived, which can be used to

develop water-stress-based deficit irrigation strategies for enhancing water use efficiency and thereby conserving water resources in agricultural production.

9.2. Limitations and Future Work

This integrated model facilitates communications among different planners and policymakers and enables a better understanding of the carbon-energy-water nexus. Although the current study focuses on a rapidly urbanizing catchment in southeast China, the framework could be generalized to other urbanizing catchments, especially in developing countries also with rapid population and economic change. The domain of analysis and the choice of sub-modules could have regional variations. For example, in regions with a higher proportion of agriculture industry, the sub-modules for irrigation water demand should be improved based on the results reported in Chapters 5-8. In addition, the emphasis of this dissertation is to capture the cross-sector interactions and feedbacks and to provide an integrated view of the impacts of carbon mitigation strategies on all industrial sectors in the economic system. Therefore, the impacts of using different technologies on the carbon-energy-water interactions in a single sector are not simulated yet, which limits its application in single sector planning. This limitation could be improved in the future with the availability of detailed sector data, which is still challenging in developing countries normally with insufficient data collections and accessibility.

In Chapter 2, the effects of carbon mitigation on pollutants discharge in construction, transport, and services sectors are not considered yet, mainly due to the lack of data. In China, the water pollutant discharges from these three sectors are

assumed to be related to residential activities and thereby were not reported separately. Considering the projected economic output decrease in these sectors with carbon mitigation, the co-benefits on the water pollutant discharge may be underestimated.

In Chapter 3, how water policy could affect energy consumption and carbon control target is also relevant, but not considered in this dissertation. The Chinese government has raised targets on total water consumption and water intensity in terms of GDP, which has co-benefits or trade-offs with carbon mitigation targets and deserves further quantitative evaluation.

In Chapter 4, the calculation of the direct GHG emission from the sewer system caused by sediment deposition using constant CH₄ and CO₂ emission factors is due to the lack of field measurements. The emission factors are found to be related to pipeline size and length, as well as water quality. Therefore, the average EFs for CH₄ and CO₂ with sewer length higher than 1 km used in the calculation may have high uncertainty.

In Chapter 5, agrometeorological stations are located in the cropped areas, and weather data are typically measured at 2 m above an extensive surface of grass or short crop. However, the meteorological data used in the study were from the weather stations of the National Oceanic and Atmospheric Administration in the U.S., likely leading to bias in later calculations and comparisons.

In Chapter 6, the major uncertainty is also from the variations of the gridded weather dataset used, which may affect the magnitudes and spatial distributions of ET_o, ET_o trends, S_A, S_{u2}, and the PT coefficient at the global scale.

In Chapter 7, only one model from the NMME was selected for the real-time seasonal weather forecast. It is interesting to use all the available models in the NMME dataset and then compare the performance of individual models. The precipitation forecast still shows high variability.

In Chapter 8, to validate the method in estimating crop water stress index, the hourly field data of canopy temperature covering the whole growing season is expected. From the first season experiment, only five days' data were collected due to technical problems during field measurements. Therefore, the current analysis only focused on the comparison of the four lower boundary models. Nevertheless, the validation can still be performed using any published field measurements in the future.

REFERENCES

- Abtew, W., 1996. Evapotranspiration measurements and modeling for three wetland systems in south Florida. *Water Resour Bull* 32, 465-473.
- Ackerman, F., Fisher, J., 2013. Is there a water-energy nexus in electricity generation? Long-term scenarios for the western United States. *Energ Policy* 59, 235-241.
- Adachi, S.A., Tomita, H., 2020. Methodology of the Constraint Condition in Dynamical Downscaling for Regional Climate Evaluation: A Review. *J Geophys Res-Atmos* 125.
- Adhikari, P., Omani, N., Ale, S., DeLaune, P.B., Thorp, K.R., Barnes, E.M., Hoogenboom, G., 2017. Simulated Effects of Winter Wheat Cover Crop on Cotton Production Systems of the Texas Rolling Plains. *T Asabe* 60, 2083-2096.
- Agam, N., Cohen, Y., Berni, J.A.J., Alchanatis, V., Kool, D., Dag, A., Yermiyahu, U., Ben-Gal, A., 2013. An insight to the performance of crop water stress index for olive trees. *Agr Water Manage* 118, 79-86.
- Ahn, J.H., Kim, S., Park, H., Rahm, B., Pagilla, K., Chandran, K., 2010. N₂O Emissions from Activated Sludge Processes, 2008-2009: Results of a National Monitoring Survey in the United States. *Environmental Science & Technology* 44, 4505-4511.
- Akhavan, S., Mousabeygi, F., Peel, M.C., 2018. Assessment of eight reference evapotranspiration (ET_o) methods considering Koppen climate class in Iran. *Hydrolog Sci J* 63, 1468-1481.

- Allen, R.G., 1998. Crop evapotranspiration: guidelines for computing crop water requirements.
- Allen, R.G., Pruitt, W.O., 1986. Rational Use of the Fao Blaney-Criddle Formula. *J Irrig Drain E-Asce* 112, 139-155.
- Amatya, D.M., Skaggs, R.W., Gregory, J.D., 1995. Comparison of Methods for Estimating Ref-Et. *J Irrig Drain Eng* 121, 427-435.
- Ambrose, R.B., 1987. A hydrodynamic and water quality model-model theory, User's manual, programmers' guide. U.S. Environmental Protection Agency, Athens Georgia, EPA/600/3-87/039.
- Arent, D., Pless, J., Mai, T., Wiser, R., Hand, M., Baldwin, S., Heath, G., Macknick, J., Bazilian, M., Schlosser, A., Denholm, P., 2014. Implications of high renewable electricity penetration in the US for water use, greenhouse gas emissions, land-use, and materials supply. *Appl Energ* 123, 368-377.
- Arnold, J.G., Moriasi, D.N., Gassman, P.W., Abbaspour, K.C., White, M.J., Srinivasan, R., Santhi, C., Harmel, R.D., van Griensven, A., Van Liew, M.W., Kannan, N., Jha, M.K., 2012. Swat: Model Use, Calibration, and Validation. *T Asabe* 55, 1491-1508.
- Aschonitis, V.G., Papamichail, D., Demertzi, K., Colombani, N., Mastrocicco, M., Ghirardini, A., Castaldelli, G., Fano, E.A., 2017. High-resolution global grids of revised Priestley-Taylor and Hargreaves-Samani coefficients for assessing ASCE-standardized reference crop evapotranspiration and solar radiation`. *Earth Syst Sci Data* 9, 615-638.

- Aumont, O., Ethe, C., Tagliabue, A., Bopp, L., Gehlen, M., 2015. PISCES-v2: an ocean biogeochemical model for carbon and ecosystem studies. *Geosci Model Dev* 8, 2465-2513.
- Azhar, A.H., Perera, B.J.C., 2011. Evaluation of Reference Evapotranspiration Estimation Methods under Southeast Australian Conditions. *J Irrig Drain Eng* 137, 268-279.
- Babbar, R., 2014. Pollution risk assessment based on QUAL2E-UNCAS simulations of a tropical river in Northern India. *Environ Monit Assess* 186, 6771-6787.
- Bakhtiari, B., Ghahreman, N., Liaghat, A.M., Hoogenboom, G., 2011. Evaluation of Reference Evapotranspiration Models for a Semiarid Environment Using Lysimeter Measurements. *J Agr Sci Tech-Iran* 13, 223-237.
- Ballester, C., Jiménez-Bello, M.A., Castel, J.R., Intrigliolo, D.S., 2013. Usefulness of thermography for plant water stress detection in citrus and persimmon trees. *Agr Forest Meteorol* 168, 120-129.
- Bao, Z.Y., Sun, S.C., Sun, D.Z., 2015. Characteristics of direct CO₂ emissions in four full-scale wastewater treatment plants. *Desalin Water Treat* 54, 1070-1079.
- Bao, Z.Y., Sun, S.C., Sun, D.Z., 2016. Assessment of greenhouse gas emission from A/O and SBR wastewater treatment plants in Beijing, China. *Int Biodeter Biodegr* 108, 108-114.
- Barbero, R., Abatzoglou, J.T., Hegewisch, K.C., 2017. Evaluation of Statistical Downscaling of North American Multimodel Ensemble Forecasts over the Western United States. *Weather and Forecasting* 32, 327-341.

- Barnston, A.G., Tippet, M.K., 2017. Do Statistical Pattern Corrections Improve Seasonal Climate Predictions in the North American Multimodel Ensemble Models? *J Climate* 30, 8335-8355.
- Beaulieu, J.J., Arango, C.P., Hamilton, S.K., Tank, J.L., 2008. The production and emission of nitrous oxide from headwater streams in the Midwestern United States. *Global Change Biol* 14, 878-894.
- Beaulieu, J.J., Tank, J.L., Hamilton, S.K., Wollheim, W.M., Hall, R.O., Mulholland, P.J., Peterson, B.J., Ashkenas, L.R., Cooper, L.W., Dahm, C.N., Dodds, W.K., Grimm, N.B., Johnson, S.L., McDowell, W.H., Poole, G.C., Valett, H.M., Arango, C.P., Bernot, M.J., Burgin, A.J., Crenshaw, C.L., Helton, A.M., Johnson, L.T., O'Brien, J.M., Potter, J.D., Sheibley, R.W., Sobota, D.J., Thomas, S.M., 2011. Nitrous oxide emission from denitrification in stream and river networks. *P Natl Acad Sci USA* 108, 214-219.
- Beck, H.E., Zimmermann, N.E., McVicar, T.R., Vergopolan, N., Berg, A., Wood, E.F., 2018. Present and future Koppen-Geiger climate classification maps at 1-km resolution. *Sci Data* 5.
- Bellvert, J., Marsal, J., Girona, J., Gonzalez-Dugo, V., Fereres, E., Ustin, S.L., Zarco-Tejada, P.J., 2016. Airborne Thermal Imagery to Detect the Seasonal Evolution of Crop Water Status in Peach, Nectarine and Saturn Peach Orchards. *Remote Sens-Basel* 8.
- Beven, K., 1979. A sensitivity analysis of the Penman-Monteith actual evapotranspiration estimates. *J Hydrol* 44, 169-190.

- Bezerra, B.G., Bezerra, J.R.C., da Silva, B.B., dos Santos, C.A.C., 2015. Surface energy exchange and evapotranspiration from cotton crop under full irrigation conditions in the Rio Grande do Norte State, Brazilian Semi-Arid. *Bragantia* 74, 120-128.
- Blaney, H.F., Criddle, W.D., 1950. Determining water requirements in irrigated areas from climatological and irrigation data, Aug. 1950, slightly rev. Feb. 1952. ed.
- Brown, L.C., Barnwell, T.O., 1987. The enhanced stream water quality models QUAL2E and QUAL2E-UNCAS: documentation and user manual. US Environmental Protection Agency. Office of Research and Development. Environmental Research Laboratory.
- Cameron, C., Yelverton, W., Dodder, R., West, J.J., 2014. Strategic responses to CO2 emission reduction targets drive shift in U.S. electric sector water use. *Energy Strateg Rev* 4, 16-27.
- Census and Statistics Department of Hong Kong, 2016. Census and statistics department of Hong Kong Statistics, <http://www.censtatd.gov.hk/hkstat/sub/so30.jsp>.
- Chandel, M.K., Pratson, L.F., Jackson, R.B., 2011. The potential impacts of climate-change policy on freshwater use in thermoelectric power generation. *Energy Policy* 39, 6234-6242.
- Cheng, B.B., Dai, H.C., Wang, P., Xie, Y., Chen, L., Zhao, D.Q., Masui, T., 2016. Impacts of low-carbon power policy on carbon mitigation in Guangdong Province, China. *Energy Policy* 88, 515-527.
- Clawson, K.L., Jackson, R.D., Pinter, P.J., 1989. Evaluating Plant Water-Stress with Canopy Temperature Differences. *Agron J* 81, 858-863.

- Clemmer, S., Rogers, J., Sattler, S., Macknick, J., Mai, T., 2013. Modeling low-carbon US electricity futures to explore impacts on national and regional water use. *Environ Res Lett* 8.
- Colaizzi, P.D., Barnes, E.M., Clarke, T.R., Choi, C.Y., Waller, P.M., Haberland, J., Kostrzewski, M., 2003. Water stress detection under high frequency sprinkler irrigation with water deficit index. *J Irrig Drain Eng* 129, 36-43.
- Cole, J.J., Caraco, N.F., 2001. Emissions of nitrous oxide (N₂O) from a tidal, freshwater river, the Hudson River, New York. *Environmental Science & Technology* 35, 991-996.
- Constantin, J., Willaume, M., Murgue, C., Lacroix, B., Therond, O., 2015. The soil-crop models STICS and AqYield predict yield and soil water content for irrigated crops equally well with limited data. *Agr Forest Meteorol* 206, 55-68.
- Cooper, D.C., Sehlke, G., 2012. Sustainability and Energy Development: Influences of Greenhouse Gas Emission Reduction Options on Water Use in Energy Production. *Environmental Science & Technology* 46, 3509-3518.
- Daelman, M.R.J., van Voorthuizen, E.M., van Dongen, U.G.J.M., Volcke, E.I.P., van Loosdrecht, M.C.M., 2012. Methane emission during municipal wastewater treatment. *Water Res* 46, 3657-3670.
- Dai, H.C., 2012. Integrated assessment of China's provincial low carbon economy development towards 2030 : Jiangxi Province as an example. Tokyo Institute of Technology.

- Dai, H.C., Masui, T., Matsuoka, Y., Fujimori, S., 2011. Assessment of China's climate commitment and non-fossil energy plan towards 2020 using hybrid AIM/CGE model. *Energ Policy* 39, 2875-2887.
- Dai, H.C., Masui, T., Matsuoka, Y., Fujimori, S., 2012. The impacts of China's household consumption expenditure patterns on energy demand and carbon emissions towards 2050. *Energ Policy* 50, 736-750.
- Dai, H.C., Xie, X.X., Xie, Y., Liu, J., Masui, T., 2016. Green growth: The economic impacts of large-scale renewable energy development in China. *Appl Energ* 162, 435-449.
- Danabasoglu, G., Bates, S.C., Briegleb, B.P., Jayne, S.R., Jochum, M., Large, W.G., Peacock, S., Yeager, S.G., 2012. The CCSM4 Ocean Component. *J Climate* 25, 1361-1389.
- Davies, J.A., Allen, C.D., 1973. Equilibrium, Potential and Actual Evaporation from Cropped Surfaces in Southern Ontario. *Journal of Applied Meteorology and Climatology* 12, 649-657.
- de Kok, J.L., Kofalk, S., Berlekamp, J., Hahn, B., Wind, H., 2009. From Design to Application of a Decision-support System for Integrated River-basin Management. *Water Resour Manag* 23, 1781-1811.
- Deryng, D., Sacks, W.J., Barford, C.C., Ramankutty, N., 2011. Simulating the effects of climate and agricultural management practices on global crop yield. *Global Biogeochem Cy* 25.
- DHI, 1993. MIKE II. Users and Reference Manual Horsholm, Denmark.

- Didari, S., Ahmadi, S.H., 2019. Calibration and evaluation of the FAO56-Penman-Monteith, FAO24-radiation, and Priestly-Taylor reference evapotranspiration models using the spatially measured solar radiation across a large arid and semi-arid area in southern Iran. *Theor Appl Climatol* 136, 441-455.
- Djaman, K., O'Neill, M., Diop, L., Bodian, A., Allen, S., Koudahe, K., Lombard, K., 2019. Evaluation of the Penman-Monteith and other 34 reference evapotranspiration equations under limited data in a semiarid dry climate. *Theor Appl Climatol* 137, 729-743.
- Dodder, R., Felgenhauer, T., Yelverton, W., King, C., 2012. Water and Greenhouse Gas Tradeoffs Associated with a Transition to a Low Carbon Transportation System. *Proceedings of the Asme International Mechanical Engineering Congress and Exposition*, 2011, Vol 1, 531-547.
- Doll, P., Siebert, S., 2002. Global modeling of irrigation water requirements. *Water Resour Res* 38.
- Dong, H.J., Dai, H.C., Dong, L., Fujita, T., Geng, Y., Klimont, Z., Inoue, T., Bunya, S., Fujii, M., Masui, T., 2015. Pursuing air pollutant co-benefits of CO₂ mitigation in China: A provincial leveled analysis. *Appl Energ* 144, 165-174.
- Dong, L., Liang, H.W., 2014. Spatial analysis on China's regional air pollutants and CO₂ emissions: emission pattern and regional disparity. *Atmos Environ* 92, 280-291.
- Doorenbos, J., Pruitt, W.O., 1976. Guidelines for predicting crop water requirements, Rev. ed.

- Doulgeris, C., Georgiou, P., Papadimos, D., Papamichail, D., 2012. Ecosystem approach to water resources management using the MIKE 11 modeling system in the Strymonas River and Lake Kerkini. *J Environ Manage* 94, 132-143.
- Dzotsi, K.A., Basso, B., Jones, J.W., 2015. Parameter and uncertainty estimation for maize, peanut and cotton using the SALUS crop model. *Agricultural Systems* 135, 31-47.
- Eichinger, W.E., Parlange, M.B., Stricker, H., 1996. On the concept of equilibrium evaporation and the value of the Priestley-Taylor coefficient. *Water Resour Res* 32, 161-164.
- Englehardt, J.D., Wu, T.T., Bloetscher, F., Deng, Y., du Pisani, P., Eilert, S., Elmir, S., Guo, T.J., Jacangelo, J., LeChevallier, M., Leverenz, H., Mancha, E., Plater-Zyberk, E., Sheikh, B., Steinle-Darling, E., Tchobanoglous, G., 2016. Net-zero water management: achieving energy-positive municipal water supply. *Environ Sci-Wat Res* 2, 250-260.
- Er-Raki, S., Chehbouni, A., Khabba, S., Simonneaux, V., Jarlan, L., Ouldbba, A., Rodriguez, J.C., Allen, R., 2010. Assessment of reference evapotranspiration methods in semi-arid regions: Can weather forecast data be used as alternate of ground meteorological parameters? *J Arid Environ* 74, 1587-1596.
- Ermolieva, T.Y., Ermoliev, Y.M., Havlik, P., Mosnier, A., Leclere, D., Kraksner, F., Khabarov, N., Obersteiner, M., 2015. Systems Analysis of Robust Strategic Decisions to Plan Secure Food, Energy, and Water Provision Based on the Stochastic Globiom Model. *Cybern Syst Anal* 51, 125-133.

- Evenson, J.P., Rose, C.W., 1976. Seasonal-Variations in Stomatal Resistance in Cotton. *Agr Meteorol* 17, 381-386.
- FAO, 2016. The state of food and agriculture 2016. Climate change, agriculture and food security. Food and Agriculture Organization of the United Nations, Rome.
- FAO, 2018. The future of food and agriculture – Alternative pathways to 2050. Food and Agriculture Organization of the United Nations, Rome.
- Fisher, J.B., Tu, K.P., Baldocchi, D.D., 2008. Global estimates of the land-atmosphere water flux based on monthly AVHRR and ISLSCP-II data, validated at 16 FLUXNET sites. *Remote Sens Environ* 112, 901-919.
- Florke, M., Schneider, C., McDonald, R.I., 2018. Water competition between cities and agriculture driven by climate change and urban growth. *Nat Sustain* 1, 51-58.
- Foley, J., de Haas, D., Yuan, Z.G., Lant, P., 2010. Nitrous oxide generation in full-scale biological nutrient removal wastewater treatment plants. *Water Res* 44, 831-844.
- Gain, A.K., Giupponi, C., 2015. A dynamic assessment of water scarcity risk in the Lower Brahmaputra River Basin: An integrated approach. *Ecol Indic* 48, 120-131.
- Gao, F., Feng, G., Ouyang, Y., Wang, H.X., Fisher, D., Adeli, A., Jenkins, J., 2017. Evaluation of Reference Evapotranspiration Methods in Arid, Semiarid, and Humid Regions. *J Am Water Resour As* 53, 791-808.
- Gebrechorkos, S.H., Hulsmann, S., Bernhofer, C., 2019. Statistically downscaled climate dataset for East Africa. *Sci Data* 6.

- Gleaton, C., Robinson, J., 2016. Facts about Texas and US agriculture Texas AgriLife Extension, Department of Agricultural Economics, Texas A&M University, College Station, TX.
- González-Dugo, M.P., Moran, M.S., Mateos, L., Bryant, R., 2006. Canopy temperature variability as an indicator of crop water stress severity. *Irrigation Sci* 24, 233.
- Gonzalez-Dugo, V., Zarco-Tejada, P.J., Fereres, E., 2014. Applicability and limitations of using the crop water stress index as an indicator of water deficits in citrus orchards. *Agr Forest Meteorol* 198, 94-104.
- Griffith, D.R., Barnes, R.T., Raymond, P.A., 2009. Inputs of Fossil Carbon from Wastewater Treatment Plants to US Rivers and Oceans. *Environmental Science & Technology* 43, 5647-5651.
- Guisasola, A., de Haas, D., Keller, J., Yuan, Z., 2008. Methane formation in sewer systems. *Water Res* 42, 1421-1430.
- Guitjens, J.C., 1982. Models of Alfalfa Yield and Evapo-Transpiration. *J Irr Drain Div-Asce* 108, 212-224.
- Gutierrez, M., Norton, R., Thorp, K.R., Wang, G.Y., 2012. Association of Spectral Reflectance Indices with Plant Growth and Lint Yield in Upland Cotton. *Crop Sci* 52, 849-857.
- Gutierrez, O., Sudarjanto, G., Ren, G., Ganigue, R., Jiang, G.M., Yuan, Z.G., 2014. Assessment of pH shock as a method for controlling sulfide and methane formation in pressure main sewer systems. *Water Res* 48, 569-578.

- Gutmann, E.D., Rasmussen, R.M., Liu, C.H., Ikeda, K., Gochis, D.J., Clark, M.P., Dudhia, J., Thompson, G., 2012. A Comparison of Statistical and Dynamical Downscaling of Winter Precipitation over Complex Terrain. *J Climate* 25, 262-281.
- Haddeland, I., Heinke, J., Biemans, H., Eisner, S., Florke, M., Hanasaki, N., Konzmann, M., Ludwig, F., Masaki, Y., Schewe, J., Stacke, T., Tessler, Z.D., Wada, Y., Wisser, D., 2014. Global water resources affected by human interventions and climate change. *P Natl Acad Sci USA* 111, 3251-3256.
- Hahn, B.M., Kofalk, S., de Kok, J.L., Berlekamp, J., Evers, M., 2009. Elbe DSS: A Planning Support System for Strategic River Basin Planning. *Geojournal Lib* 95, 113-136.
- Hamrick, J.M., 2006. EFDC technical memorandum. Fairfax: Tetra Tech, Inc.
- Han, M., Zhang, H.H., DeJonge, K.C., Comas, L.H., Gleason, S., 2018. Comparison of three crop water stress index models with sap flow measurements in maize. *Agr Water Manage* 203, 366-375.
- Hanasaki, N., Kanae, S., Oki, T., Masuda, K., Motoya, K., Shirakawa, N., Shen, Y., Tanaka, K., 2008. An integrated model for the assessment of global water resources Part 1: Model description and input meteorological forcing. *Hydrol Earth Syst Sc* 12, 1007-1025.
- Hargreaves, G.H., Samani, Z.A., 1985. Reference Crop Evapotranspiration from Temperature. *Appl Eng Agric* 1, 96-99.

- Harris, I., Osborn, T.J., Jones, P., Lister, D., 2020. Version 4 of the CRU TS monthly high-resolution gridded multivariate climate dataset. *Sci Data* 7.
- Hawkins, E., Osborne, T.M., Ho, C.K., Challinor, A.J., 2013. Calibration and bias correction of climate projections for crop modelling: An idealised case study over Europe. *Agr Forest Meteorol* 170, 19-31.
- Heaps, C.G., 2016. Long-range Energy Alternatives Planning (LEAP) system. [Software version: 2017.0.11]. Stockholm Environment Institute. Somerville, MA, USA.
- Hermans, R., Hahn, B., 2007. Towards a User Oriented Generic Tool for River Basin Management: the Example of the Elbe DSS in Germany. *Proceedings of the 3rd International Yellow River Forum on Sustainable Water Resources Management and Delta Ecosystem Maintenance*, Vol Vi, 93-99.
- Ho, C.K., Stephenson, D.B., Collins, M., Ferro, C.A.T., Brown, S.J., 2012. Calibration Strategies A Source of Additional Uncertainty in Climate Change Projections. *B Am Meteorol Soc* 93, 21-26.
- Hollermann, B., Giertz, S., Diekkruger, B., 2010. Benin 2025-Balancing Future Water Availability and Demand Using the WEAP 'Water Evaluation and Planning' System. *Water Resour Manag* 24, 3591-3613.
- Hoogenboom, G., C.H. Porter, K.J. Boote, V. Shelia, P.W. Wilkens, U. Singh, J.W. White, S. Asseng, J.I. Lizaso, L.P. Moreno, W. Pavan, R. Ogoshi, L.A. Hunt, Tsuji, G.Y., Jones., J.W., 2019. *The DSSAT crop modeling ecosystem*. Burleigh Dodds Science Publishing, Cambridge, United Kingdom.

- Howells, M., Hermann, S., Welsch, M., Bazilian, M., Segerstrom, R., Alfstad, T., Gielen, D., Rogner, H., Fischer, G., van Velthuisen, H., Wiberg, D., Young, C., Roehrl, R.A., Mueller, A., Steduto, P., Ramma, I., 2013. Integrated analysis of climate change, land-use, energy and water strategies. *Nat Clim Change* 3, 621-626.
- HSECSM, 1996-2007. Report on the environmental state in Shenzhen City (In Chinese), in: Municipality, H.S.E.C.o.S. (Ed.). Human Settlements & Environment Commission of Shenzhen Municipality, Shenzhen.
- HSECSM, 2011-2014. Report on the environmental state in Shenzhen City (In Chinese). Human Settlements & Environment Commission of Shenzhen Municipality, Shenzhen.
- Hu, J.D., 2007. Strategy research on water quality improvement in Shenzhen River and Deep Bay, 1st ed. Science Press, Beijing (In Chinese).
- Huang, W.L., Ma, D., Chen, W.Y., 2017. Connecting water and energy: Assessing the impacts of carbon and water constraints on China's power sector. *Appl Energ* 185, 1497-1505.
- Hussey, K., Pittock, J., 2012. The Energy-Water Nexus: Managing the Links between Energy and Water for a Sustainable Future. *Ecol Soc* 17.
- Idso, S.B., Jackson, R.D., Pinter, P.J., Reginato, R.J., Hatfield, J.L., 1981. Normalizing the Stress-Degree-Day Parameter for Environmental Variability. *Agr Meteorol* 24, 45-55.
- IEA, 2009. World energy outlook 2009. International Energy Agency. OECD, Paris.

- IEA, 2015. CO₂ emissions by product and flow. International Energy Agency.
- Ihuoma, S.O., Madramootoo, C.A., 2017. Recent advances in crop water stress detection. *Comput Electron Agr* 141, 267-275.
- Illich, N., 2006. "WEAP21 - A demand-, priority-, and preference-driven water planning Model: Part 1" - by David Yates, Jack Sieber, David Purkey, and Annette Huber-Lee. *Water Int* 31, 272-273.
- IPCC, 2006. (Intergovernmental Panel on Climate Change). "Guidelines for national greenhouse gas inventories."
- IPCC, 2014. *Climate Change 2014: Mitigation of Climate Change* (eds Edenhofer, O. et al.)
- IPCC, 2021. *Climate Change 2021: The Physical Science Basis. Contribution of Working Group I to the Sixth Assessment Report of the Intergovernmental Panel on Climate Change*. Cambridge University Press. I.
- Jackson, R.D., Idso, S.B., Reginato, R.J., Pinter, P.J., 1981. Canopy Temperature as a Crop Water-Stress Indicator. *Water Resour Res* 17, 1133-1138.
- Jackson, R.D., Kustas, W.P., Choudhury, B.J., 1988. A Reexamination of the Crop Water-Stress Index. *Irrigation Sci* 9, 309-317.
- Jalalifarahani, H.R., Slack, D.C., Kopec, D.M., Matthias, A.D., 1993. Crop Water-Stress Index Models for Bermudagrass Turf - a Comparison. *Agron J* 85, 1210-1217.
- Jarvis, P.G., McNaughton, K.G., 1986. Stomatal Control of Transpiration - Scaling up from Leaf to Region. *Adv Ecol Res* 15, 1-49.

- Jensen, D.T., Hargreaves, G.H., Temesgen, B., Allen, R.G., 1997. Computation of ETo under nonideal conditions. *J Irrig Drain Eng* 123, 394-400.
- Jensen, M.E., Haise, H.R., 1963. Estimating Evapotranspiration from Solar Radiation. *Journal of Irrigation and Drainage Division Proceedings of the American Society of Civil Engineers*, 15-41.
- Jiang, L., Wu, F., Liu, Y., Deng, X.Z., 2014. Modeling the Impacts of Urbanization and Industrial Transformation on Water Resources in China: An Integrated Hydro-Economic CGE Analysis. *Sustainability-Basel* 6, 7586-7600.
- Jin, P.K., Gu, Y.G., Shi, X., Yang, W.N., 2019. Non-negligible greenhouse gases from urban sewer system. *Biotechnol Biofuels* 12.
- Jones, J.W., Hoogenboom, G., Porter, C.H., Boote, K.J., Batchelor, W.D., Hunt, L.A., Wilkens, P.W., Singh, U., Gijsman, A.J., Ritchie, J.T., 2003. The DSSAT cropping system model. *Eur J Agron* 18, 235-265.
- Jones, P.G., Thornton, P.K., 2013. Generating downscaled weather data from a suite of climate models for agricultural modelling applications. *Agricultural Systems* 114, 1-5.
- JPC, 2016. Japan Productivity Center (JPC) Productivity Statistics of Japan Productivity center, <http://www.jpc-net.jp/eng/stats/>.
- Kaini, S., Nepal, S., Pradhananga, S., Gardner, T., Sharma, A.K., 2020. Representative general circulation models selection and downscaling of climate data for the transboundary Koshi river basin in China and Nepal. *Int J Climatol*.

- Kampschreur, M.J., Temmink, H., Kleerebezem, R., Jetten, M.S.M., van Loosdrecht, M.C.M., 2009. Nitrous oxide emission during wastewater treatment. *Water Res* 43, 4093-4103.
- Katerji, N., Ferreira, I., Mastrorilli, M., Losavio, N., 1990. A Simple Equation to Calculate Crop Evapotranspiration - Results of Several Years of Experimentation. *International Symposium on Scheduling of Irrigation for Vegetable Crops under Field Condition*, Vols 1 and 2 278, 477-489.
- Katerji, N., Rana, G., 2011. Crop Reference Evapotranspiration: A Discussion of the Concept, Analysis of the Process and Validation. *Water Resour Manag* 25, 1581-1600.
- Keating, B.A., Carberry, P.S., Hammer, G.L., Probert, M.E., Robertson, M.J., Holzworth, D., Huth, N.I., Hargreaves, J.N.G., Meinke, H., Hochman, Z., McLean, G., Verburg, K., Snow, V., Dimes, J.P., Silburn, M., Wang, E., Brown, S., Bristow, K.L., Asseng, S., Chapman, S., McCown, R.L., Freebairn, D.M., Smith, C.J., 2003. An overview of APSIM, a model designed for farming systems simulation. *Eur J Agron* 18, 267-288.
- Kendall, M.G., 1955. *Rank Correlation Methods*. Charles Griffin, London.
- Khan, Z., Linares, P., Garcia-Gonzalez, J., 2017. Integrating water and energy models for policy driven applications. A review of contemporary work and recommendations for future developments. *Renew Sust Energ Rev* 67, 1123-1138.

- Kim, H., Chen, W.M., 2018. Changes in energy and carbon intensity in Seoul's water sector. *Sustain Cities Soc* 41, 749-759.
- Kimball, B.A., Boote, K.J., Hatfield, J.L., Ahuja, L.R., Stockle, C., Archontoulis, S., Baron, C., Basso, B., Bertuzzi, P., Constantin, J., Deryng, D., Dumont, B., Durand, J.L., Ewert, F., Gaiser, T., Gayler, S., Hoffmann, M.P., Jiang, Q.J., Kim, S.H., Lizaso, J., Moulin, S., Nendel, C., Parker, P., Palosuo, T., Priesack, E., Qi, Z.M., Srivastava, A., Stella, T., Tao, F.L., Thorp, K.R., Timlin, D., Twine, T.E., Webber, H., Willaume, M., Williams, K., 2019. Simulation of maize evapotranspiration: An inter-comparison among 29 maize models. *Agr Forest Meteorol* 271, 264-284.
- Klemes, V., 1986. Operational Testing of Hydrological Simulation-Models. *Hydrolog Sci J* 31, 13-24.
- Ko, J., Piccinni, G., Marek, T., Howell, T., 2009. Determination of growth-stage-specific crop coefficients (Kc) of cotton and wheat. *Agr Water Manage* 96, 1691-1697.
- Kohler, M.E., Nordenson, T.J., Fox, W.E., 1955. Evaporation from pans and lakes. Weather Bureau Research Paper 38, US Department of Commerce: Washington, DC.
- Kraucunas, I., Clarke, L., Dirks, J., Hathaway, J., Hejazi, M., Hibbard, K., Huang, M.Y., Jin, C.L., Kintner-Meyer, M., van Dam, K.K., Leung, R., Li, H.Y., Moss, R., Peterson, M., Rice, J., Scott, M., Thomson, A., Voisin, N., West, T., 2015. Investigating the nexus of climate, energy, water, and land at decision-relevant

- scales: the Platform for Regional Integrated Modeling and Analysis (PRIMA). Climatic Change 129, 573-588.
- Krzeminski, P., van der Graaf, J.H.J.M., van Lier, J.B., 2012. Specific energy consumption of membrane bioreactor (MBR) for sewage treatment. Water Sci Technol 65, 380-392.
- Kyle, P., Davies, E.G.R., Dooley, J.J., Smith, S.J., Clarke, L.E., Edmonds, J.A., Hejazi, M., 2013. Influence of climate change mitigation technology on global demands of water for electricity generation. Int J Greenh Gas Con 13, 112-123.
- Lautenbach, S., Berlekamp, J., Graf, N., Seppelt, R., Matthies, M., 2009. Scenario analysis and management options for sustainable river basin management: Application of the Elbe DSS. Environ Modell Softw 24, 26-43.
- Lavers, D., Luo, L.F., Wood, E.F., 2009. A multiple model assessment of seasonal climate forecast skill for applications. Geophys Res Lett 36.
- Lhomme, J.P., 1997. A theoretical basis for the Priestley-Taylor coefficient. Bound-Lay Meteorol 82, 179-191.
- Li, H.J., Peng, D.C., Liu, W.B., Wei, J.L., Wang, Z.F., Wang, B.F., 2016. N₂O generation and emission from two biological nitrogen removal plants in China. Desalin Water Treat 57, 11800-11806.
- Li, M.Q., Dai, H.C., Xie, Y., Tao, Y., Bregnbæk, L., Sandholt, K., 2017. Water conservation from power generation in China: A provincial level scenario towards 2030. Appl Energ 208, 580-591.

- Li, M.Q., Dai, H.C., Xie, Y., Tao, Y., Bregnbæk, I., Sanholt, K., 2017. Water conservation from power generation in China: A provincial level scenario towards 2030. *Appl Energ.*
- Li, W.W., Yu, H.Q., Rittmann, B.E., 2015a. Chemistry: Reuse water pollutants. *Nature* 528, 29-31.
- Li, X., Feng, K.S., Siu, Y.L., Hubacek, K., 2012. Energy-water nexus of wind power in China: The balancing act between CO₂ emissions and water consumption. *Energy Policy* 45, 440-448.
- Li, X., Zhao, Y., Shi, C.L., Sha, J., Wang, Z.L., Wang, Y.Q., 2015b. Application of Water Evaluation and Planning (WEAP) model for water resources management strategy estimation in coastal Binhai New Area, China. *Ocean Coast Manage* 106, 97-109.
- Liang, J., Yang, Q., Sun, T., Martin, J.D., Sun, H., Li, L., 2015. MIKE 11 model-based water quality model as a tool for the evaluation of water quality management plans. *J Water Supply Res T* 64, 708-718.
- Liao, X.W., Tian, Y.J., Gan, Y.W., Ji, J.P., 2020. Quantifying urban wastewater treatment sector's greenhouse gas emissions using a hybrid life cycle analysis method - An application on Shenzhen city in China. *Sci Total Environ* 745.
- Lin, L., Chen, Y.D., 2018. Evaluation of Future Water Use for Electricity Generation under Different Energy Development Scenarios in China. *Sustainability-Basel* 10.

- Liu, D.F., Qiao, P., Zhang, L.P., Song, M., Liu, S., 2012. Application of QUAL2E Model to Analysis the Permissible Pollution Bearing Capacity of Water Bodies in City Water Area. *Advances in Environmental Science and Engineering*, Pts 1-6 518-523, 2385-2390.
- Liu, L., Hejazi, M., Patel, P., Kyle, P., Davies, E., Zhou, Y.Y., Clarke, L., Edmonds, J., 2015. Water demands for electricity generation in the US: Modeling different scenarios for the water-energy nexus. *Technol Forecast Soc* 94, 318-334.
- Liu, X.Y., Xu, C.Y., Zhong, X.L., Li, Y.Z., Yuan, X.H., Cao, J.F., 2017. Comparison of 16 models for reference crop evapotranspiration against weighing lysimeter measurement. *Agr Water Manage* 184, 145-155.
- Liu, Y., Cheng, X., Lun, X.X., Sun, D.Z., 2014. CH₄ emission and conversion from A(2)O and SBR processes in full-scale wastewater treatment plants. *J Environ Sci-China* 26, 224-230.
- Liu, Y.L., Hejazi, M., Kyle, P., Kim, S.H., Davies, E., Miralles, D.G., Teuling, A.J., He, Y.J., Niyogi, D., 2016a. Global and Regional Evaluation of Energy for Water. *Environmental Science & Technology* 50, 9736-9745.
- Liu, Y.W., Tugtas, A.E., Sharma, K.R., Ni, B.J., Yuan, Z.G., 2016b. Sulfide and methane production in sewer sediments: Field survey and model evaluation. *Water Res* 89, 142-150.
- Loulou, R., Remme, U., Kanudia, A., Lehtilä, A., Goldstein, G, 2005. Documentation for the times model. Technical Report DM 70046/ICC03080. IEA Energy

- Macknick, J., Sattler, S., Averyt, K., Clemmer, S., Rogers, J., 2012. The water implications of generating electricity: water use across the United States based on different electricity pathways through 2050. *Environ Res Lett* 7.
- Madadgar, S., AghaKouchak, A., Shukla, S., Wood, A.W., Cheng, L.Y., Hsu, K.L., Svoboda, M., 2016. A hybrid statistical-dynamical framework for meteorological drought prediction: Application to the southwestern United States. *Water Resour Res* 52, 5095-5110.
- Makkink, G.F., 1957. Testing the Penman formula by means of lysimeters. *Journal of the Institution of Water Engineers* 11, 277-288.
- Mann, H.B., 1945. Non-parametric tests against trend. *Econometrica* 13, 163-171.
- Mannina, G., Butler, D., Benedetti, L., Deletic, A., Fowdar, H., Fu, G.T., Kleidorfer, M., McCarthy, D., Mikkelsen, P.S., Rauch, W., Sweetapple, C., Vezzaro, L., Yuan, Z.G., Willems, P., 2018. Greenhouse gas emissions from integrated urban drainage systems: Where do we stand? *J Hydrol* 559, 307-314.
- Mannina, G., Cosenza, A., Gori, R., Garrido-Baserbac, M., Sobhani, R., Rosso, D., 2016. Greenhouse Gas Emissions from Wastewater Treatment Plants on a Plantwide Scale: Sensitivity and Uncertainty Analysis. *J Environ Eng* 142.
- Martinez-Hernandez, E., Leach, M., Yang, A.D., 2017. Understanding water-energy-food and ecosystem interactions using the nexus simulation tool NexSym. *Appl Energ* 206, 1009-1021.

- Matsoukas, C., Benas, N., Hatzianastassiou, N., Pavlakis, K.G., Kanakidou, M., Vardavas, I., 2011. Potential evaporation trends over land between 1983-2008: driven by radiative fluxes or vapour-pressure deficit? *Atmos Chem Phys* 11, 7601-7616.
- McCarty, P.L., Bae, J., Kim, J., 2011. Domestic Wastewater Treatment as a Net Energy Producer-Can This be Achieved? *Environmental Science & Technology* 45, 7100-7106.
- McCuen, R.H., 1974. A SENSITIVITY AND ERROR ANALYSIS CF PROCEDURES USED FOR ESTIMATING EVAPORATION¹. *JAWRA Journal of the American Water Resources Association* 10, 486-497.
- McNaughton, K.G., Jarvis, P.G., 1983. Predicting effects of vegetation changes on transpiration and evaporation [Mathematical models]. v. 7.
- Merryfield, W.J., Lee, W.S., Boer, G.J., Kharin, V.V., Scinocca, J.F., Flato, G.M., Ajayamohan, R.S., Fyfe, J.C., Tang, Y.M., Polavarapu, S., 2013. The Canadian Seasonal to Interannual Prediction System. Part I: Models and Initialization. *Monthly Weather Review* 141, 2910-2945.
- Mesonet, 2021. Oklahoma Mesonet. <https://www.mesonet.org>.
- Miralles, D.G., Holmes, T.R.H., De Jeu, R.A.M., Gash, J.H., Meesters, A.G.C.A., Dolman, A.J., 2011. Global land-surface evaporation estimated from satellite-based observations. *Hydrol Earth Syst Sc* 15, 453-469.

- Modala, N.R., Ale, S., Goldberg, D.W., Olivares, M., Munster, C.L., Rajan, N., Feagin, R.A., 2017. Climate change projections for the Texas High Plains and Rolling Plains. *Theor Appl Climatol* 129, 263-280.
- Moran, M.S., Clarke, T.R., Inoue, Y., Vidal, A., 1994. Estimating Crop Water-Deficit Using the Relation between Surface-Air Temperature and Spectral Vegetation Index. *Remote Sens Environ* 49, 246-263.
- Musenze, R.S., Werner, U., Grinham, A., Udy, J., Yuan, Z.G., 2014. Methane and nitrous oxide emissions from a subtropical estuary (the Brisbane River estuary, Australia). *Sci Total Environ* 472, 719-729.
- Nandagiri, L., Kovoov, G.M., 2006. Performance evaluation of reference evapotranspiration equations across a range of Indian climates. *J Irrig Drain Eng* 132, 238-249.
- Narapusetty, B., Collins, D.C., Murtugudde, R., Gottschalck, J., Peters-Lidard, C., 2018. Bias correction to improve the skill of summer precipitation forecasts over the contiguous United States by the North American multi-model ensemble system. *Atmos Sci Lett* 19.
- Navarro-Racines, C., Tarapues, J., Thornton, P., Jarvis, A., Ramirez-Villegas, J., 2020. High-resolution and bias-corrected CMIP5 projections for climate change impact assessments. *Sci Data* 7.
- NBS, 2012. China statistical yearbook 2012 (In Chinese). China Statistics Press, Beijing.
- Nielsen-Gammon, J.W., Banner, J.L., Cook, B.I., Tremaine, D.M., Wong, C.I., Mace, R.E., Gao, H.L., Yang, Z.L., Gonzalez, M.F., Hoffpauir, R., Gooch, T., Kloesel,

- K., 2020. Unprecedented Drought Challenges for Texas Water Resources in a Changing Climate: What Do Researchers and Stakeholders Need to Know? *Earth's Future* 8.
- Ning, S.K., Chang, N.B., Yang, L., Chen, H.W., Hsu, H.Y., 2001. Assessing pollution prevention program by QUAL2E simulation analysis for the Kao-Ping River Basin, Taiwan. *J Environ Manage* 61, 61-76.
- Niu, K.Y., Wu, J., Qi, L., Niu, Q.X., 2019. Energy intensity of wastewater treatment plants and influencing factors in China. *Sci Total Environ* 670, 961-970.
- NPC, 2016. National People's Congress (NPC). 13th Five-Year Plan for economic and social development.
- O'Shaughnessy, S.A., Evett, S.R., Colaizzi, P.D., Howell, T.A., 2012. A crop water stress index and time threshold for automatic irrigation scheduling of grain sorghum. *Agr Water Manage* 107, 122-132.
- OECD, 2012. OECD Environmental Outlook to 2050.
- Osroosh, Y., Peters, R.T., Campbell, C.S., Zhang, Q., 2016. Comparison of irrigation automation algorithms for drip-irrigated apple trees. *Comput Electron Agr* 128, 87-99.
- Paliwal, R., Sharma, P., Kansal, A., 2007. Water quality modelling of the river Yamuna (India) using QUAL2E-UNCAS. *J Environ Manage* 83, 131-144.
- Pan, T., Zhu, X.D., Ye, Y.P., 2011. Estimate of life-cycle greenhouse gas emissions from a vertical subsurface flow constructed wetland and conventional wastewater treatment plants: A case study in China. *Ecol Eng* 37, 248-254.

- Parlange, M.B., Katul, G.G., 1992. Estimation of the Diurnal-Variation of Potential Evaporation from a Wet Bare Soil Surface. *J Hydrol* 132, 71-89.
- Pascolini-Campbell, M., Reager, J.T., Chandanpurkar, H.A., Rodell, M., 2021. A 10 per cent increase in global land evapotranspiration from 2003 to 2019. *Nature* 593, 543-+.
- Payero, J.O., Irmak, S., 2006. Variable upper and lower crop water stress index baselines for corn and soybean. *Irrigation Sci* 25, 21-32.
- Penman, H.L., 1948. Natural Evaporation from Open Water, Bare Soil and Grass. *Proc R Soc Lon Ser-A* 193, 120-&.
- Pereira, A.R., 2004. The Priestley-Taylor parameter and the decoupling factor for estimating reference evapotranspiration. *Agr Forest Meteorol* 125, 305-313.
- PGSZM, 2008. Urban Master Planning of Shenzhen (2007-2020), The People's Government of Shenzhen Municipality (PGSZM), Shenzhen (In Chinese).
- Priestley, C.H.B., Taylor, R.J., 1972. On the Assessment of Surface Heat Flux and Evaporation Using Large-Scale Parameters. *Monthly Weather Review* 100.
- Privette, C.V., Smink, J., 2017. Assessing the potential impacts of WWTP effluent reductions within the Reedy River watershed. *Ecol Eng* 98, 11-16.
- Purkey, D., C. Heaps, J. Sieber and M. Davis, 2011. Energy-Water-Climate Planning for Development Without Carbon in Latin America and the Caribbean. Stockholm Environment Institute, U.S.

- Qin, H.P., Su, Q., Khu, S.T., 2011. An integrated model for water management in a rapidly urbanizing catchment. *Environ Modell Softw* 26, 1502-1514.
- Qin, H.P., Su, Q., Khu, S.T., 2013. Assessment of environmental improvement measures using a novel integrated model: A case study of the Shenzhen River catchment, China. *J Environ Manage* 114, 486-495.
- Qin, H.P., Su, Q., Khu, S.T., Tang, N., 2014. Water Quality Changes during Rapid Urbanization in the Shenzhen River Catchment: An Integrated View of Socio-Economic and Infrastructure Development. *Sustainability-Basel* 6, 7433-7451.
- Qu, S., Liang, S., Xu, M., 2017. CO₂ Emissions Embodied in Interprovincial Electricity Transmissions in China. *Environmental Science & Technology* 51, 10893-10902.
- Quijano, J.C., Zhu, Z., Morales, V., Landry, B.J., Garcia, M.H., 2017. Three-dimensional model to capture the fate and transport of combined sewer overflow discharges: A case study in the Chicago Area Waterway System. *Sci Total Environ* 576, 362-373.
- Racoviceanu, A.I., Karney, B.W., Kennedy, C.A., Colombo, A.F., 2007. Life-Cycle Energy Use and Greenhouse Gas Emissions Inventory for Water Treatment Systems. *J Infrastruct Syst* 13, 261-270.
- Rana, G., Katerji, N., 1998. A Measurement Based Sensitivity Analysis of the Penman-Monteith Actual Evapotranspiration Model for Crops of Different Height and in Contrasting Water Status. *Theor Appl Climatol* 60, 141-149.

- Ren, Y.G., Wang, J.H., Li, H.F., Zhang, J., Qi, P.Y., Hu, Z., 2013. Nitrous oxide and methane emissions from different treatment processes in full-scale municipal wastewater treatment plants. *Environ Technol* 34, 2917-2927.
- Robock, A., Vinnikov, K.Y., Schlosser, C.A., Speranskaya, N.A., Xue, Y.K., 1995. Use of Midlatitude Soil-Moisture and Meteorological Observations to Validate Soil-Moisture Simulations with Biosphere and Bucket Models. *J Climate* 8, 15-35.
- Rost, S., Gerten, D., Bondeau, A., Lucht, W., Rohwer, J., Schaphoff, S., 2008. Agricultural green and blue water consumption and its influence on the global water system. *Water Resour Res* 44.
- Rothausen, S.G.S.A., Conway, D., 2011. Greenhouse-gas emissions from energy use in the water sector. *Nat Clim Change* 1, 210-219.
- Saha, S., Nadiga, S., Thiaw, C., Wang, J., Wang, W., Zhang, Q., Van den Dool, H.M., Pan, H.L., Moorthi, S., Behringer, D., Stokes, D., Pena, M., Lord, S., White, G., Ebisuzaki, W., Peng, P., Xie, P., 2006. The NCEP Climate Forecast System. *J Climate* 19, 3483-3517.
- Sen, P.K., 1968. Estimates of the Regression Coefficient Based on Kendall's Tau. *Journal of the American Statistical Association* 63, 1379-1389.
- Sheffield, J., Goteti, G., Wood, E.F., 2006. Development of a 50-year high-resolution global dataset of meteorological forcings for land surface modeling. *J Climate* 19, 3088-3111.

- Shiri, J., Nazemi, A.H., Sadraddini, A.A., Marti, P., Fard, A.F., Kisi, O., Landaras, G., 2019. Alternative heuristics equations to the Priestley-Taylor approach: assessing reference evapotranspiration estimation. *Theor Appl Climatol* 138, 831-848.
- Singer, M.B., Asfaw, D.T., Rosolem, R., Cuthbert, M.O., Miralles, D.G., MacLeod, D., Quichimbo, E.A., Michaelides, K., 2021. Hourly potential evapotranspiration at 0.1 degrees resolution for the global land surface from 1981-present. *Sci Data* 8.
- Singh, P., Carliell-Marquet, C., Kansal, A., 2012. Energy pattern analysis of a wastewater treatment plant. *Appl Water Sci* 2, 221-226.
- Singh, V.P., Xu, C.Y., 1997. Evaluation and generalization of 13 mass-transfer equations for determining free water evaporation. *Hydrol Process* 11, 311-323.
- Smith, K., Liu, S.M., Liu, Y., Guo, S.J., 2018. Can China reduce energy for water? A review of energy for urban water supply and wastewater treatment and suggestions for change. *Renew Sust Energ Rev* 91, 41-58.
- Su, Q., Dai, H., Lin, Y., Chen, H., Karthikeyan, R., 2018. Modeling the carbon-energy-water nexus in a rapidly urbanizing catchment: A general equilibrium assessment. *J Environ Manage* 225, 93-103.
- Su, Q., Dai, H.C., Chen, H., Lin, Y., Xie, Y., Karthikeyan, R., 2019. General Equilibrium Analysis of the Cobenefits and Trade-Offs of Carbon Mitigation on Local Industrial Water Use and Pollutants Discharge in China. *Environmental Science & Technology* 53, 1715-1724.

- Su, Q., Qin, H.P., Fu, G.T., 2014. Environmental and ecological impacts of water supplement schemes in a heavily polluted estuary. *Sci Total Environ* 472, 704-711.
- Su, Q., Qin, H.P., Zhao, Z.J., 2009. Modeling effects of regional industrial structure adjustment on water resource balance and water quality improvement. *China Environmental Science* Vol.29, 767-772.
- SZMG, 2016. 13th Five-Year Plan for economic and social development of Shenzhen. Shenzhen Municipal Government, Shenzhen.
- SZUPLRB, 2003. Water supply system plan and sewage system plan of Shenzhen (2001-2020), Shenzhen Urban Planning and Land Resources Bureau (SZUPLRB), Shenzhen (In Chinese).
- SZUPLRB, 2011. Sewage and WWTPs system plan of Shenzhen (2011-2020), Shenzhen Urban Planning and Land Resources Bureau (SZUPLRB), Shenzhen (In Chinese).
- Tabari, H., 2010. Evaluation of Reference Crop Evapotranspiration Equations in Various Climates. *Water Resour Manag* 24, 2311-2337.
- Talati, S., Zhai, H.B., Kyle, G.P., Morgan, M.G., Patel, P., Liu, L., 2016. Consumptive Water Use from Electricity Generation in the Southwest under Alternative Climate, Technology, and Policy Futures. *Environmental Science & Technology* 50, 12095-12104.

- Theil, H., 1950. A Rank-Invariant Method of Linear and Polynomial Regression Analysis. Proceedings of the Royal Netherlands Academy of Sciences 53, Part I: 386-392, Part II: 521-525, Part III: 1397-1412.
- Thornthwaite, C.W., 1948. An Approach toward a Rational Classification of Climate. Geogr Rev 38, 55-94.
- Tian, X., Geng, Y., Dai, H.C., Fujita, T., Wu, R., Liu, Z., Masui, T., Yang, X., 2016. The effects of household consumption pattern on regional development: A case study of Shanghai. Energy 103, 49-60.
- Trajkovic, S., Kolakovic, S., 2009. Estimating Reference Evapotranspiration Using Limited Weather Data. J Irrig Drain Eng 135, 443-449.
- Turc, L., 1961. Water requirements assessment of irrigation, potential evapotranspiration: Simplified and updated climatic formula. Annales Agronomiques, 13-49.
- UN, 2019. United Nations, World Population Prospects 2019.
- UNFCCC, 2015. Adoption of the Paris Agreement. Proposal by the President. 2015, United Nations Framework Convention on Climate Change (UNFCCC), http://unfccc.int/documentation/documents/advanced_search/items/6911.php?prir ef=600008831.
- USEPA, 2012. Global Non-CO2 GHG Emissions: 1990-2030.
- Valipour, M., Sefidkouhi, M.A.G., Raeini-Sarjaz, M., 2017. Selecting the best model to estimate potential evapotranspiration with respect to climate change and magnitudes of extreme events. Agr Water Manage 180, 50-60.

- van Dam, J.C., Groenendijk, P., Hendriks, R.F.A., Kroes, J.G., 2008. Advances of modeling water flow in variably saturated soils with SWAP. *Vadose Zone J* 7, 640-653.
- Vernieres, G., Rienecker, M.M., Kovach, R., Keppenne, C.L., 2012. The GEOS-iODAS: Description and evaluation. NASA Tech. Rep. Series on Global Modeling and Data Assimilation NASA/TM-2012-104606, p. 73.
- Vicente-Serrano, S.M., Azorin-Molina, C., Sanchez-Lorenzo, A., Revuelto, J., Moran-Tejeda, E., Lopez-Moreno, J.I., Espejo, F., 2014. Sensitivity of reference evapotranspiration to changes in meteorological parameters in Spain (1961-2011). *Water Resour Res* 50, 8458-8480.
- Wang, C.Y., Wang, R.R., Hertwich, E., Liu, Y., 2017. A technology-based analysis of the water-energy-emission nexus of China's steel industry. *Resour Conserv Recy* 124, 116-128.
- Wang, H.T., Yang, Y., Keller, A.A., Li, X., Feng, S.J., Dong, Y.N., Li, F.T., 2016. Comparative analysis of energy intensity and carbon emissions in wastewater treatment in USA, Germany, China and South Africa. *Appl Energ* 184, 873-881.
- Wang, J.H., Zhang, J., Xie, H.J., Qi, P.Y., Ren, Y.G., Hu, Z., 2011. Methane emissions from a full-scale A/A/O wastewater treatment plant. *Bioresource Technol* 102, 5479-5485.
- Wang, P., Dai, H.C., Ren, S.Y., Zhao, D.Q., Masui, T., 2015. Achieving Copenhagen target through carbon emission trading: Economic impacts assessment in Guangdong Province of China. *Energy* 79, 212-227.

- Wang, W.G., Shao, Q.X., Peng, S.Z., Xing, W.Q., Yang, T., Luo, Y.F., Yong, B., Xu, J.Z., 2012. Reference evapotranspiration change and the causes across the Yellow River Basin during 1957-2008 and their spatial and seasonal differences. *Water Resour Res* 48.
- Wen, Z.G., Xu, C., Zhang, X.Y., 2015. Integrated Control of Emission Reductions, Energy-Saving, and Cost-Benefit Using a Multi-Objective Optimization Technique in the Pulp and Paper Industry. *Environmental Science & Technology* 49, 3636-3643.
- Wisser, D., Frohking, S., Douglas, E.M., Fekete, B.M., Vorosmarty, C.J., Schumann, A.H., 2008. Global irrigation water demand: Variability and uncertainties arising from agricultural and climate data sets. *Geophys Res Lett* 35.
- Wu, R., Dai, H.C., Geng, Y., Xie, Y., Masui, T., Liu, Z.Q., Qian, Y.Y., 2017. Economic Impacts from PM2.5 Pollution-Related Health Effects: A Case Study in Shanghai. *Environmental Science & Technology* 51, 5035-5042.
- Wu, R., Dai, H.C., Geng, Y., Xie, Y., Mosui, T., Tian, X., 2016. Achieving China's INDC through carbon cap-and-trade: Insights from Shanghai. *Appl Energ* 184, 1114-1122.
- WWAP, 2014. United Nations World Water Assessment Programme (WWAP). The United Nations World Water Development Report 2014: Water and Energy. United Nations Educational, Scientific and Cultural Organization (UNESCO), Paris.

- Xie, Y., Dai, H.C., Dong, H.J., Hanaoka, T., Masui, T., 2016. Economic Impacts from PM_{2.5} Pollution-Related Health Effects in China: A Provincial-Level Analysis. *Environmental Science & Technology* 50, 4836-4843.
- Xing, J., Wang, S.X., Chatani, S., Zhang, C.Y., Wei, W., Hao, J.M., Klimont, Z., Cofala, J., Amann, M., 2011. Projections of air pollutant emissions and its impacts on regional air quality in China in 2020. *Atmos Chem Phys* 11, 3119-3136.
- Xiong, S.Q., Ji, J.P., Ma, X.M., 2019. Comparative Life Cycle Energy and GHG Emission Analysis for BEVs and PhEVs: A Case Study in China. *Energies* 12.
- Xu, C.Y., Singh, V.P., 2000. Evaluation and generalization of radiation-based methods for calculating evaporation. *Hydrol Process* 14, 339-349.
- Xu, C.Y., Singh, V.P., 2001. Evaluation and generalization of temperature-based methods for calculating evaporation. *Hydrol Process* 15, 305-319.
- Xu, C.Y., Singh, V.P., 2002. Cross comparison of empirical equations for calculating potential evapotranspiration with data from Switzerland. *Water Resour Manag* 16, 197-219.
- Xu, J.Z., Peng, S.Z., Ding, J.L., Wei, Q., Yu, Y.M., 2013. Evaluation and calibration of simple methods for daily reference evapotranspiration estimation in humid East China. *Arch Agron Soil Sci* 59, 845-858.
- Yan, X., Li, L., Liu, J.X., 2014. Characteristics of greenhouse gas emission in three full-scale wastewater treatment processes. *J Environ Sci-China* 26, 256-263.

- Yates, D., Purkey, D., Sieber, J., Huber-Lee, A., Galbraith, H., 2005. WEAP21 - A demand-, priority-, and preference-driven water planning model Part 2: Aiding freshwater ecosystem service evaluation. *Water Int* 30, 501-512.
- Yazdandoost, F., Moradian, S., Zakipour, M., Izadi, A., Bavandpour, M., 2020. Improving the precipitation forecasts of the North-American multi model ensemble (NMME) over Sistan basin. *J Hydrol* 590.
- Yoshida, H., Monster, J., Scheutz, C., 2014. Plant-integrated measurement of greenhouse gas emissions from a municipal wastewater treatment plant. *Water Res* 61, 108-118.
- Yu, S., He, L., Lu, H.W., 2016. An environmental fairness based optimisation model for the decision-support of joint control over the water quantity and quality of a river basin. *J Hydrol* 535, 366-376.
- Zarco-Tejada, P.J., González-Dugo, V., Berni, J.A.J., 2012. Fluorescence, temperature and narrow-band indices acquired from a UAV platform for water stress detection using a micro-hyperspectral imager and a thermal camera. *Remote Sens Environ* 117, 322-337.
- Zhang, Q.H., Yang, W.N., Ngo, H.H., Guo, W.S., Jin, P.K., Dzakpasu, M., Yang, S.J., Wang, Q., Wang, X.C., Ao, D., 2016. Current status of urban wastewater treatment plants in China. *Environ Int* 92-93, 11-22.
- Zhang, R.S., Fujimori, S., Dai, H.C., Hanaoka, T., 2018. Contribution of the transport sector to climate change mitigation: Insights from a global passenger transport

model coupled with a computable general equilibrium model. *Appl Energ* 211, 76-88.

Zhang, X.D., Vesselinov, V.V., 2016. Energy-water nexus: Balancing the tradeoffs between two-level decision makers. *Appl Energ* 183, 77-87.

APPENDIX A

SUPPLEMENTARY DATA OF CHAPTER 2

Table A1 Selected Indicators of Shenzhen and Their Percentages in China in 2007.

Indicator	Value	% of China
Population (million)	9.12	0.7%
GDP (billion US\$)	86.4	2.4%
GDP per capita (US\$)	9464	351%
Import (billion US\$)	66.1	7.0%
Export (billion US\$)	96.3	7.9%
Coal consumption (PJ)	148.6	0.3%
Petroleum consumption (PJ)	579.9	4.1%
Natural gas consumption (PJ)	83.6	3.1%
Water consumption (billion ton)	18.0	0.7%

Sources: China Statistical Yearbook, 2008; China Energy Statistical Yearbook 2008 (2007 price).

Table A2 Sector Classification of the CGE Model.

No.	Sector	No.	Sector
1	Agriculture	12	Transport equipment
2	Extraction of natural gas	13	Machinery
3	Other Mining	14	Electronic equipment
4	Textiles and clothing	15	Other manufacturing
5	Paper and paper products	16	Waste manufacturing
6	Food production	17	Water supply
7	Textiles	18	Electricity production and supply
8	Chemicals	19	Manufactured gas
9	Non-metal products	20	Construction
10	Metal smelting and pressing	21	Transport
11	Metal products	22	Service

Table A3 Average Water Intensity (2011-2014) in Different Sectors (mean \pm standard deviation; n=4).

No.	Sector	Water use intensity t/10 ⁴ RMB (1990s)	Time period
1	Agriculture	1099.80 \pm 374.42	2000-2015 ^a
2	Extraction of natural gas ^d	14.20	2012 ^b
3	Other mining	12.73	2014 ^b
4	Textiles and clothing	54.60 \pm 2.76	2011-2014
5	Paper and paper products	6.01 \pm 1.94	2011-2014
6	Food production	10.47 \pm 2.14	2011-2014
7	Petrol oil	0.71	2012 ^b
8	Chemicals	3.81 \pm 0.85	2011-2014
9	Non-metal products	11.80 \pm 4.35	2011-2014
10	Metal smelting and pressing	6.49 \pm 2.83	2011-2014
11	Metal products	14.25 \pm 1.67	2011-2014
12	Transport equipment	7.06 \pm 6.12	2011-2014
13	Machinery	3.49 \pm 0.73	2011-2014
14	Electronic equipment	3.28 \pm 0.10	2011-2014
15	Other manufacturing	4.73 \pm 1.59	2011-2014
16	Waste manufacturing	2.50 \pm 3.22	2011-2013 ^c
17	Water supply	7.20	2011 ^b
18	Electricity production and supply	24.88 \pm 4.36	2011-2014
19	Manufactured gas ^d	33.43	2012 ^b
20	Construction	6.60 \pm 0.44	2011-2014
21	Transport	7.84 \pm 0.40	2011-2014
22	Service	7.84 \pm 0.40	2011-2014

Note: ^a n = 16; ^b n = 1; ^c n = 1; ^d data from national average. National Bureau of Statics of China, China statistical yearbook 2012. Beijing, China: China Statistics Press; 2012.

Table A4 Estimated Parameter Values for Water Use Intensity.

Industry type	α	WR	Lower 95% (WR)	Upper 95% (WR)	R ²	Time period
Primary industry	0.066**	1.069	1.029	1.109	0.531	2000-2015
Secondary industry*	-0.082**	0.914	0.915	0.927	0.982	2000-2015
Tertiary industry	-0.078**	0.925	0.910	0.940	0.908	2003-2015
Construction sector	-0.110**	0.896	0.862	0.931	0.779	2003-2015

Note: *Shenzhen's total water withdrawal includes primary industry, secondary industry (construction sector is calculated separately), Tertiary industry, residential sector and environment and ecosystems water use. ** indicate significance at the 1% confidence level. WR= e^{α_i} is considered the water intensity change rate (WR) of the *ith* industry.

Table A5 Average Major Pollutant Discharge Intensity (2011-2014) in Different Sectors. (mean value \pm standard deviation, n=4) Units: RMB (in 1990 Price).

No.	COD _{Cr} (t/billion)	NH ₃ -N (t/billion)	Petroleum (t/billion)	V-ArOH (kg/billion)
2 ^c	10.19	0.31	0.128	0.002
3	95.55 ^a	2.04 ^a	-	-
4	236.03 \pm 23.42	17.75 \pm 3.72	0.016 \pm 0.008	-
5	42.96 \pm 12.11	3.76 \pm 0.81	0.004 \pm 0.002	-
6	112.4 \pm 46.26	10.14 \pm 5.02	0.001 \pm 0.000	-
7	2.97	1.21	-	-
8	28.57 \pm 14.49	1.60 \pm 1.07	0.019 \pm 0.010	0.120 ^a
9	75.20 \pm 53.02	6.76 \pm 2.57	0.002 \pm 0.001	-
10	62.43 \pm 27.92	4.31 \pm 1.39	0.183 \pm 0.043	-
11	111.17 \pm 36.63	8.14 \pm 1.80	0.068 \pm 0.023	0.020 ^a
12	39.79 \pm 8.36	4.12 \pm 1.42	0.002 \pm 0.003	-
13	24.34 \pm 4.64	2.07 \pm 0.64	0.014 \pm 0.009	-
14	29.28 \pm 1.47	2.37 \pm 0.24	0.003 \pm 0.001	-
15	34.32 \pm 16.61	2.74 \pm 0.86	0.142 \pm 0.050	0.010 ^a
16	3.19 \pm 1.41 ^b	0.22 \pm 0.18 ^b	-	-
17	39.38 ^a	4.73 ^a	-	-
18	49.44 \pm 18.12	5.69 \pm 1.98	0.0002 \pm 0.0000	-
19 ^c	5.87 ^a	2.06 ^a	0.0166 ^a	0.003 ^a

Note: ^a n = 1; ^b n = 3; ^c data from the national average. National Bureau of Statics of China, China statistical yearbook 2012. Beijing, China: China Statistics Press; 2012.

* Petroleum has three years data.

Table A6 Average Heavy Metal(loid)s Discharge Intensity (2011-2014) in Different Sectors. (mean value \pm standard deviation, n=4) Units: RMB (in 1990 Price).

No.	P _b (kg/billion)	Cr ⁶⁺ (kg/billion)	Hg (kg/billion)	Cd (kg/billion)	As (kg/billion)
5	-	0.04 \pm 0.08	-	-	-
8	0.06 \pm 0.00	0.01 \pm 0.00	-	0.011 ^a	0.12 ^a
10	-	0.28 \pm 0.15	-	-	-
11	0.47 \pm 0.02	8.13 \pm 2.42	0.002 \pm 0.000	0.096 ^a	-
12	-	0.14	-	-	-
13	0.13 \pm 0.03	0.04 \pm 0.02	0.11 \pm 0.01	0.004 \pm 0.003	0.0004 ^a
14	0.11 \pm 0.09	0.07 \pm 0.02	0.01 \pm 0.02	0.064 \pm 0.034	0.24 \pm 0.06
15	0.06 \pm 0.00	0.81 \pm 0.62	0.13 \pm 0.22	0.010 ^a	0.13 ^a
18	-	-	1.05 \pm 0.21	-	-

Note: ^a n = 1. National Bureau of Statics of China, China statistical yearbook 2012. Beijing, China: China Statistics Press; 2012.

* Pb, Cr⁶⁺, Hg, Cd, and As have three years data.

Table A7 Estimated parameter values for pollutant intensity.

No.	β	PR	Lower 95% (PR)	Upper 95% (PR)	R ²	Time period
2	-0.203***	0.817	0.718	0.929	0.623	2002-2011 ^a
3	-0.227	0.561	0.394	1.612	0.064	2002-2011 ^a
4	-0.228***	0.796	0.709	0.895	0.655	1996-2007
5	-0.418***	0.658	0.606	0.715	0.945	2002-2011 ^a
6	0.005	1.005	0.954	1.059	0.005	1996-2007
7	-0.167***	0.846	0.815	0.879	0.930	2002-2011 ^a
8	-0.195***	0.823	0.755	0.896	0.775	1996-2007
9	-0.091	0.913	0.708	1.176	0.061	1996-2007
10	0.152	1.164	0.853	1.589	0.137	1996, 1999-2007
11	-0.028	0.972	0.876	1.079	0.035	1996-2007
12	-0.195***	0.823	0.755	0.896	0.775	2002-2011 ^a
13	-0.356***	0.700	0.640	0.766	0.913	2002-2011 ^a
14	-0.049	0.952	0.883	1.027	0.173	1996-2007
15	-0.272***	0.762	0.667	0.870	0.674	1996-2007
16	-0.045	0.956	0.689	1.327	0.751	2002, 2010-2011 ^a
17	0.149	1.161	0.810	1.663	0.102	2002-2011 ^a
18	-0.370***	0.691	0.636	0.749	0.931	1996-2000; 2005-2007
19	-0.427***	0.653	0.450	0.946	0.467	2002-2011 ^a

Note: ^a data from the national dataset. National Bureau of Statics of China, China statistical yearbook 2003-2012. Beijing, China: China Statistics Press; 2003-2012. Other data from Shenzhen Environmental quality report. Human Settlements & Environment Commission of Shenzhen Municipality, Report on the environmental state in Shenzhen City, Shenzhen, China. 1996-2007.

^b $PR = e^{\beta_i}$ is considered the pollutant intensity change rate (PR) of the *i*th industry.

***, **, * indicates significance at the 1%, 5% and 10% confidence level, respectively. For those p-value is higher than 10% confidence level, we assume PR=1, which means a constant PR is used.

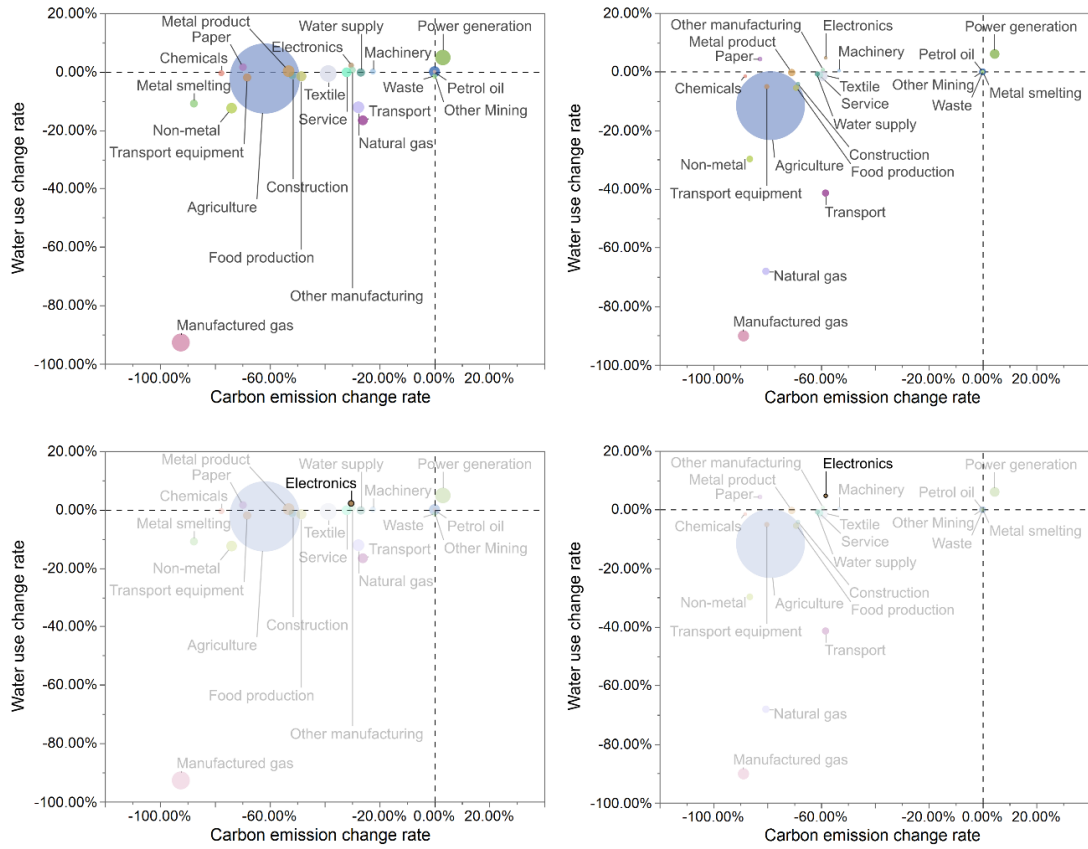


Figure A1 The carbon emission change rate (NDC compared with the BaU scenario) versus water use change rate (NDC compared with the BaU scenario). (Bubble size indicates water use intensity).

The appendix provides a technical description of the CGE model. This CGE model is based upon the model structure of Dai (2012). We follow the CGE framework of Dai (2012) and build a one-region dynamic CGE model to study the NDC issue for Shenzhen.

A.1 Production

Each producer maximizes profit subject to the production technology. Activity output of each sector follows a nested constant elasticity of substitution (CES)

production function. Each sector has two types of production functions; one uses the existing capital stock, and another uses new investment (Masui et al., 2011). The difference between these two subsectors is the efficiency and mobility of capital among the sectors. Inputs are categorized into material commodities, energy commodities, land, labor, capital, and resource.

The producer maximizes its profit by choosing its output level and inputs use, depending on their relative prices as well as its technology. The producer's problem can be expressed as:

$$\max: \pi_j = p_j \cdot Z_j - (\sum_{i=1}^N p_i \cdot X_{i,j} + \sum_{f=1}^F \omega_f \cdot V_{f,j}) \quad \text{Equation (A1)}$$

subject to (s.t.):

$$Z_j = v_j [X_{1,j}, X_{2,j}, \dots, X_{N,j}; V_{1,j} \dots, V_{f,j}] \quad \text{Equation (A2)}$$

where π_j is the profit of j -th producers; Z_j is the output of j -th sector; $X_{i,j}$ is the intermediate inputs of i -th goods in j -th sector, $V_{f,j}$ is the f -th primary factor inputs in j -th sector; p_j is the price of the j -th composite commodity; ω_f is the f -th factor price; and v_j is the share parameter in the CES production function.

A.2 Basic sectors

For the basic production functions, activity output is determined by a fixed coefficient aggregation of non-energy and energy intermediate commodities, and primary factors (Figure A2). The composite of non-energy inputs takes the Leontief form. Energy and the value added bundle are nested by energy inputs and valued added

bundle, respectively. The value added bundle is a CES function of primary factors, capital, and labor. The composite of energy inputs is a CES aggregation of electricity and fossil fuels. Fossil fuels are further disaggregated into coal, gas, and oil.

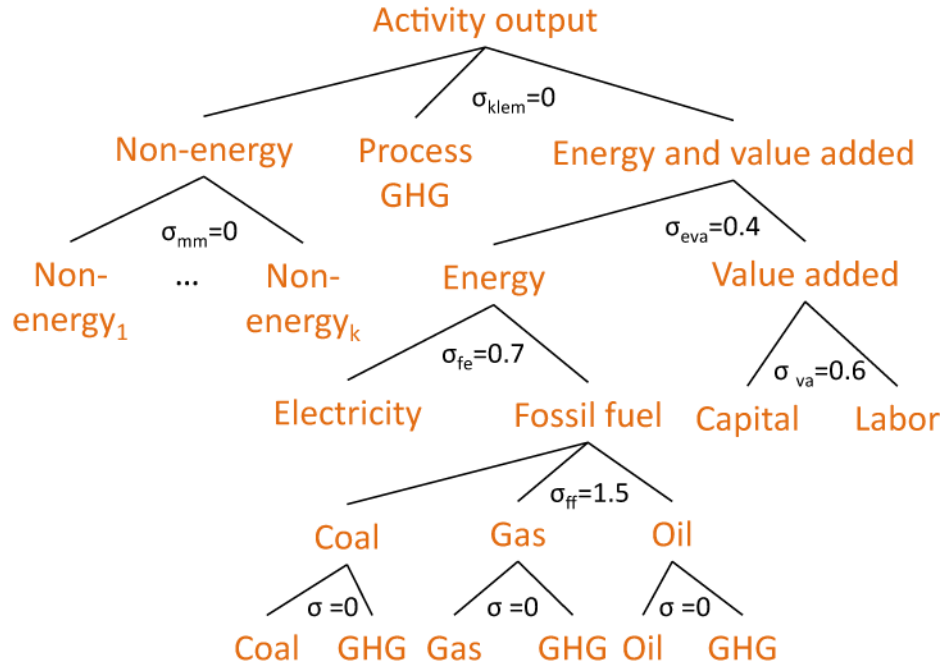


Figure A2 Production tree of basic sectors. σ is the elasticity of substitution for inputs.

There are four levels in the above production tree. At each level, a virtual firm is assumed to maximize the corresponding profit subject to the production technology. At the top-level, the output is a Leontief function of the quantities of value-added and aggregate energy input and aggregate intermediate input, associated with process GHG emissions:

$$\max: \pi_j^z = p_j^z \cdot Q_j - (p_j^{vae} \cdot QVAE_j + p_j^{inta} \cdot QINTA_j + p^{ghg} \cdot QGHG_{j,act,ghg})$$

Equation (A3)

s.t.

$$Q_j = \min\left(\frac{QVAE_j}{qvae_j}, \frac{QINTA_j}{qinta_j}, \frac{QGHG_{j,act,ghg}}{qghg_{j,act,ghg}}\right)$$

Equation (A4)

where π_j^z is the profit of the j -th firm producing gross domestic output Q_j at the top level; Q_j is the gross domestic output of the j -th firm; $QVAE_j$ is the value added and energy composite input; $QINTA_j$ is the composite intermediate input; $QGHG_{j,act,ghg}$ is the process emissions of GHGs per unit of output; p_j^z is the price of j -th gross domestic output; p_j^{vae} is the price of composite goods of factor and energy; p_j^{inta} is the price of composite intermediate goods; p^{ghg} is the GHG emission price; $qvae_j$ is the technical coefficient transforming the composite amounts of value added and energy inputs to Q_j ; $qinta_j$ is the technical coefficient transforming the composite amounts of non-energy intermediate inputs to Q_j ; and $qghg_{j,act,ghg}$ is the technical coefficient transforming the process GHG emissions to Q_j .

At the second level of the production tree, there are two virtual firms with profit-maximization problems. First, composite value added and energy input take CES the functional form with aggregation of value added input and total energy input:

$$\max: \pi_j^{vae} = p_j^{vae} \cdot QVAE_j - (p_j^{va} \cdot QVA_j + p_j^{fe} \cdot QFE_j)$$

Equation (A5)

s.t.

$$QVAE_j = \alpha_j^{vae} \cdot (\delta_j^{vae} \cdot QVA_j^{-\rho_j^{vae}} + (1 - \delta_j^{vae}) \cdot QFE_j^{-\rho_j^{vae}})^{\frac{-1}{\rho_j^{vae}}} \quad \text{Equation (A6)}$$

Second, aggregate non-energy intermediate input is defined as Leontief function of disaggregated intermediate input:

$$\max: \pi_j^{inta} = p_j^{inta} \cdot QINTA_j - (\sum_i p_j^q \cdot QINT_{i,j}) \quad \text{Equation (A7)}$$

s.t.

$$QINTA_j = \min(\frac{QINT_{i,j}}{qint_{i,j}}) \quad \text{Equation (A8)}$$

Where π_j^{vae} is the profit of j -th firm producing composite input of value added and energy; π_j^{inta} is the profit of j -th firm producing composite intermediate input; QVA_j is the aggregate value added input; QFE_j is the aggregate energy input (electricity and fossil energy); $QINT_{i,j}$ is the i -th non-energy inputs in j -th firm; p_j^{vae} is the price of composite value added input; p_j^{fe} is the price of the composite energy input (including electricity and fossil fuel); p_j^q is the price of the i -th composite goods; $qint_{i,j}$ is the amounts of each input required per unit of composite intermediate input; α_j^{vae} is the shift (or efficiency) parameter in the CES function; δ_j^{vae} is the CES share parameter, $0 \leq \delta_j^{vae} \leq 1$, $\sum_j \delta_j^{vae} = 1$; ρ_j^{vae} is the CES substitution parameter, in which the elasticity of substitution between value added and energy, σ , equals $\frac{1}{(1+\rho)}$; and σ_j^{vae} is the elasticity of substitution between value added bundle and energy.

At the third level of the production tree, there are two virtual firms with profit-maximization problems as well. First, composite value added input is CES aggregation of capital and labor input:

$$\max: \pi_j^{va} = p_j^{va} \cdot QVA_j - (pl \cdot QLAB_j + pk_j \cdot QCAP_j) \quad \text{Equation (A9)}$$

s.t.

$$QVA_j = \alpha_j^{va} \cdot (\delta_j^{cap} \cdot QCAP_j^{-\rho_j^{va}} + \delta_j^{lab} \cdot QLAB_j^{-\rho_j^{va}})^{\frac{-1}{\rho_j^{va}}} \quad \text{Equation (A10)}$$

And composite energy input is CES aggregation of electricity input and fossil fuel input:

$$\max: \pi_j^{fe} = p_j^{fe} \cdot QFE_j - (p_{\text{"ele"}}^q \cdot QELE_j + p_j^{fos} \cdot QFOS_j) \quad \text{Equation (A11)}$$

s.t.

$$QFE_j = \alpha_j^{fe} \cdot (\delta_j^{ele} \cdot QELE_j^{-\rho_j^{fe}} + (1 - \delta_j^{ele}) \cdot QFOS_j^{-\rho_j^{fe}})^{\frac{-1}{\rho_j^{fe}}} \quad \text{Equation (A12)}$$

where π_j^{va} is the profit of j -th firm producing composite input of value added; π_j^{fe} is the profit of j -th firm producing composite input of energy; $QCAP_j$ is the capital input required per unit of value added input; $QLAB_j$ is the labor input required per unit of value added input; $QELE_j$ is the electricity input required for per unit of composite energy input; $QFOS_j$ is the composite fossil fuel input required for per unit of composite energy input; pl is the labor wage; pk_j is the capital price in j -th sector; $p_{\text{"ele"}}^q$ is the price of the composite goods of electricity; p_j^{fos} is the price of composite fossil fuel

input in j -th sector; α_j^{fe} is the shift (or efficiency) parameter in the CES function; δ_j^{fe} , δ_j^{cap} , δ_j^{lab} are CES share parameters, $0 \leq \delta_j^* \leq 1$, $\sum_i \delta_j^* = 1$; ρ_j^{fe} is the CES substitution parameter, in which the elasticity of substitution between electricity and composite fossil fuel, σ , equals $\frac{1}{(1+\rho)}$; σ_j^{va} is the elasticity of substitution between capital and labor; and σ_j^{vae} is the elasticity of substitution between electricity and fossil fuel.

At the fourth level of the production function, composite fossil fuel is CES aggregation of coal, crude oil, natural gas, coke, petrol oil, and manufactured gas:

$$\max: \pi_j^{fos} = p_j^{fos} \cdot QFOS_j - (\sum_{fos} p_{fos}^q \cdot QFF_{fos,j}) \quad \text{Equation (A13)}$$

s.t.

$$QFOS_j = \alpha_j^{ff} \cdot (\sum_{fos} \delta_j^{ff} \cdot QFF_{fos,j}^{-\rho_j^{ff}})^{\frac{-1}{\rho_j^{ff}}} \quad \text{Equation (A14)}$$

where π_j^{fos} is the profit of j -th firm producing composite input of fossil fuel; $QFF_{fos,j}$ is the CES shift (or efficiency) parameter; p_{fos}^q is the price of fossil fuel input; α_j^{ff} is the shift (or efficiency) parameter in the CES function; δ_j^{ff} is the CES share parameter, $0 \leq \delta_j^{ff} \leq 1$, $\sum_i \delta_j^{ff} = 1$; ρ_j^{ff} is the CES substitution parameter, in which the elasticity of substitution among fossil fuels, σ , equals $\frac{1}{(1+\rho)}$; and σ_j^{ff} is the elasticity of substitution among fossil fuels.

A.3 Energy transformation sector

Energy transformation sectors include gas production and supply, petroleum and nuclear fuel processing, and coking. The energy bundle is linked at the top level in order to maintain the first-law of thermal efficiency of the conversion of primary energy to the secondary energy (Figure A3). Functions at other levels are the same as the basic sectors.

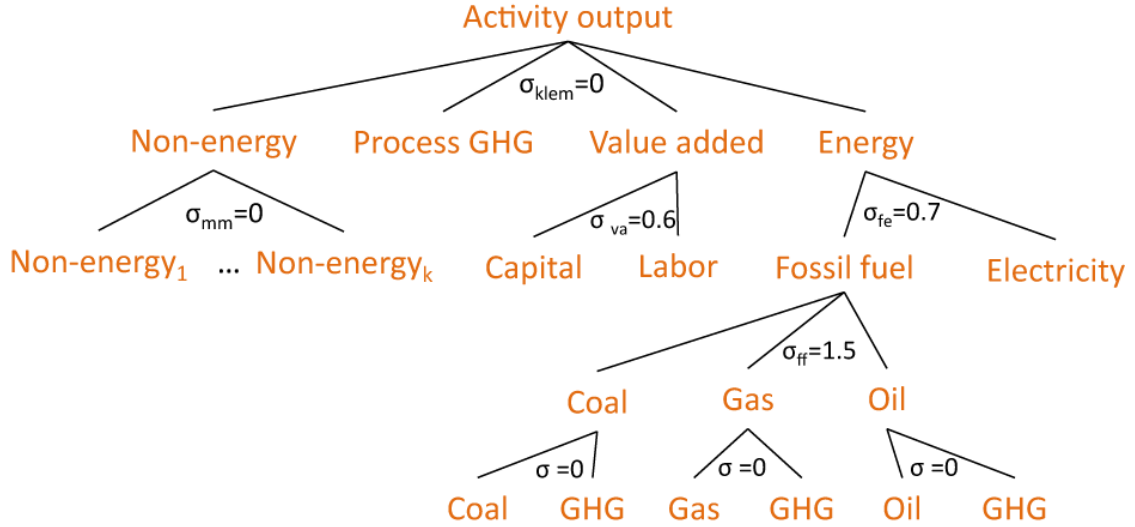


Figure A3 Production tree of energy transformation sectors. σ is the elasticity of substitution for inputs.

Thus the problem is expressed as:

$$\max: \pi_{r,j}^z = p_j^z \cdot Z_j - (p_j^{vae} \cdot QVAE_j + p_j^{fe} \cdot QFE_j + p_j^{inta} \cdot QINTA_j + p^{ghg} \cdot$$

$$QGHG_{j,act,ghg})$$

Equation (A15)

s.t.

$$Q_j = \min\left(\frac{QVAE_j}{qvae_j}, \frac{QFE_j}{qfe_j}, \frac{QINTA_j}{qinta_j}, \frac{QGHG_{j,act,ghg}}{qghg_{j,act,ghg}}\right) \quad \text{Equation (A16)}$$

where QFE_j is the aggregate energy input (electricity and fossil energy) and qfe_j is the technical coefficient transforming aggregate energy inputs to Q_j .

A.4 Household Consumption

Household and government are final consumers. The representative household endows primary factors to the firms and receives income from the rental of primary factors (labor and capital), rents from fixed factors (land and natural resources) and lump-sum transfer from the government (e.g., carbon tax revenue of government). The income is then used for either investment or final consumption. The objective of household consumption is to maximize utility by choosing levels of consumption goods following the Cobb-Douglas preferences, subject to commodity prices and budget constraints. The agent's problem is expressed as:

$$\max: \mu_h[X_1^p, \dots, x_i^p] = A^p \cdot \prod_{i=1}^N (X_i^p)^{\alpha_i^p} \quad \text{Equation (A17)}$$

s.t.

$$EH = \sum_i p_j^q \cdot X_i^p = \sum_{f=1}^F \omega_f \cdot V_f + \sum_j pld \cdot QLAND_j + \sum_{res,j} p_j^{res} \cdot QRES_j + T^{cab} - T^d - S^p \quad \text{Equation (A18)}$$

$$T^{cab} = pghg_{CO_2} \cdot TEMS_{CO_2} \quad \text{Equation (A19)}$$

$$T^d = \tau^d \cdot \sum_f \omega_f \cdot V_f \quad \text{Equation (A20)}$$

$$S^p = sr^p \cdot \sum_f \omega_f \cdot V_f \quad \text{Equation (A21)}$$

where μ_h is the utility function of households; EH is the household expenditure; X_i^p is the household consumption of i -th commodity; V_f is the f -th primary factor endowment by household; $QLAND_j$ is the j -th land use; pld is the price of land; $QRES_j$ is the quantity of resource; p_j^{res} is the shadow price of resource; S^p is the household savings; $TEMS_{CO2}$ is the CO₂ emissions; $pghg_{CO2}$ is the carbon price; T^d is the direct tax; τ^d is the direct tax rate; sr^p is the average propensity to save by the household; ω_f is the Price of the f -th primary factor; A^p is the scaling parameter in Cobb-Douglas function; and α_i^p is the share parameter in Cobb-Douglas function, $0 \leq \alpha_i^p \leq 1$, $\sum_i \alpha_i^p = 1$.

A.5 Government

The government is assumed to collect taxes, including direct tax on household income, ad valorem production tax (indirect tax) on gross domestic output, ad valorem import tariff on imports, and carbon tax. Based on a Cobb-Douglas demand function, the government spends its revenue on public services which are provided to the whole society and on the goods and services which are provided to the households free of charge or at low prices. The model assumes that the revenue from carbon tax is recycled to the representative agent as a lump-sum transfer.

$$\max: \mu_g[x_1^g, \dots, x_i^g] = A^g \cdot \prod_{i=1}^N (x_i^g)^{\alpha_i^g} \quad \text{Equation (A22)}$$

s.t.

$$\sum_i p_{r,i} \cdot x_{r,i}^g = T_r^d + \sum_j T_{r,j}^z + \sum_j T_{r,j}^m - S^g \quad \text{Equation (A23)}$$

$$T_{r,j}^z = \tau_{r,j}^z \cdot p_{r,j} \cdot Z_{r,j} \quad \text{Equation (A24)}$$

$$T_{r,i}^m = \tau_{r,i}^m \cdot pm_{r,i} \cdot M_{r,i} \quad \text{Equation (A25)}$$

$$S_r^g = sr_r^g \cdot (T_r^d + \sum_j T_{r,j}^z + \sum_j T_{r,j}^m) \quad \text{Equation (A26)}$$

where μ_g is the utility function of government; x_i^g is the government consumption of i -th commodity; S^g is the government savings; T_j^z is the production tax on the j -th commodity; T_j^m is the import tariff on the j -th commodity; τ_j^z is the production tax rate on the j -th commodity; τ_i^m is the import tariff rate on the i -th commodity; sr^g is the average propensity to save by the government; Z_j is the gross domestic output of the j -th commodity; M_i is the import of the i -th commodity; pm_i is the price of the i -th imported commodity; A^g is the scaling parameter in Cobb-Douglas function; and α_i^g is the share parameter in Cobb-Douglas function, $0 \leq \alpha_i^g \leq 1$, $\sum_i \alpha_i^g = 1$.

A.6 Investment and savings

Investment is an important part of final demand. In the CGE model, a virtual agent receives all the savings from the household, government and the external sector to purchase goods for domestic investment. The virtual investment agent is assumed to maximize the utility based on a Cobb-Douglas demand function subject to its (virtual) income constraint. Mathematically, the investment problems can be described as follows:

$$\max: \mu_v[x_1^v, \dots, x_i^v] = A^v \cdot \prod_{i=1}^N (x_i^v)^{\alpha_i^v} \quad \text{Equation (A27)}$$

s.t.

$$\sum_i p_{r,i} \cdot x_{r,i}^v = S_r^p + S_r^g + \varepsilon \cdot S_r^f \quad \text{Equation (A28)}$$

where μ_v is the utility of virtual investment agent; S^f is the current account deficits in foreign currency terms (or alternatively foreign savings); ε is the exchange rate; x_i^v is the demand for the i -th investment goods; A^v is the scaling parameter in Cobb-Douglas function; and α_i^v is the share parameter in Cobb-Douglas function, $0 \leq \alpha_i^v \leq 1$, $\sum_i \alpha_i^v = 1$.

A.7 International transaction

The CGE model is a small open economy model that includes the interaction of commodity trade with the rest of the world. This model assumes the small open economy specifications, meaning that such an economy is small enough for its policies not to alter world prices or incomes. The implicit implication from the small-country assumption is that export and import prices are exogenously given for the economy. In this study, future international prices are fixed to be the same level for non-energy commodities whereas increase by 3% yearly for energy commodities compared to the 2005 level.

Two types of price variables are distinguished. One is export prices in terms of the domestic currency p_i^e and import prices as p_i^m ; and the other is prices in terms of the foreign currency p_i^{We} and p_i^{Wm} . They are linked with each other as follows:

$$p_i^e = \varepsilon \cdot p_i^{We} \quad \text{Equation (A29)}$$

$$p_i^m = \varepsilon \cdot p_i^{Wm} \quad \text{Equation (A30)}$$

Furthermore, we assume that the economy faces balance of payments constraints, which is described with export and import prices in foreign currency terms:

$$\sum_i p_i^{We} \cdot E_{r,i} + S_r^f = \sum_i p_i^{Wm} \cdot M_i \quad \text{Equation (A31)}$$

where E_i is the export of i -th commodity; M_i is the import of i -th commodity; p_i^{We} is the export price in terms of foreign currency; p_i^e is the export price in terms of domestic currency; p_i^{Wm} is the import price in terms of foreign currency; and p_i^m is the import price in terms of domestic currency.

Substitution between imports and domestic goods.

The Armington assumption is adopted, that is, the domestic and imported goods are imperfectly substitutable for each other. This implies that households and firms do not directly consume or use imported goods but instead a so-called “Armington composite goods,” which is made up of imported and locally produced goods.

In the CGE model, the Armington composite goods at this level is created by virtual firms which maximize their profits by choosing a proper combination of imported and locally produced goods. The solution of their profit-maximization problem leads to their input demands for imported and domestic goods, which depend on the corresponding relative prices domestic and imported goods. Mathematically, this problem can be expressed as:

$$\max: \pi_i^{md} = p_i^{md} \cdot Q_i^{md} - [(1 + \tau_i^m) \cdot p^m \cdot M_i + p_i^d \cdot D_i^d] \quad \text{Equation (A32)}$$

s.t.

$$Q_i^{md} = \alpha_i^{md} \cdot (\delta_i^m \cdot M_i^{-\rho_i^{md}} + \delta_j^d \cdot D_i^{-\rho_i^{md}})^{\frac{-1}{\rho_j^{md}}} \quad \text{Equation (A33)}$$

where π_i^{md} is the profit of the firm producing the i -th Armington composite goods of import and locally produced goods; Q_i^{md} is the i -th Armington composite goods of import and locally produced goods; D_i^d is the i -th locally produced goods; p_i^{md} is the Armington price of the i -th imported and locally produced goods; p_i^d is the price of the i -th locally produced goods; τ_i^m is the import tariff rate on the i -th commodity; α_i^{md} is the shift (or efficiency) parameter in the Armington composite goods production function; δ_i^m, δ_j^d are the input share parameters in the Armington composite goods production function ($0 \leq \delta_i^m \leq 1$, $0 \leq \delta_j^d \leq 1$, $\delta_i^m + \delta_j^d = 1$), and ρ_i^{md} is the CES substitution parameter, in which the elasticity of substitution between imported and domestic goods, σ , equals $\frac{1}{(1+\rho)}$.

A.8 Transformation between Exports and Domestic Goods

On the supply side, the produced commodities are distributed to the international market and local market by a two-level nested constant elasticity of transformation function. Similar to the treatment of import, a virtual firm transforms the gross domestic output into exports and domestic goods as follows:

$$\max: \pi_i^{dx} = (p_i^e \cdot E_i + p_i^{dd} \cdot D_i^s) - (1 + \tau_i^z) \cdot p_i^z \cdot Q_i^{dx} \quad \text{Equation (A34)}$$

s.t.

$$Q_i^{dx} = \alpha_i^{dx} \cdot (\delta_i^e \cdot E_i^{\rho_{r,i}^{dx}} + \delta_i^d \cdot D_i^s \rho_i^{dx})^{\frac{1}{\rho_i^{dx}}} \quad \text{Equation (A35)}$$

where π_i^{dx} is the profit of the firm engaged in the i -th transformation; Q_i^{dx} is the gross domestic output of the i -th goods; D_i^s is the i -th goods supplied to domestic market; p_i^z is the price of the i -th gross domestic output; p_i^{dd} is the price of domestically supplied goods; τ_i^z is the production tax rate on the i -th commodity; α_i^{dx} is the shift (or efficiency) parameter in the transformation function; $\delta_i^e, \delta_{r,j}^d$ are share parameters in the transformation function ($0 \leq \delta_i^e \leq 1, 0 \leq \delta_j^d \leq 1, \delta_i^e + \delta_i^d = 1$); and ρ_i^{dx} is the transformation elasticity parameter, in which the elasticity of substitution between imported and domestic goods, equals $\frac{1}{\rho-1}$.

A.9 Market Clearance Conditions

The above sections describe the behavior of economic agents, such as the households, firms, government, investment agents, and the interactions with the rest of the world. The final step is to impose the market-clearing conditions to all commodities and factor markets as follows:

$$Q_i = x_i^p + x_i^g + x_i^v + \sum_j x_{i,j} \quad \text{Equation (A36)}$$

$$\sum_j v_{f,j} = V_f \quad \text{Equation (A37)}$$

A.10 Macro Closure

In a CGE model, the issue of macro closure is the choice of exogenous variables among all variables in the model, mainly including investment and saving macro closure, and current account balance macro closure. In this model, investment is

exogenously assumed. In addition, the foreign exchange rate is fixed, and thus the balance of payment is an endogenous variable.

APPENDIX B

SYDWEM CALIBRATION AND VALIDATION

Table B1 Estimated Parameter Values for GRP Growth Model.

Administrative area	c	b_L	b_K	R^2
Luohu District	0.0425	0.200	0.880	0.801
Futian District	0.0475	0.170	0.615	0.641
Nanshan District	0.0528	0.200	0.800	0.793
Buji Town	0.0399	0.150	0.619	0.746

Table B2 Input Parameter Values of SyDWEM (Shenzhen Statistic Bureau, 1982-2009).

Parameters	Unit	Values	
		1990	2009
Net investment	Billion Yuan (in 1990 price)		
- Luohu District		1.8	3.4
- Futian District		1.4	8.8
-Nanshan District		2.5	18.6
- Buji Town		1.5	7.0
Retail price indexes	%	100	230
Depreciation rate	%	6	6
The ratio of population to number of labors	%	65	76
Average birth rate	‰	2.76	2.67
Average death rate	‰	1.11	0.33
Water consumption per capita	L/d	178	243
BOD₅ generation per capita	g/d	36.0	36.0
NH₃-N generation per capita	g/d	11.1	11.1
BOD₅ per unit GRP of different industries	t/billion Yuan		
-Labour intensive secondary industry		575.4	575.4
-Technology intensive secondary industry		42.0	42.0
-Capital intensive secondary industry		134.4	134.4

Note: ^a Ratio of reclaimed wastewater to water consumption.

Table B2 Input Parameter Values of SyDWEM Continued (Shenzhen Statistic Bureau, 1982-2009).

Parameters	Unit	Values	
		1990	2009
NH₃-N per unit GRP of different industries	t/billion Yuan		
-Labour intensive secondary industry		62.2	62.2
-Technology intensive secondary industry		6.7	6.7
-Capital intensive secondary industry		10.4	10.4
Water transfer quota	M m ³ /d	0.26	2.65
^a Reclaimed wastewater reuse ratio	%	0	5
The ratio of wastewater generation to water	%	90	90
Volumetric wastewater treatment rate	%		
-Binhe WWTP service area		43	85
-Luofang WWTP service area		51	87
-Caopu WWTP service area		0	45
-Nanshan WWTP service area		43	79
BOD₅ removal rate in different WWTPs	%		
-Binhe WWTP service area		60	80
-Luofeng WWTP service area		60	80
-Caopu WWTP service area		0	80
-Nanshan WWTP service area		60	80
NH₃-N removal rate in different WWTPs	%		
-Binhe WWTP service area		48	48
-Luofeng WWTP service area		75	75
-Caopu WWTP service area		0	20
-Nanshan WWTP service area		20	20

Table B3 Industrial Structure of Different Administrative Areas in 2025.

Administrative area	GRP proportion of primary, secondary, and tertiary industries		Proportion of labor, technology, and capital-intensive secondary industries	
	C0E0/C0E1	C1E0/C1E1	C0E0/C0E1	C1E0/C1E1
Total (2007)	0.05;41.72;58.23	0.05;41.72;58.23	18.39;62.44;19.17	18.39;62.44;19.17
Total (2025)	0.00;16.58;83.42	0.00;17.00;83.00	22.46;31.52;46.02	18.67;29.95;51.38
Luohu District (2025)	0.01;5.85;94.14	0.01;6.34;93.65	73.57;14.79;11.64	67.54;19.54;12.92
Futian District (2025)	0.00;7.39;92.61	0.00;7.88;92.12	24.83;39.90;35.27	8.12;52.70;39.18
Nanshan District (2025)	0.00;22.08;77.91	0.00;22.49;77.51	5.82;36.79;58.79	3.98;30.72;65.30
Buji Town (2025)	0.01;22.67;77.32	0.01;23.07;76.92	78.40;9.84;11.76	73.94;13.00;13.06

Table B4 Labor Productivity, Water Use Efficiency, and Pollutant Load per GRP in 2010 and 2025 (in 1990 Price).

Scenario	Labor productivity (Yuan)		Water use efficiency (Yuan/m ³)		BOD ₅ loading per GRP ton/billion Yuan		NH ₃ -N loading per GRP ton/billion Yuan	
	2010	2025	2010	2025	2010	2025	2010	2025
C0E0	68,588	212,750	444	734	58.7	33.44	6.4	3.4
C0E1	68,588	212,750	458	853	58.7	33.44	6.4	3.4
C1E0	73,050	220,350	419	726	56.5	32.15	6.0	3.2
C1E1	73,050	220,350	454	965	56.5	32.15	6.0	3.2

Table B5 Labor Productivity, Water Use Efficiency of Different Industries under C0E0 in 2010 and 2025 (in 1990 Price).

Type of industry	Labor productivity (Yuan per capita)		Water use efficiency (Yuan/m ³)		BOD ₅ loading per GRP (ton/billion Yuan)		NH ₃ -N loading per GRP (ton/billion Yuan)	
	2010	2025	2010	2025	2010	2025	2010	2025
Primary industry	23,489	23489	7	9	-	-	-	-
Secondary	89,177	376,349	320	531	157.8	163.3	17.6	18.0
-labor	25,211	63,797	169	300	575.4	575.4	62.2	62.2
-Technology	63,601	207,086	617	1106	42.0	42.0	6.7	6.7
-Capital	240,436	1071,100	175	312	134.4	134.4	10.4	10.4
Tertiary industry	59,792	232,158	606	882	-	-	-	-

According to the estimation by Qin et al. (2014), the pollutant load from primary industry (agriculture) is much smaller compared to other industries in Shenzhen, e.g., the COD load from agriculture is estimated to account for only 0.1% of total pollutant load in 2009. Thus, it was omitted in the study. Water pollutant loads from tertiary industry are included in the estimation of domestic pollutant generation.

APPENDIX C

SUPPLEMENTARY DATA OF CHAPTER 4

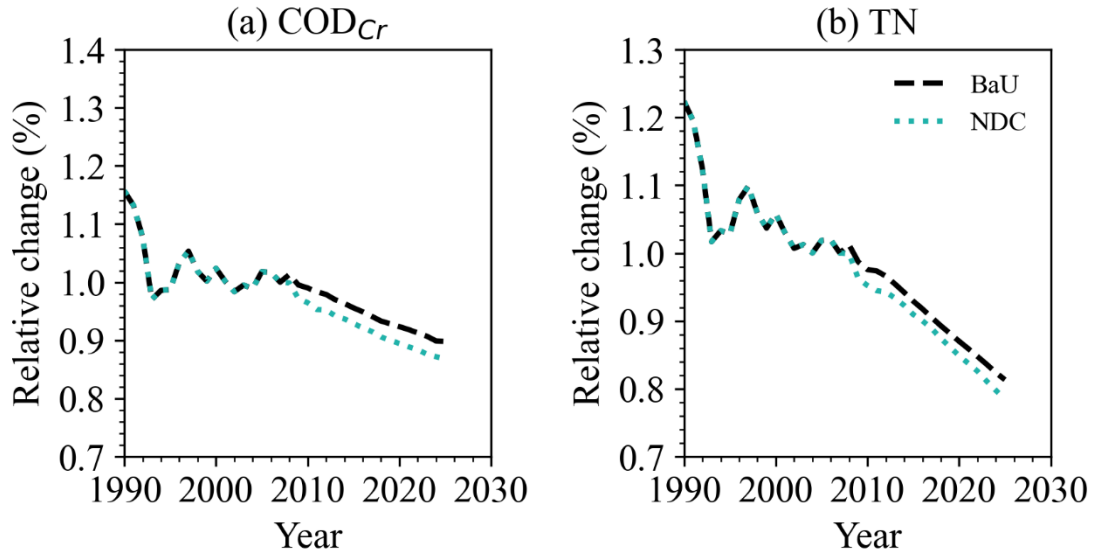


Figure C1 Relative change of mean WWTPs influent concentrations of (a) COD_{Cr} and (b) TN compared with the 2007 level under BaU and NDC scenarios.

Table C1 Methane and CO_2 Emissions from Sub-main and Main Sewer Systems.

Types	Sewer types (kg/km/day)	
	Sub-main sewer	Main sewer
CH_4	11.01 ± 0.22	13.21 ± 0.20
CO_2	21.97 ± 0.021	26.55 ± 0.50

Table C2 Emission Factors in This Study

Emission factor	Values	Technologies	Reference	Study area
CO ₂ *	0.017	A/O	Bao et al. (2016)	Beijing
kgCO ₂	/kg	A/O	Bao et al. (2015)	Beijing
COD _{removed}	0.032	A ² /O	Yan et al. (2014)	Beijing
	0.064	A ² O	Bao et al. (2015)	Beijing
	0.023	Reversed A ² /O	Yan et al. (2014)	Beijing
	0.084	OD	Bao et al. (2015)	Beijing
	0.026	OD	Yan et al. (2014)	Beijing
	0.035	SBR	Bao et al. (2016)	Beijing
	0.108	SBR	Bao et al. (2015)	Beijing
<i>Average:</i>	0.0517 ± 0.0322			
N ₂ O	0.00270	A/O	Bao et al. (2016)	Beijing
kg N ₂ O	/kg	A ² /O	Ren et al. (2013)	Qingdao
TN _{removed}	0.00230	Reversed A ² /O	Yan et al. (2014)	Beijing
	0.00145	Reversed A ² /O	Ren et al. (2013)	Qingdao
	0.00200	OD	Ren et al. (2013)	Qingdao
	0.00360	OD	Yan et al. (2014)	Beijing
	0.00515	SBR	Bao et al. (2016)	Beijing
<i>Average</i>	0.00268 ± 0.0013			
CH ₄ emissions	0.00196	A/O	Bao et al. (2016)	Beijing
kg CH ₄ /kg	0.00144	A ² /O	Ren et al. (2013)	Qingdao
COD _{removed}	0.00146	Reversed A ² /O	Ren et al. (2013)	Qingdao
	0.00930	OD	Ren et al. (2013)	Qingdao
	0.00217	OD	Li et al. (2016)	Xi'an
	0.00670	SBR	Bao et al. (2016)	Beijing
<i>Average</i>	0.00384 ± 0.0033			

Table C3 CO₂ Emissions Intensity from Chemicals, Machinery, and Service Industrial Sectors under BaU and NDC scenarios in Shenzhen (kg CO₂-eq/10³ RMB) (in 1990 Price).

Scenario	Sector	2007	2010	2011	2012	2015	2020	2025
BaU	Chemicals	345.1	402.0	409.2	418.5	448.1	504.4	562.2
	Machinery	99.0	120.8	127.9	131.9	145.2	173.2	205.3
	Service	41.2	48.1	49.1	50.4	54.1	60.5	67.7
NDC	Chemicals	345.1	402.0	409.2	418.5	448.1	112.4	94.4
	Machinery	99.0	120.8	127.9	131.9	145.2	132.8	127.2
	Service	41.2	48.1	49.1	50.4	54.1	41.0	37.0

APPENDIX D

EQUATIONS AND SUPPLEMENTARY DATA OF CHAPTER 5

Latent heat of vaporization (λ):

$$\lambda = 2.501 - (2.361 \times 10^{-3}) \times T \quad \text{Equation (D1)}$$

where λ is the latent heat of vaporization of water, MJ/kg; and T ($^{\circ}\text{C}$) is the mean air temperature.

Saturation vapor pressure (e_s):

$$e_s = 0.611 \exp\left(\frac{17.27 \times T}{T + 237.3}\right)$$
$$\overline{e_s} = \left[0.611 \exp\left(\frac{17.27 \times T_{max}}{T_{max} + 237.3}\right) + 0.611 \exp\left(\frac{17.27 \times T_{min}}{T_{min} + 237.3}\right)\right] / 2 \quad \text{Equation (D2)}$$

where T_{max} and T_{min} are the maximum and minimum air temperature ($^{\circ}\text{C}$), respectively; e_s is the saturation vapor pressure, kPa; and $\overline{e_s}$ is the mean saturation vapor pressure for a day, week, or month.

Actual vapor pressure (e_a):

$$e_a = e_s \times RH/100 \quad \text{Equation (D3)}$$

where e_a is the actual vapor pressure, kPa, respectively; and RH is the relative humidity, %.

Vapor pressure deficit (D):

$$D = e_s - e_a = (1 - RH/100)e_s \quad \text{Equation (D4)}$$

where D is the vapor pressure deficit, kPa.

Slope of vapor pressure curve (Δ):

$$\Delta = \frac{4098 \times e_s}{(T+237.3)^2} = \frac{2504 \exp\left(\frac{17.27 \times T}{T+237.3}\right)}{(T+237.3)^2} \quad \text{Equation (D5)}$$

Psychrometric constant (γ):

$$\gamma = \frac{c_p p}{\varepsilon \lambda} \quad \text{Equation (D6)}$$

$$p = 101.3 \times \left(\frac{293 - 0.0065z}{293}\right)^{5.26} \quad \text{Equation (D7)}$$

where γ is the psychrometric constant, kPa °C⁻¹; C_p is the specific heat of moist air, 1.013×10⁻³ MJ kg⁻¹ °C⁻¹; ε is the ratio of molecular weight of water and dry air, i.e., 18.02/28.97=0.622; and p is the atmospheric pressure (kPa) at elevation z (m).

Net shortwave radiation (R_{ns}):

$$R_{ns} = (1 - \alpha)R_s \quad \text{Equation (D8)}$$

where R_{ns} is the net shortwave radiation, MJ m⁻² d⁻¹; R_s is the incoming solar radiation, MJ m⁻² d⁻¹; and α is albedo, which is 0.23 for the hypothetical reference grass. If the incoming solar radiation is not available, then it can be calculated using Equation (D9):

Incoming solar radiation (R_s):

$$R_s = (0.25 + 0.5 n/N)R_a \quad \text{Equation (D9)}$$

where n is the actual duration of sunshine (hour); N is the maximum possible duration of daylight hours; n/N is the relative sunshine duration; R_a is the extraterrestrial radiation,

MJ m⁻² d⁻¹.

Net longwave radiation (R_{nl}):

$$R_{nl} = \sigma \left(\frac{T_{min}^4 + T_{max}^4}{2} \right) (0.34 - 0.14 \times \sqrt{e_a}) (1.35 \times \frac{R_s}{R_{so}} - 0.35) \quad \text{Equation (D10)}$$

where R_{nl} is the net outgoing longwave radiation, MJ m⁻² d⁻¹; σ is the Stefan-Boltzmann constant, 4.903×10⁻⁹ MJ K⁻⁴ m⁻² d⁻¹; and R_{so} is the short-wave radiation, MJ m⁻² d⁻¹.

Net radiation (R_n):

$$R_n = R_{ns} - R_{nl} \quad \text{Equation (D11)}$$

For month soil heat flux (G), the equation suggested by Allen (1998) is as follows:

$$G = 0.14 \times (T_i - T_{i-1}) \quad \text{Equation (D12)}$$

where G is the monthly soil heat flux, MJ m⁻² d⁻¹; and T_i and T_{i-1} are the mean air temperature at month i and $i-1$, respectively.

Wind profile relationship:

$$u_2 = u_h \frac{4.87}{\ln(67.8h - 5.42)} \quad \text{Equation (D13)}$$

where u_2 is the wind speed at 2m above the ground, m/s; and u_h is the wind speed measured at h m above the ground, m/s.

Sensitivity coefficients of temperature:

$$\frac{\partial e_s}{\partial T} = \frac{2504 \exp \left(\frac{17.27 \times T}{T + 237.3} \right)}{(T + 237.3)^2} = \Delta \quad \text{Equation (D14)}$$

$$\frac{\partial \Delta}{\partial T} = \frac{\partial \Delta}{\partial e_s} \frac{\partial e_s}{\partial T} = \frac{4098}{(T+237.3)^2} \frac{\partial e_s}{\partial T} = \frac{4098\Delta}{(T+237.3)^2} \quad \text{Equation (D15)}$$

$$\frac{\partial D}{\partial T} = \frac{\partial D}{\partial e_s} \frac{\partial e_s}{\partial T} = (1 - RH)\Delta \quad \text{Equation (D16)}$$

Table D1 Relative Error (%) of the Temperature-based Methods compared with FAO-PM Simulation in Warm, Transition, and Cool Seasons using Default Values.

	Thornthwaite_T			Blaney-Criddle_T			Hargreaves and Samani_T	
Stations	W	T	C	W	T	C	W	T
<i>Semi-arid climate</i>								
S1	-33	-65	-87	-8	-11	8	-11	-18
S2	-29	-63	-84	-6	-10	9	-10	-17
S3	-28	-61	-82	-11	-12	10	-12	-16
S4	-19	-56	-80	-2	-2	16	-11	-14
S9	-18	-54	-79	-1	1	22	-4	-6
<i>Arid climate</i>								
S8	-29	-65	-82	-13	-18	11	-13	-22
<i>Subhumid subtropical climate</i>								
S5	-16	-54	-81	0	8	31	-7	-6
S6	-5	-45	-74	7	20	45	-4	1
S10	-10	-49	-75	6	12	33	-6	-5
S12	1	-40	-69	12	21	43	-3	3
<i>Humid subtropical climate</i>								
S7	9	-35	-63	30	39	76	16	21
S11	14	-27	-58	23	31	54	1	5
S13	17	-30	-58	36	44	76	10	14
S14	12	-31	-61	25	35	62	6	11
S15	18	-21	-49	19	31	63	-4	4
<i>Semi-arid</i>	-25	-60	-82	-6	-7	13	-10	-14
<i>Subhumid</i>	-8	-47	-75	6	15	38	-5	-2
<i>Humid</i>	14	-29	-58	27	36	66	6	11
<i>All regions</i>	-10	-48	-72	6	10	36	-4	-5

Note: W means warm season; T means transition season; C means cool season; and relative error within $\pm 20\%$ are bold. Blue color means the relative error of all the stations is within $\pm 20\%$.

Table D2 Relative Error (%) of the Radiation-based Methods compared with FAO-PM Simulation in Warm, Transition, and Cool Seasons using Default Values.

Stations	Makkink_R			Priestley and Taylor_R			Jensen-Haise_R			Turc_R			Abtew_R		
	W	T	C	W	T	C	W	T	C	W	T	C	W	T	C
<i>Semi-arid climate</i>															
S1	-32	-35	-41	-16	-30	-46	0	-31	-60	-20	-27	-57	-17	-35	-55
S2	-32	-36	-40	-15	-30	-45	5	-25	-52	-19	-24	-44	-14	-31	-49
S3	-34	-35	-38	-18	-30	-42	4	-19	-43	-20	-20	-34	-15	-27	-43
S4	-32	-33	-39	-14	-26	-41	10	-14	-41	-18	-20	-33	-13	-27	-46
S9	-31	-32	-36	-12	-23	-36	12	-10	-36	-17	-17	-28	-9	-22	-42
<i>Arid climate</i>															
S8	-31	-34	-32	-20	-34	-41	8	-19	-38	-6	-7	-24	-11	-28	-40
<i>Subhumid subtropical climate</i>															
S5	-32	-32	-38	-13	-22	-39	11	-13	-44	-18	-18	-36	-11	-25	-46
S6	-29	-28	-33	-7	-15	-29	19	-2	-29	-14	-11	-21	-6	-19	-37
S10	-28	-30	-38	-8	-19	-37	19	-6	-34	-13	-14	-26	-7	-22	-42
S12	-26	-27	-33	-2	-12	-27	24	3	-22	-10	-11	-17	-4	-16	-33
<i>Humid subtropical climate</i>															
S7	-18	-19	-25	11	-1	-16	36	11	-16	0	1	-7	7	-7	-27
S11	-23	-26	-34	6	-6	-21	31	11	-13	-6	-7	-13	-1	-13	-30
S13	-17	-19	-26	14	1	-14	39	16	-11	2	2	-5	5	-9	-27
S14	-22	-24	-30	6	-5	-18	31	11	-13	-5	-5	-9	1	-12	-28
S15	-24	-25	-30	5	-3	-13	32	17	-3	-5	-7	-7	-1	-10	-23
<i>Semi-arid</i>	-32	-34	-39	-15	-28	-42	6	-20	-46	-19	-22	-39	-14	-28	-47
<i>Subhumid</i>	-29	-29	-36	-8	-17	-33	18	-5	-32	-14	-14	-25	-7	-21	-40
<i>Humid</i>	-21	-23	-29	8	-3	-16	34	13	-11	-3	-3	-8	2	-10	-27
<i>All regions</i>	-28	-30	-35	-7	-18	-31	18	-6	-31	-12	-13	-24	-7	-21	-38

Note: W means warm season; T means transition season; C means cool season; and relative error within $\pm 20\%$ is bold. Blue color means the relative error of all the stations is within $\pm 20\%$.

Table D3 Regression Relationships (Y=ax) between Reference Evapotranspiration of FAO-PM and the Temperature-based Methods using Calibrated Values.

Stations	Thornthwaite_T			Blaney-Criddle_T			Hargreaves and Samani_T		
	S	R ²	E	S	R ²	E	S	R ²	E
<i>Semi-arid climate</i>									
S1	1.12	0.74	1.56	1.02	0.84	0.68	1.01	0.94	0.53
S2	1.13	0.71	1.68	1.02	0.79	0.74	1.01	0.93	0.52
S3	1.12	0.72	1.76	1.02	0.76	0.81	1.01	0.94	0.52
S4	1.12	0.73	1.6	1.02	0.8	0.69	1.01	0.93	0.5
S9	1.11	0.73	1.55	1.02	0.74	0.73	1.01	0.94	0.47
<i>Arid climate</i>									
S8	1.15	0.66	2	1.03	0.74	0.87	1.01	0.91	0.66
<i>Subhumid subtropical climate</i>									
S5	1.1	0.78	1.43	1.03	0.75	0.76	1.01	0.93	0.53
S6	1.09	0.78	1.31	1.03	0.67	0.76	1.01	0.92	0.48
S10	1.13	0.69	1.54	1.03	0.59	0.83	1.02	0.87	0.62
S12	1.1	0.74	1.34	1.02	0.69	0.64	1.01	0.94	0.38
<i>Humid subtropical climate</i>									
S7	1.09	0.76	1.05	1.02	0.76	0.49	1	0.97	0.24
S11	1.09	0.71	1.19	1.02	0.59	0.58	1.01	0.91	0.37
S13	1.1	0.73	1.06	1.02	0.76	0.44	1.01	0.95	0.28
S14	1.1	0.93	1.16	1.02	0.65	0.56	1.01	0.94	0.31
S15	1.07	0.75	1.11	1.02	0.42	0.63	1.01	0.88	0.39
<i>Semi-arid</i>	1.12	0.73	1.63	1.02	0.79	0.73	1.01	0.94	0.51
<i>Subhumid</i>	1.11	0.75	1.41	1.03	0.68	0.75	1.01	0.92	0.50
<i>Humid</i>	1.09	0.78	1.11	1.02	0.64	0.54	1.01	0.93	0.32
<i>All regions</i>	1.11	0.74	1.42	1.02	0.70	0.68	1.01	0.93	0.45

Note: S means slope and E means root mean square error (RMSE) (mm d⁻¹).

Table D4 Regression Relationships (Y=ax) between Reference Evapotranspiration of FAO-PM and the Temperature-based Methods using Calibrated Values.

Stations	Makkink_R			Priestley and Taylor_R			Jensen-Haise_R			Turc_R			Abtew_R		
	W	T	C	W	T	C	W	T	C	W	T	C	W	T	C
<i>Semi-arid climate</i>															
S1	1.01	0.93	0.51	1.03	0.87	0.84	1.02	0.85	1.06	1.02	0.91	1.01	0.93	0.51	1.03
S2	1.01	0.94	0.48	1.03	0.86	0.88	1.05	0.84	1.05	1.01	0.94	1.01	0.94	0.48	1.03
S3	1.01	0.94	0.48	1.03	0.87	0.85	1.03	0.88	0.94	1.01	0.96	1.01	0.94	0.48	1.03
S4	1.01	0.93	0.47	1.03	0.88	0.78	1.03	0.88	0.88	1.01	0.94	1.01	0.93	0.47	1.03
S9	1.01	0.95	0.43	1.02	0.88	0.73	1.03	0.89	0.81	1.01	0.95	1.01	0.95	0.43	1.02
<i>Arid climate</i>															
S8	1.01	0.96	0.41	1.03	0.86	0.92	1.03	0.87	0.99	1.01	0.96	1.01	0.96	0.41	1.03
<i>Subhumid subtropical climate</i>															
S5	1.01	0.93	0.53	1.03	0.89	0.74	1.03	0.9	0.82	1.01	0.93	1.01	0.93	0.53	1.03
S6	1.01	0.93	0.46	1.02	0.91	0.6	1.02	0.91	0.68	1.01	0.93	1.01	0.93	0.46	1.02
S10	1.01	0.92	0.49	1.03	0.85	0.81	1.04	0.86	0.86	1.01	0.93	1.01	0.92	0.49	1.03
S12	1.01	0.96	0.33	1.01	0.92	0.53	1.02	0.9	0.64	1.01	0.96	1.01	0.96	0.33	1.01
<i>Humid subtropical climate</i>															
S7	1.00	0.97	0.22	1.01	0.94	0.38	1.02	0.91	0.53	1.00	0.97	1.00	0.97	0.22	1.01
S11	1.01	0.93	0.33	1.02	0.90	0.51	1.02	0.88	0.59	1.01	0.94	1.01	0.93	0.33	1.02
S13	1.00	0.97	0.21	1.01	0.93	0.38	1.02	0.90	0.51	1.00	0.97	1.00	0.97	0.21	1.01
S14	1.01	0.94	0.31	1.01	0.92	0.46	1.01	0.90	0.57	1.01	0.95	1.01	0.94	0.31	1.01
S15	1.00	0.96	0.27	1.01	0.94	0.38	1.01	0.93	0.46	1.00	0.96	1.00	0.96	0.27	1.01
<i>Semi-arid</i>	1.01	0.94	0.47	1.03	0.87	0.82	1.03	0.87	0.95	1.01	0.94	1.01	0.94	0.47	1.03
<i>Subhumid</i>	1.01	0.94	0.45	1.02	0.89	0.67	1.03	0.89	0.75	1.01	0.94	1.01	0.94	0.45	1.02
<i>Humid</i>	1.00	0.95	0.27	1.01	0.93	0.42	1.02	0.90	0.53	1.00	0.96	1.00	0.95	0.27	1.01
<i>All regions</i>	1.01	0.94	0.40	1.02	0.89	0.65	1.03	0.89	0.76	1.01	0.95	1.01	0.94	0.40	1.02

Note: S means slope and E means root mean square error (RMSE) (mm d⁻¹).

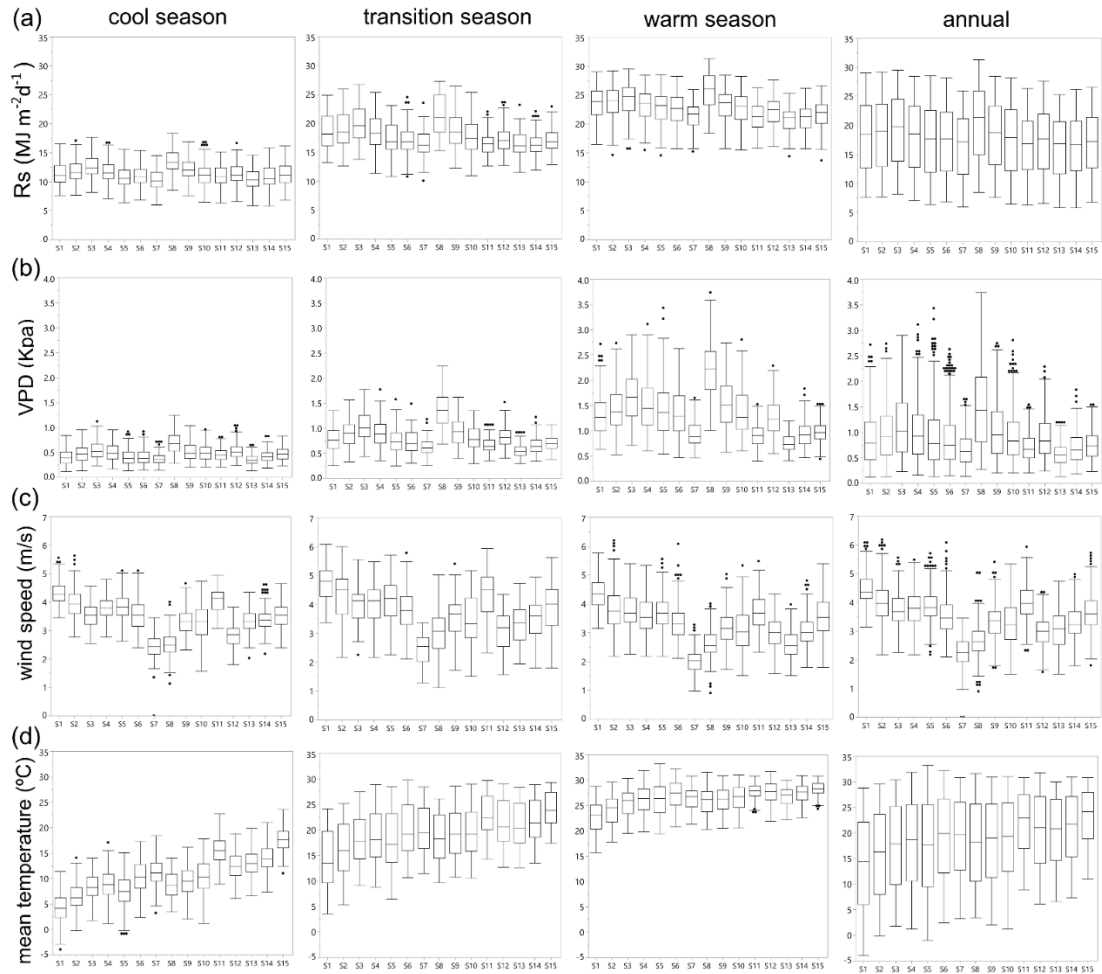


Figure D1 Seasonal and annual variation of (a) R_s , (b) vapor pressure deficit (VPD), (c) wind speed, and (d) mean temperature at each station from 1961 to 2010. Boxplots show the 25th, 50th, 75th percentiles, and extremes.

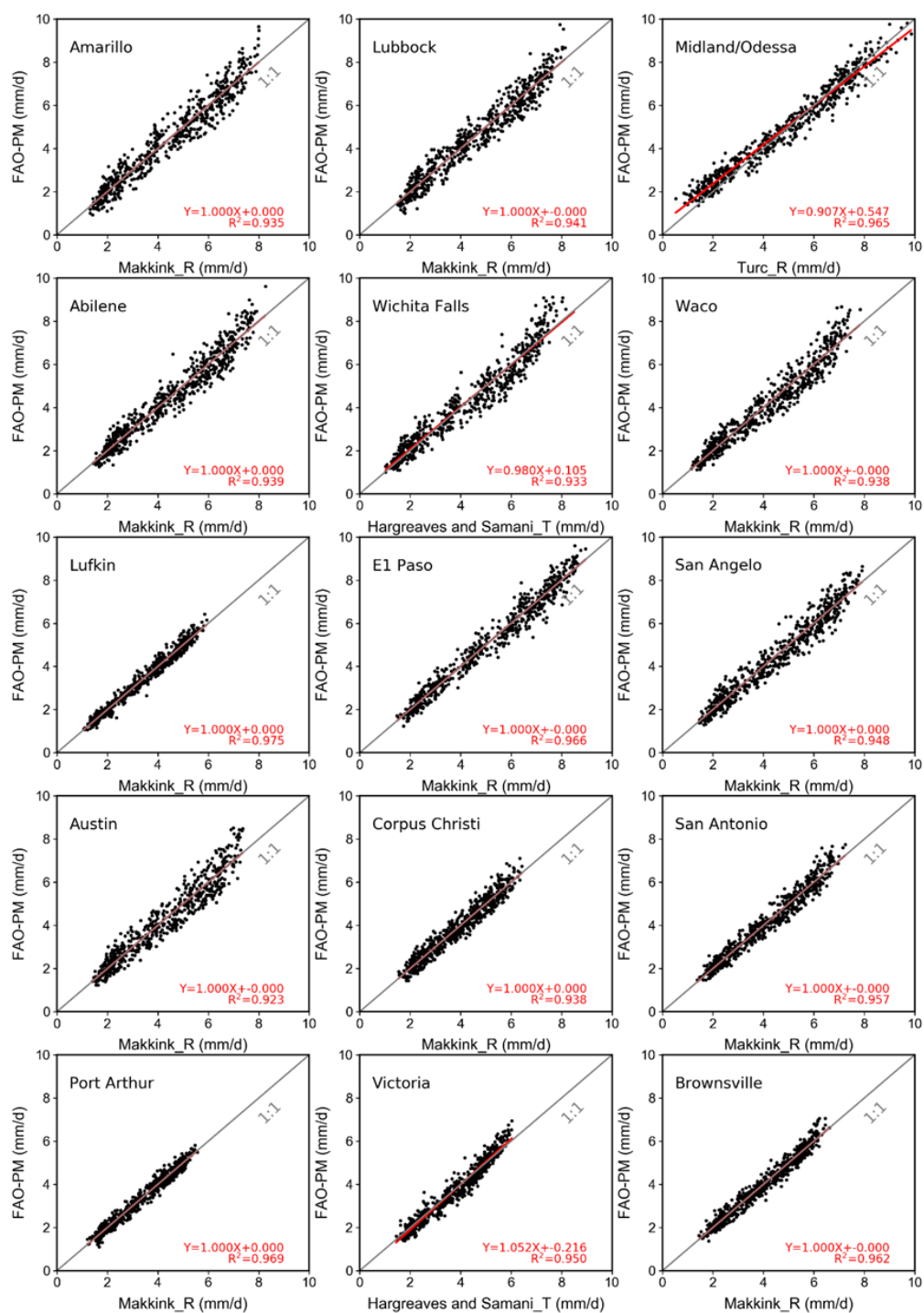


Figure D2 Model with least RMSE for each station with calibrated constant values. Red lines represent the fitted linear function.

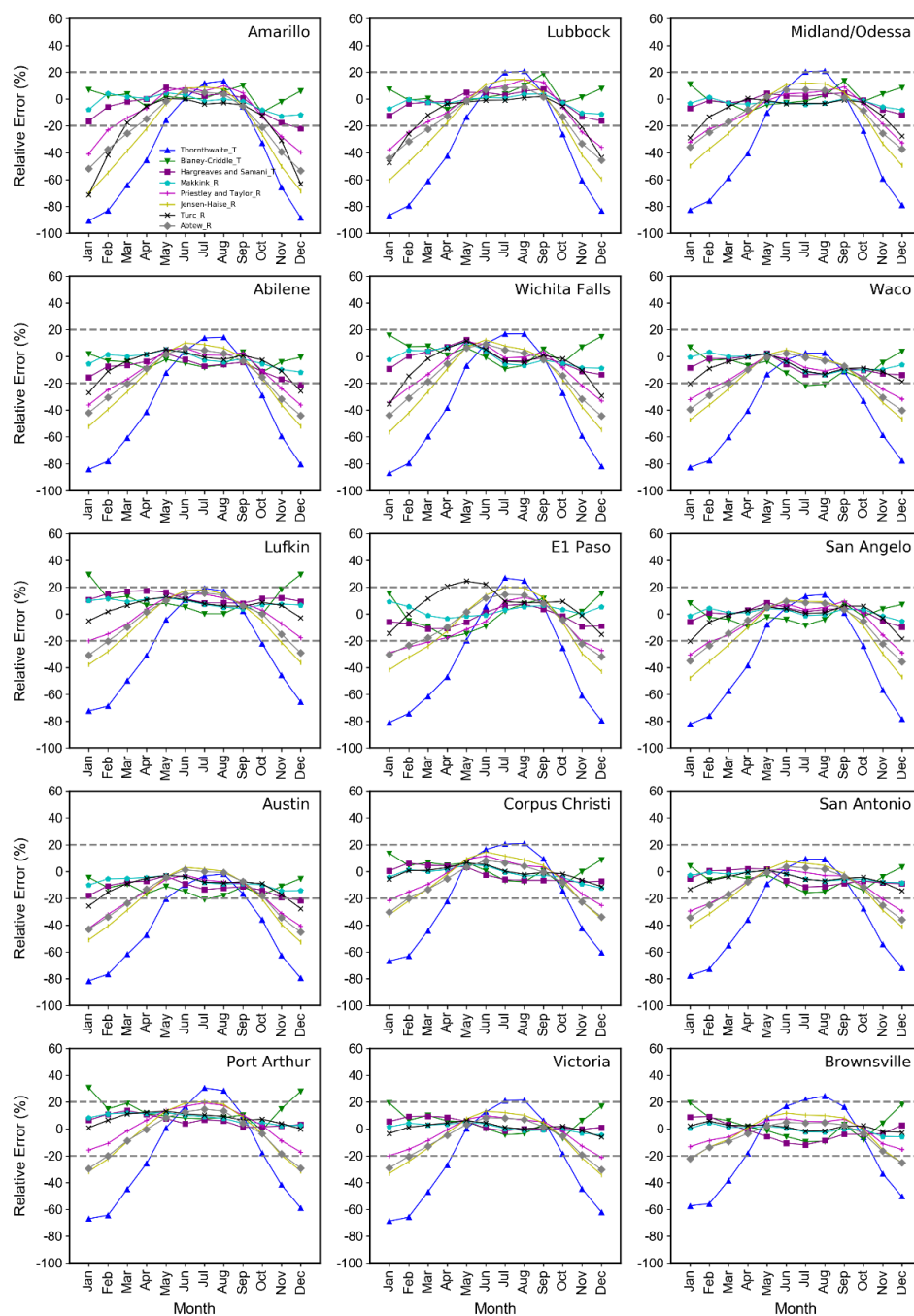


Figure D3 Relative error of the mean monthly reference evapotranspiration estimates of each model using regional average parameters at each station from 1961 to 2010 (Three climatic regions).

APPENDIX E
SUPPLEMENTARY DATA OF CHAPTER 6

Actual vapor pressure (e_a):

$$e_a = \frac{qp}{\varepsilon} \quad \text{Equation (E1)}$$

where e_a is the actual vapor pressure, kPa; q is the specific humidity, g/g; ε is the ratio of molecular weight of water and dry air, i.e., $18.02/28.97=0.622$; and p is the atmospheric pressure (kPa) at elevation z (m).

Relative humidity (%):

$$\text{RH} = e_a / e_s \times 100 \quad \text{Equation (E2)}$$

where e_s is the saturated vapor pressure, kPa.

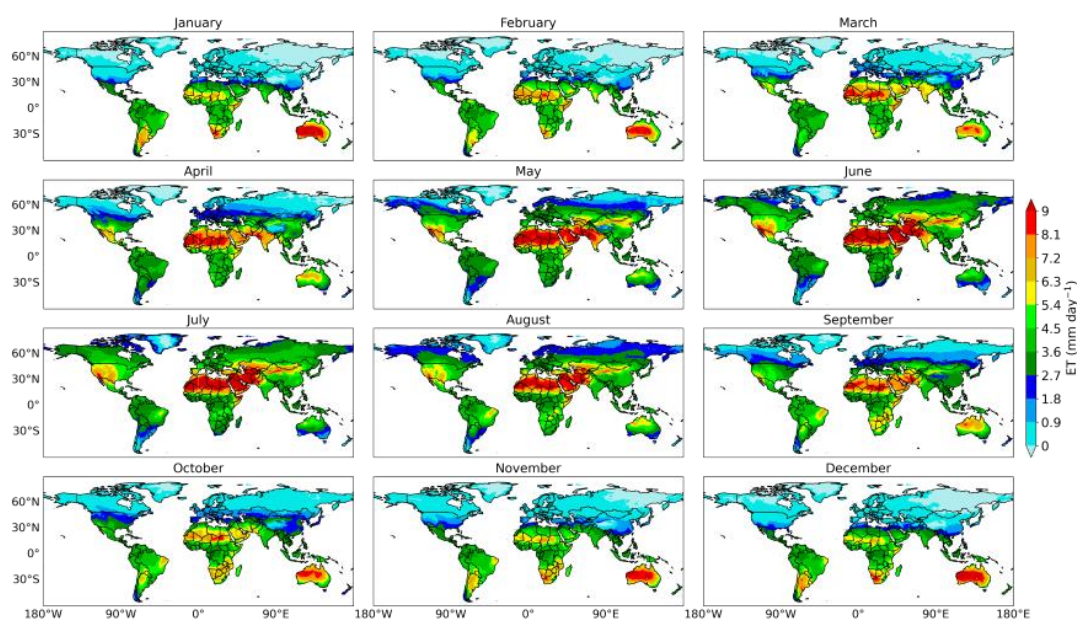


Figure E1 Mean monthly ET_0 using FAO-PM method from 1948 to 2016.

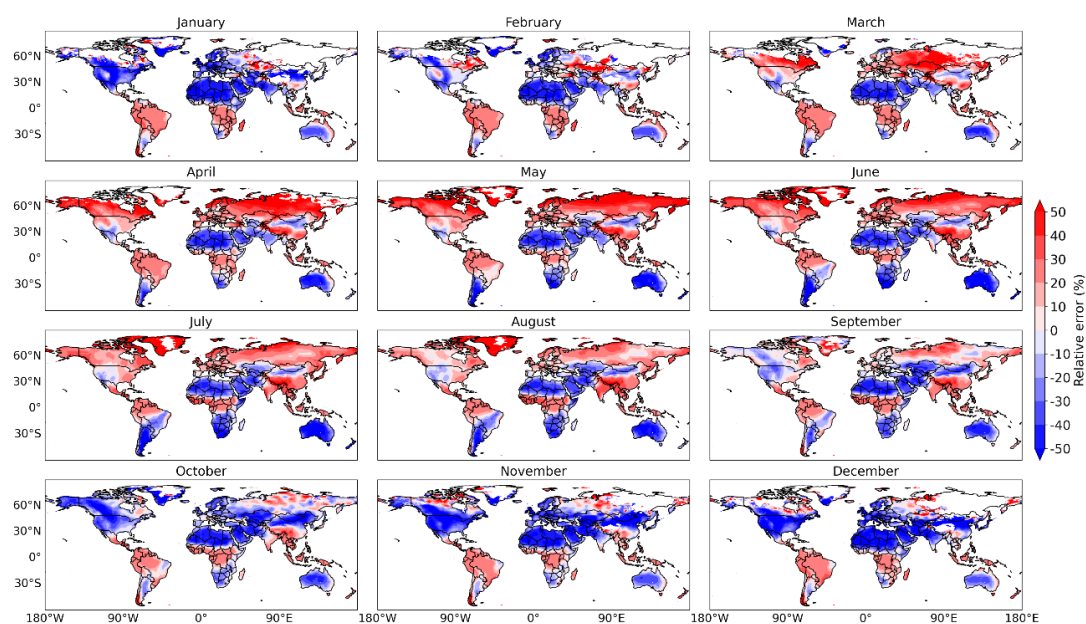


Figure E2 Relative error (%) of mean monthly ET_0 using Priestley-Taylor method compared with FAO-PM method from 1948 to 2016.

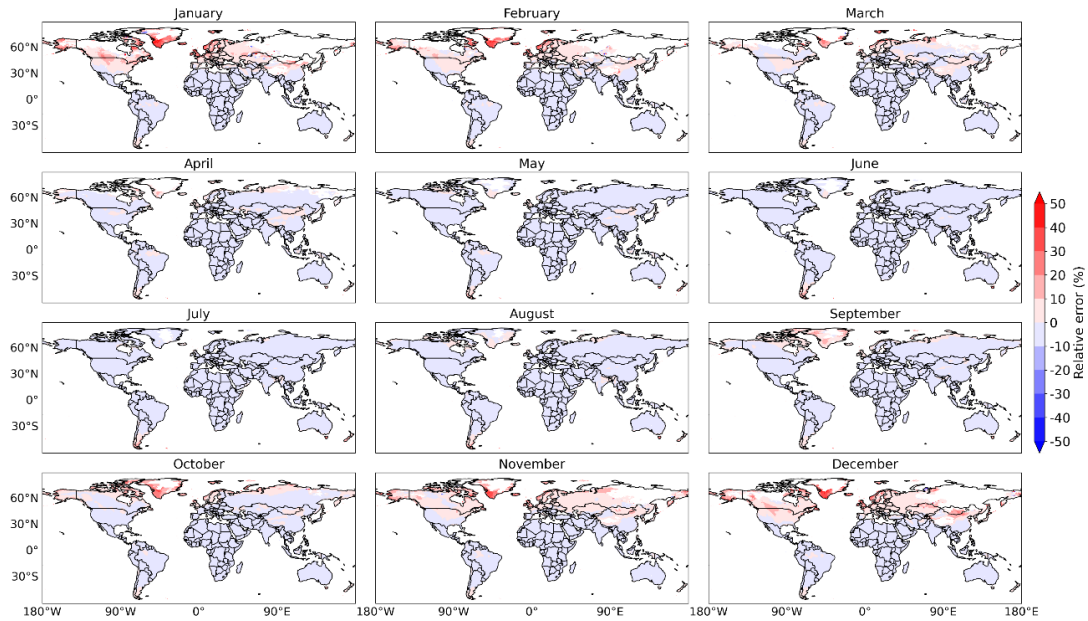


Figure E3 Relative error (%) of mean monthly ET_0 using the adjusted Priestley-Taylor method (ET_PT_Su) compared with FAO-PM method from 1948 to 2016.

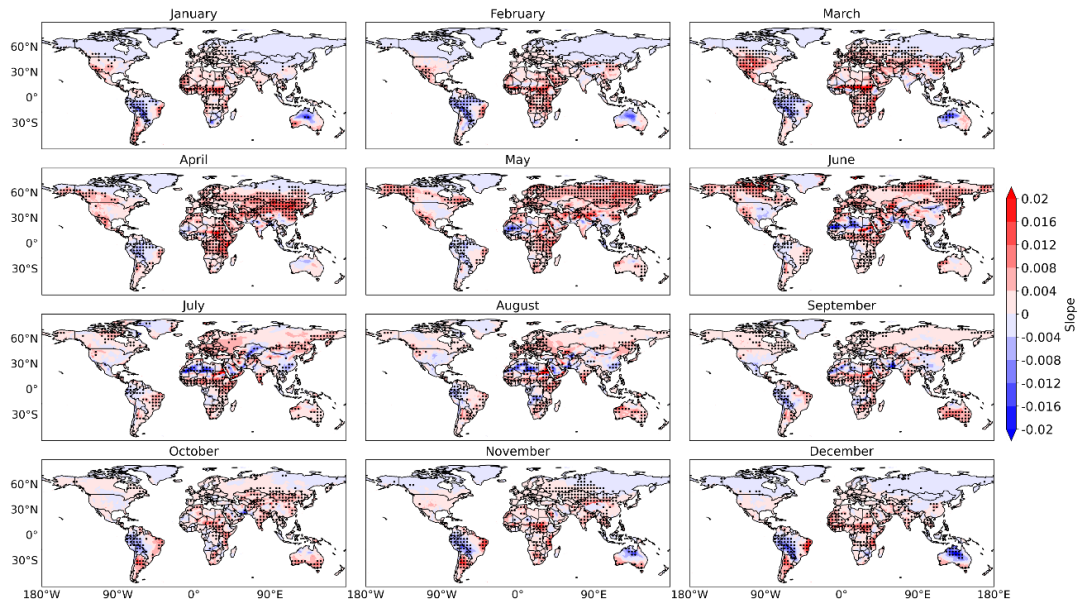


Figure E4 Mann-Kendal trend test of monthly ET_0 using FAO-PM method from 1948 to 2016. Black dots indicate significance at $p=0.05$ level, and shading is the Theil-Sen slope in the unit of mm/day.

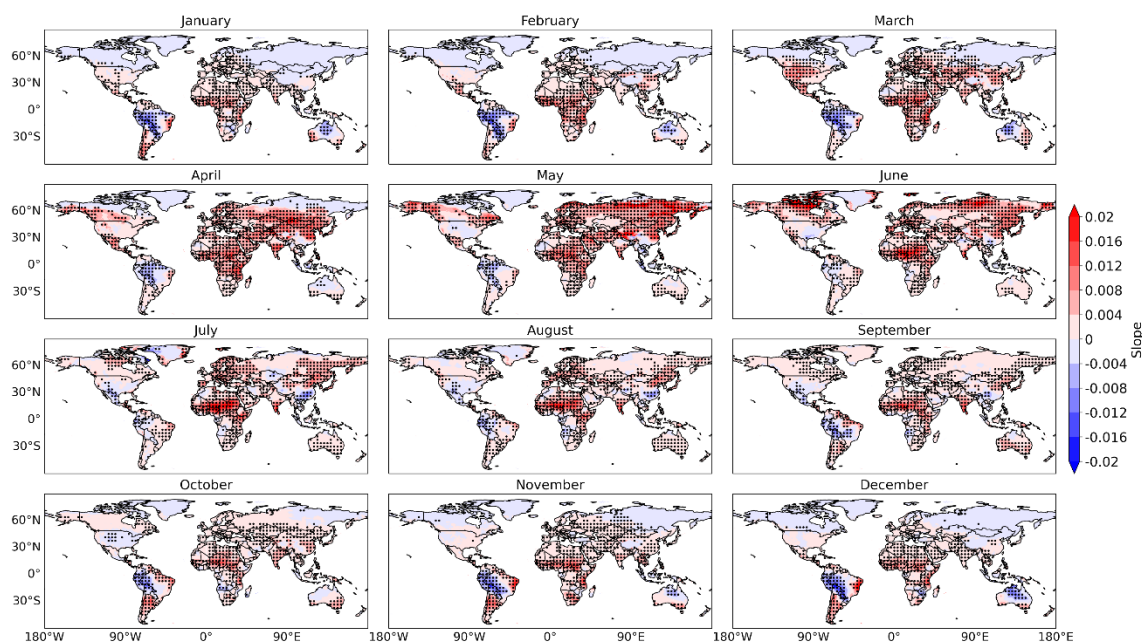


Figure E5 Mann-Kendal trend test of monthly ET_0 using Priestley-Taylor method from 1948 to 2016. Black dots indicate significance at $p=0.05$ level, and shading is the Theil-Sen slope in the unit of mm/day.

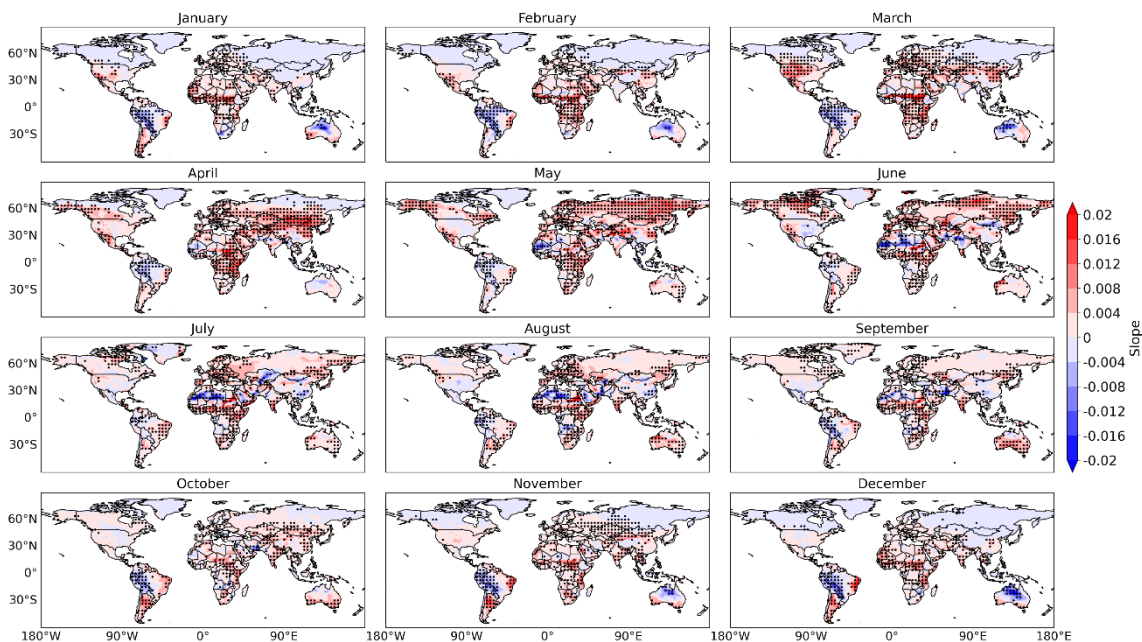


Figure E6 Mann-Kendal trend test of monthly ET_0 using the adjusted Priestley-Taylor method (ET_{PT_Su}) from 1948 to 2016. Black dots indicate significance at $p=0.05$ level, and shading is the Theil-Sen slope in the unit of mm/day.

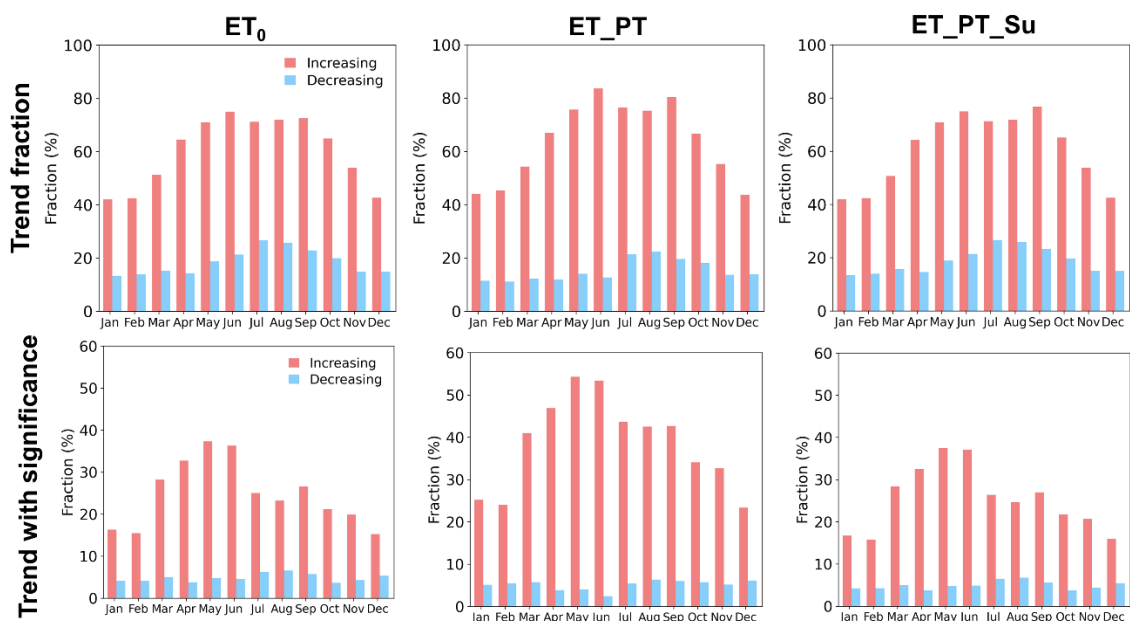


Figure E7 Percentage of global land surface with positive and negative trends of reference evapotranspiration estimated using FAO-PM, ET_{PT} , and ET_{PT_Su} methods. Trends with significance at $p=0.05$ level from 1948 to 2016.

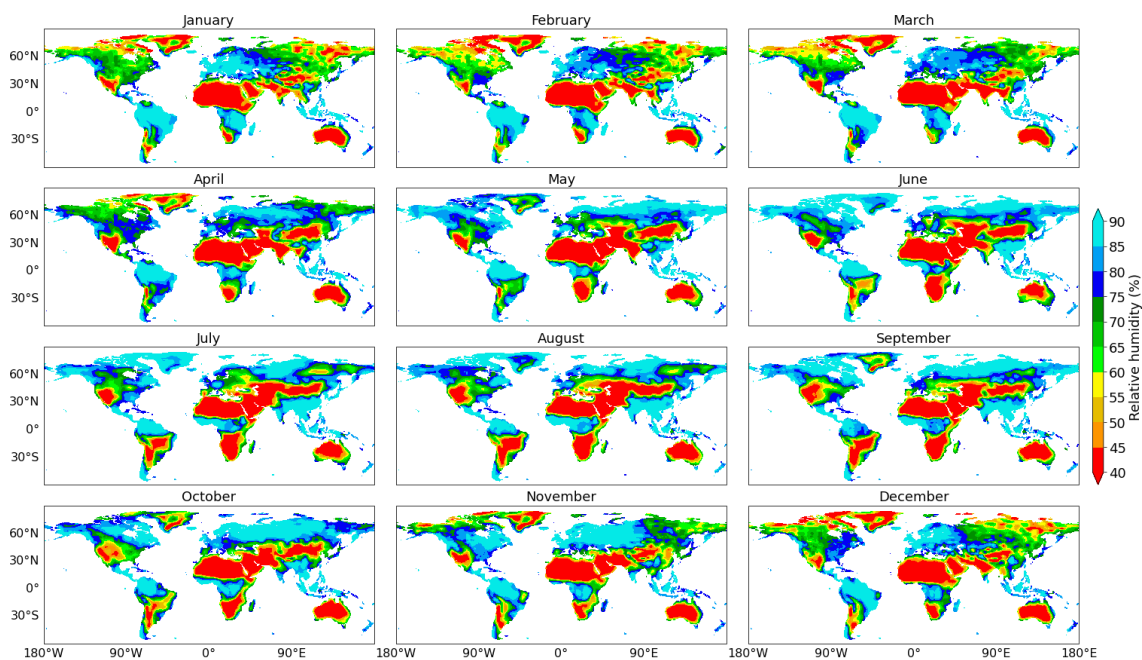


Figure E8 Mean monthly relative humidity (%) from 1948 to 2016.

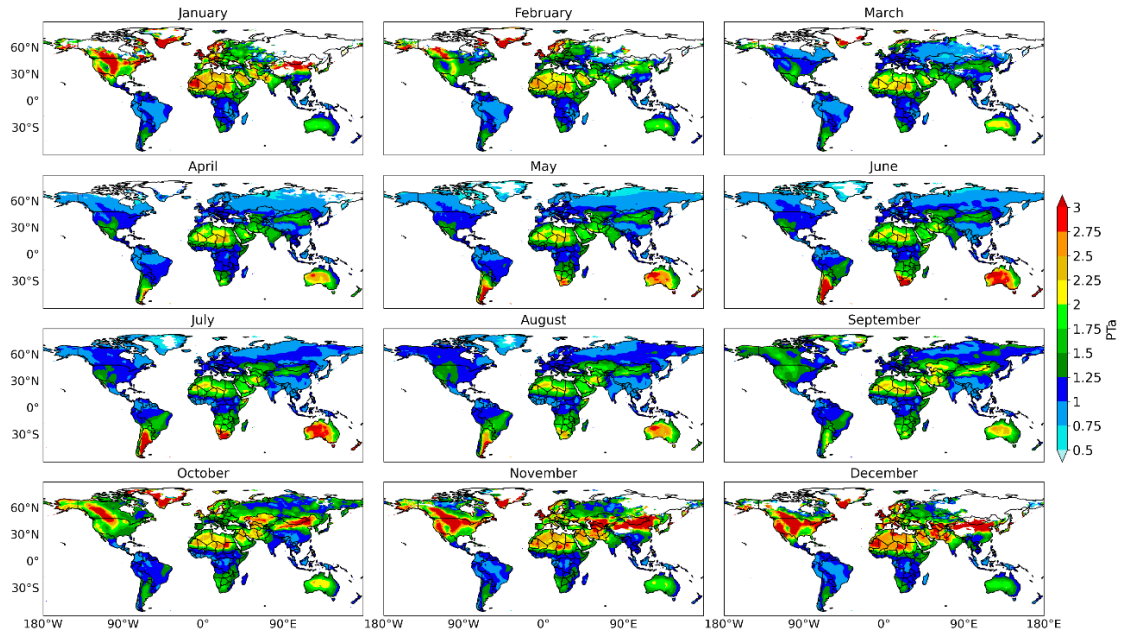


Figure E9 Monthly mean theoretical PT coefficient from 1948 to 2016.

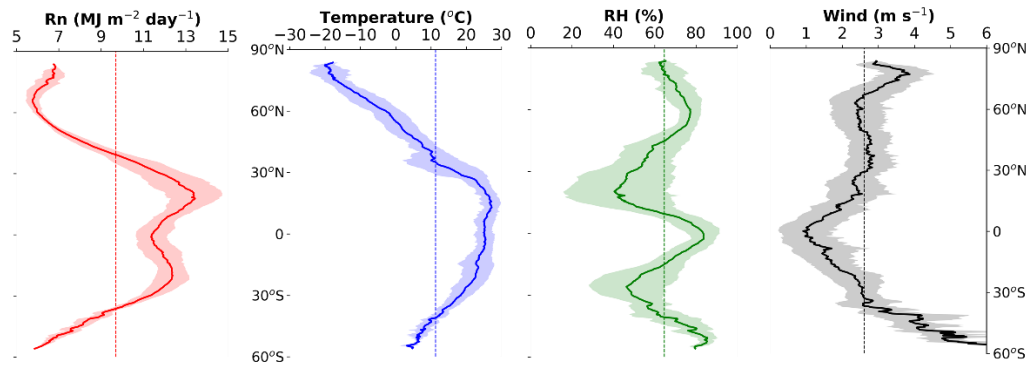


Figure E10 Latitudinal profiles of ET_0 from 1948 to 2016. Shading denotes the standard deviation among the latitudinal ET_0 . Antarctica is excluded since the PGF data did not report values in Antarctica.

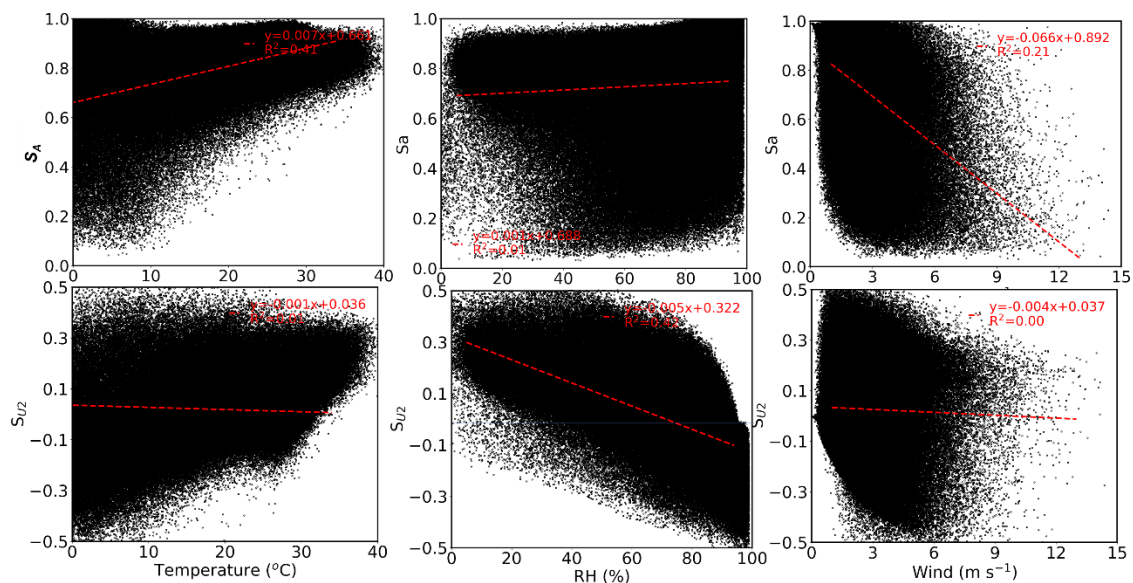


Figure E11 Linear regression of S_A and S_{u2} against air temperature, RH, and wind speed. Daily data in 2015 was used.

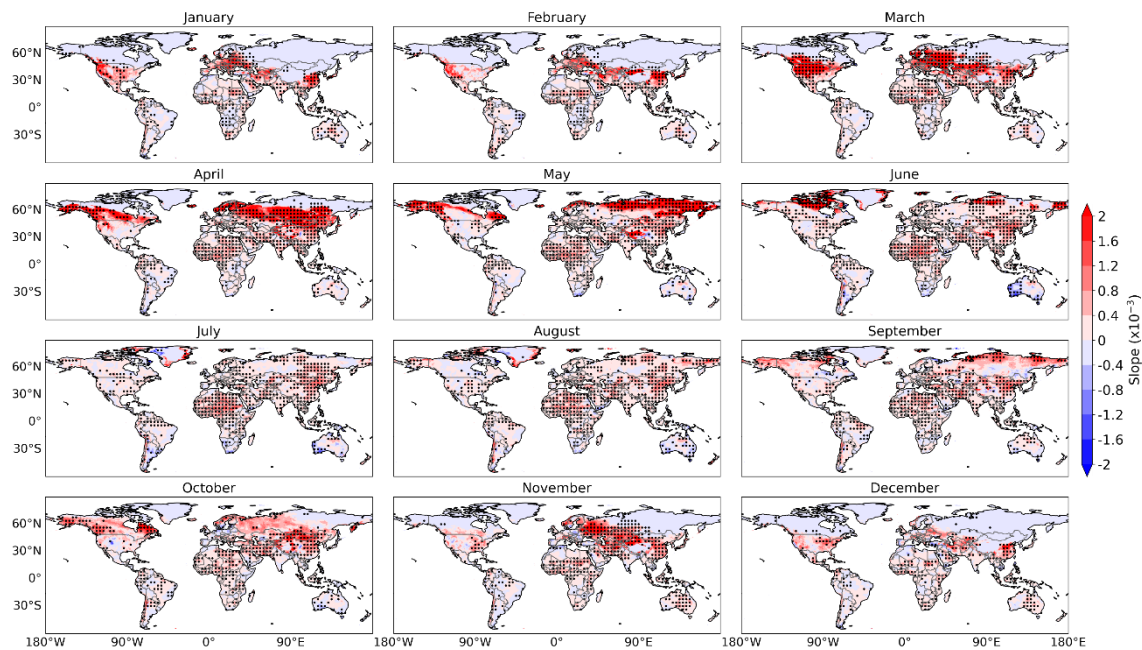


Figure E12 Mann-Kendal trend test of the monthly S_A from 1948 to 2016. Black dots indicate significance at $p=0.05$ level, and shading is the Theil-Sen slope.

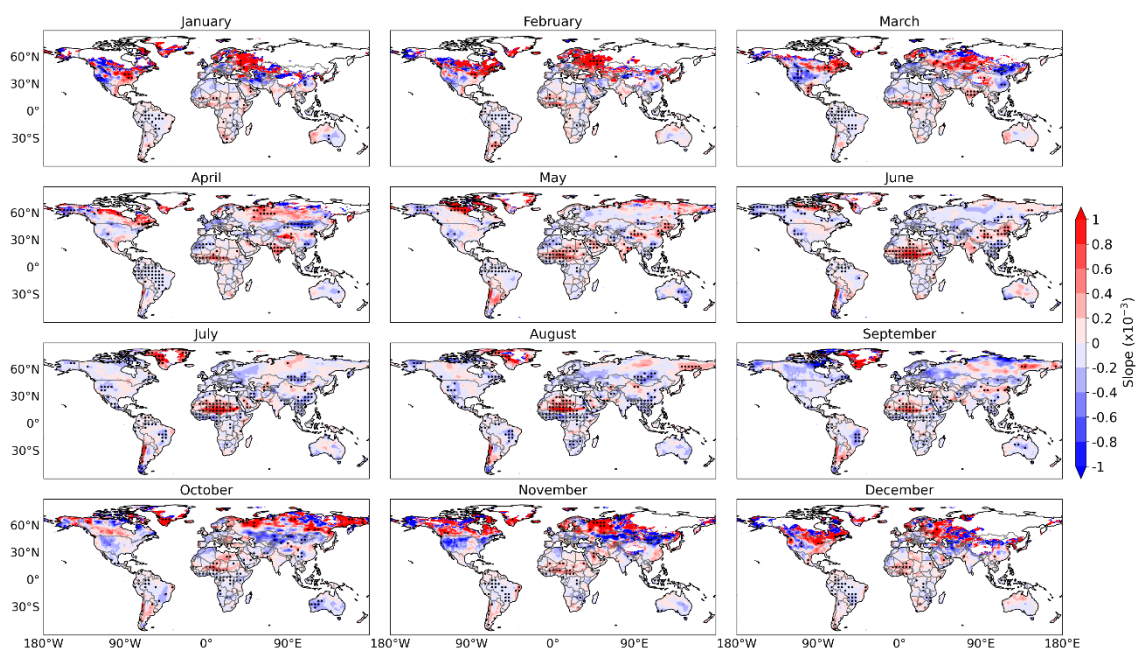


Figure E13 Mann-Kendal trend test of the monthly S_{ra} ($-S_{U2}$) from 1948 to 2016. Black dots indicate significance at $p=0.05$ level, and shading is the Theil-Sen slope.

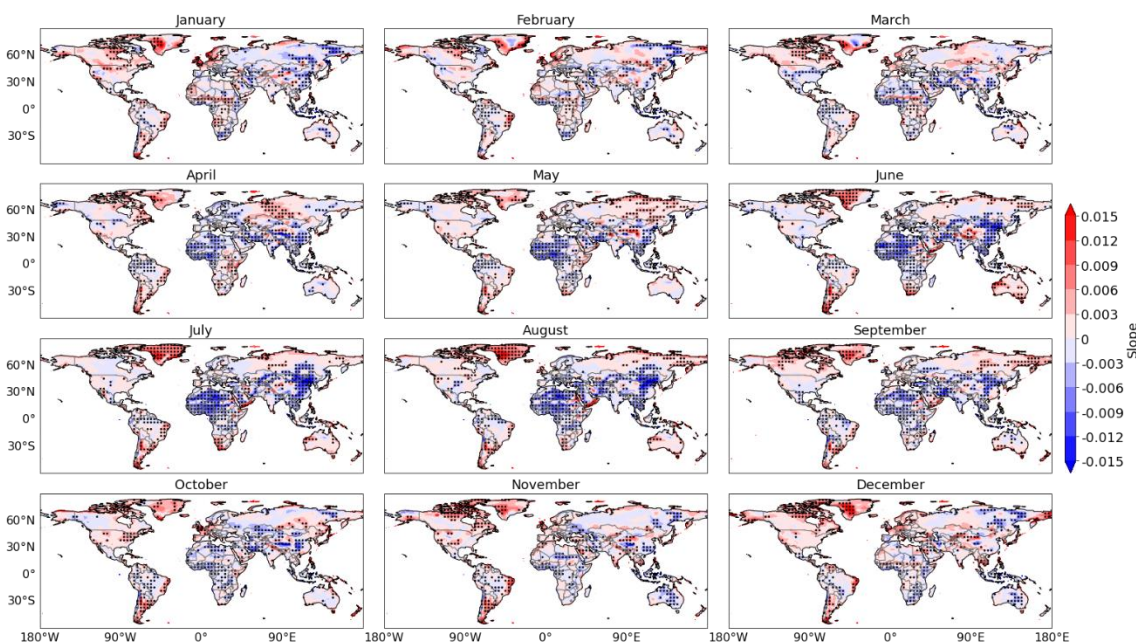


Figure E14 Mann-Kendal trend test of the monthly wind speed from 1948 to 2016. Black dots indicate significance at $p=0.05$ level, and shading is the Theil-Sen slope.

APPENDIX F

SUPPLEMENTARY DATA OF CHAPTER 7

Extraterrestrial radiation, R_a , can be calculated as:

$$R_a = \frac{24(60)}{\pi} G_{so} d_r [\omega_s \sin(\varphi) \sin(\delta) + \cos(\varphi) \cos(\delta) \sin(\omega_s)] \quad (\text{Equation F1})$$

where G_{so} is the solar constant = 0.0820 MJ m⁻² min⁻¹; d_r is the relative distance of the sun from the earth; δ is the declination, i.e., the difference between the magnetic north and the true north; ω_s is the sunset hour angle in radians for latitude <55°; and φ is the latitude in radians (1 radian = $\frac{\pi}{180}$ degrees, negative for southern latitudes).

$$d_r = 1.0 + 0.033 \cos\left(\frac{2\pi}{365} J\right) \quad (\text{Equation F2})$$

$$\delta = 0.409 \sin\left(\frac{2\pi}{365} J - 1.39\right) \quad (\text{Equation F3})$$

where J is the Julian day between 1 (1 January) and 365 or 366 (31 December).

The sunset hour angle in radians for latitude <55°, ω_s can be calculated as:

$$\omega_s = \arccos [-\tan(\varphi) \times \tan(\delta)] \quad (\text{Equation F4})$$

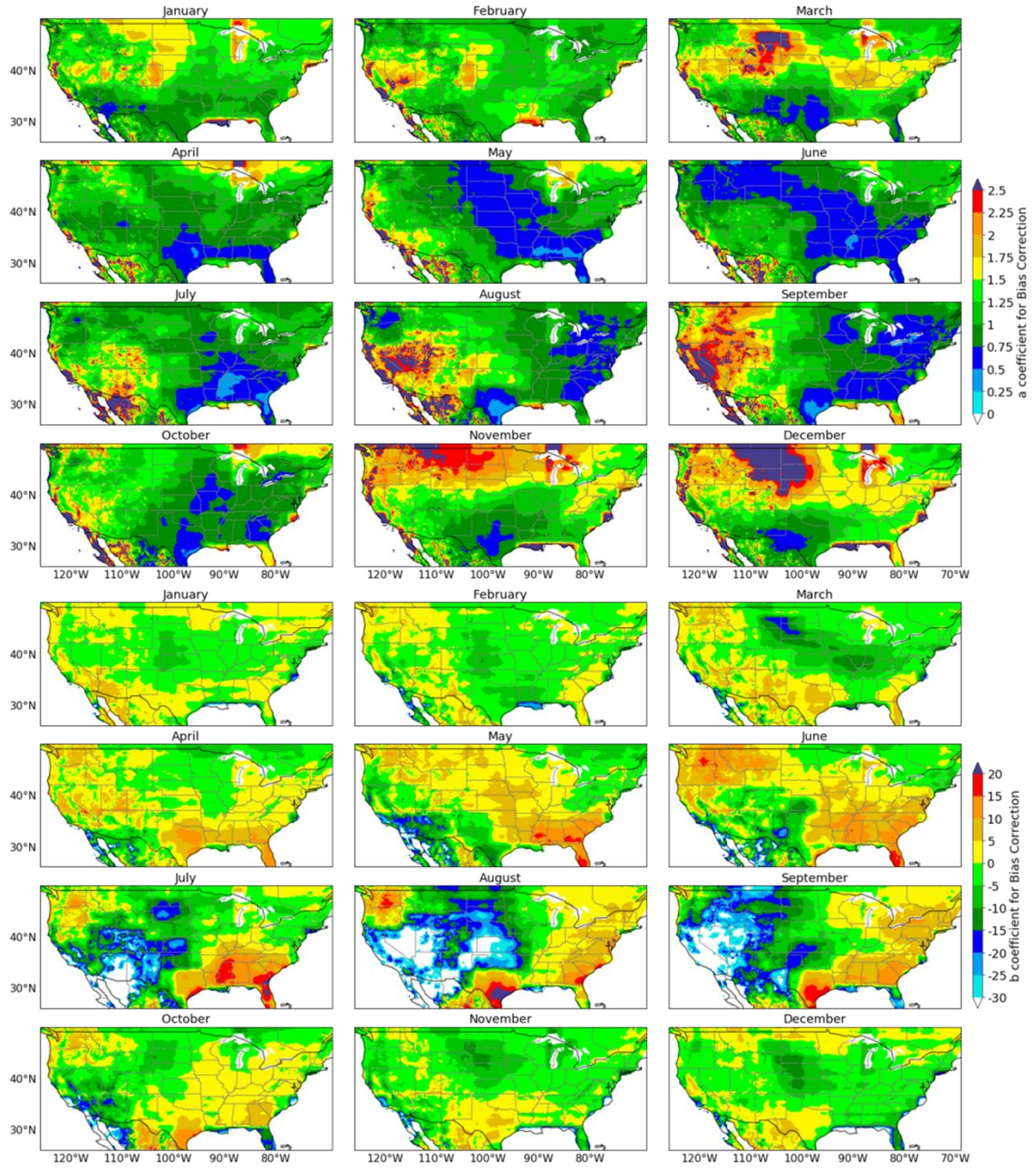


Figure F1 Calibrated parameters of T_{max} for downscaling method. $a = \frac{\sigma_{0,ref}}{\sigma_{M,ref}}$, and $b = \overline{O_{ref}} - \frac{\sigma_{0,ref}}{\sigma_{M,ref}} \overline{M_{ref}}$.

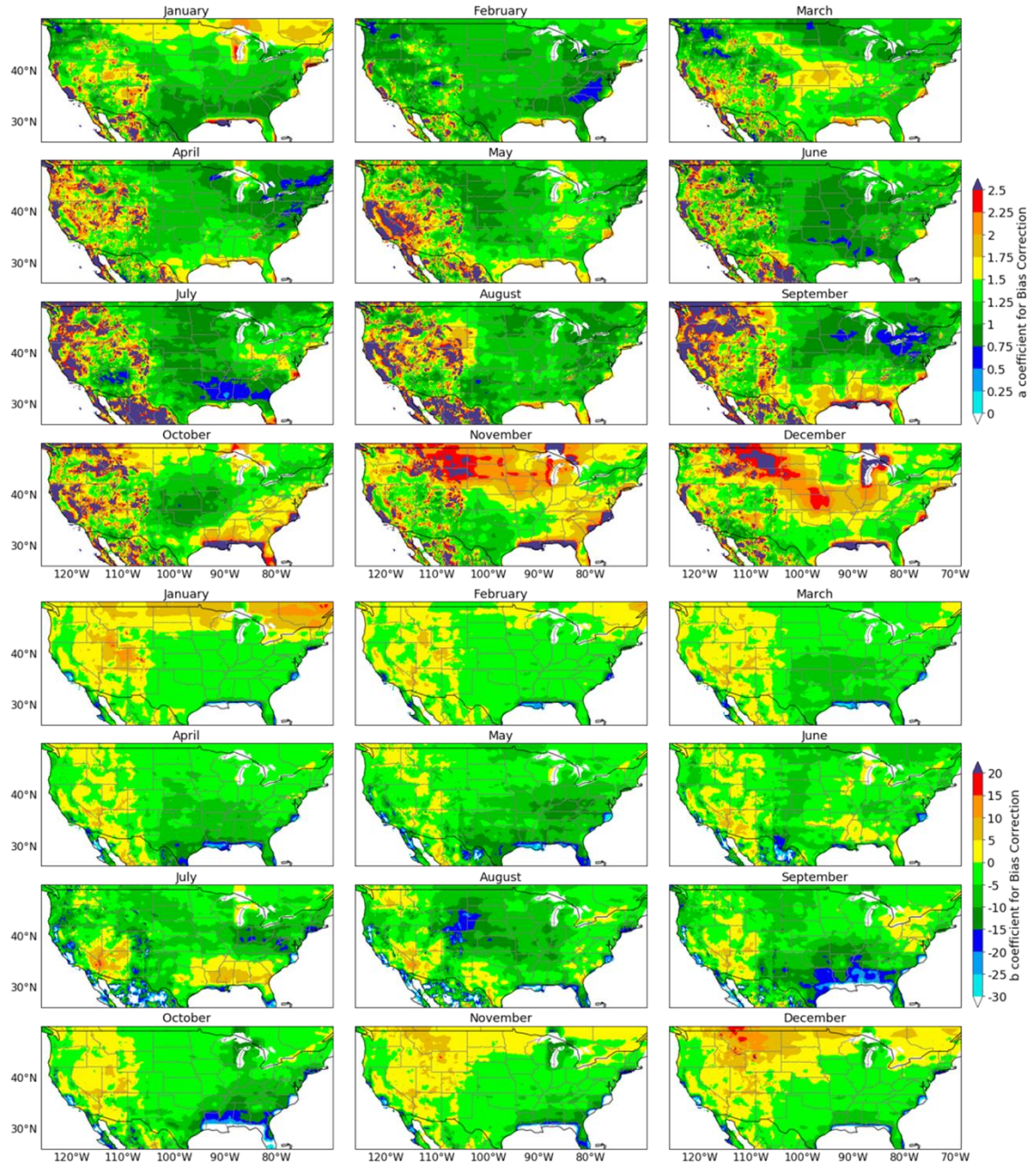


Figure F2 Calibrated parameters of T_{min} for downscaling method. $a = \frac{\sigma_{O,ref}}{\sigma_{M,ref}}$, and $b = \frac{\overline{O_{ref}} - \frac{\sigma_{O,ref}}{\sigma_{M,ref}} \overline{M_{ref}}}{\sigma_{M,ref}}$.

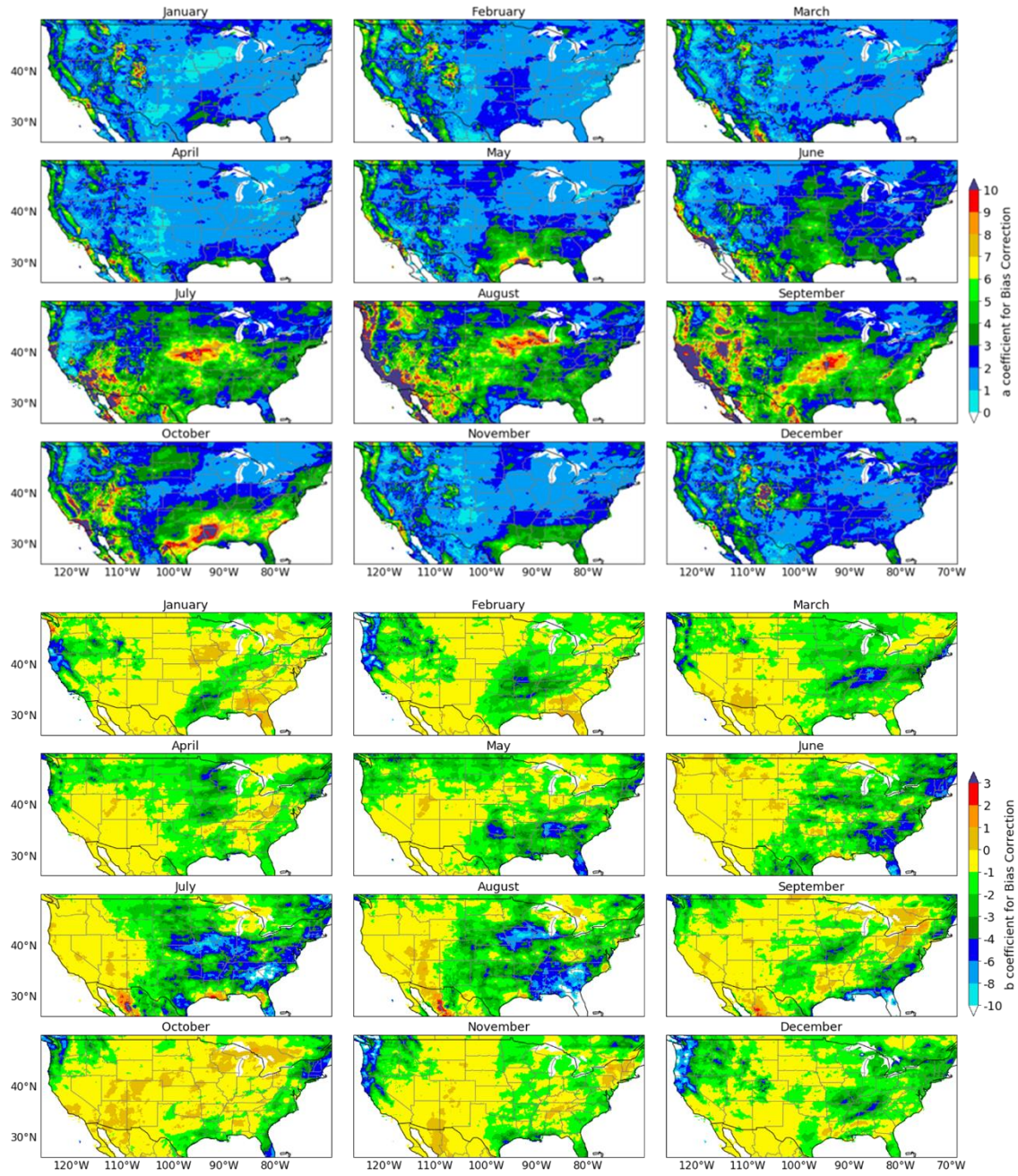


Figure F3 Calibrated parameters of precipitation for downscaling method. $a = \frac{\sigma_{0,ref}}{\sigma_{M,ref}}$, and $b = \overline{O_{ref}} - \frac{\sigma_{0,ref}}{\sigma_{M,ref}} \overline{M_{ref}}$.

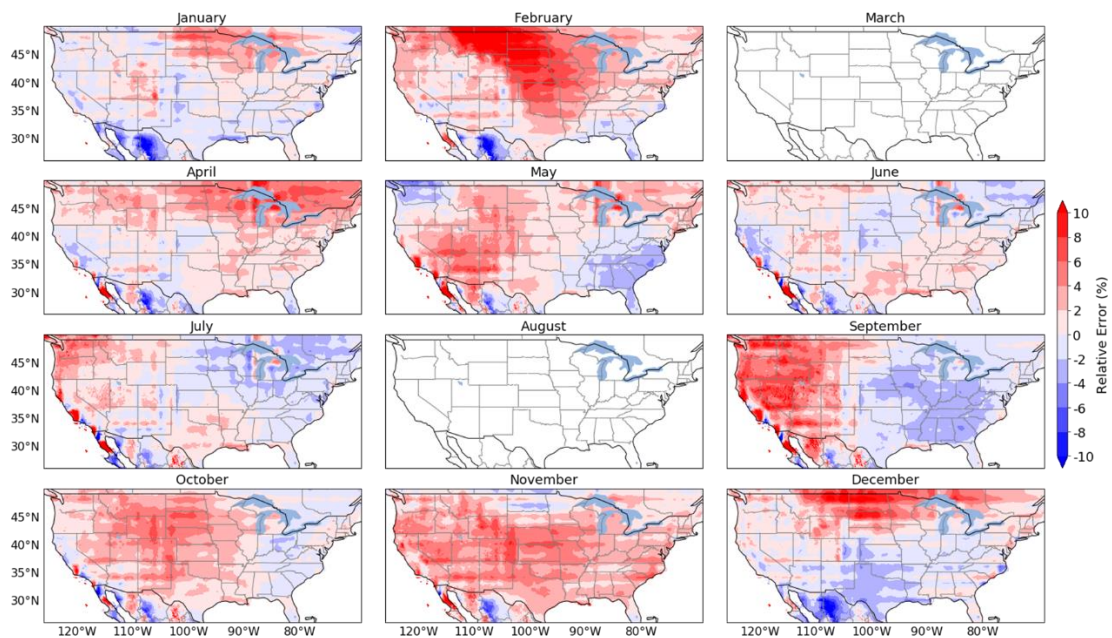


Figure F4 Relative error (%) of the monthly mean maximum temperature of downscaled CanCM4 relative to DAYMET in 2019. Blank indicates that data is unavailable.

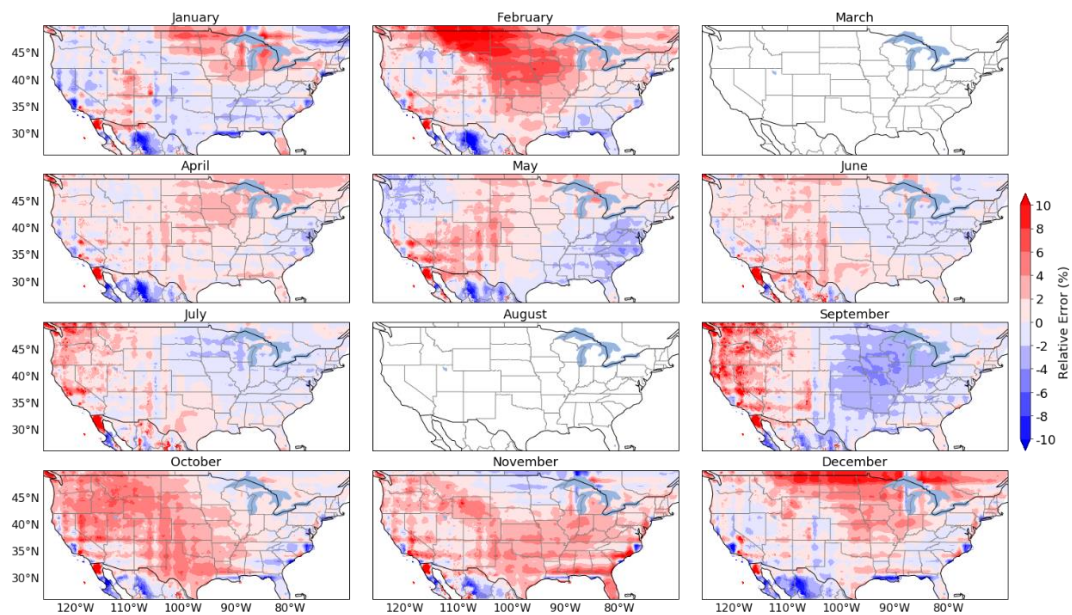


Figure F5 Relative error (%) of the monthly mean minimum temperature downscaled CanCM4 relative to DAYMET in 2019. Blank indicates that data is unavailable.

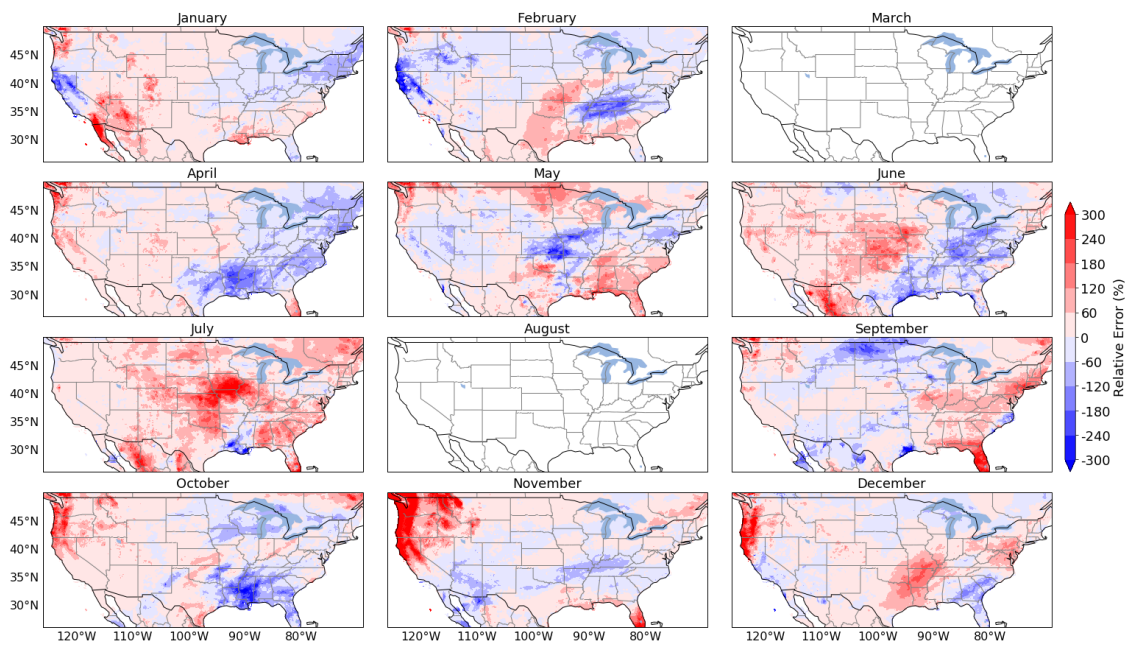


Figure F6 Relative error (%) of the monthly total precipitation downscaled CanCM4 relative to DAYMET in 2019. Blank indicates that data is unavailable.

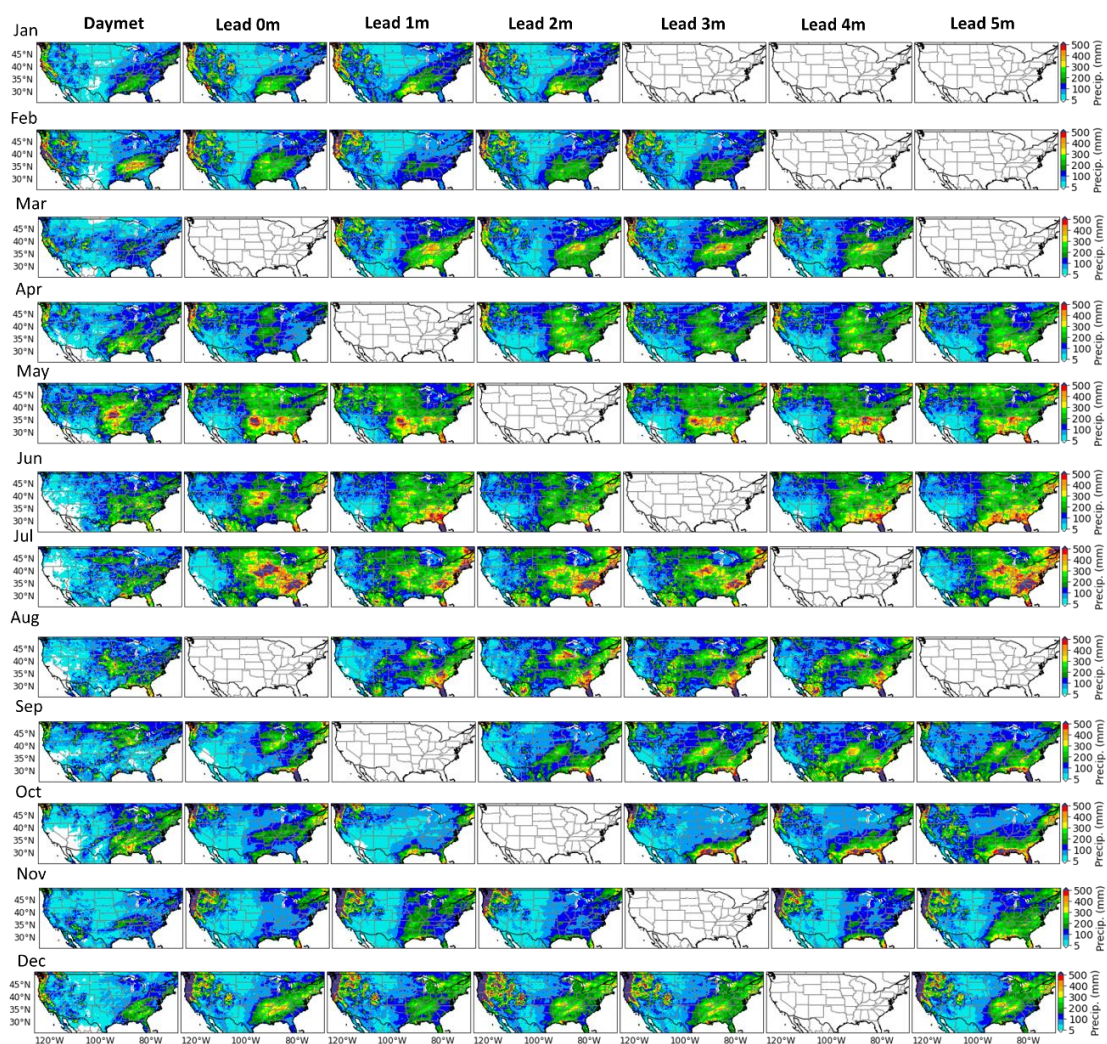


Figure F7 Precipitation prediction of the downscaled method at different lead times in 2019. Blank indicates that data is unavailable.

APPENDIX G

SUPPLEMENTARY DATA OF CHAPTER 8

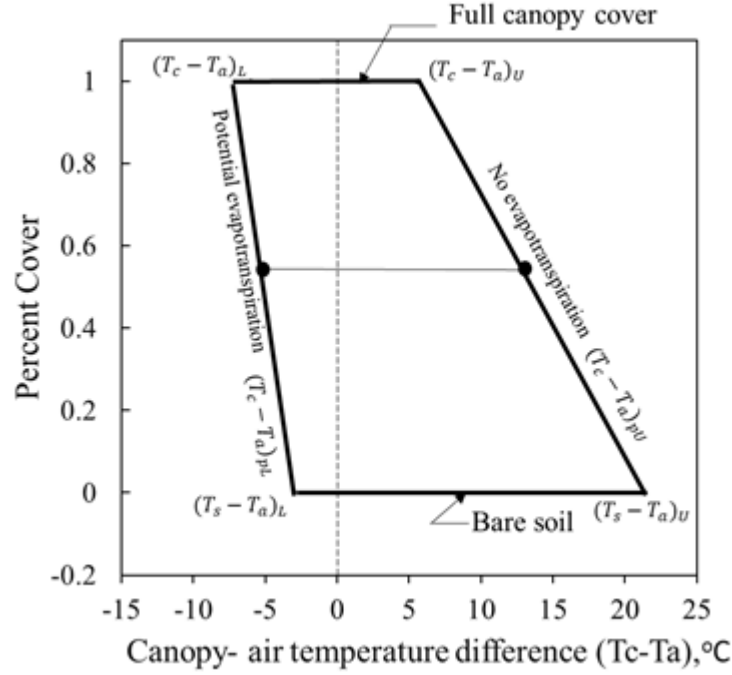


Figure G1 Illustration of different boundary conditions using the WDI method.

Adjusted water stress index or water deficit index (WDI) for low canopy coverage can be calculated as:

$$WDI = \frac{(T_c - T_a) - (T_c - T_a)_{pu}}{(T_s - T_a)_{pu} - (T_c - T_a)_{pl}} \quad \text{Equation (G1)}$$

$$(T_c - T_a)_{pu} = p(T_c - T_a)_U + (1 - p)(T_s - T_a)_U \quad \text{Equation (G2)}$$

$$(T_c - T_a)_{pl} = p(T_c - T_a)_L + (1 - p)(T_s - T_a)_L \quad \text{Equation (G3)}$$

For full-cover, well-watered vegetation, the lower boundary $(T_c - T_a)_L$ is calculated as:

$$(T_c - T_a)_L = \frac{r_a}{\rho C_p} \frac{\gamma(1 + \frac{r_{c_min}}{r_a})}{\Delta + \gamma(1 + \frac{r_{c_min}}{r_a})} (R_n - G) - \frac{e_a^* - e_a}{\Delta + \gamma(1 + \frac{r_{c_min}}{r_a})} \quad \text{Equation (G4)}$$

For full-cover, vegetation with no available water, the upper boundary $(T_c - T_a)_U$ can be calculated as:

$$(T_c - T_a)_U = \frac{r_a}{\rho C_p} \frac{\gamma(1 + \frac{r_{c_max}}{r_a})}{\Delta + \gamma(1 + \frac{r_{c_max}}{r_a})} (R_n - G) - \frac{e_a^* - e_a}{\Delta + \gamma(1 + \frac{r_{c_max}}{r_a})} \quad \text{Equation (G5)}$$

where r_{c_min} and r_{c_max} are the maximum and minimum canopy resistance (r_c); T_c is the canopy temperature ($^{\circ}\text{C}$); T_a is the air temperature from the local sensor ($^{\circ}\text{C}$); $(T_c - T_a)_U$ is the upper boundary of $(T_c - T_a)$ for full-cover vegetation with no available water, representing dry surface condition; $(T_c - T_a)_L$ is the lower boundary of $(T_c - T_a)$ for full-cover, well-water vegetation, representing non-water-stressed baselines.

For saturated bare soil, $r_c = 0$ (the case of a free water surface). The lower boundary $(T_s - T_a)_L$ is:

$$(T_s - T_a)_L = \frac{r_a}{\rho C_p} \frac{\gamma}{\Delta + \gamma} (R_n - G) - \frac{e_a^* - e_a}{\Delta + \gamma} \quad \text{Equation (G6)}$$

For dry bare soil, $r_c = \infty$, the lower boundary $(T_s - T_a)_u$ is described as:

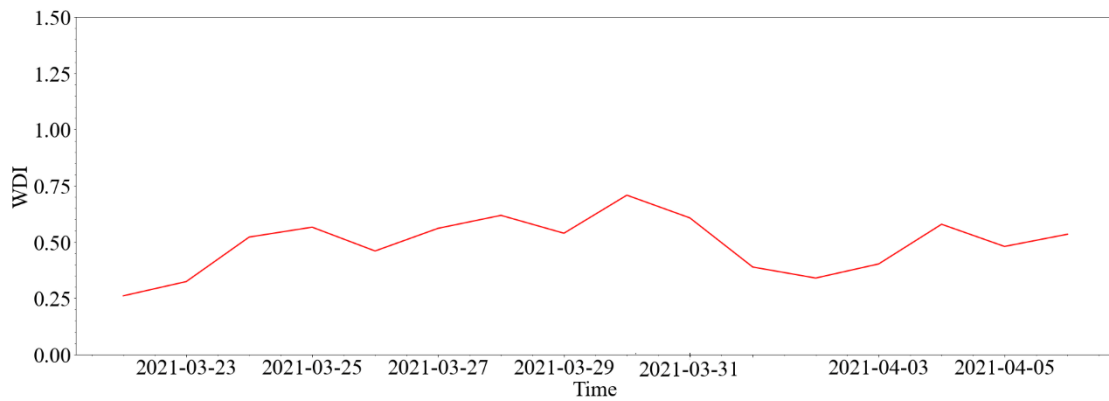
$$(T_s - T_a)_U = \frac{r_a(R_n - G)}{\rho C_p} \quad \text{Equation (G7)}$$

Adjust R_n and G for saturated and bare soil conditions.

Table G1 Major Parameters to Calculate the Four boundaries.

Parameters	$(T_c - T_a)_L$	$(T_c - T_a)_U$	$(T_s - T_a)_L$	$(T_s - T_a)_U$
Albedo	0.23	0.23	0.16	0.23
LAI at Full cover	4	4	-	-
Maximum height (m)	1.2	1.2		
R_n ($\text{MJ m}^{-2} \text{d}^{-1}$)	$0.77 R_s$	$0.77 R_s$	$0.84 R_s$	$0.77 R_s$
G ($\text{MJ m}^{-2} \text{d}^{-1}$)	$0.1 R_n$	$0.1 R_n$	$0.3 R_n$	$0.3 R_n$
Canopy resistance (m s^{-1})	25	1000	-	-
Aerodynamic resistance (m s^{-1})	$\frac{26.12}{U_z}$	$\frac{26.12}{U_z}$	53	53

Note: Albedo values for dry and wet soil are from [Fontes, Adan Fimbres, 1996. Soil albedo in relation to soil color, moisture, and roughness. The University of Arizona] Soli types are fine-loamy, mixed, superactive, thermic Typic Haplustalfs, TX.

**Figure G2 WDI test in irrigation field with bare soil in 2021.**